UNIVERSIDAD DE ANTIOQUIA

EVALUATION OF OLEORESIN-BASED COMPOUNDS AS ADDITIVES TO DIESEL FUELS

Author

Duban Fabián García Navas

Universidad de Antioquia

Facultad de Ingeniería, Departamento de Ingeniería Química

Medellín, Colombia

2020

This page intentionally left blank

Evaluation of oleoresin-based compounds as additives to diesel fuels

Duban Fabián García Navas

A thesis submitted in conformity with the requirements
for the degree of Doctor of Chemical Engineering.

Advisor.

Felipe Bustamante Londoño, Doctor of Chemical Engineering

Co-Advisor.

Edwin Alexis Alarcón Durango, Doctor of Chemical Engineering

Universidad de Antioquia
Facultad de Ingeniería, Departamento de Ingeniería Química.
Medellín, Colombia
2020.

This page intentionally left blank

Abstract

Evaluation of oleoresin-based compounds as additives to diesel fuels

Duban Fabián García Navas
https://orcid.org/0000-0001-7964-7437

Doctor of Chemical Engineering

Chemical Engineering Graduate Program

Despite the marked reduction in proven reserves of fossil fuels and their contribution to global warming, it is expected that diesel engines will continue to play a key role in road transportation worldwide : on the one hand, diesel engines present high power-output, fuel and thermal efficiency, and durability; and, on the other, new technologies still need to overcome technical limitations and reach the stage of economic viability. Furthermore, as the road to cleaner and environmentally-friendly transportation would include biofuels, sustainability issues should be considered, such as the feedstock used in the production of the biofuel. In particular, conifer trees, which are encountered in many places on earth and may growth in otherwise barren soils, produce pine oleoresin by bleeding; pine oleoresin can be also obtained as a byproduct of Kraft process in the pulp industry. Turpentine oil and the non-volatile rosin or colophony are then obtained by distillation of oleoresin. Turpentine has been tested as additive (i.e., below 1%) in several fuel formulations and directly as component (i.e., up to 40%) in diesel fuels, and its transformation, e.g., hydrogenation (to remove unsaturation) and oxyfunctionalization, has been proposed. Prior transformations are required to use of rosin as fuel, however, to break its heavy and complex molecules into smaller hydrocarbons.

In this work, the potential of oleoresin-oxygenated molecules as components or additives of diesel fuel was evaluated. Firstly, the combustion of five molecules which can be obtained from oleoresin by oxyfunctionalization (i.e., nopol, terpineol — with α-terpineol as the main isomer, myrtenol, borneol, and abietic acid methyl ester — AAME) was studied to assess their influence on emissions of the main pollutants (carbon monoxide — CO, unburned hydrocarbons — UHC, and nitrogen oxides — NOx) and flame characteristics (i.e., temperature and height) in non-premixed co-flow laminar flames of *n*-heptane + oleoresin derivative blends. CO and UHC

emission were reduced and the flame temperature was increased (leading to an increase in NOx emissions) in the blends with alcohols, which suggests an improvement in the combustion. Nopol stands out between the alcohols probably due to the longest sidechain where the hydroxyl group is attached in. Conversely, AAME, which, although soluble in *n*-heptane at low content, is solid at ambient conditions, showed a deterioration in the combustion.

The Prins condensation reaction was then performed to transform β-pinene from turpentine into nopol without previous separation (the molecule with best performance in the combustion tests), with high conversion and high selectivity (>99%). The reaction was scaled-up to 10 L with minor impact on the performance. Furthermore, the properties of blends of the oxyfunctionalized turpentine in diesel up to 20 % vol. are within the limits established by European Standard EN 590:2013 (diesel fuel with high quality). In addition, this blend was used as fuel in a Euro 6 direct injection engine to evaluate the influence of oxyturpentine on performance and emissions. A reduction in particulate number, particulate matter and nitrogen oxides, and an increase in carbon monoxide and hydrocarbon emissions (as it has been reported for oxygenated fuels such as alcohols) was observed. All emissions were under the limits established by the NEDC protocol (a valid protocol for vehicle testing currently in Colombia and other American, Asian and African countries), suggesting a high potential of the oxygenated turpentine as component of diesel fuel.

Keywords: fuel production; turpentine; rosin; nopol; emissions; catalysis; engine

Acknowledgements

The financial support of the project was granted by *Universidad de Antioquia* and *Departamento Administrativo de Ciencia, Tecnología e Innovación* – COLCIENCIAS through the projects PRG2014-1091 (internal code ES84150111) and 37-1-693 (contract FP44842-124-2017), respectively. COLCIENCIAS support my doctoral scholarship through the call 727 of 2015. These institutions are widely acknowledged by me and my advisors.

The development of the project experimental part was performed in the laboratories of Environmental Catalysis Research Group at Universidad de Antioquia (Medellín, Colombia) and in the Fuel and Engines Group at University of Castilla-La Mancha (Ciudad Real, Spain). I am very grateful with these research centers.

The professor Edwin Alarcón was the first person which receive to me at Medellín. He was a strong support in my doctoral degree. I am very grateful about him. Likewise, the professor Felipe Bustamante agreed my thesis work, and from the first moment he has been encouraging me and supporting the progress of the project. The professor Magín Lapuerta opened the doors of their team and advise my internship in Spain, which enhance notably the results of the project. The professor Aida Villa was always willing to support me.

I also acknowledge to all the people from Environmental Catalysis Research Group (specially Juan Miguel, Ivan, Ana, Sara, Alex, Lina and Juan Pablo) and Fuel and Engines Group (David, Ángel, Pepe, Rayda, Rocío and Alexis), because they support me technically and personally.

My parents, brothers, sister, wife and daughter are also acknowledged because they are the mind support to the daily work.

Thanks to everyone.

This page intentionally left blank

Dedication

To my wonderful-wife Leidy and my great-daughter Martina.

This page intentionally left blank

Table of contents

List of tables

Chapter 1

Chapter 2

Chapter 3

Chapter 4

Chapter 5

Chapter 6

Chapter 7

Appendices

List of figures

Chapter 1

Chapter 2

Chapter 3

Chapter 4

Chapter 5

Chapter 6

Chapter 7

Appendices

Nomenclature

The most frequently used notation in this Thesis is presented.

Abbreviations,

AA	Atomic absorption
AAME	Abietic acid methyl ester
CD	Combustion delay
CFPP	Cold filter plugging point
DCN	Derived-cetane number
DOC	Diesel oxidation catalyst
DPF	Diesel particle filter
DSC	Differential scanning calorimetry
DVPE	Dry vapor pressure equivalent
EEPS	Engine Exhaust Particle Sizer
EGR	Ehaust gas recirculation
EOS	Equation of state
Exp	Experimental
FID	Flame ionization detector
FTIR	Fourier-transform infrared
GC	Gas crhomathography
H/C	Hydrogen-to-carbon molar ratio
HAB	Height above burner
HATR	Horizontal attenuated total reflectance
HC	Hydrocarbons
HFRR	High frequency reciprocating rig
HHV	Higher heating value
HSP	Hansen solubility parameter
HV	Heating value
ID	Ignition delay
LHV	Lower heating value
LNT	Lean NOx trap
ME	methyl ester
MS	Mass spectrometry
MTABr	Myristyl-trimethyl-ammonium bromide

MW	Molecualr weight
ND	Not data or Not detected
NDIR	Non-dispersive infrared spectroscopy
NEDC	New European Driving Cycle
NM	Not measured
NOx	Nitrogen oxides
OESI	Oxygenated-extended sooting index
PM	Particulate matter
PN	Particulate number
PTFE	Poly-tetra-fluoro-ethylene
TCD	Thermal conductivity detector
TEOS	Tetra-ethyl-orthosilicate
TMAH	Tetra-methyl-ammonium hydroxide
TPD	Temperature programmed desorption
TSI	Threshold sooting index
UHC	Unburnt hydrocarbons
vol.	In vol basis
WSD	Wear scar diameter
wt.	In weight basis
XRD	X-ray difraction

English symbols,

A	Air flow
D	Particle diameter
EI	Emission index
F	Fuel flow
GC_B	Group Contribution of Benson
GC_J	Group Contribution of Joback
H	Height of flame
H_o	Flame height for pure *n*-heptane
H_{Prod}	Enthalpy of products
H_{React}	Enthalpy of reactants
$\dot{m}$	Mass flow
p_c	Critical pressure
Q	Heat/ volumetric flow
S	Molar stoichiometric oxidezer-to-fuel ratio
T_{ad}	Adiabatic flame temperature

T_∞	Surrounding temperature
T_b	Boiling temperature
T_c	Critical temerature
T_m	Melting temperature
T_o	Flame temperature for pure *n*-heptane
t_R	Retention time
Wn	Acid number
x	Number of carbon atoms
x_i	Molar fraction of *i*
y	Number of hydrogen atoms
y_i	Mass fraction of *i*
z	Number of oxygen atoms
ΔH_f^0	Standard heat of formation
ΔH_v^0	Standard heat of vaporization

Greek symbols,

α	Thermal diffusivity
ε	Emissivity
ϕ	Equialence ratio
κ	Thermal conductivity
ρ	Density
τ	Torque
ν	Kinematic viscosity
ω	Acentric factor

This page intentionally left blank

Chapter 1. Introduction

1.1 Alternative fuels

1.1.1 Background

Because of the higher power output, fuel and thermal efficiency, torque, and durability of the diesel engine in comparison to the spark ignition engine, road transportation is a major consumer of diesel fuel [1]. Thence, it is expected that diesel fuel will continue to play a key role in global market. Therefore, it is important to design diesel additives and/or components from diverse and renewable sources, at low costs and in green processes, which could improve the combustion of diesel fuels.

Oxygenated compounds have shown improvements in the combustion of typical fuels [2]. These compounds can improve the combustion, increase the engine performance and reduce some pollutants [3], and may be obtained from renewable sources. In recent years, different alcohols, such as methanol, ethanol, butanol and 1-pentanol have been studied in blends with diesel and diesel/biodiesel, with concentrations of up to 30 vol. %. Reductions in emissions and viscosity were found, whereas energy performance was similar to pure diesel or diesel/biodiesel blends [4]–[7].

Currently, the use of blends of (up to 10 vol. %) biodiesel and diesel is mandatory in Colombia. The biodiesel, obtained from crude palm oil, is an oxygenated compound with higher density and viscosity than conventional diesel. Due to the oxygenated nature of biodiesel, an improvement of combustion process is evidenced. By increasing the ratio of biodiesel in the blends, the smoke opacity and temperature, and hydrocarbon, carbon monoxide and carbon dioxide emissions, are decreased [8]. The oxygen content contributes to reduction in soot and particulate material, as

well as polycyclic aromatic hydrocarbons. In addition, engine performance of diesel/biodiesel blends is very similar to that of petroleum diesel [1], [9], [10].

The oxygen content of *n*-alcohols is higher than that of biodiesel [1] which would translate into better combustion of alcohol + fuel blends. Use of alcohols in diesel and biodiesel blends influences other fuel properties, such as lubricity (related to the engine durability) and flash point (related to the risk associated to storage and transport of fuels) [11].

The engine tests at transient conditions with three different fuels (neat diesel fuel and diesel fuel blended with either biodiesel or *n*-butanol) show that combustion behavior and stability during the first transient cycles are affected mostly by the biodiesel blend and less by the *n*-butanol blend. The biodiesel blend resulted in a significant increase in smoke opacity, whereas there was a decrease with the *n*-butanol blend [12] suggesting that alcohols influence better than biodiesel the combustion in transient conditions.

Biodiesel and normal alcohols have shown positive influence in engine tests, reducing some pollutants at similar engine performance, but drawbacks such as the high viscosity and cold-flow properties of biodiesel, and high volatility, low viscosity and latent heat of normal alcohols, impact the injection and diffusion of the fuel blend. Therefore, the study of new oxygenated molecules may help improving diesel properties, such as stability, volatility, viscosity, cold-flow properties, lubricity, or flash point, and simultaneously reduce pollutant emissions.

1.1.2 Production of alternative fuels

Renewable and alternative fuels are obtained from biomass, which is naturally available or cultivated with this purpose. Biomass represents vegetable crops, forest production, alga, and animal and vegetable wastes. The majority of biomass requires prior treatment and transformation to be used as fuel. A classification of methods to produce alternative fuels from biomass is based on the feedstock and the product obtained, as shown in Figure 1.1 [13].

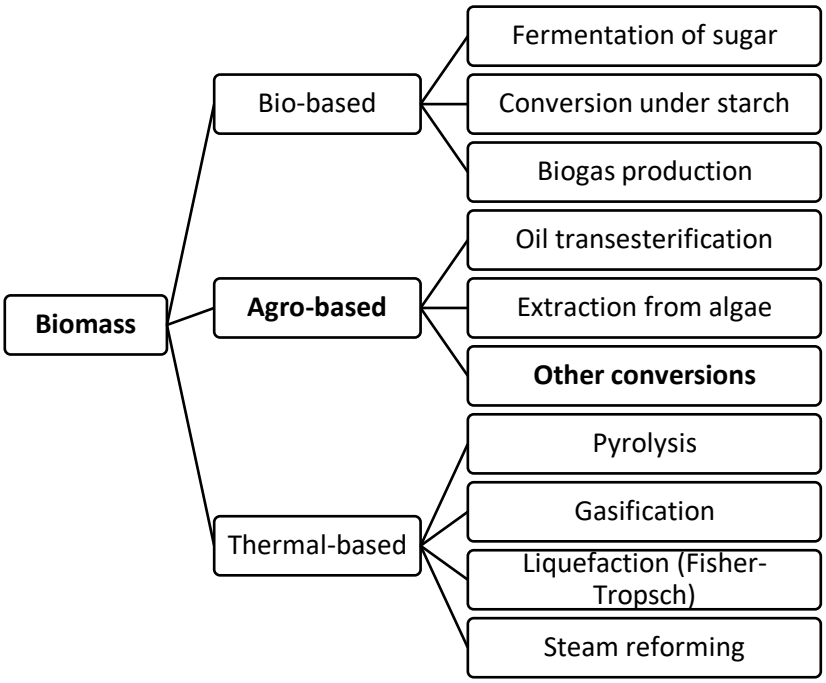

Figure 1.1. Production of alternative fuels from biomass [13]

Bio-based production of fuels involves the utilization of microorganisms, for instance, the fermentation of sugar to obtain ethanol or *n*-butanol. Gasification and pyrolysis are typical examples of treatments with temperature to obtain gas and liquid alternative fuels. Production of biodiesel from vegetable oils, on the other hand, requires the cultivation and crops of seeds by farming methods, which later are treated to be transformed into fuels with processes as transesterification.

Other transformations from biomass have been investigated, such as hydrogenation, cracking, esterification, condensations, among others, using residues to obtain molecules with fuel properties. Generally, these transformations involve catalysts which increase fuel yield while reducing reaction times or dispensing with hazardous substances. Heterogeneous catalysts are preferred because they are easily separated from reaction products, their disposal is relatively easy and, in some cases, they are low-cost materials. Thus, from a technical, environmental and economical standpoint its use should be encouraged.

1.1.3 Scaling procedures

Novel reactions to synthesize fuels are usually conducted and optimized at lab scale, in fact, a few mL is produced. Thus, scaling-up of the reaction plays an important

role in the evaluation of the actual potential of biomass-derived fuels. There are three types of scaling-up approaches: physical, experimental and fundamental (or phenomenological). The fundamental approach involves the solution of a detailed (and complex) model of the system, while the experimental one is based on trial and error, thus being a lengthy and costly process. Physical approach, on the other hand, is based on dimensionless numbers and variables, and relationships to relate the same process at different scales [14].

In particular, reaction scaling-up should ensure similar conditions in the large and laboratory scales, especially chemical thermodynamics and kinetics: if these factors are conserved, the chemistry should be identical in the new scale. For heterogeneous reactions, however, heat and mass transfer accompany the chemical reaction, and is necessary to guarantee that both transfer processes are similar in the new scale [15]. This topic is further discussed in Appendix A.

1.2 Oleoresin as biofuel

1.2.1 Oleoresin components

Oleoresin is a complex mixture of volatile monoterpenes (turpentine) and less volatile diterpene resin acids (colophony or rosin) obtained from conifer trees (see Figure 1.2).

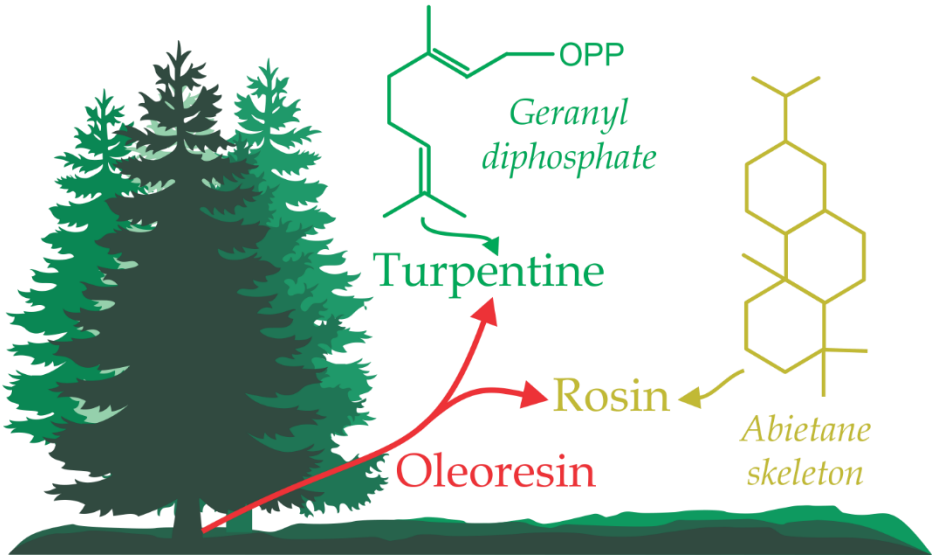

Figure 1.2. Oleoresin components

Although the composition of the oleoresin depends on the type of the conifer tree, in general the content of turpentine (with α- and β-pinene as the main components) is less than 20%, and the fraction of rosin is up to 80% (where 90% are isomeric abietic acids and 10% is a mixture of dihydroabietic and dehydroabietic acids); distillation is necessary to separate the turpentine and the rosin [16]–[19].

Main compounds of rosin have chemical structure from abietane skeleton, whereas a common carbocationic reaction starting with the ionization of the geranyl diphosphate substrate has been established as the mechanism for all monoterpene synthesis [20].

Turpentine is a mixture of monoterpenes, where α and β-pinene are the major components, and β-myrcene, limonene, camphene and Δ3-carene are among the minor components. Molecular structures of main components of turpentine are presented in Figure 1.3.

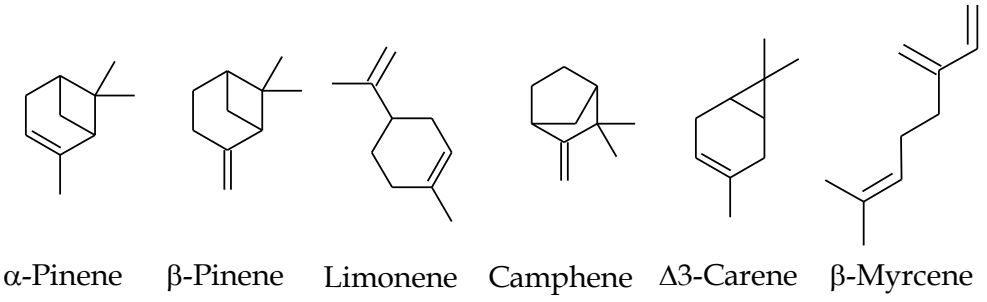

Figure 1.3. Molecular structure for main components of turpentine

Table 1.1. Composition of turpentine from different parts of the world. Data collected from [19], [21], [22] and from own measurements

Compound[a]	CAS	Composition (% wt.)				
		USA	Indonesia	North Europa	China	Spain[b]
α -pinene	80-56-8	40-70	73-87	55-70	40-70	70-76
β-pinene	127-91-3	15-35	1-2	2-6	4-15	14-20
Limonene	138-86-3	--	1-2	--	--	2-4
β-Myrcene	123-35-3	--	~1	--	--	~1
Δ3-carene	13466-78-9	2-10	7-19	7-30	0-5	<1
Camphene	79-92-5	1-2	~1	~1	1-2	1-2

[a]Molecular formula for all compounds is $C_{10}H_{16}$; [b]own measurements

Composition depends on the origin of turpentine. Typical composition of turpentine from different parts of the world is shown in Table 1.1. In all cases α-pinene is the

main component, but turpentine from USA, China and Spain have relatively high contents of β-pinene. The amount of camphene, limonene, Δ3-carene and myrcene is usually low.

Depending on the recovery method there are different kinds of rosin: wood rosin (extracted from pine stumps), gum rosin (tapped from living pine trees), and tall oil rosin (obtained as a by-product in paper pulp production) [18]. Typical composition of rosin from different countries [23] and that measured for rosin commercially available in Colombia is shown in Table 1.2 (the rosin composition was determined by gas chromatography; the methodology is presented in Chapter 3).

Table 1.2. Composition of rosin from different parts of the world. Data collected from [23] and obtained from own measurements

Compound*	**Concentration (% wt.)**					
(acids)	**USA**	**China**	**Honduras**	**India**	**Spain**	**Colombia****
Pimaric	5.1	9.2	9.6	9.2	8.7	2.3
Sandaracopimaric	1.8	2.7	2.2	1.5	1.5	0.0
Communic	2.8	0.0	0.0	0.0	0.0	0.0
Isopimaric	17.0	1.5	17.0	20.0	0.0	11.2
Levopimaric/ Palustric	25.0	22.0	21.0	11.0	27.0	29.7
Dehydroabietic	5.7	4.3	12.0	2.0	1.9	19.7
Abietic	22.0	44.0	22.0	38.0	36.0	21.1
Neoabietic	20.0	15.0	15.0	18.0	24.0	10.9
Others	0.6	1.3	1.2	0.3	0.9	5.1

[a]Molecular formula for all acids is $C_{20}H_{30}O_2$ except dehydroabietic acid ($C_{20}H_{28}O_2$); [b]Locally commercial

According to Table 1.2, abietic acid is the main component of rosin, followed by neoabietic, isopimaric and levopimaric/palustric acids. Communic acid is present only in rosin from the USA, and at low concentration. In addition, levopimaric and palustric acids are usually reported together due to the difficulty to separate them by gas chromatography, specifically after the derivatization (a necessary step to successfully separate the resin acids; details in Chapter 3).

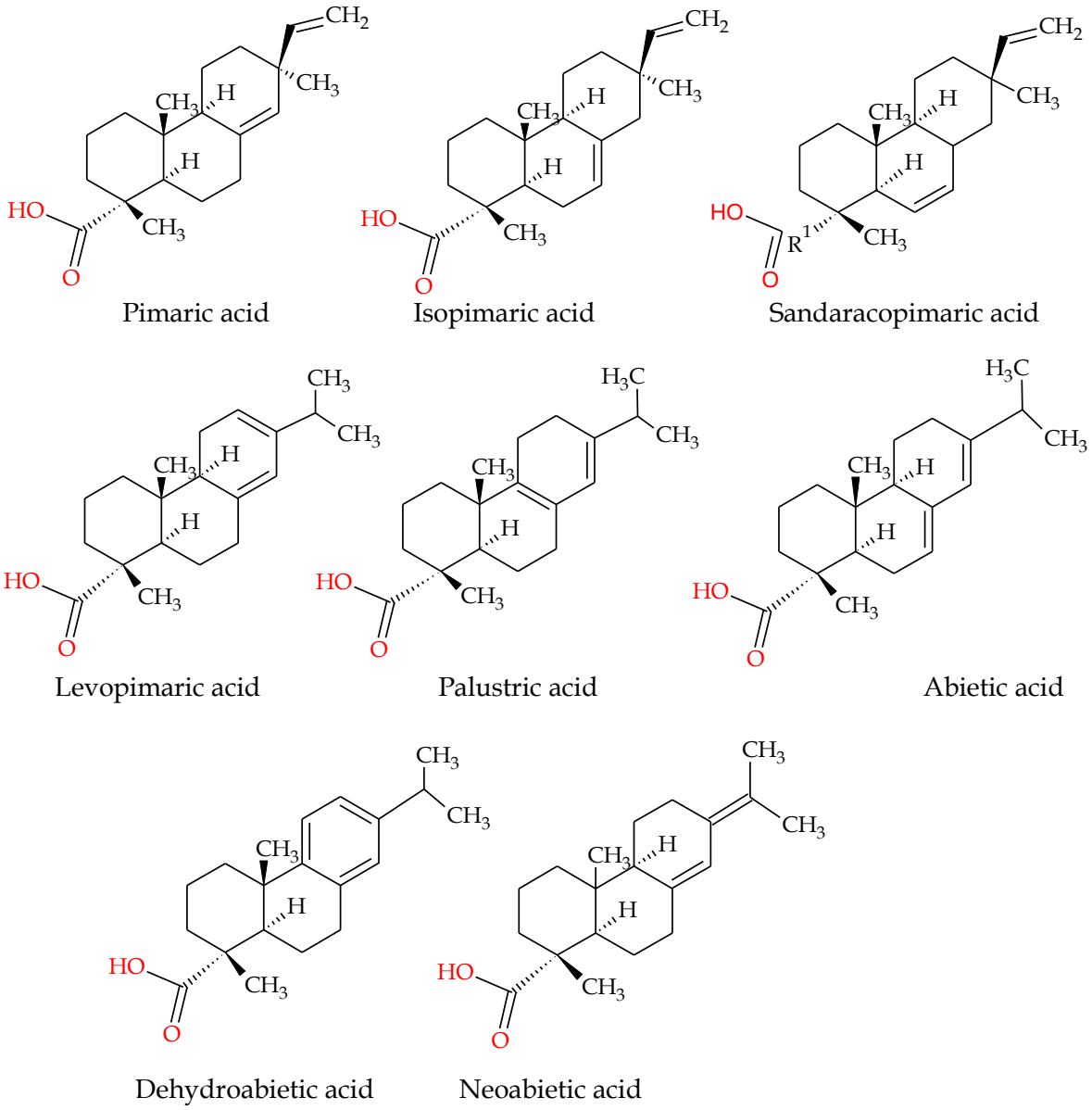

Figure 1.4. Molecular structure for main components rosin

Molecular structures for main components of rosin are shown in Figure 1.4. As a result of the presence of these heavy and complex structures, rosin displays very high viscosity and cannot be used directly as fuel in compression ignition engines.

It is expected that the two main products of distillation of oleoresin, namely, turpentine and rosin, can be transformed into fuel components or additives. Oxygenated compounds from oleoresin present features common to some fuels, and some of these compounds have been studied as components or additive (mainly as a part of additive formulations) of diesel, gasoline and aviation fuels. In

comparison to rosin, the application of turpentine as fuel is facilitated because of its liquid nature and properties apparently similar than those for some fuel and the easier chemical transformation of its components. The next sections show some applications of turpentine and rosin as fuels, either as component or additive of diesel, gasoline and aviation fuels.

1.2.2 Turpentine as fuel

Turpentine had been used as additive in several fuel formulations, performing a key role in decreasing emissions and increasing the useful energy by providing higher calorific value to the fuel, without emissions of harmful species; furthermore, additives from turpentine are obtained in a simple process at low cost [24]–[30]. As constitutive component of fuel, turpentine had been assessed in gasoline (contents between 3-7 vol. % would be suitable for running the engine) [31] and diesel (20-40 vol. % turpentine would provide a performance similar to pure diesel) [32], [33] engines. In addition, a blend of colza oil, paraffinic hydrocarbons, additives and turpentine (content between 10-30 wt.%) was reported to yield a fuel with a reduction in pollutant emissions and improvement in engine performance [34].

Regarding the transformation of turpentine to alternative fuels, α-pinene can be hydrated to produce α-terpineol in the presence of acid catalysts. The reaction product (α-terpineol, unreacted pinene and some minor quantities of other by-products and impurities) has been blended with diesel and biodiesel, and injected to a compression-ignition engine, showing improvements in engine performance and reducing some pollutants, such as carbon monoxide and dioxide [35]–[37].Besides, α-terpineol has been recently used as an octane booster for gasoline fuel. Due to its high-energy density and oxygen content, terpineol improved the brake thermal efficiency and reduced total fuel consumption, displaying similar performance than typical gasoline. Besides, total hydrocarbon and carbon monoxide emissions were reduced [38], [39].

On the other hand, Harvey and coworkers tested a new fuel obtained by selective isomerization and dimerization of pinenes under moderate conditions (100°C and atmospheric pressure), using the heterogeneous acid catalysts Montmorillonite-K10

and Nafion. Then, the mixture of dimers was upgraded through hydrogenation over PtO_2 and fractional distillation. Although the high viscosity may limit their application as stand-alone fuels, their low freezing points suggest that they can be major components of high density fuel mixtures or additives to conventional fuels [40], [41].

Price *et al.* [42] tested mixtures of myrcene, the product of limonene hydrogenation, and diesel fuel, in a fraction larger than 10 vol. %. The presence of these molecules in the fuel lowered the cloud point as well as the fuel viscosity, compared to the base diesel fuel.

In general, several works deal with turpentine and its derivatives, in blends with diesel or gasoline. It is demonstrated that the presence of these molecules improves engine performance by increasing the useful energy and reducing some pollutants, such as carbon monoxide and carbon dioxide, due to a better combustion of the fuels [43]–[47].

1.2.3 Rosin as fuel

To use rosin as fuel, Clark and coworkers reported its conversion into lower molecular weight compounds by catalytic cracking over silica-zirconia-alumina catalyst, at atmospheric pressure and temperature between 350- 500°C in a tubular reactor. The oil product was a complex mixture of hydrocarbons (80-90%) with some phenolic and acidic materials, with a specific gravity of 0.9-0.91 at 25°C [48].

Coll and coworkers proposed the hydrotreatment of abietic and dehydroabietic acid compounds over commercial NiMo and CoMo catalysts, which allowed obtaining saturated hydrocarbons (mainly saturated tricyclic rings) that could be used as diesel fuel additives. The authors claim that the direct use of tall oil rosin is not possible because of poor rheological properties at low temperatures, contamination of the lubricating oil, coking of the diesel engine, and excessive corrosion in some engine parts. Since hydrotreatment is a mature technology in oil refineries, it could be applied without substantial modifications to other types of organic compounds, in particular by removal of carboxylic groups to produce a hydrocarbon and carbon dioxide and the hydrogenation of the unsaturated bonds. The liquid products display

a density between 30 to 45°API and the cetane index of the liquid product is between 28 and 43 [49], [50].

Mikulec and coworkers tested three commercial hydrocracking catalysts in the hydrotreating of the crude depitched tall oil (volatile fraction of crude tall oil distillation): NiW/γ-Al_2O_3-zeolite, Ni-Mo, and Ni-W hydrotreating catalysts. NiW and NiMo catalysts were found to be active for hydrotreating a mixture of crude depitched tall oil and atmospheric gas oil. The reaction pathway of crude tall oil involves hydrogenation of double bonds, decarboxylation, hydrodeoxygenation, isomerization, and hydrocracking of alkane and cyclic structures at 360–380ºC and hydrogen pressure of 5.5 MPa. A liquid product with Cetane number between 55 and 58, which is high for a diesel, was obtained with all catalysts. The density ranges between 0.832 and 0.839 g/mL at 15°C [51].

Recently, Anthonykutty and coworkers studied the conversion of crude tall oil over commercial NiMo catalyst to produce a wide range of hydrocarbons, mainly paraffins. They found that at lower temperatures (<400°C) selective deoxygenation routes, such as hydrodeoxygenation, decarboxylation, and decarbonylation, were the most important reactions; at higher temperatures, cracking (thermal or catalytic) and dehydrogenation were evidenced, with cycloalkanes and aromatics as main products, which can be used in fuel blends [52], [53].

Xiao-an and coworkers tested an acid-activated clay in the production of abietane (which is a hydrocarbon molecule that can be used as diesel compound) from rosin in a batch reactor with a water separator, at 270°C for 2 h. The hexadecane number of abietane was 39, lower than that required for diesel fuels (45). Therefore, blends of abietane and additives, such as octyl nitrate and α-olefin were prepared in order to increase this value. The blend of α-olefin and abietane shows a hexadecane number of 52 and density of 0.880 g/mL, when the α-olefin dosage was about 20% [54].

Bernas and coworkers studied the thermal decarboxylation of abietic acid followed by the hydrogenation over Pd/C and Ru/C under hydrogen pressure. The first step (hydrogenation of rosin acid) produces dihydroabietic and tetrahydroabietic acids,

followed by a thermal non-catalytic decarboxylation in toluene which takes place at 200–300°C. The cyclic unsaturated hydrocarbons obtained have a molecular weight of 234–256 g/mol [55].

Gürü and coworkers synthesized organic compounds of Mn, Mg, Cu and Ca using abietic acid from colophony, which were used as diesel fuel additives. The results showed that the Mn-based compound yielded the greatest decrease in freezing point, increase in cetane number, and decrease in viscosity and flash point, as well as reduction of some pollutants, such as carbon monoxide and sulphur dioxide [56], [57].

1.3 Problem statement and hypothesis

Fuels play a key role in different human activities. Nowadays, a change aimed at replacing the fossil fuels is ongoing driven by the strong reduction of proved reserves of fossil sources and the impact on global warming. In the next decades, however, use of diesel fuel is expected to continue because no current technologies can satisfy the need of ground transportation on a low-cost basis [1].

Biofuels are very attractive from an environmental point of view because they can be produced from renewable sources and reduce the life-cycle of greenhouses gases. However, social and economic factors must also be considered. In particular, the feedstock used in the production of biofuels should guarantee food security, and proper use of land and fertilizers, among other aspects [58]. In addition, benefits such as improving the engine performance and the positive environmental impact from reduce pollutant emissions are expected from these biofuels.

Oleoresin from conifer trees (which are encountered in many places on earth and may grow in otherwise barren soils) is composed of rosin and turpentine, which can be transformed into oxygenated molecules to be used as additives or components of diesel fuel. However, an evaluation of the influence on combustion, engine performance and emissions of oleoresin-derived compounds blended with diesel is required to assess their potential as biofuels.

Therefore, this Thesis is based on the following hypotheses:

- ★ Oxyfunctionalization of main components of oleoresin is possible through chemical reactions with heterogeneous catalysis.
- ★ Oxygenated molecules from oleoresin will display fuel-like properties and, thus, will positively influence the combustion (i.e., reducing pollutants, increasing combustion efficiency, etc.). Furthermore, their impact on engine tests, either in diesel and/or biodiesel blends, will be favorable.
- ★ Oxyfunctionalization of the oleoresin can be scaled-up to produce the large amounts required to be used as fuel component.

1.4 Objectives

1.4.1 Main objective

Evaluate the potential of oleoresin-based compounds as diesel additives.

1.4.2 Specific objectives

- ★ Evaluate the combustion performance, in terms of emissions, of model oleoresin-derivatives (turpentine and colophony) using *n*-heptane as diesel surrogate.
- ★ Synthesize the best performance oxyfunctionalized molecule from turpentine and the derivate molecule from colophony.
- ★ Evaluate the combustion performance of the synthesized oleoresin-based additive with diesel blends.
- ★ Evaluate the engine performance of the synthesized oleoresin-based additive with commercial diesel/biodiesel blends.

1.5 Aim and structure of the thesis

Potential of turpentine- and rosin-derived compounds as additives and/or components of diesel fuel was evaluated by selecting molecules which can be oxyfunctionalized, and determining their combustion performance in terms of emissions. The selection was based on the results of laminar-flame tests with model molecules; specifically, molecules displaying reduction in emissions of carbon monoxide and increase in flame temperature were chosen for the next stage. The chemical synthesis of the selected molecules was performed at lab-scaled in a heterogeneous catalytic process which was then scaled-up to produce large

amounts (e.g., 10 L) of the component/additive fuel. Finally, the synthesized molecules were evaluated on the laminar-flame test, their main physico-chemical fuel properties were measured or estimated, and their influence on engine performance and emissions were assessed in an engine test bench.

A scheme of the organization of this dissertation is shown in Figure 1.5.

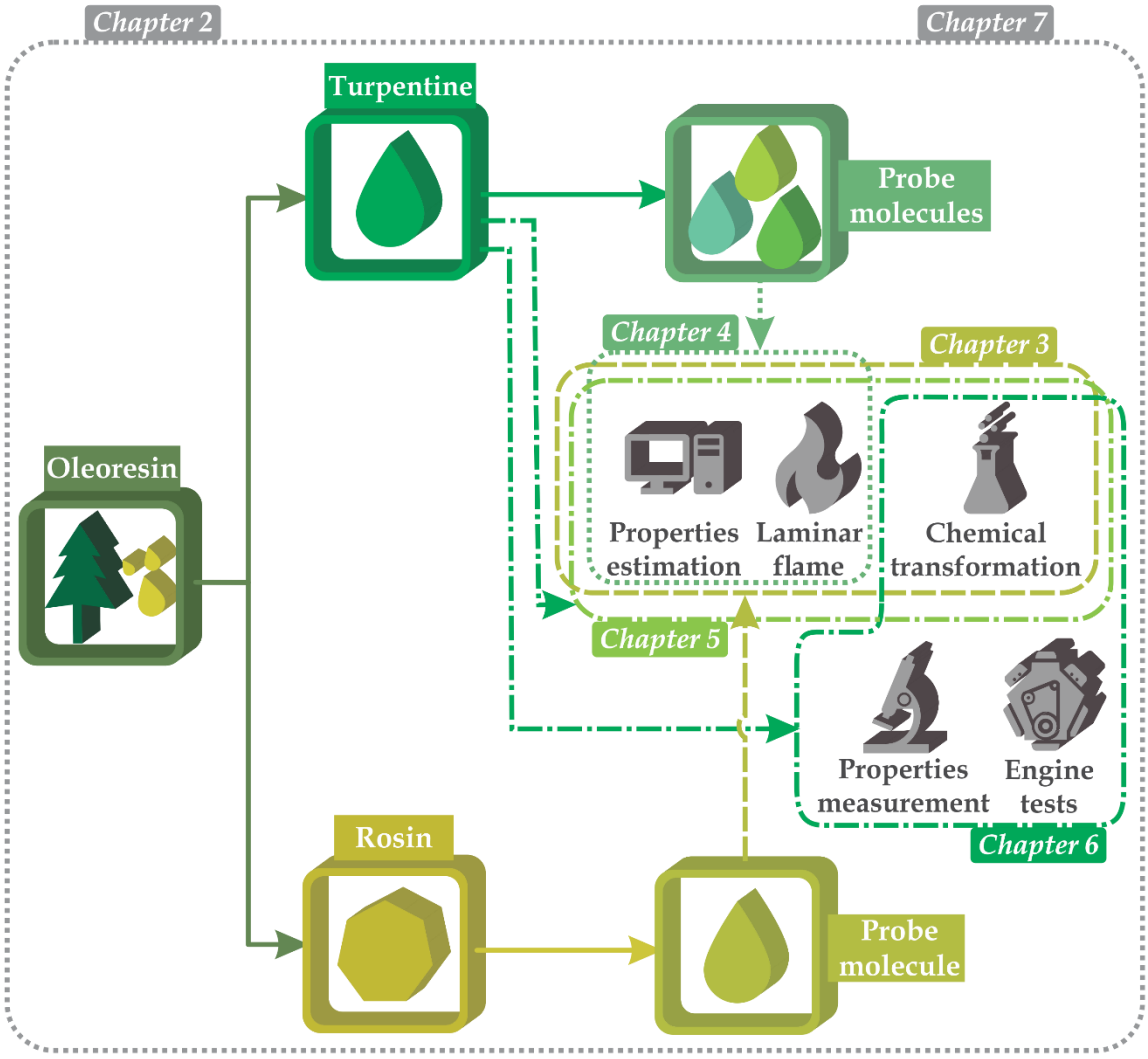

Figure 1.5. Scheme of distribution of chapters in the thesis

Chapter 2 is devoted to an overall literature review, and to establish the required theoretical framework, involving measuring and diagnostic techniques for fuel properties, for instance, burner and engines tests. Chapter 3 deals with the chemical transformation of rosin; in addition, the evaluation of the rosin-derived compounds as fuels is presented; specifically, property estimations and combustion tests in a

diffusion- and laminar-flame burner are presented and discussed. Some compounds proposed as test molecules from turpentine were also evaluated to select the best one based on emissions and estimated properties, Chapter 4. Once the best molecule from turpentine was selected, Chapter 5 deals with its chemical transformation through heterogenous catalysis, and the evaluation of the "as-reaction" product, i.e., without further purification, in combustion tests. Chapter 6 scales-up the reaction to produce large amounts of the additive/component, and presents the results of engine bench tests. Finally, the conclusions of the work are collected in Chapter 7.

1.6 Financial support

The project was developed with financial support from *Departamento Administrativo de Ciencia, Tecnología e Innovación* – COLCIENCIAS through a Doctoral scholarship (call 727 of 2015) and the project 37-1-693 (contract FP44842-124-2017), and University of Antioquia through the project PRG2014-1091 (ES84150111). In addition, the Environmental Catalysis Research Group from Universidad de Antioquia (Prof. Aída Luz Villa Holguín), and the Engines and Fuels Group from University of Castlla-La Mancha (Prof. Magin Lapuerta Amigo), provided logistic support for the development of the project. Finally, Repsol and BioOils Energy from Spain provided the diesel and biodiesel samples, respectively, used in this work.

Chapter 2. Theoretical framework

This chapter presents some concepts on the main properties of fuels, as well as the procedures to evaluate the performance of fuels, mainly flame analysis at laboratory scale and tests in an actual engine bench. Measurement of emissions is also briefly discussed.

2.1 Fuel properties

2.1.1 Fuel composition

Typically, purity of alternative fuels is determined by gas chromatography (GC), thin layer chromatography (TLC), liquid chromatography (LC), and gel permeation chromatography (GPC) [59]. The water content is an important parameter to ensure phase stability during the storage of blends of fossil fuels + alternative fuels (e.g., alcohols). The Karl Fischer titration is commonly used to determine the water content in organic liquids, specifically, Coulometric Karl Fischer (measuring range 0.02 to 5% wt.). In diesel fuel, low content of water is required (i.e., European Standard EN 590-2014 states a maximum content of water in diesel fuels of 200 ppm), and, accordingly, Karl Fischer standard EN 10337 (equivalent to ASTM D4928) is used.

2.1.2 Physical properties

The main methods to measure physical properties of fuels are presented in the Guide to ASTM Test methods for the analysis of petroleum products and lubricants [60], and a brief overview is included here.

2.1.2.1 Density

Most common standard tests to measure density of liquid fuels are ASTM D1298, D1217, D1480, D1481, D1657, D4052 and D5002, based on gravimetry, pycnometer, hydrometer, oscillating frequency or digital meters. The density is often measured in a climatic chamber and reported at a reference temperature and relative

humidity (15°C and 45 %, respectively). In Europe, the standard EN 590:2013+A1 establish a range between 775 and 840 kg/m^3 for the density of diesel fuels.

2.1.2.2 Viscosity

Viscosity is a very important parameter of a fuel because it influences important steps in compression engines, such as the atomization inside the combustion chamber. Moreover, some combustion properties may also be affected by viscosity: for instance, at high viscosity, nitrogen oxides (NOx) emissions decrease but unburned hydrocarbons (UHC) and particulate matter (PM) increase significantly [61]. Several standards have been proposed to measure the viscosity of liquids. In particular, for liquid fuels the standard test method of transparent and opaque liquids ASTM D455 (equivalent to EN 3104), which quantifies the kinematic viscosity of a sample by measuring the time for a volume of liquid to flow under gravity through a calibrated glass capillary viscosimeter at 40°C, is the most used. The standard EN 590:2013+A1 establish a range between 2 and 4.5 mm^2/s for the viscosity of diesel fuels in Europe.

2.1.2.3 Vapor pressure

Emission of vapors to the atmosphere is directly related to the vapor pressure of the fuel. Thus, vapor pressure is an important physical property of a fuel. ASTM D323 (related to ASTM D4953) is one of the most used methods to determine the vapor pressure of fuels. Briefly, the liquid sample is connected to a vapor chamber, and both are immersed in a bath at 100°F until a constant pressure is observed. ASTM D6378 (based on ASTM D5191 and equivalent to EN 3007) was developed to automate this test.

2.1.2.4 Lubricity

The lubricity represents the capacity of a fluid to reduce friction between solids: it is a measure of how the friction and/or wear is reduced. Thus, lubricity is not a material property and direct measurement is not possible. However, as the fuel takes a part in the lubrication process in modern diesel engines, its lubricity is very important, and some additives have been developed to increase it.

The EN 12156-1 standard test (equivalent to ASTM D 6079) evaluates the diesel fuel lubricity using a high frequency reciprocating rig (HFRR), where a vibrator arm holding a 200 mg non-rotating steel ball is lowered until it contacts a test disk completely submerged in the sample, causing a rub against the disk with a 1 mm stroke at frequency of 50 Hz for 75 min. Then, the ball is removed and the dimensions of the major and minor axes of the wear scar are recorded, generally by optical magnification. In Europe, the standard EN 590:2013+A1 establishes a maximum value of 460 µm for the diameter of wear scar.

2.1.3 Thermal properties

2.1.3.1 Volatility

Volatility is typically measured based on the atmospheric distillation test of the standard EN 3405 (equivalent to ASTM D86). Volatility characteristics of a liquid fuel influence the performance of a fuel in a combustion. Thus, factors such as the potential evaporative fuel loss during storage, potential of fire hazard and the ambient influences of fuel volatility (i.e. cold start limitations and potential vapor lock) can be analyzed from volatility characteristics of fuels [62].

The standards EN 3405 and 3924 establish that the maximum content of distillated at 250°C must be lower than 65 % vol., the content of distillate at 350°C must be higher than 85% vol., and the 95 % vol. of distillated must be recovered with a maximum temperature of 360°C.

2.1.3.2 Estimation of thermal properties

Different methodologies have been proposed to estimate thermal properties, group additivity methods being the most popular [63]. Joback and Reid [64] developed a family of group-contribution from a set of molecular groups to estimate thermal properties, such as normal boiling and melting temperatures, heat capacity, and critical properties. The method uses structural information until chemical groups (first-order methodology).

In this work, the critical compressibility factor, volume, pressure and temperature, and heat capacity were computed by using Joback methodology. Estimation of these properties with different methods amply used for molecules similar to those derived

from oleoresin (i.e., Benson's and Joback's method) were conducted elsewhere [65], and no significant difference was observed. Estimation equations are summarized in Table 2.1.

Table 2.1. Equations to estimate properties with Joback [64]

Property	Equation	
Boiling temperature (K)	$T_b = 198.2 + \sum \mathrm{GC}_J$	**Equation 2.1**
Melting temperature (K)	$T_m = 122.5 + \sum \mathrm{GC}_J$	**Equation 2.2**
Critical temperature (K)	$T_c = \frac{T_b}{\left(0.548 + 0.965 \sum \mathrm{GC}_J - \left(\sum \mathrm{GC}_J\right)^2\right)}$	**Equation 2.3**
Critical pressure (bar)	$p_c = \left(0.113 + 0.0032 n_A - \sum \mathrm{GC}_J\right)^2$	**Equation 2.4**
Critical volume (cm^3/mol)	$v_c = 17.5 + \sum \mathrm{GC}_J$	**Equation 2.5**
Critical factor of compressibility	$Z_c = P_c V_c / R T_c$	**Equation 2.6**
Heat capacity, ideal gas (J/mol.K)	$C_p^0 = \sum (a) - 37.93 + \left(\sum (b) + 0.210\right) T + \left(\sum (c) + 3.91 \times 10^{-4}\right) T^2 + \left(\sum (d) + 2.06 \times 10^{-7}\right) T^3$	**Equation 2.7**

GC_J group contribution of Joback; n_A total number of atoms; a, b, c and d have GC_J values to be computed as a function of temperature

2.1.4 Thermochemical properties

2.1.4.1 Adiabatic flame temperature

The adiabatic flame temperature is the temperature that the combustion products would reach with no heat loss due to radiation, convention or conduction. Adiabatic flame temperature can be defined at constant-pressure or constant-volume combustion. For a fuel-air mixture burning adiabatically at constant pressure, the absolute enthalpy of the reactants at initial state (subscript i) equals that for the products at the final state (subscript ad), Equation 2.8,

$$H_{\text{react.}}(T_i, p) = H_{\text{prod.}}(T_{ad}, p) \quad \textbf{Equation 2.8}$$

Equation 2.8 defines the constant-pressure adiabatic flame temperature. For the evaluation of this temperature, knowledge of the composition of the combustion products is necessary. In the case of constant-volume adiabatic flame temperature, by the first law of thermodynamics and applying the ideal-gas law, Equation 2.9,

$$H_{\text{react.}}(T_i, p_i) - H_{\text{prod.}}(T_{ad}, p_{ad}) - R\left(N_{\text{react.}}T_i - N_{\text{prod.}}T_{ad}\right) = 0 \quad \textbf{Equation 2.9}$$

where N is the number of moles of the species. The composition of products depends on temperature and pressure, making the calculation of adiabatic temperature difficult. Moreover, due to the high temperature, dissociation species (e.g., OH, H) are expected to be present along with the complete oxidation species (i.e., CO_2 and H_2O).

There are several ways to obtain the equilibrium composition, primarily based on the species present and their chemical reactions. Then, from the fuel / air composition and thermal properties (i.e., heat of formation and heat capacity), and the equivalence ratio and initial pressure and temperature, the final temperature is iterated to achieve a difference of enthalpy equals to zero for the process [66].

2.1.4.2 Heat of combustion

Heat of combustion (also called heating value, HV) is the chemical energy released when a chemical compound undergoes complete combustion. Numerically is equivalent to the enthalpy of reaction but with opposite sign, Equation 2.10,

$$HV = -\Delta H_R = H_{\text{Reac}} - H_{\text{Prod}} \quad \textbf{Equation 2.10}$$

The enthalpy of reactants and products can be computed from Equation 2.11,

$$H_{\text{Reac/Prod}} = \sum N_i \times \bar{h}_i \quad \textbf{Equation 2.11}$$

where $\bar{h}_i$ is the molar absolute enthalpy for species i and N_i represents the mol for species i. The molar enthalpy is obtained from the enthalpy of formation at a standard reference state for species i ($\bar{h}^0_{f_i}(T_{\text{ref}})$) and the enthalpy change from T_{ref} to the actual T ($\overline{\Delta h}_{s_i}$), according to Equation 2.12 (assuming there is no change in the state of aggregation between the reference and final states),

$$\bar{h}_i(T) = \bar{h}^0_{f_i}(T_{\text{ref}}) + \Delta\bar{h}_{s_i} \quad \textbf{Equation 2.12}$$

The standard reference state typically is 25°C and 1 atm. Heat of combustion can be computed by assuming that the all water in the reaction products is condensed out; this upper limit is commonly known as Higher Heating Value (HHV), whereas if water is not condensed the Lower Heating Value (LHV) is obtained [67], [68].

Heating values of mixtures can be obtained from composition and heating values of pure species according to Equation 2.13,

$$HV = \sum HV_i \times x_i \qquad \textbf{Equation 2.13}$$

where HV_i is the heating value for pure species *i* (mass basis) and x_i is the mass fraction.

Heat of combustion for liquid fuels is typically measured with a bomb calorimeter. ASTM D240 is used to determine the heat of combustion by burning a weighted sample in an oxygen bomb calorimeter under controlled conditions, with a repeatability and reproducibility of 0.13 and 0.40 MJ/kg, respectively.

2.1.4.3. Estimation of Thermochemical Properties

Estimation of thermochemical properties has been commonly performed by group additivity. In particular, Joback's method can be used to estimate the heat of formation, which, in turn, can be used to estimate heating values [64], Equation 2.14,

$$\Delta h_f^0 = \sum \mathrm{GC}_J \qquad \textbf{Equation 2.14}$$

where GC_J represent the group contribution of Joback.

Benson method has been widely used to estimate thermochemical properties of pure compounds, such as enthalpy and Gibbs energy of formation, and heat capacity, of different chemical compounds [63], [69]–[71]. The method establishes a hierarchy of additivity: atomic > bond > group [72], [73], allowing it to capture the information of neighbors (i.e., second-order methodology). Although Joback's method can also be used to estimate thermochemical properties, the second-order group contribution method of Benson has been proved to be more precise [74].

Heat of formation (kJ/mol) from Benson can be obtained by Equation 2.15,

$$\Delta h_f^0 = \sum \mathrm{GC}_B \qquad \textbf{Equation 2.15}$$

where GC_B is the group contribution of Benson.

Lower heating value (LHV, MJ/kg) for a species *i* can be obtained from its heat of formation, Equation 2.16.

$$LHV = \frac{\Delta h^0_{f,\text{comb. prod.}} - \Delta h^0_{f,i}}{MW_i} - \Delta h^0_{\text{v},i} \qquad \textbf{Equation 2.16}$$

where MW_i is the molecular weight of the species, $\Delta h^0_{f,i}$ and $\Delta h^0_{f,\text{comb. prod.}}$ the heat of formation of the species and major combustion products (usually CO_2 and water), respectively, and $\Delta h^0_{\text{v},i}$ is the heat of vaporization.

From the principle of corresponding states and by using the Pitzer correlation, heat of vaporization (kJ/mol) is determined according to Equation 2.17.

$$\Delta h^0_{\text{v}} = RT_c \left(7.08\left(1 - {}^{298.15}/_{T_c}\right)^{0.354} + 10.95\left(1 - {}^{298.15}/_{T_c}\right)^{0.456} \omega\right) \qquad \textbf{Equation 2.17}$$

where ω is the acentric factor, which can be obtained by implementing the Lee-Kesler method of vapor pressure and by using the critical temperature and pressure, and the boiling temperature, according to Equation 2.18.

$$\ln\left({}^{1}/_{p_c}\right) = f^{(0)} + \omega \cdot f^{(1)}$$

$$f^{(0)} = 5.92714 - \frac{6.09648 \cdot T_c}{T_b} - 1.28862 \cdot \ln\left({}^{T_b}/_{T_c}\right) + 0.169347\left({}^{T_b}/_{T_c}\right)^6 \qquad \textbf{Equation 2.18}$$

$$f^{(1)} = 15.2518 - \frac{15.6875 \cdot T_c}{T_b} - 13.4721 \cdot \ln\left({}^{T_b}/_{T_c}\right) + 0.43577\left({}^{T_b}/_{T_c}\right)^6$$

2.1.5 Combustion properties

2.1.5.1 Flash point

The flash point temperature is a measure of the ignitability limit for a mixture of fuel and air formed above a liquid fuel, and, thus, is directly related to the potential hazards of the fuel. Several procedures have been standardized to measure the flash point: Cleveland open cup, Pensky Martens closed cup tester, tag closed tester, and continuously closed cup flash point. The first three methods (ASTM

standards D56, D92 and D93) are currently used, with D93 being the most popular and cited in regulations and specifications (equivalent to standard EN 2719). This standard is widely used for fuel and lube oils, suspension of solids and other liquids. Briefly, the sample is heated slowly at constant rate with continuous stirring, and a flame is driven into the cup at regular intervals; the temperature at which the vapor above the sample ignites is the flash point.

2.1.5.2 Smoke point

The smoke point is the maximum height of a flame without smoke, that is, at flame heights larger than the smoke point the flame produces smoke. Thus, a high smoke point number indicates a fuel with low tendency to produce smoke. Smoke point can be related to the propensity of soot formation.

The measurement of smoke point of liquid fuels is based on standard ASTM D1322. A sample is burned in an enclosed wick-fed lamp and the flow of air is changed until smoke appears in the chimney of the system, registering the height of flame. The smoke point is related to the sooting tendency by using the threshold sooting index (TSI) concept. The TSI is a numerical scale which compares the formation of soot as a function of molecular weight and smoke point of the fuel.

2.1.5.3 Ignition delay and derived-cetane number

The ignition delay (ID) is defined as the time between the start of injection and the start of combustion. It consists of physical delay due to atomization, vaporization and mixing of air and fuel, and pre-combustion reactions. The derived-cetane number (DCN) is an inverse function of ignition delay: the higher the DCN value, the shorter the ID of a fuel. Both ID and DCN can provide a measure of the ignition characteristics of diesel fuels in compression ignition engines. These properties are typically measured in a CFR engine which reproduces the ignition delay time for a determinate sample of fuel but using a mixture of hexadecane and metal-naphthalene.

The standard EN 16715 (equivalent to ASTM D7170) depicts a procedure to measure ID and DCN in a combustion-heated, temperature-controlled, constant-volume chamber, where the sample is directly injected into a previously compressed

air. Each injection produces a single-shot, compression ignition combustion cycle. The ignition delay is measured using sensors that detect the start of fuel injection and the start of significant combustion for each cycle, and the values are averaged. In addition, by using a mathematical expression it is possible to obtain a derived-cetane number.

Generally, ignition characteristics depend on the number of carbons, and the higher the carbon number on the molecule the better the ignition [61]. Aromatics and paraffins usually have very poor and very good ignition characteristics, respectively. In Europe, the standard EN 590:2013+A1 establish a minimal value of DCN of 51 for diesel fuels.

2.1.6 Cold flow properties

2.1.6.1 Pour point

The pour point is a measurement of the lowest temperature to which a fuel can be cooled with free flow. It is a measure of manipulability of the fuel; at values lower than the pour point, the fuel cannot flow in a free form. Pour point is determined by cooling a sample at a specific rate and examining its flow characteristics at intervals of 3°C, based on ASTM D97, D99 and D5853. The lowest temperature at which movement of the sample is observed is recorded as the pour point.

2.1.6.2 Cloud point

The cloud point is the temperature at which a hazy or waxy crystallization begins to appear in the fuel when it is cooled. ASTM D2500 is used for petroleum products by cooling the sample at specific rate and examining it periodically; the temperature at which haziness is first observed at the bottom of the test jar is recorded as the cloud point. Other standard tests (ASTM D5771, D5772 and D5773) use different instruments (ISL®, Herzog and phase technology), which are considered more precise than D2500. The maximum cloud point for Europe diesel (standard EN 23015) is -34°C for highest class and -10°C for lowest class diesel fuel.

2.1.6.3 Cold filter plugging point

The cold filter plugging point (CFPP) is the lowest temperature at which a certain amount of diesel fuel still passes through a standardized filtration device in a

specified time when cooled under specific conditions. ASTM D6371 describes the procedure where the sample is cooled at intervals of 1°C into a pipette under a controlled vacuum through a filter; the procedure is repeated until the amount of wax crystals that have separated out of the fuel is sufficient to stop or slow down the flow so that the time to fill the pipette exceeds 60 s or the fuel completely fails to return to the jar. The limit of CFPP for Europe (standard EN 590:2014) depends on the grade of the diesel fuel, for instance, for fuels at the lowest grade (grade A) the maximum CFPP is 5°C, and that for the highest grade (grade F) is -20°C.

2.2 Evaluation of fuels

2.2.1 Stoichiometry

The stoichiometry of the combustion reaction of an oxygenated hydrocarbon is shown in Equation 2.19,

$$C_xH_yO_z + aO_2 \rightarrow xCO_2 + \frac{y}{2}H_2O + \text{others} \qquad \textbf{Equation 2.19}$$

Other species are assumed in traces. The stoichiometric coefficient of oxidizer can be obtained by balancing Equation 2.19, as expressed by Equation 2.20,

$$a = x + y/4 - z/2 \qquad \textbf{Equation 2.20}$$

The mass ratio between oxidizer and fuel indicates whether the fuel-oxidizer mixture is rich, stoichiometric or lean. For air as oxidizer, Equation 2.21,

$$(A/F) = \frac{\dot{m}_A}{\dot{m}_F} \qquad \textbf{Equation 2.21}$$

where A and F represent air and fuel, respectively.

The mass stoichiometric oxidizer-fuel ratio, by considering an air composition of 21% of O_2 and 79% of N_2, can be obtained from Equation 2.22,

$$(A/F)_{\text{Stoichiometric}} = 4.76a\left(\frac{MW_A}{MW_F}\right) \qquad \textbf{Equation 2.22}$$

where, *MW* is the molecular weight.

The equivalence ratio (ϕ) is used to indicate quantitatively the ratio of fuel and oxidizer according to Equation 2.23,

$$\phi = \frac{(A/F)_{\text{Stoichiometric}}}{(A/F)} \qquad \textbf{Equation 2.23}$$

If oxidizer is supplied in a value lower than the stoichiometric value ($\phi > 1$) the mixture is said to be fuel-reach, while supplying more than the stoichiometric oxidizer ($\phi < 1$) results in a fuel-lean [67].

In co-flow flames, $\phi > 1$ corresponds to an underventilated flame, and $\phi < 1$ to an overventilated flame.

2.2.2 Quantification of emissions

In order to measure the combustion products, it is common first to collect a sample by means of a probe. After removing particulate matter and moisture from the sample (e.g., with filters and traps), the gas stream is analyzed by gas chromatography, infrared spectroscopy or chemiluminescence [75], [76].

It is important to ensure that all emissions are quantified on the same basis. For instance, NOx concentration measured on dry basis must be converted to the wet basis used with permanent gases, or vice versa. Besides, a standardization of the measured concentration must be performed. The conversion between different basis and the standardization are detailed in Appendix B

Emission indices have also been used to report the emissions. In particular, emission indices facilitate the comparison of different experimental configurations, and, as they express the amount of pollutant formed per mass of fuel, isolate the effects of combustion efficiency or dilution [77]. Emission index can be represented as Equation 2.24,

$$EI_i = \frac{\dot{m}_i^E}{\dot{m}_F} \qquad \textbf{Equation 2.24}$$

where EI_i is the emission index of species i and, $\dot{m}_i^E$ and $\dot{m}_F$ are the mass flow of emitted (combustion products) and fuel consumed species. If CO_2 and CO are the only carbon-containing species in the stream of reaction products, the emission index of a species i, according to Equation 2.24, can be obtained from the molar fractions of the species, CO_2 and CO (x_i, x_{CO2} and x_{CO}), the number of mole of carbon in one mole of fuel (x) and the molecular weight of fuel and species i (MW_{Fuel} and MW_i), Equation 2.25,

$$EI_i = \left(\frac{x \cdot x_i}{x_{CO2} + x_{CO}}\right)\left(\frac{MW_i}{MW_{\text{Fuel}}}\right) \qquad \textbf{Equation 2.25}$$

The uncertainties associated to the measurements can be used to estimate the error of the emission indices by using the method of error propagation, which provides a set of rules to assign an error to a magnitude from the uncertainties of the measurements and the mathematical operations involved in its calculation. The main rules of error propagation are summarized in Table 2.2 [78].

Table 2.2. Main rules of error propagation

Operation	Error rule	Example
Addition and subtraction	Sum of absolute uncertainties	$M_1 \pm M_2 = (x \pm y) \pm (\delta x + \delta y)$
Multiplication and division	Sum of relative uncertainties	$M_1 \times/\div M_2 = (x \times/\div y) \pm \left[(x \times/\div y)\left({\delta x}/{x} + {\delta y}/{y}\right)\right]$
Constant product	Sum of relative	$kM_1 = (kx) \pm k\delta x$
Power	Product of the power and relative uncertainties	${M_1}^n = (x^n) \pm \left[nx^n\left({\delta x}/{x}\right)\right]$

$M_1 = (x \pm \delta x)$; $M_2 = (y \pm \delta y)$

The mathematical expression obtained from the application of rules for error propagation to emission indices is shown in Appendix C.

2.2.3 Laminar diffusion flames

2.2.3.1 Background

Regarding the physical separation of the fuel and oxidizer streams, flames can be classified as premixed and nonpremixed (or diffusion). In addition, nonpremixed flames can be classified according to the configuration of the fuel and oxidizer supply as jet, coflow, counterflow and crossflow diffusion flames. In jet flames, quiescent air is the oxidizer and the fuel flows through a burner port, whereas the other configurations also involve the flow of the oxidizer stream.

Figure 2.1 shows the typical configuration of coflow diffusion flames, as well as the concentration and temperature profiles in a cross section of the flame. Generally, in coflow flames, air (as oxidizer) stream flows through an annular region surrounding the fuel port (see Figure 2.1a). Fuel and oxidizer diffuse radially and mix through

diffusion in the combustion zone [13]. A maximum on fuel concentration is observed in the centerline of the flame and falls rapidly at the reaction zone in the flame front (see Figure 2.1b).

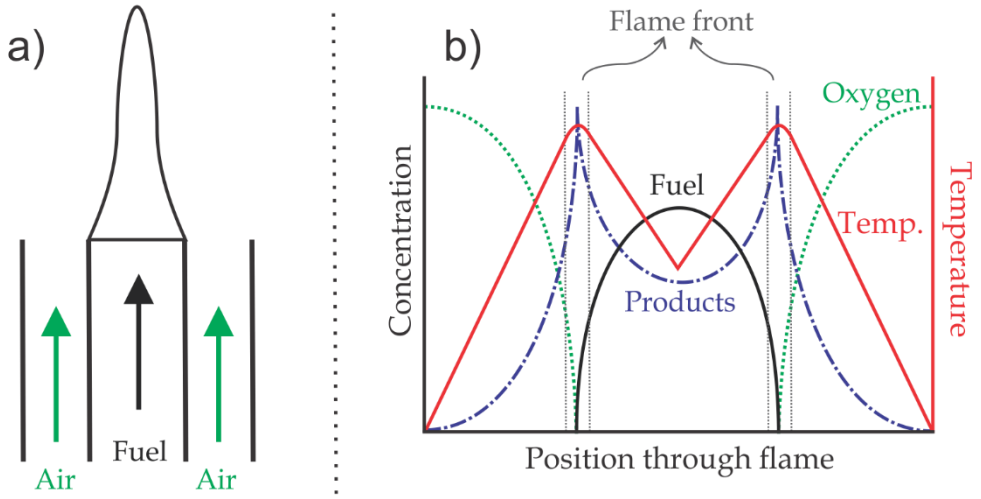

Figure 2.1. Coflow diffusion flames: a) configuration and b) spatial concentration profiles [67]

The oxygen concentration decreases from the oxidizer stream until the flame front. The concentration of products shows a maximum in the reaction zone and falls away in both oxidizer and fuel zones. Temperature has a behavior similar to product concentrations (i.e., presents a maximum in the flame front). Combustion products are formed and heat of combustion is released in the flame front, and then are transported away in both directions [79].

A distinctive characteristic of a diffusion flame is that the burning (or fuel consumption) rate is determined by the rate of diffusion of fuel and oxidizer to the flame front [80]. In co-flow diffusion flames the ratio between inwards / outwards diffusion of reactions products (resulting from bulk velocity) translates into steady-state concentration at the centerline of the flame [67], [80].Laminar diffusion flames have been used to get insight into soot formation and to design combustion equipment [67].

The shape of the flame depends on the equivalence ratio. In particular, when the air stream surrounds the fuel stream, overventilated flames display a closed, elongated form, whereas underventilated flames present a fan-shaped form [80]. In addition, in the concentric configuration the flame height does not depend on the diameter of the

inner tube (e.g., fuel stream) and velocity, but on the volumetric flowrate: several combinations of diameter and velocity can yield the same flame height [67].

Other characteristics of diffusion flames can be evidenced as a function of the velocity of fuel. Figure 2.2 displays the behavior of flame height and the velocity in the fuel port. In laminar flames, height flame is directly proportional to Reynolds number. When velocity of fuel port surpasses a critical value (i.e., the start of transition between laminar and turbulent regimes), however, flame height decreases and reaches a plateau. In addition, the transition between laminar and turbulent regimes is shortened and achieves a constant also at the breakpoint of the flame (defined as the flame height when the fluctuations of the flame shape and yellow luminosity are significantly high). When this velocity is very high, the flame begins to separate considerably from the fuel port (i.e., liftoff of the flame), and larger velocities lead to blows off [81], [82].

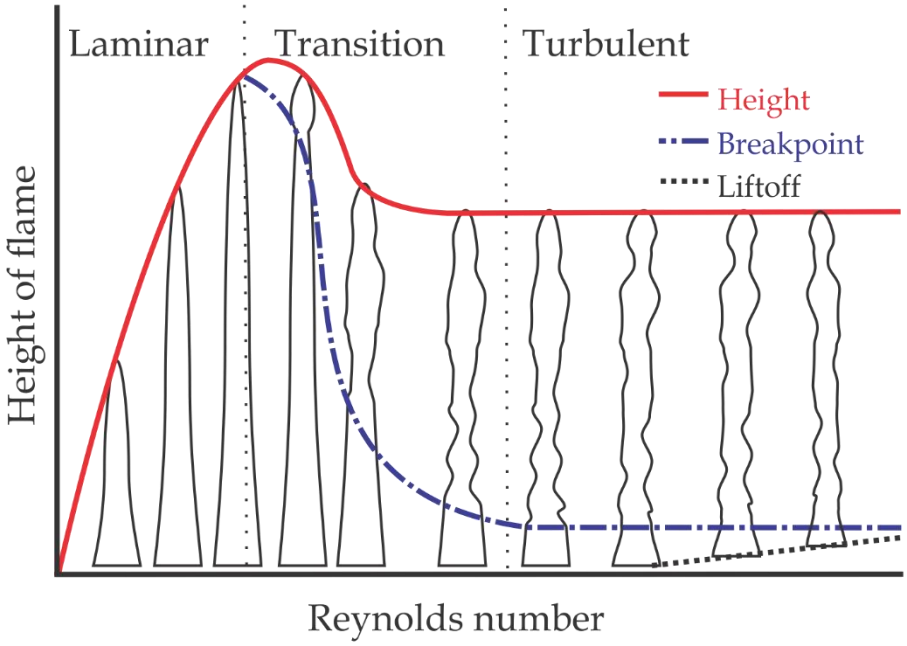

Figure 2.2. Flame height versus fuel port velocity [81], [82]

Flame height is an important parameter in the design of burners and combustion chambers. Theoretical analysis of diffusion flames has been carried out to obtain the height of flame, mainly in jet configuration, and one of the most recognized methods is that by Burke and Schumann. Likewise, empirical correlations have been

proposed to estimate the height even over other configurations, for instance, co-flow diffusion flames. Some of these correlations are shown in Table 2.3.

Table 2.3. Correlations to estimate height of diffusion flames

Roper theoretical [83]	$H = \frac{1}{4\pi\upsilon_\infty}\frac{Q}{\ln\left(1+{}^{1}/_{S}\right)}\left(\frac{T_\infty}{T_F}\right)\left(\frac{T_\infty}{T_P}\right)^{0.67}$	**Equation 2.26**
Roper experimental [83]	$H = 1330.675\frac{Q_F\left({}^{T_\infty}/_{T_F}\right)}{\ln\left(1+{}^{1}/_{S}\right)}$	**Equation 2.27**
Mishra [76]	$H = \frac{\rho Q_F}{4\pi\left({}^{k_g}/_{C_p}\right)}$	**Equation 2.28**

H is the height of flame (m); C_p is the specific heat (J/kg.K); D_∞ is the mean diffusion coefficient evaluated at T_∞ (m^2/s); $k_g$is the thermal conductivity (J/m.K.s); Q_F is the volumetric flow rate of the fuel (m^3/s); S is the molar stoichiometric oxidizer-to-fuel ratio; T_∞ is the oxidizer stream temperature (K); T_F is the fuel stream temperature (K); T_p is the mean flame temperature (K); υ_∞ is the cinematic viscosity of oxidizer (m^2/s)

For fuels represented as $C_xH_yO_z$, the molar stoichiometric air to fuel ratio used in correlations of Table 2.3, may be expressed as Equation 2.29,

$$S = \frac{\left(x+{}^{y}/_{4}-{}^{z}/_{2}\right)\left(1-x_{\mathrm{Dil}}\right)}{x_{O_2}} \qquad \textbf{Equation 2.29}$$

where x_{O_2} is the mole fraction of oxygen in oxidizer stream and x_{Dil} is the mole fraction of fuel diluent (i.e., carrier gas).

2.2.3.2 Evaluation of laminar diffusion flames

2.2.3.2.1. Species concentration

Typically, NO_2 and NO concentrations are measured by the chemiluminescence technique, where the primary principle is a photo-physical detection of the signal emitted as electronically excited NO_2^* decays to the ground state following the chemical reaction of NO with ozone [84]. Once in the analyzer, the sample is mixed with ozone, causing the reactions expressed in Equation 2.30 and Equation 2.31,

$$NO + O_3 \rightarrow NO_2^* + O_2 \qquad \textbf{Equation 2.30}$$

$$NO + O_3 \rightarrow NO_2 + O_2 \qquad \textbf{Equation 2.31}$$

NO_2^* reverts to NO_2 emitting electromagnetic radiation in the wavelength between 600-3000 nm and with maximum intensity about 1200 nm. The chemiluminescence signal is then detected by photo-electrically detector, considering that with an excess

of ozone the signal is proportional to the NO-concentration of the sample gas. If NO_2 of the sample is first converted into NO (for instance, by reduction with carbon or metallic active material), it is possible to measure NO_2-concentration [76], [84].

GC analysis is the most popular method to quantify emissions of hydrocarbon species and permanent gases. In GC, the components of the sample are separated using specific columns, and then are quantified by a detector; most popular detectors are flame ionization detectors (FID) and thermal conductivity detectors (TCD) [76]. The selection of the column depends on the nature of the substances to be separated. Appendix D summarizes the most relevant GC parameters typically used to analyze combustion emissions. For example, to separate CO and CO_2 by GC, an arrangement of two packed columns and a TCD detector is necessary. Porapak column in series with molecular sieve column is a common configuration which allows to analyze other permanent gases (e.g., H_2, N_2, O_2). For hydrocarbons, FID detector, and HP PLOT Q, DB-1 and PLOT Al_2O_3 capillary columns have been reported.

2.2.3.2.2. Flame size and shape

Flame shape and size can be analyzed by image (and video) processing. Normal visible-range cameras have been used to obtain the dimensions of flames. Specifically, once recorded the video or image, filters and noise reducers may be applied to improve their quality. Then, the image is converted to binary format and, by analyzing pixels, it is possible to obtain its area, equivalent diameter, perimeter and other shape parameters [85]. Some computer programs, such as Matlab®, include a toolbox or package for image processing which facilitates the analysis of images.

2.2.3.2.3. Temperature

R or S type thermocouples are commonly used to determine the temperature of flames because their fine wire (< 50 μm) causes minor interference on the flame [76]. In temperature measurement with thermocouples, errors resulting from heat transfer (which are important at high temperature) should be accounted for. In particular, from an energy balance in the joint of thermocouple, and neglecting

energy loss by conduction and energy storage due to the small dimensions [76], Equation 2.32,

$$T_g = T_b + \frac{\sigma\varepsilon}{h}(T_b^4 - T_\infty^4) \quad \textbf{Equation 2.32}$$

where T_∞, T_b and T_g are surrounding, thermocouple joint and gas temperatures, respectively, σ is the Stefan-Boltzmann constant (5.67x-8 W/m^{2}K^4), ε is the emissivity of the thermocouple surface, and h is the convective heat transfer coefficient (W/m^{2}K). Convective heat transfer can be obtained from Prandtl ($Pr = \upsilon/\alpha$) and Reynolds ($Re = VD_T/\upsilon$) numbers, which depend on gas properties and thermocouple dimensions [76], Equation 2.33.

$$Nu = \frac{hD_T}{k} = 0.42Pr^{0.2} + 0.57Pr^{0.33}Re^{0.5} \quad \textbf{Equation 2.33}$$

Wire emissivity (ε), thermal conductivity (k), thermal diffusivity (α), and kinematic viscosity (υ) can be obtained by the following expressions, Equation 2.34 (valid for $0.01 < Re < 105$ and $T > 1250\ K$) [76],

$$\begin{aligned} \varepsilon &= 9.35 \times 10^{-5} \cdot T_b + 0.6 \\ k &= 3.75 \times 10^{-5} \cdot T_b + 0.04 \\ \upsilon &= 2.5 \times 10^{-7} \cdot T_b - 1.43 \times 10^{-4} \\ \alpha &= 2.89 \times 10^{-7} \cdot T_b - 1.23 \times 10^{-4} \end{aligned} \quad \textbf{Equation 2.34}$$

2.2.4 Engine tests

2.2.4.1 Background

Typical experimental setup for engine tests include an engine designed for combustion research, which allows measure and/or control of temperature, pressure, fluid flow rate, and force or torque. In addition, an exhaust gas analyzer coupled with a particle analyzer, and a device to measure the mass changes of fuel consumption are commonly implemented in the engine. This experimental setup allows to analyze fuel consumption, power output and emissions of particulate matter, nitrogen oxides, carbon oxide, unburned hydrocarbons, carbon dioxide and aromatics.

Brake engine performance is defined as an analysis of the complete engine as a thermodynamic system, and deals with the work transfers to/from the engine. Figure 2.3 shows the simplest and earliest means of measuring brake performance of engine using a friction dynamometer or brake, used to establish some important concepts [86].

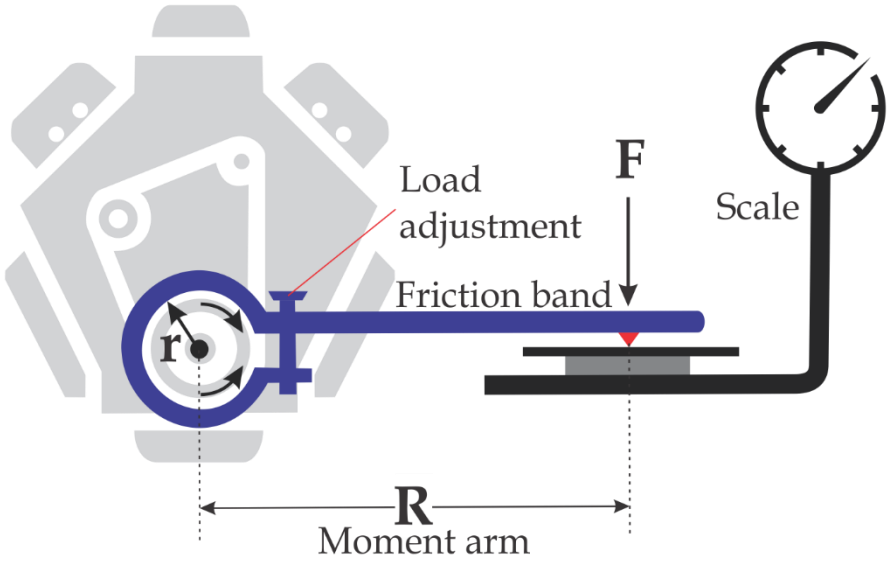

Figure 2.3 Scheme of dynamometer of the type friction band [86]

★ Mechanical efficiency (η_{mech}) is a measure of how effective the engine is at reducing internal losses. It relates the brake work ($\dot{W}_B$) to the indicate work ($\dot{W}_I$) (or power), see Equation 2.35. Indicated work can be obtained from an indicated engine analysis, considering the fuel-air mixture as a system and by an integration in pressure and volume in the combustion chamber,

$$\eta_{\text{mech}} = \frac{\dot{W}_B}{\dot{W}_I} \times 100 \qquad \textbf{Equation 2.35}$$

★ Brake work is related to the friction force (f) acting through a distance ($2\pi r$) in one revolution, according to Equation 2.36; r is the drive shaft wheel radius.

$$\dot{W}_B = 2\pi r \times f \qquad \textbf{Equation 2.36}$$

★ Brake torque (τ) is the amount of work a prime mover can produce. It is, therefore, a measure of how large a load a given engine can pull. It can be represented by the product of a moment arm and the corresponding brake force

according to Equation 2.37 (see Figure 2.3). In a dynamometer, the driveshaft torque is absorbed and conduces to a dynamic equilibrium with the moment arm (R) and load (F),

$$\tau = rf = RF \qquad \textbf{Equation 2.37}$$

★ Brake power (BHP) is the power measured at the crankshaft just outside the engine. It can be determined from torque and speed (N) according to Equation 2.38,

$$BHP = 2\pi\tau N \qquad \textbf{Equation 2.38}$$

★ Brake mean effective pressure ($BMEP$) is the calculation of the engine cylinder pressure that would give the measured BHP. It can be obtained from the brake power, number of power strokes per revolution (n), stroke length (L) and area (A), and the number of cylinders (C), Equation 2.39,

$$BMEP = \frac{BHP \cdot n}{L \cdot A \cdot N \cdot C} \qquad \textbf{Equation 2.39}$$

★ Brake thermal efficiency (η_{brake}) evaluates how well an engine converts the heat from a fuel to mechanical energy. It is defined as the brake power of a heat engine as a function on thermal input from the fuel, and can be determined from BHP, mass flow of fuel ($\dot{m}_{fuel}$) and calorific value of the fuel (HV), Equation 2.40,

$$\eta_{\text{brake}} = \frac{BHP}{\dot{m}_{fuel} HV} \qquad \textbf{Equation 2.40}$$

★ Brake heat rate (BHR) is the inverse of the brake thermal efficiency, Equation 2.41. It expresses the ideal fuel-air energy addition required by an engine per unit of brake power output,

$$BHR = \frac{\dot{m}_{fuel} HV}{BHP} \qquad \textbf{Equation 2.41}$$

★ Brake specific fuel consumption ($BSFC$) represents the normalized fuel consumption to the brake engine power output according to Equation 2.42,

$$BSFC = \frac{\dot{m}_{fuel}}{BHP} \qquad \textbf{Equation 2.42}$$

2.2.4.2 Protocols for engine tests

A test cycle is a protocol which specifies the conditions under which the engine (or vehicle) must be operated during an engine test in order to ensure reproducibility

and repeatability. The most important parameters in an engine tests are speed, load, and temperature of operation.

Several protocols for engine tests have been issued by different governments and institutions. The most important are those from USA, European Union and Japan, and are classified according to the type of vehicle (light or duty) or the type of test (chassis or engine dynamometer). The Worldwide Harmonized Light Vehicles Test Cycle (WLTC) and New European Driving Cycle (NEDC) are some of the most important and used cycles. The main differences between these cycles are the maximum velocity, the time and distance for the cycle, the number of phases which represent the road types and the average speed, those for WLTC being higher than NEDC.

2.2.4.3 Diagnostic techniques

In diesel engines, the fuel is injected into the cylinder which is already filled with air at high pressure and temperature. The autoignition of air/fuel mix starts the combustion processes. If enough oxygen is available, the hydrocarbons can be completely oxidized. In practice, however, the exhaust gases contain incomplete combustion products (e.g., carbon monoxide, unburned hydrocarbons, etc.) [87].

Fuel and air mass or volume flow rates must be measured in an engine test. Fuel consumption can be obtained using either volume or weight measurements; modern systems use photocell burettes to automatically measure the fuel consumption. For air flow, the pressure and temperature at the intake must be monitored, for instance with an orifice meter complemented with a thermometer [86].

The dynamometer, together with the engine, is the core of the engine tests. Several types of dynamometer have been developed. The simplest dynamometer is the prony brake, which uses a brake drum attached to the engine, developing a constant resisting torque for a given friction band pressure, which regulates the engine load. The water brake dynamometer is a hydraulic or fluid power absorption system. The engine torque is transmitted through a pump driven by an engine. A fan brake dynamometer is also fluid power absorption system, which uses the resistance of

air. Other dynamometers use electrical as opposed to mechanical means of loading [86].

The concentration of engine pollutants is usually measured in engine tests. Over 90% vol. of the typical exhaust gas composition consists of CO_2, N_2 and water, the other compounds (e.g., CO, NOx, UHC, SO_2, PM) being in much lower concentrations. Techniques to measure the concentration of the main components of the combustion discussed in Section 2.2.3.2 can also be used to the exhaust gas from engine also. Specialized sampling techniques must be used, generally by separation of the main sample, to obtain reliable values of trace compounds. Optical and spectroscopy techniques often have been used to measure low-concentration compounds.

Analysis of particulate matter accompany the modern engine test. Collecting and conditioning the gas sample containing PM, separation of PM and measurement of desired properties, are the steps for particulate matter analysis. Usually, a sample of the flue gas is taken by a vacuum pump and directed to the particle-analyzing train (e.g., filter, impinger, etc.). Sampling plays a key role on the characterization of PM: homogeneity (point of sample extraction), humidity (ambient temperature and air dilution according to the dew point of sample), kinetics (ideally isokinetic pump aspiration) and losses in transport (e.g., by deposition of PM in the lines), are important factors to obtain a representative samples [84], [88].

Mass concentration of PM can be measured by different methods, mainly by gravimetric (filters and impactor) and *in-situ* (tapered-element oscillating microbalance — TEOM) techniques. Particle size distribution is analyzed according to the aerodynamic properties (i.e., cascade impactor and aerodynamic particle sizer — APS), electrical mobility (electrostatic classifier, such as differential mobility analyzer — DMA) and light scattering/laser desorption/ionization (aerodynamic mass spectrometry — AMS, and white light-scattering analyzers) [84]. Chemical and internal structure, and morphology of PM are important characteristics to understand the soot formation. Thus, X-ray diffraction, phase contrast electron and dark field microscopy have been used to study the internal structure of soot, high-resolution

transmission electron microscopy (HRTEM) has been used to study morphology (which allows to determine the size distribution of particles), and FTIR analysis have been performed to analyze the chemical structure [89].

Chapter 3. Fuel characteristics of rosin-derived compounds

This chapter presents the results of the evaluation of rosin-derived compounds, particularly abietic acid methyl ester (AAME), as component and/or additive of diesel fuel. Due to scarcity of published information on the properties and impacts of rosin and rosin-derivates as fuels, estimations of thermal and thermochemical properties were performed. In addition, a section is devoted to the synthesis of AAME from commercially available rosin in Colombia. The influence of AAME in combustion tests is analyzed from emissions of carbon monoxide, carbon dioxide, nitrogen oxides (NOx = NO + NO_2) and unburned hydrocarbons, and temperature and flame size, by using a laminar flame in a coflow burner.

3.1 Estimation of some fuel properties

3.1.1 Background

In Section 1.2.3 it was mentioned that the use of rosin as fuel component involves the previous transformation of resinic acids into light hydrocarbons, for instance by hydrotreatment or hydrocracking. Although the obtained hydrocarbons displayed good performance as fuel components, these processes demand high amounts of energy. Thus, in this chapter the transformation of rosin is evaluated at mild reaction conditions. Esterification and reduction reactions appear to be appropriate because their products (esters and alcohols) have been typically used as fuels, and these reactions can be performed using heterogenous catalysts. In the case of esterification, considering that the resin acids of rosin are heavy molecules, only methyl esterification is proposed.

Due to scarce information on thermal and thermochemical properties of rosin and rosin-derived products, estimation of these properties was also performed. Indeed, beyond evident advantages such as economizing experiments, obtaining

information from molecules difficult to separate in pure form (e.g., rosin) is very relevant in order to evaluate the feasibility of certain chemical transformations.

3.1.2 Methodology

Adiabatic flame temperature of the molecules was estimated by using the fuel properties (e.g., enthalpy of formation, heat capacity, etc.), at atmospheric pressure and temperature (0.87 bar and 298 K). The equivalence ratio (ϕ, defined as the ratio of the actual fuel/air ratio to the stoichiometric value) was varied in the estimations. Specifically, the temperature was iterated until the enthalpy loss between reactants and combustion products was below a defined tolerance, at constant pressure. The source code, developed by Lapuerta and coworkers [66], involves the chemical equilibrium of 32 species and 63 chemical reactions.

Estimations of thermal and thermochemical properties were performed based on group additivity methods described in Sections 2.1.3 and 2.1.4. Group additivity methods are popular and reliable for estimating thermal and thermochemical properties, and Benson's and Joback's were implemented to estimate properties of rosin and rosin-derivates.

Methods to estimate thermal and thermochemical properties depend on the type of molecules (molecular structure, weight, and complexity). It is known that these methods are not highly accurate, often showing both over- and under-predictions. Thus, in order to get better insight the analysis (with the exception of adiabatic flame temperature) was not performed on the property of the rosin component (e.g., abietic acid) itself but on the change of the property between the rosin component and the rosin-derivative obtained by the corresponding chemical transformation (e.g., methyl abietate, for the case of esterification); for instance, the change in melting temperature for the esterification product is calculated as the difference between the melting temperature of the (e.g.) abietic acid and that of the (e.g.) methyl abietate. In particular, since the purpose of the transformations reviewed in this work is to use rosin-derivates as fuel, negative changes in boiling / melting temperatures and positive changes in heating values are desired.

The studied chemical transformations of rosin were (see Figure 3.1): reduction (*r*), esterification (*e*) and isomerization (*i*) of rosin compounds; isomerization was studied as a previous step of reduction (r_i) and/or esterification (e_i). Direct reduction of acids from rosin leads to the formation of alcohols, while the reaction between carboxylic acids and an alcohol produces methyl esters (ME). Isomerization, on the other hand, is proposed because the solid state of rosin is due to only some components.

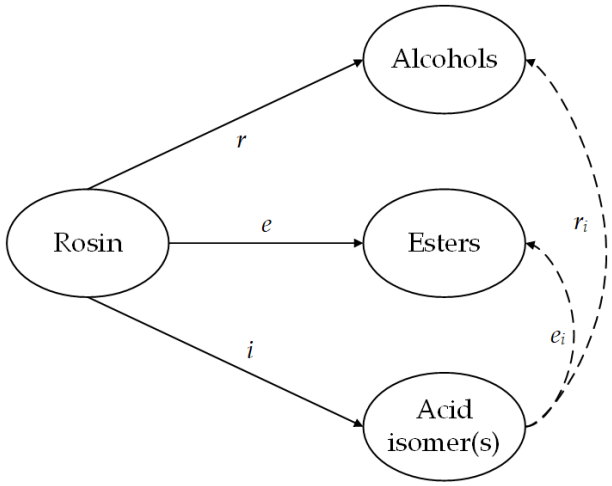

Figure 3.1. Transformations of rosin

These transformations of rosin aimed at improving the properties of resin acids. In particular, a decrease in viscosity, as well as in fusion and boiling temperature, is expected by performing reduction and methyl esterification of resin acids, which are solid at normal conditions. Isomerization is analyzed as a previous homogenization step for diverse acids from rosin before undergoing reduction and/or methyl esterification.

Composition of rosin from different countries and its main components was presented in Section 1.2.3. A detailed literature review of experimental data, especially of boiling and melting temperature, for pure components of rosin and the products of esterification and reduction reactions was performed; the findings are shown in Table 3.1. Only abietic acid and its derivates (AAME and abietyl alcohol) have experimental boiling and melting temperatures reported in the literature. In general, boiling temperatures of resin acids from rosin and rosin-derived molecules are scarce, while melting temperatures have been reported more often than boiling ones for rosin compounds and its derivates.

Table 3.1. Boiling and melting temperatures of rosin components and rosin-derived molecules

	Compound	Acid	Methyl ester (ME)	Alcohol
T_b[a] (°C)	Dehydroabietic	ND	ND	177 [90]
	Abietic	315-385 [91]	362.5 [92]	164 [93]
T_m[b] (°C)	Pimaric	218-219 [94]	ND	85-86 [95]
	Sandaracopimaric	218 [96]	67-68 [97]	ND
	Isopimaric	175 [98]	ND	86-87 [99]
	Levopimaric	150-152 [100]	63-64 [101]	ND
	Palustric acid	163-164 [102]	ND	ND
	Dehydroabietic	171-171.5 [102]	62.3-63.9 [103]	ND
	Abietic	172-174 [104][105]	25-84 [92] [101]	79-81 [106]
	Neoabietic	165-167 [107]	61.5-62 [108]	96-97 [109]

[a] Boiling temperature; [b] Melting temperature; ND no experimental data

3.1.3 Methyl esterification of rosin

Influence of the esterification reaction on the estimated melting and boiling temperatures is shown in Figure 3.2; the average from experimental values in Table 3.1 and the corresponding upper and lower limits are also presented as comparison. Joback method predicts the same change of boiling temperatures under esterification reaction for pimaric, isopimaric, levopimaric, dehydroabietic, abietic and neoabietic acids (ΔT_b^e=-64.8°C), while for sandaracopimaric and palustric acids change was -54.8 and -59.5°C, respectively. The decrease in boiling temperature of abietic acid after methyl esterification, calculated from experimental data in Table 3.1 is -12.5°C, which is lower than that estimated with Joback method (only the upper limit of the experimental temperature change is close to Joback estimation). Although Joback method typically overestimates boiling and melting temperatures, abietic acid has a wide range of experimental boiling temperatures, and the experimental value of boiling temperature of AAME is in the middle of this range. Theoretically, a reduction in boiling temperature is expected after esterification. Thence, some experimental data of boiling temperature for abietic acid might be erroneous.

The changes of melting temperature after esterification estimated with Joback method are very close to the expected from the experimental values for neoabietic and dehydroabietc acids, while the group contribution method underestimates the change in temperature for sandaracopimaric and abietic acids (although for abietic

acid it is within the experimental deviation) and overestimates that for levopimaric acid.

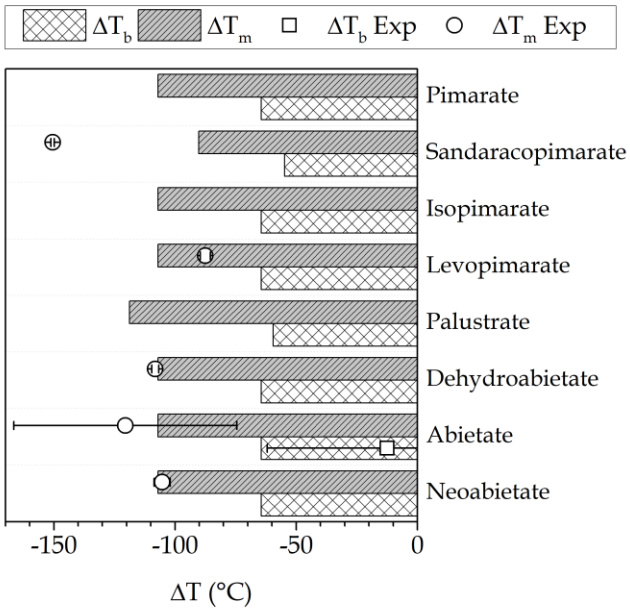

Figure 3.2. Changes in melting and boiling temperature due to methyl esterification of rosin

Pimaric skeleton is shared by pimaric, isopimaric and sandaracopimaric acids, the only difference being the position of an instauration inside the rings (see Figure 1.4). Nevertheless, the change in melting temperature calculated from the experimental data in Table 3.1 is significantly higher for sandaracopimaric acid without apparent reason. In general, good agreement was obtained with Joback method for changes in melting temperatures under esterification reaction of rosin compounds.

Estimated changes in lower heating value after esterification of rosin compounds, calculated by Benson and Joback methods, are shown in Figure 3.3. In general, results from Joback's are higher than Benson's, probably due to Joback neglecting the contribution of neighboring groups. In any case, esterification of rosin components into the corresponding methyl esters has a minor effect on heating values, because an increase of about 0.5 MJ/kg is estimated.

Under the assumption that all components of rosin are completely converted in the reaction, the esterification of rosin commercially available in Colombia translates into a reduction of melting temperature of 110.6°C, a reduction in boiling temperature of

62.9°C and an increase in heating values about 0.5 MJ/kg, which are appreciable changes in properties of methyl rosinate with respect to rosin. Despite the acid group being removed from their molecular structure, a high tendency to remain as solid of methyl rosinate is still maintained, with a minor increase in heating values.

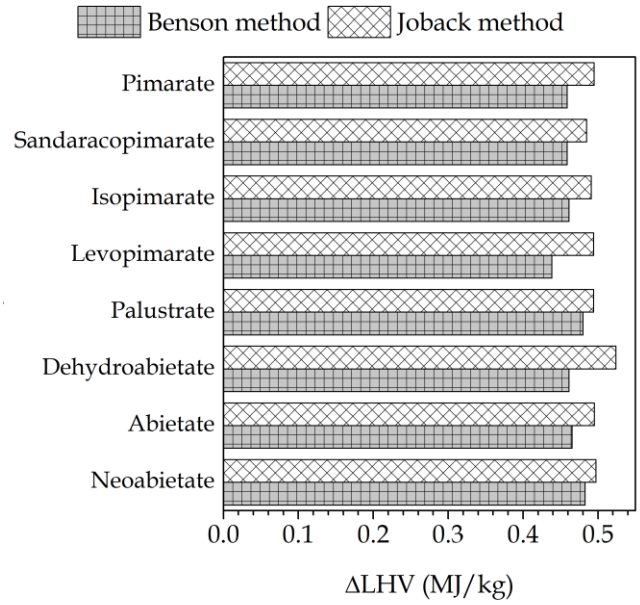

Figure 3.3. Changes of lower heating value due to methyl esterification of rosin

If methyl rosinate components are compared with typical methyl esters from vegetable oils (i.e., biodiesel), melting temperatures of the former are higher than those of methyl stearate and palmitate (38.9 and 33.5°C [110], respectively). Considering that biodiesel has often experienced filter clogging problems derived from both impurities (mainly mono-, di- and triglycerides and glycerol) and saturated esters, the reduction in melting point of methyl rosinate compounds seems to be insufficient for fuel applications.

Adiabatic flame temperatures for rosin-derived compounds of methyl esterification (methyl ester of rosin - ME rosinate, and particularly AAME) were calculated at “ambient conditions” (i.e., constant pressure, initial pressure and temperature of 0.87 bar and 298 K, respectively) and “engine conditions” (i.e., constant pressure, initial pressure and temperature of 80 bar and 900 K, respectively), and compared with that for a diesel of reference ($C_{15.18}H_{29.13}$) and biodiesel from palm oil ($C_{18.01}H_{34.97}O_2$), Figure 3.4.

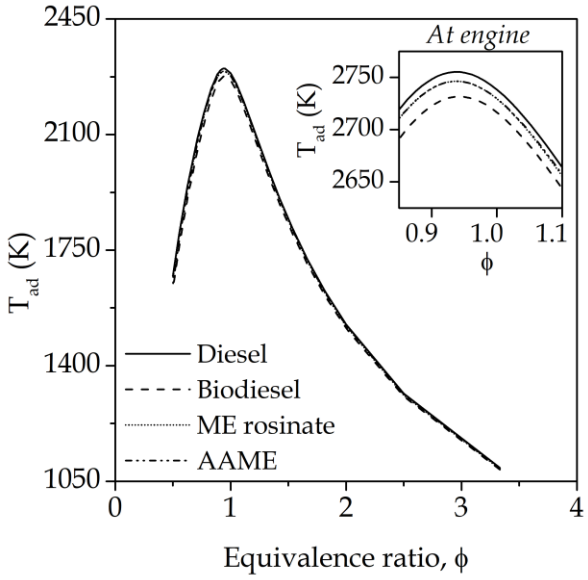

Figure 3.4. Adiabatic flame temperature for ME rosinate, AAME, diesel and biodiesel at "ambient conditions" (i.e., constant pressure) and "engine conditions" (i.e., constant volume, shown in insert)

At "ambient conditions", similar values of adiabatic flame temperature are observed for ME rosinate, AAME and diesel, with biodiesel displaying slightly lower values. At "engine conditions", differences are evidenced, diesel displaying the highest adiabatic flame temperature, followed by rosinol and ME rosinate (practically the same profile than AAME), and biodiesel (the lowest temperature).

Some properties of fuels, including the heat of formation from Benson method (Equation 2.15) for ME rosinate, AAME, diesel and biodiesel are shown in Table 3.2.

Table 3.2. Main properties of AAME, diesel and biodiesel

Fuel	MW (g/mol)	% O	H/C	Δh_f^0 (MJ/mol)
Diesel	211.7	0.0	1.92	-22.21
Biodiesel	283.5	11.3	1.94	-79.91
ME rosinate	316.5	10.2	1.52	-62.81
AAME	316.5	10.2	1.52	-62.60

Diesel is the lightest fuel and, as a result of the absence of oxygen in its molecules, it is expected to deliver more energy in combustion. Although ME rosinate and AAME are heavier than biodiesel, their heats of formation are higher, thereby the energy extracted from them in combustion is higher than from biodiesel. Properties of ME rosinate and AAME are very similar because the main component of ME rosinate is

AAME, and the corresponding properties of other components of ME rosinate are similar to AAME.

3.1.4 Reduction of rosin

Change in melting and boiling temperature due to reduction reaction of rosin are shown in Figure 3.5. Variations in boiling temperature for alcohols derived from rosin are slightly lower than those of the corresponding methyl esters. Similarly to the esterification of rosin, the change in boiling temperature calculated with the only experimental value available in the literature (see Table 3.1) is significantly larger than the estimated value. In addition, the change in boiling temperature for abietyl alcohol from experimental reports shows high dispersion due to the high dispersion of experimental boiling temperatures for abietic acid.

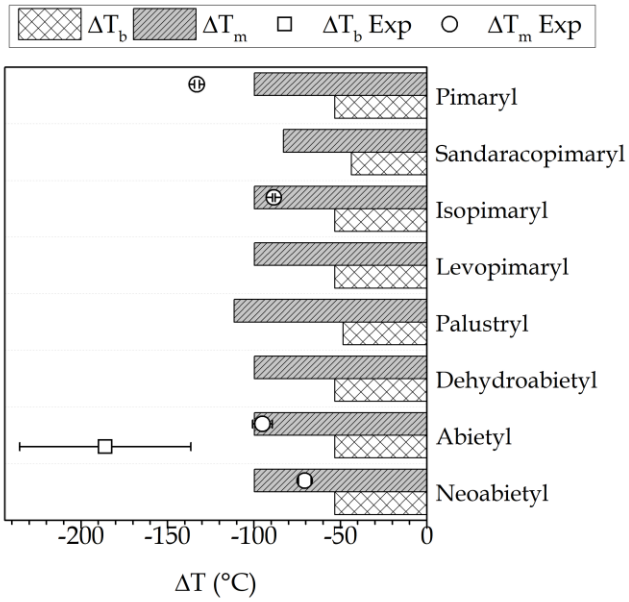

Figure 3.5. Change in melting and boiling temperature due to reduction of rosin

Experimental and estimated changes in melting temperatures from reduction of abietic and isopimaric acids are very similar. Difference in melting temperature resulting from the reduction reaction of neoabietic and pimaric acids are over- and under-estimated by Joback method, respectively, but estimations and experimental data are of the same order of magnitude. As in the case of esterification, alcohols from abietic and levopimaric acids display the lowest melting temperatures (15°C lower than those of other alcohols derived from rosin compounds).

Estimated change in lower heating value for the reduction of rosin compounds, calculated with Joback and Benson methods, are shown in Figure 3.6. Unlike the estimated changes in lower heating values due to esterification of rosin, Benson's results are higher than Joback's probably as a result of the contribution of hydroxyl groups from Benson's being higher than from Joback's, whereas that for carboxyl groups is lower. In all cases (lower heating values from Joback and Benson methods), no significant differences are observed between the different compounds. The reduction reaction of rosin compounds shows a stronger effect on the lower heating value than esterification: lower heating values are increased in more than 3 MJ/kg, which is a significant change.

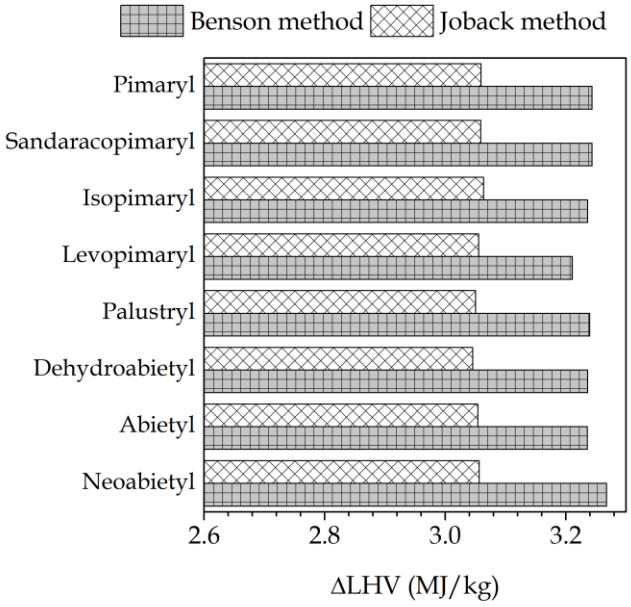

Figure 3.6. Delta of lower heating values due to reduction of rosin

The reduction reaction of rosin commercially available in Colombia, results in a reduction in both melting temperature (103.4°C) and boiling temperature (51.8°C), along with an increase in lower heating value (about 3 MJ). Melting and boiling temperatures of alcohols from rosin are 7.2 and 11.1°C lower than methyl rosinate's, respectively, indicating higher propensity of the reduced compounds from rosin to remain as solids in comparison to methyl esters. On the other hand, reduction of rosin yields products with higher heating values than rosin and its esterification products.

Adiabatic flame temperatures for rosinol (the derived-compound from reduction of rosin) were obtained at the same conditions than the products of esterification of rosin (i.e., “ambient conditions” and “engine conditions”), and also compared with diesel and biodiesel from palm oil, Figure 3.7.

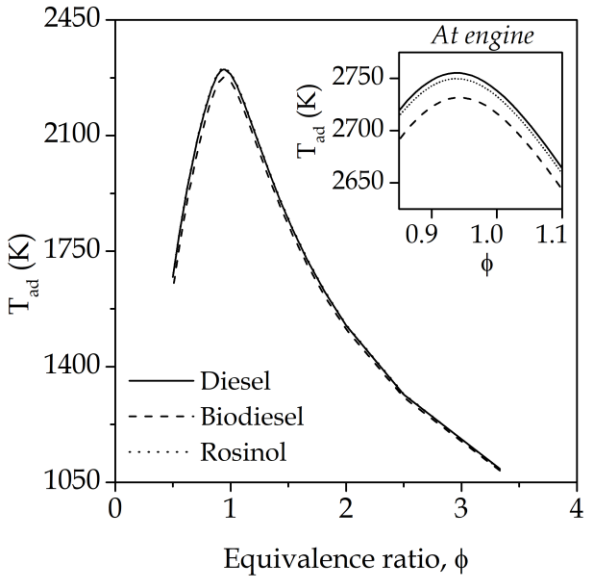

Figure 3.7. Adiabatic flame temperature for rosinol, diesel and biodiesel at “ambient conditions” (i.e., constant pressure) and “engine conditions” (i.e., constant volume, shown in insert)

Adiabatic flame temperatures for rosinol and diesel are similar even at “engine conditions”. The molecular weight, oxygen content and heat of formation for rosinol are 288.5, 5.5% and -47.23 MJ/kg, respectively. The heat of formation of rosinol is significantly higher than that for biodiesel (see Table 3.2). Similarly, adiabatic flame temperatures for rosinol are higher than for ME rosinate, probably due to its lower molecular weight and oxygen content.

3.1.5 Isomerization of rosin

Significant differences in melting and boiling temperatures between the rosin compounds can be observed in Table 3.1. Pimaric and sandaracopimaric acids display the highest melting temperatures, which makes them the most propense rosin compounds to remain solid. Thus, their presence in the raw material implies that unmodified rosin is unsuitable for fuel applications. On the other hand, levopimaric acid has the lowest melting temperature. In fact, the difference in melting

temperature between levopimaric and pimaric acid is around 65°C, which is somewhat large given their structural similarity. Therefore, isomerization of rosin compounds may improve the potential of rosin as feedstock for fuels by removing the acids with high melting temperature.

Unfortunately, experimental information for some rosin-derivates (methyl esters and alcohols shown in Table 3.1) is missing. Hence, estimated properties may help select a target compound for isomerization, which would undergo further reduction and/or esterification. Reaction products of reduction / esterification of levopimaric and abietic acids showed the lowest melting and boiling temperatures; thus, these acids are good candidates as target products in the isomerization reaction. In addition, both reduction and esterification yield rosin-derivates with similar lower heating values (i.e., around 36.4 MJ/kg after methyl esterification and around 38.9 MJ/kg after reduction, estimated with Benson method), thus, isomerization apparently does not influence this property.

3.1.6 Remarks of the section

- ★ A significant decrease in melting and boiling temperatures and an increase in heating values can be expected by performing the reduction and esterification of rosin, that is, the melting / boiling temperature and heating value of the reaction product are lower and higher, respectively, than the corresponding compound of rosin.
- ★ Esterification of rosin compounds yields esters with melting temperatures around 108°C lower than resin acids, while the heating values is slightly increased. Besides, adiabatic flame temperature of the product of methyl esterification of rosin is lower than that for diesel, but higher than that for biodiesel.
- ★ Reduction of rosin yields alcohols with melting temperatures higher than those for esters, but higher heating values and adiabatic flame temperatures (closely similar to diesel) are obtained.
- ★ Molecules derived from levopimaric and abietic acids displayed the best thermal properties among rosin compounds, with similar lower heating values, making these acids good candidates for an isomerization reaction.

3.2 Production of methyl esters of rosin

3.2.1 Background

Rosin is composed mainly by resin acids, namely, abietic, dehydroabietic, neoabietic, palustric, pimaric, isopimaric and levopimaric [18], which are readily esterified yielding products with interesting properties. For instance, AAME (CAS 127-25-3; mw: 316.47; mf: $C_{21}H_{32}O_2$) is a colorless-to-yellow thick liquid, almost odorless, 360-365°C boiling point, 190°C flash point and 1.040 g/cc density at 20°C. It is insoluble in water, soluble in organic solvents (alcohols, ether, etc.) and aliphatic hydrocarbons. Combustible when exposed to heat or flame it can react with oxidizers. Heated to decomposition emits irritating fumes and acrid smoke. The uses of AAME are similar to methyl rosinate, including plasticizer, solvent for vinyl and cellulosic materials [111–114].

Typically, sulfuric acid has been used as catalyst in the esterification of resin acids. Esterification of abietic and dehydroabietic acids with this catalyst displayed high yield (up to 90%), and a purification by ester extraction was necessary [115]. Acidic functional ionic liquids (1-(3-sulfonic group)propyl-3-methylimidazole *p*-toluenesulfonate) have been used to catalyze the esterification of abietic acid with methyl alcohol obtaining ca. 90% conversion and easy reusability of the catalyst [116]. Other processes use esters, such as dimethyl sulfate, methyl sulfate and dimethyl carbonate, as methyl donors in the esterification. In these reactions, lithium hydroxide and potassium carbonate have been used as catalysts, obtaining yields ca. 99% [117]–[119].

Different catalysts have been reported for the esterification of rosin with different alcohols. Lewis and Brönsted acids, such as acetic acid, sulfuric acid and *p*-toluenesulfonic acid, are suitable. On the other hand, most studies on heterogeneous catalysis have been conducted on the esterification of rosin with polyols using different materials: oxides (e.g., calcium, zinc magnesium aluminum and rare metal), alkaline hydroxides (e.g., calcium and magnesium hydroxides), organic and inorganic salts (e.g., iron chloride, calcium formate and calcium phosphate), and acidic-functionalized ionic liquids [120], [121].

Studies on the heterogenous esterification of rosin with methanol are scarce. Recently, ZnO supported on spent fluidized-catalytic-cracking catalyst (ZnO/SFCCR) was applied to the esterification of rosin with methyl alcohol under subcritical CO_2 conditions. CO_2 acts as auxiliary catalyst, improves mass transfer and adjusts pH to values between 3.54 and 3.91; conversion ca. 97% was obtained at 5 h reaction time, 220°C and without solvent [122]. On the other hand, acidic groups as *p*-toluenesulfonic and sulfuric acids were incorporated into MCM-41, achieving high activity in the esterification of rosin with methyl alcohol, i.e., 88% conversion, at 220°C and 5 h reaction time [123]. Steric effects and low molecular size of methyl alcohol with respect to rosin, together with the fact that the acid group in resin acids is attached to a tertiary carbon, makes the esterification of rosin with methyl alcohol a very difficult reaction [122], [123].

3.2.2 Methodology

3.2.2.1 Materials

Rosin (technical grade: Colophony WW®, 64-78°C softening point, and 146-169 mg/g acid number) was supplied by Protokimica (Medellín, Colombia). Methyl alcohol and acetone (Ph. Eur. Reag., purity >99.0%), and analytically-pure potassium acid phthalate were purchased from Merck. Potassium hydroxide, toluene, isopropyl alcohol, diethyl ether, ethyl alcohol and magnesium oxide, all analytically grade, were purchased from JT Baker. Analytical grade Amberlyst® 15 and dimethyl carbonate (technical grade), abietic acid methyl ester (analytical assay not available), and tetra-methyl-ammonium hydroxide solution at 25 wt.% in methyl alcohol were purchased from Sigma-Aldrich. Titanium dioxide (Hombikat®, analytically pure) was purchased from Sachtleben Chemie. γ-Alumina (analytical grade) was purchased from Alpha-Aesar. Kaolin and calcium carbonate (analytical assay not available) were acquired in the local market. In addition, a low-cost a calcium-based material (a mixture of CaO, $Ca(OH)_2$ and $CaCO_3$) available in the local market was also evaluated.

3.2.2.2 Rosin and reaction product characterization

Rosin and the reaction products were characterized by GC and GC-MS, based on ASTM D5974-15. A derivatization (i.e., methylation with tetra-methyl-ammonium

hydroxide — TMAH) was necessary for individual rosin acids identification; specifically, titration of samples previously diluted in methyl alcohol/diethyl ether solution was carried out with TMAH 6 wt.% titration/methylation solution and phenolphthalein as indicator. The same derivatization procedure was followed for the reaction products.

Quantification was made by area percentage method, according to ASTM D5974-15. GC analysis was performed in an Agilent Technologies 7890 equipped with a flame ionization detector (FID). A 1 µL sample was separated using an HP-5 ((5%-Phenyl)-methylpolysiloxane) capillary column (30-m legth x 0.32-mm i.d., 0.25-µm film thickness) (Agilent J&W). Helium was used as carrier gas with an average linear velocity of 20 cm/s; the initial temperature (150°C) was held for 5 min and, then, a 5°C/min heating ramp up to 250°C (held for 10 min) was used. The split ratio, inlet injection temperature and detector temperature were 100 : 1, 300°C and 325°C, respectively.

Peak identification was conducted by gas chromatography mass spectrometry (GC-MS) using an Agilent 7890 GC system coupled to Agilent 5975C VL MSD triple quadrupole mass detector. Chromatographic conditions were as above. Electron-impact mass spectra were recorded every second at an electron energy of 70 eV. In addition, Fourier-transform infrared (FTIR) spectra of feed and reaction product were performed in a Perkin Elmer Spectrum 65 with a horizontal attenuated total reflectance (HATR) attachment from 600 to 4000 cm^{-1}. Reaction product was concentrated by roto-evaporation in a Heidolph V-800 with vacuum control in automatic mode.

3.2.2.3 Catalyst characterization

XRD patterns of materials were recorded by using a Bruker D8 Advance coupled with CuKα1 radiation generated at 40 kV and 40 mA, 2θ from 5º to 70º with a step size of 0.05º. Fourier-transform infrared (FTIR) spectra for fresh and post reaction samples of catalysts were collected in a Perkin Elmer Spectrum 65 on diffuse reflection mode (Pike) with KBr powder. Temperature-programmed desorption profiles with CO_2 were obtained in a Micromeritics Autochem 2920. The temperature

programmed desorption of CO_2 (TPD-CO_2) was conducted in helium flow at 50 mL/min until 850°C with a heating ramp of 10°C/min. Previous pretreatment of the samples was performed by heating at 200°C for 60 min with a heating rate of 10°C/min under helium flow of 50 mL/min.

3.2.2.4 Catalyst activity

The catalyst activity was evaluated performing the chemical reaction represented in Figure 3.8 (R represents the skeleton for each resin acid, see Figure 1.4).

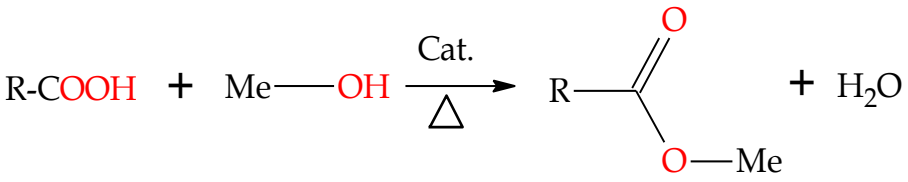

Figure 3.8. Scheme of rosin esterification reaction with methyl alcohol

The sample of rosin, methyl alcohol, and catalyst was placed in a flask (50 mL) equipped with temperature control, a condenser and magnetic stirring. Reaction temperature was maintained at 64°C (reflux temperature) and stirring at 500 rpm. Different reaction conditions (i.e., solvent, reaction time, reactant molar ratio, and catalyst load) were evaluated, and the catalyst was removed by filtration; in some cases, a subsequent centrifugation was performed.

Conversion was calculated with the acid value of reactants and products, Equation 3.3.1,

$$\text{Conversion}\ (\%) = 100 * \left(1 - \frac{Wn_{\text{f}}}{Wn_{\text{i}}}\right) \qquad \textbf{Equation 3.3.1}$$

where Wn is the acid number and, subscripts i and f represent the initial and final conditions for each reaction. The conversion of rosin was used as criterion to assess the esterification reaction. The acid value was determined according to ASTM D465-15. The dissolved reaction product (or rosin dissolved in methyl alcohol or isopropyl alcohol / toluene mixture) and 4-5 drops of phenolphthalein indicator was titrated with a standard solution of potassium hydroxide; titration solution was standardized with potassium acid phthalate solution. Acid number in mg_{KOH}/g_{sample} was computed as Equation 3.3.2,

$$Wn = \frac{V \cdot C \cdot M}{m}$$ **Equation 3.3.2**

where V is the volume of potassium hydroxide used in titration (mL), C is the concentration of potassium hydroxide solution (mol/L), m is the weight of the sample (g) and M is the molecular weight of potassium hydroxide (56.11 g/mol).

3.2.2.5 Catalyst stability

The reusability of the catalyst was assessed by using the same catalyst and reaction conditions in five reaction cycles. After each cycle, the catalyst was washed for one hour with methyl alcohol at the same reaction temperature and stirring, filtered and dried.

3.2.3 Results and discussion

3.2.3.1 Overall results

The most relevant results of this study on the esterification reaction of rosin with methyl alcohol are summarized in Table 3.3.

Table 3.3. Relevant results from rosin esterification

Entry	Catalyst	Solvent	Rosin/MeOH[a]	Conversion (%)
1	Ca[b]	None	748	45
2	MgO	None	748	26
3	TiO_2	None	748	27
4	Al_2O_3	None	748	18
5	Kaolin	None	748	7
6	Amberlyst	None	748	4
7	Ca[b]	Acetone	187	35
8	Ca[b]	Ethanol	187	48
9	Ca[b]	2-Propanol	187	35
10	MgO	Toluene	187	6
11	$CaCO_3$	Toluene	187	30
12	Ca[b]	None	60	45
13*	Ca[b]	None	187	55
14	Ca[b]	None	523	45
15	Ca[b]	None	900	47

[a]Weight ratio; [b]calcium material; *at 4.5 h reaction rime. Reaction conditions: 64°C, 500 rpm, 40% catalyst loading (with respect to rosin), 3.5 h reaction time, 1 : 1.76 volumetric ratio of methyl-alcohol : solvent.

The highest conversion is obtained with the calcium material as catalyst, at 4.5 h reaction time, 187 weight ratio of rosin : methyl-alcohol and without solvent (entry 13

in Table 3.3). Detailed analysis of the main variables influencing the reaction is presented in the following sections.

3.2.3.2 Characterization of rosin and reaction products

Rosin samples were freshly broken from a larger mass to avoid air oxidation (ASTM D5974-15). The acidity number of rosin, as measured with several samples of different weight (0.5 to 4.0 g) by using different concentrations of the titration solution (0.08, 011 and 0.49 mol/L), ranged from 145.3 mg/g to 146.0 mg/g, with an average value of 145.6 mg/g.

A chromatogram of rosin is shown in Figure 3.9. The main components of rosin are eluted between 32- and 44-min. A proper separation was achieved, as indicated by the well-defined peaks observed. The components of rosin (identified by comparison between mass spectra for each peak and NIST database) and their concentration are displayed in Table 3.4. The concentration of rosin is similar to that produced in Centro America [23], with levopimaric (4), dehydroabietic (5) and abietic (6) acids as main compounds (according to Figure 3.9).

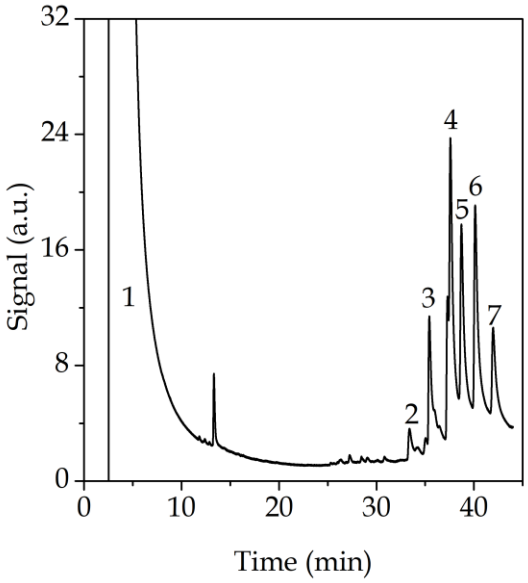

Figure 3.9. Chromatogram of rosin

Elution times in Table 3.4 are in good agreement with Hudy [124] and Volkman and coworkers [125]. Hudy [124] used polar and nonpolar packed columns for the separation of resin acid esters, obtaining similar results with both columns.

Furthermore, the differences in volatility and unsaturation of resin acid esters are the key for the separation, which is not achieved with rosin acids without esterification. Volkman and coworkers [125] reported a successful separation of the main resin acids; the elution in a nonpolar column (HP-1 methyl silicone capillary column) followed the order: pimaric, isopimaric, levopimaric, dehydroabietic, abietic and neoabietic resin acid esters.

Table 3.4. Peak identification for rosin compounds

#[a]	t_R (min)	Compound	Concentration[b] (wt.%)
	2.6	Methyl alcohol	--
2	33.4	Methyl pimarate	2.3
3	35.4	Methyl isopimarate	11.2
4	37.6	Methyl levopimarate	29.7
5	38.7	Methyl dehydroabietate	19.7
6	40.1	Methyl abietate	21.1
7	42.0	Methyl neoabietate	10.9
		Others	5.1

[a]See Figure 3.9; t_R is the retention time; [b]Solvent-free basis

FTIR spectrum of rosin is shown in Figure 3.10. The peak at 1275 cm^{-1} is assigned to stretching vibration of the carboxylic group (C—O bond), while bands at 1451 and 888 cm^{-1} can be attributed to bending vibrations of the same group (O—H bond) [126]. The intense band at 1694 cm^{-1} is assigned to the carbonyl structure (C=O) of carboxyl groups [126]. Aditionally, the bands at 2927 and 3434 cm^{-1} can be assigned to stretching vibration of hydroxyl group of adsorbed water and vibrations typicals for hydrocarbons, respectively [127]. These bands have been commonly reported for rosin [128].

The reaction product obtained with toluene as solvent (methyl-alcohol : toluene at 1 : 0.4 volume ratio), rosin:methyl-alcohol molar ratio of 1 : 186, 64°C, 3 h reaction time, and calcium-based material loaded at 40% with respect to rosin was analyzed by FTIR and GC-MS (following the same procedure than rosin characterization). The concentration of reaction products obtained by GC analysis is shown in Table 3.5 (reaction conversion >90%). Concentration of reaction products is similar to that of rosin (see Table 3.4), suggesting that all components of rosin are transformed into ester products in the reaction.

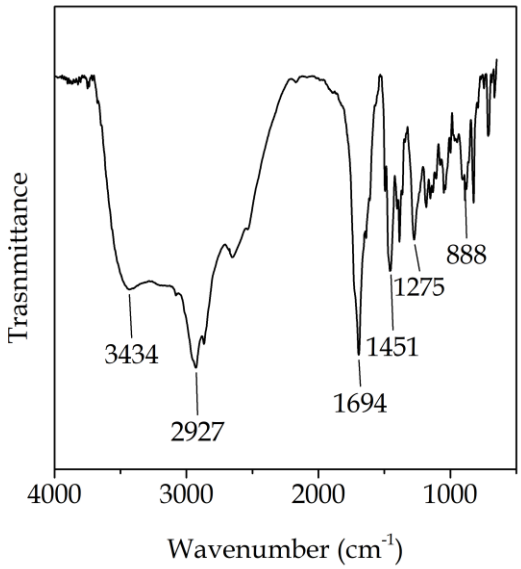

Figure 3.10. FTIR spectrum of rosin

Table 3.5. Peak identification for reaction product

t_R (min)	Compound	Concentration[a] (%)
2.6	Methyl alcohol	--
33.4	Methyl pimarate	3.6
35.4	Methyl isopimarate	10
37.6	Methyl levopimarate	27.8
38.7	Methyl dehydroabietate	18.1
40.1	Methyl abietate	18
42.0	Methyl neoabietate	11.6
	Others	10.9

t_R is the retention time; [a]Solvent-free basis.

FTIR spectrum of the product of esterification of rosin is compared with that of abietic acid methyl ester (AAME) in Figure 3.11. The FTIR analysis of reaction product was performed once volatile compounds (i.e., toluene and methyl alcohol) are removed by evaporation. A broad band at 3334 cm^{-1} is observed for both AAME and the reaction product, as well as for rosin (see Figure 3.10), and can be attributed to hydroxyl group of adsorbed water.

FTIR spectrum for AAME displays an intense band at 1727 cm^{-1} assigned to the stretching vibration of carbonyl structure (C=O); the sharp peak at 1244 cm^{-1} is

assigned to the stretching vibration of C-O bond from ester group [129]. Since IR spectra for methyl ester of rosin compounds are not available in literature, a simulation of the molecule was carried out. The optimization of the AAME geometry was performed using the Density Functional Theory (DFT) with the hybrid functional B3YLP and the electronic base 6-31G with Gaussian G09. Bands at 1727 and 1244 cm^{-1} were obtained for both elucidated and experimental IR spectra.

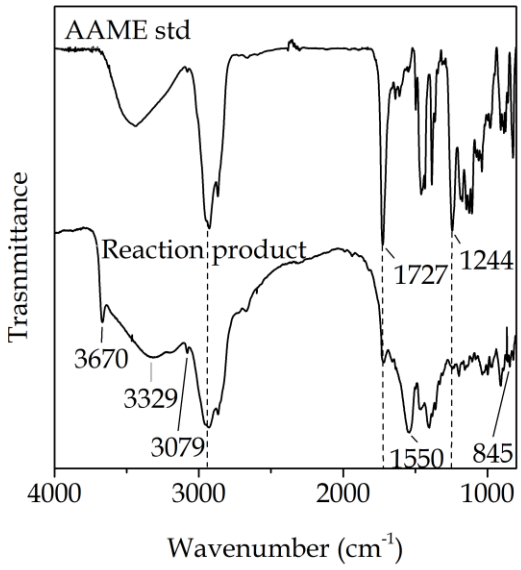

Figure 3.11. FTIR spectra of reaction product and standard abietic acid methyl ester (AAME). Reaction conditions: 64°C, 3 h reaction time, rosin : methyl-alcohol molar ratio of 1 : 186, methyl-alcohol : toluene volumetric ratio of 1 : 0.4, and calcium-based material loaded at 40% with respect to rosin.

FTIR spectrum for reaction product in Figure 3.11 shows the same bands than AAME, located at 1727 and 1244 cm^{-1}. Aditionally, bands at 3670 and 3329 cm^{-1}, which are typical for methyl alcohol (assigned to the stretching vibration of hydroxyl group [127]) are due to unreacted methyl alcohol. On the other hand, the slight peak at 3079 cm^{-1}, assigned to the stretching vibration of C-H bond, the band at 1550 cm^{-1}, assigned to the stretching vibration of C-C bond, and the sligth peak at 845 cm^{-1}, assigned to the out-of-plane bending of C-H bond, which are typical of aromatic rings, point to the presence of an aromatic ring in the reaction product [129]. Indeed, low amounts of methyl alcohol and toluene are expected in the reaction product, in agreement with the low area of the corresponding peaks, probably because rosin

and/or rosin methyl ester adsorb them, avoiding its total separation in the evaporation step.

3.2.3.3 Activity of different catalysts

Figure 3.12 shows the activity of the calcium-based material, magnesium oxide, titanium dioxide, alumina, kaolin, and Amberlyst® 15 at different loads (with respect to rosin) for the esterification of rosin with methyl alcohol.

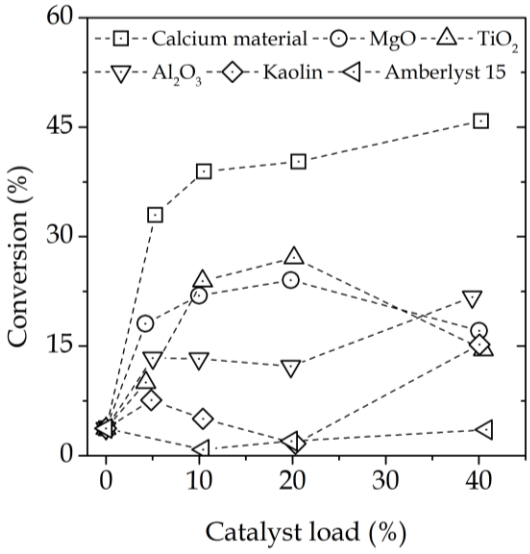

Figure 3.12. Activity of the different catalysts. Catalyst load is computed with respect to rosin. Reaction conditions: 64°C, 3 h, rosin : methyl-alcohol molar ratio of 1 : 748. Conversion without catalyst is ca. 4%

Amberlyst® 15 does not display activity for the reaction, suggesting that acidity does not promote the formation of esters under heterogeneous conditions. Conversely, the basic materials tested in this work have a significant effect on the reaction. Similar performance was displayed by magnesium oxide and titanium dioxide: both catalysts have the best performance at 20% catalyst load, achieving 23-27% conversion. Furthermore, conversion decreases at higher catalyst loads probably due to diffusional effects resulting from the high density and high loads of these materials. After an initial increase with catalyst load, conversion with alumina and kaolin decreases until 20 % catalyst load to increase again reaching 15 and 23% conversion, respectively, at a 40% catalyst load. The calcium-based material outperforms all the other materials, conversion being directly proportional to catalyst

load and reaching 46% at 40% catalyst load. The high activity of this material would be related to its basicity and/or the higher pH of the slurry [130].

3.2.3.4 Solvent effect

Acetone, toluene, and methyl, ethyl and isopropyl alcohols were evaluated as solvents in the esterification of rosin and methyl alcohol, with the calcium-based material as catalyst, Figure 3.13a. A slight increase in rosin conversion (ca. 5%) with respect to the reaction without solvent is observed with ethyl alcohol. On the other hand, acetone and isopropyl alcohol displayed similar performance on the esterification of rosin, with conversions smaller than the base case (i.e., no solvent). Thus, high basicity and polarity would be desirable for a solvent in the esterification of rosin; indeed, according to the polarity parameter of Kamlet-Taft (E_T^N), polarity decreases in the order methyl alcohol>ethyl alcohol>isopropyl alcohol>acetone, whereas according to the β parameter of Kamlet-Taft the basicity decreases in the order isopropyl alcohol>ethyl alcohol> methyl alcohol>acetone [131]. However, since toluene (non-polar solvent) displayed an adverse effect on the calcium-based material, stability tests were performed with this solvent (see below).

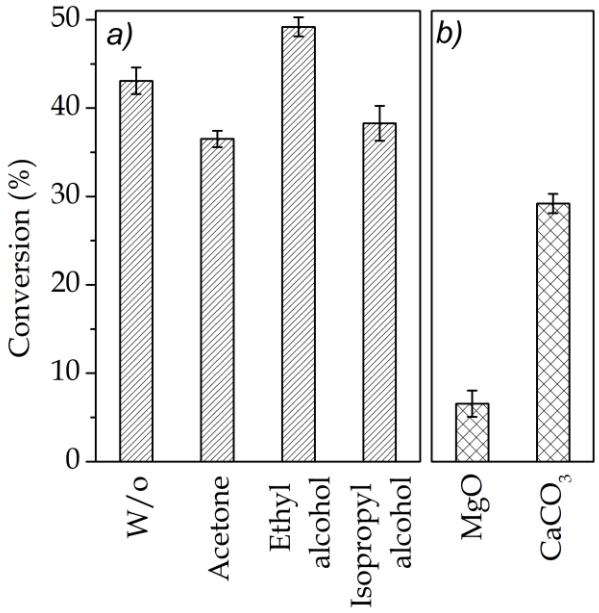

Figure 3.13. Effect of solvents on rosin esterification. a) calcium-based material as catalyst, and b) toluene as solvent. Reaction conditions: 64°C, 4.5 h and rosin : methyl-alcohol molar ratio of 1 : 187; methyl-alcohol : solvent volumetric ratio of 1 : 1.76. In the case of methyl alcohol as solvent, additional methyl alcohol was added with respect to experiment without solvent (w/o) to match the reaction volume of the experiments with other solvents

Performance of magnesium oxide and calcium carbonate as catalysts with toluene as solvent is presented in Figure 3.13b: conversions are low, around 7 and 30%, respectively. Calcium carbonate is a highly-basic material, with strong basic sites. On the other hand, magnesium oxide displays medium-strength sites. Therefore, the combination of materials with medium- and high-strength basicity with low-polarity solvents appears to be insufficient to activate the acid groups of rosin and/or the hydroxyl group of methyl alcohol.

The stability tests of the calcium-based material with toluene as solvent were performed at 64°C, 3 h, rosin : methyl-alcohol molar ratio of 1 : 186, methyl-alcohol : toluene volumetric ratio of 1 : 0.4, and a 40% load of calcium-based material (with respect to rosin). FTIR spectra for samples of the calcium-based material before and after reaction are shown in Figure 3.14.

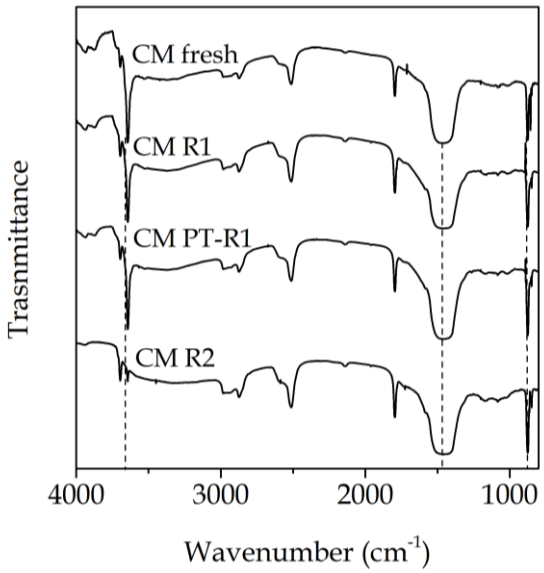

Figure 3.14. FTIR spectra of calcium-based material: fresh (CM fresh), after first reaction (CM R1), after washing treatment post first reaction (CM PT-R1), and after second reaction (CM R2), with toluene as solvent

FTIR spectra of the fresh sample of the calcium-based material depicts a shark peak at 3643 cm^{-1} associated to the stretching vibrations of OH groups of $Ca(OH)_2$ [132] and two peaks at 1452 and 876 cm^{-1} attributed to CO_3^{2-} species from $CaCO_3$ [133], indicating that calcium carbonate and calcium hydroxide are the main phases of this material. In addition, the fact that the area of the peak at 3643 cm^{-1} decreases until

it is practically absent after the second cycle of reaction, indicates that $Ca(OH)_2$ phase disappears from the bulk of the calcium-based material.

XRD patterns of samples of the calcium-based material at different cycles of esterification reaction of rosin with methyl alcohol and toluene as solvent are presented in Figure 3.14. The fresh sample of the calcium-based material shows a major peak at 25.9° indicating that calcite ($CaCO_3$) is the major phase of the material [134]. Calcium oxide and hydroxide, represented by peaks at 2θ values of 18, 46.8, 50.1 and 62.6° [135], and 28.7, 34.1, 54.8 and 64.8°, respectively [134], [135], would be present in lower concentrations. Similarly to FTIR spectra, XRD patterns in Figure 3.15 show a strong effect of reaction on the catalyst. In particular, at the end of the second reaction cycle the catalyst is composed only by calcium carbonate, the peaks of CaO and $Ca(OH)_2$ phases almost absent from the sample.

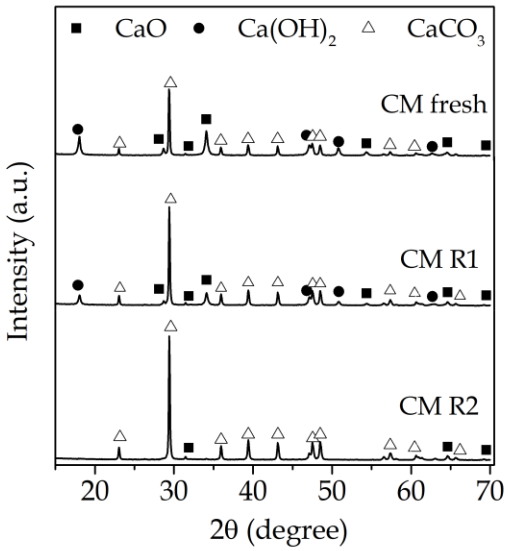

Figure 3.15. XRD patterns of calcium-based material: fresh (CM fresh), and after first (CM R1) and second reaction (CM R2), with toluene as solvent

Profiles of temperature-programmed desorption with CO_2 for samples of the calcium-based material before and after reaction with toluene as solvent are shown in Figure 3.16. TPD-CO_2 profile of the fresh sample displays three peaks around 300-320, 370-400 and 700-750°C. According to XRD and FTIR results, these peaks can be attributed to CaO, $Ca(OH)_2$ and $CaCO_3$, respectively. Therefore, the strongest base

sites in the sample of the calcium-based material are due to the presence of carbonate. $Ca(OH)_2$ phase is represented by other strong base sites (lower than that for carbonate), and a medium-strength base sites (with low availability) are due to the CaO phase.

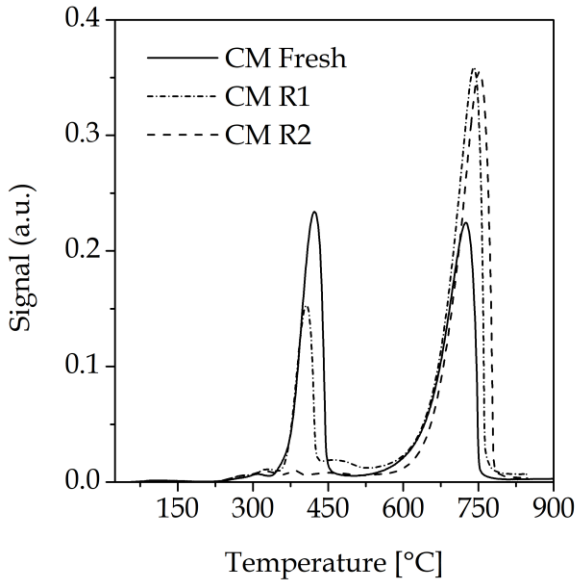

Figure 3.16. TPD-CO_2 of calcium-based material: fresh (CM fresh), and after first (CM R1) and second reaction (CM R2), with toluene as solvent

The peak between 300 and 450°C in the TPD-CO_2 profiles decreases with the number of reaction cycles suggesting a reduced availability of $Ca(OH)_2$ phase, in agreement with the FTIR and XRD results, perhaps as a result of the very low polarity of toluene facilitating the dissolution of calcium hydroxide leading to the formation of species dissolved in the solvent phase. Simultaneously, the area of the peak at 700°C is increased which is consistent with the leaching of $Ca(OH)_2$ phase. Structural changes of the calcium-based material suggest that the solvent - catalyst system toluene - calcium hydroxide is not suitable for the esterification of rosin with methyl alcohol. Furthermore, the conversion of rosin with the toluene - calcium carbonate system is low, suggesting that the calcium hydroxide phase plays an important role in the esterification of rosin.

3.2.3.5 Activity of the calcium-based material without solvent

Minor influence of the solvent on the esterification of rosin was observed (i.e., conversion was increased by 5% with ethyl alcohol). Furthermore, avoiding subsequent separation of solvents is desirable. Thus, different reaction times and ratios of reactants were evaluated to obtain improved reaction conditions for the esterification of rosin with methyl alcohol using the calcium-based material as catalyst.

As the stoichiometric ratio of rosin compounds and methyl alcohol is 1 : 1 (see Figure 3.8), the formation of rosin ester would be favored by an excess of methyl alcohol. Therefore, the rosin : methyl-alcohol molar ratio was varied; conversion of rosin at different rosin-to-methyl-alcohol molar ratios without solvent is shown in Figure 3.17; at 1 : 187 rosin : methyl alcohol molar ratio the conversion is ca. 55%, while the other ratios tested display similar values (ca. 45%).

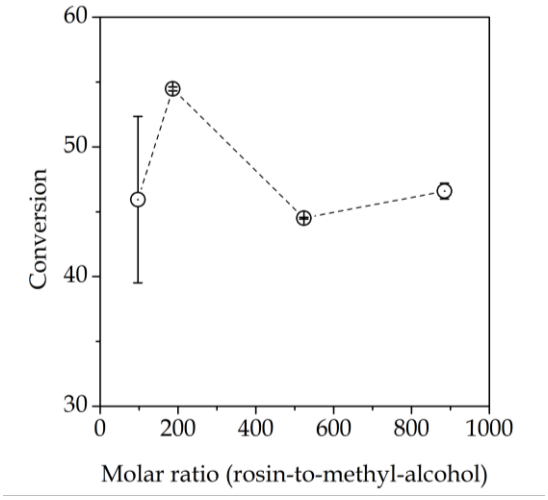

Figure 3.17. Performance of esterification of rosin as a function of reactants ratio (at 4.5 h and 40% of load of calcium-based material with respect to rosin)

After an initial increase, conversion levels off at ca. 45% at high reactant ratios, perhaps due to the competition of molecules to reach the active sites on the catalyst. On the other hand, in esterification reactions at lower reactant ratios dissolution of rosin is difficult, which may explain the reduction in catalyst activity at 1 : 97; therefore, experiments were not performed at lower rosin : methyl alcohol molar ratios. Similarly, the large variation in the conversion of rosin at 1 : 97 rosin : methyl

alcohol molar ratio (12.8 standard deviation in conversion) would be explained by this dissolution effect.

Figure 3.18 shows the conversion of rosin as a function of time. At 1 h the conversion is ca. 40%, and a (somewhat) constant conversion of ca. 45% is achieved after 3.5 h of reaction, indicating that there is little gain in further increasing the reaction time. As a result of steric effects of tricyclic skeleton of rosin compounds and the position of carboxyl group (located on a tertiary carbon atom), esterification reactions typically involve severe conditions, such as high temperatures and pressures and long reaction times, to reach high conversions [122], [123].

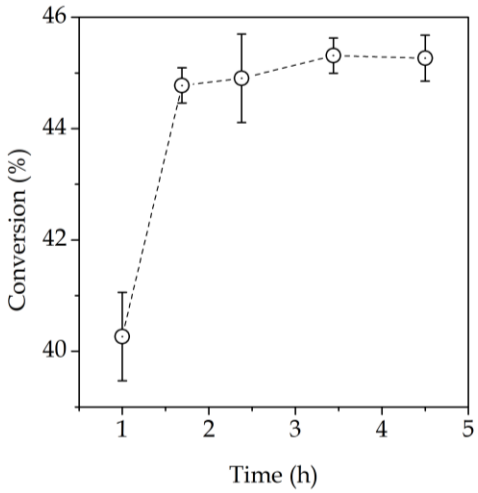

Figure 3.18. Performance of esterification of rosin as a function of time (at 64°C, rosin : methyl alcohol molar ratio of 1 : 523, and 40% calcium-based material load with respect to rosin)

3.2.3.6 Catalyst stability

Five reaction cycles were carried out to evaluate the stability of the calcium-based material in the esterification of rosin with methyl alcohol and without solvent. Fresh rosin and methyl alcohol were added to the catalyst at the beginning of each cycle to keep the same molar ratio in all cycles. Reaction conditions were the same for all cycles, namely: 64°C, 500 rpm, 2.5 h, 40% catalyst load (with respect to rosin), and rosin : methyl alcohol molar ratio of 1 : 187 and 1 : 22 for reaction without solvent and with toluene as solvent, respectively. The procedure was repeated with different amounts of initial catalyst to evaluate the repeatability of the experiment.

Conversion of rosin is decreased by ca. 50% in the second cycle, see Figure 3.19. A slight increase in the conversion of rosin is observed for the remaining cycles,

suggesting that the procedure implemented to wash the catalyst is not enough to remove the compounds adsorbed on the surface of the calcium-based material, but repetitive washing probably removes more adsorbed material.

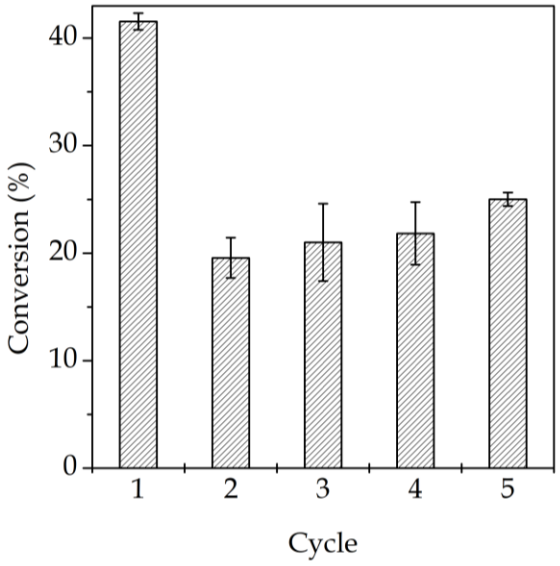

Figure 3.19. Catalyst stability. Reaction conditions: 64°C, 500 rpm, 2.5 h, 40% catalyst load (with respect to rosin) and rosin : methyl alcohol molar ratio of 1 : 187 and 1 : 22 for reaction without solvent (w/o) and with toluene as solvent (at methyl-alcohol : solvent volumetric ratio of 1 : 0.4), respectively

FTIR spectra for a sample of the calcium-based material after reaction without solvent and a sample of washed calcium-based material after reaction were compared with that for the fresh sample (see Figure 3.20). Although the spectra are similar for the fresh and used samples, some differences can be observed. The peak area at 2928 cm^{-1} is larger for the sample of the calcium-based material after reaction than the other samples. This peak can be attributed to the carboxilic group of rosin and carbonyl structure of ester group, which may suggest the presence of unreacted rosin and/or rosin methyl ester on the surface of the catalyst after reaction. After reaction and washing this area is reduced, but it is not equal to that of the fresh catalyst, suggesting that some rosin and/or rosin methyl ester are present after the washing step.

No significant difference in the XRD pattern of the sample of the calcium-based material is observed after the first reaction cycle, see Figure 3.21, whereas after five reaction cycles an appreciable reduction in intensity of peaks associated to $Ca(OH)_2$

(17.86, 46.8 and 50.86°) and CaO phases (31.86, 34.11 and 54.37°) is evidenced, suggesting a minor leaching of these phases.

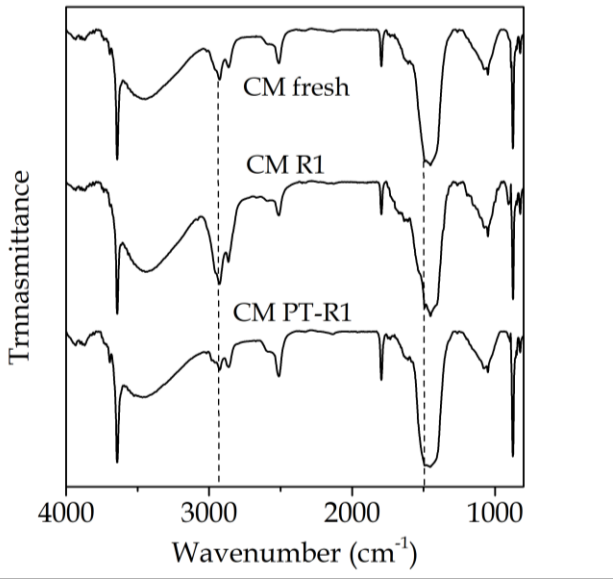

Figure 3.20. FTIR spectra for samples of calcium-based material: fresh (CM fresh), and after first reaction (CM R1) and washing (CM PT-R1); reaction was conducted without solvent.

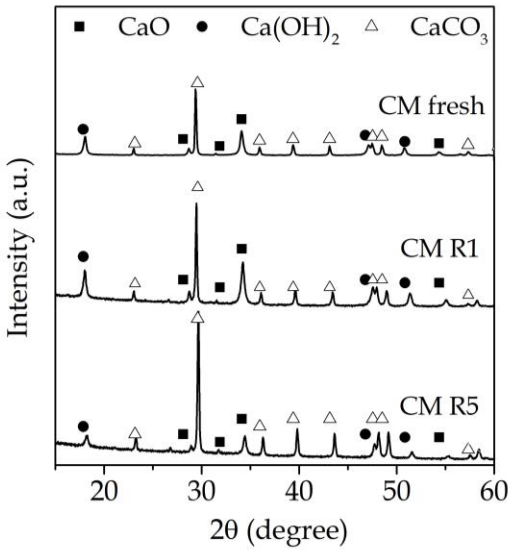

Figure 3.21. XRD patterns for fresh sample of the calcium-based material: fresh (CM fresh), and after first (CM R1) and 5th reaction cycle (CM R5); reactions were carried out without solvent.

55% conversion of rosin can be achieved with the calcium-based material as heterogeneous catalyst at 3.5 h reaction time, rosin : methyl alcohol molar ratio of 1 : 187, 64°C, 500 rpm stirring, and 40% catalyst load. However, a separation step would be required to purify the esters, for instance by liquid-liquid extraction and

column chromatography. In particular, extraction of esters using hexane has been reported [115], [117]. Firstly, washing with water (or aqueous HCl and $NaHCO_3$, or brine) is performed, and the inorganic phase is removed (drying over sodium sulfate is also performed). Then, silica columns together with the use of linear solvent gradient (isopropyl alcohol in hexane) are used for the separation/purification.

3.2.4 Remarks of the section

- ★ The esterification of rosin with methyl alcohol without solvent is promoted by basic solids. The strength of basic sites may be an important property of the catalyst to reach high activity. Although calcium carbonate has high-strength basicity, catalysts with moderate strength basic sites, such as materials with calcium hydroxide and calcium oxide phases, showed better performance. No important effect was found for the solvents tested.
- ★ A sample of a calcium-based material, composed mainly by calcium carbonate and calcium hydroxide, acquired in the local market in Colombia was evaluated as catalyst, at 40% load with respect to the rosin, 64°C and 500 rpm stirring. 55% of conversion without solvent, at 3.5 h reaction time and 1 : 187 rosin : methyl alcohol molar ratio was found in the esterification of rosin with methyl alcohol.
- ★ Under reaction conditions tested in the present work and using toluene as solvent, $Ca(OH)_2$ phase of the calcium-based material can be dissolved into the reaction matrix, as evidenced by FTIR, TPD-CO_2 and XRD analysis, suggesting that toluene is not a suitable solvent for this reaction system. In addition, the dissolved species can interact with rosin affecting the reaction, and quantification of conversion by means of the acidic number.

3.3 Laminar flames of blends of AAME + *n*-heptane

3.3.1 Background

The potential of the esterification of rosin as a source of fuels additives / components was evaluated by studying the effect of AAME in laminar flames of *n*-heptane + AAME. Although the combustion behavior in a laminar flame differs from that in a combustion chamber of a diesel engine, diffusion plays a key role in both processes, leading to a relatively high formation of nitric oxide (NO) and particulate matter (PM)

as a consequence of the high temperatures and oxidizer-fuel mixing (NO formation taking place in the lean regions of the mixture, whereas PM in the rich regions) [136], which facilitates to correlate the results of the flame. In addition, co-flow burners display high stability and reproducibility, which makes them suitable to study the behavior of the flames. The results presented in this section are, to the authors' knowledge, the first on the combustion of methyl esters from rosin (particularly AAME) in laminar flames to assess its influence on the emissions and flame characteristics.

3.3.2 Methodology

3.3.2.1 Fuel

Blends of *n*-heptane as diesel surrogate, and AAME as probe molecule of methyl ester of rosin at 0.1, 1 and 5% vol. were evaluated in the burner; combustion of pure *n*-heptane provided the baseline. Properties of *n*-heptane and AAME are summarized in Table 3.6. Although AAME has a molecular weight around three times larger than *n*-heptane, the AAME displays a lower LHV perhaps due to its high complexity and the presence of two oxygen atoms in its structure.

Table 3.6. Fuel properties

Property	***n*-Heptane**	**AAME**
Molecualr weight (g/mol)	100.2	316.5
Density[a] (g/cm$^{3)}$	0.688	1.02
Viscosity[a] (mPa.s)	0.397	ND
Boiling temperature (°C)	98	362.5
Melting temperature (°C)	-91	66.5[b]
Flash temperature[c] (°C)	-4	180
Lower heating value (kJ/kg)	48000	36467[b]

[a]Density and viscosity from [137] at 20 and 40°C, respectively; [b]estimations from present work; [c]from Scifinder; ND no information available.

3.3.2.2 Burner tests

Experimental setup is shown in Figure 3.22. Combustion tests are performed in an atmospheric pressure, co-flow, axisymmetric, non-premixed, laminar flame burner in which the fuel flows from a 25 mm inner diameter vertical tube (27 mm outer dieameter) and the oxidizer flows from the annular region between the fuel tube and a 37 mm inner diameter vertical tube. Standard air (oxidizer stream) and carrier

nitrogen (stream carrying the fuel) pass through porous metal disks to generate a uniformly-distributed velocity to keep the flame stable. The flow of the oxidizer and fuel streams are controlled by FMA 5400A/5500A series OMEGA mass flow meters.

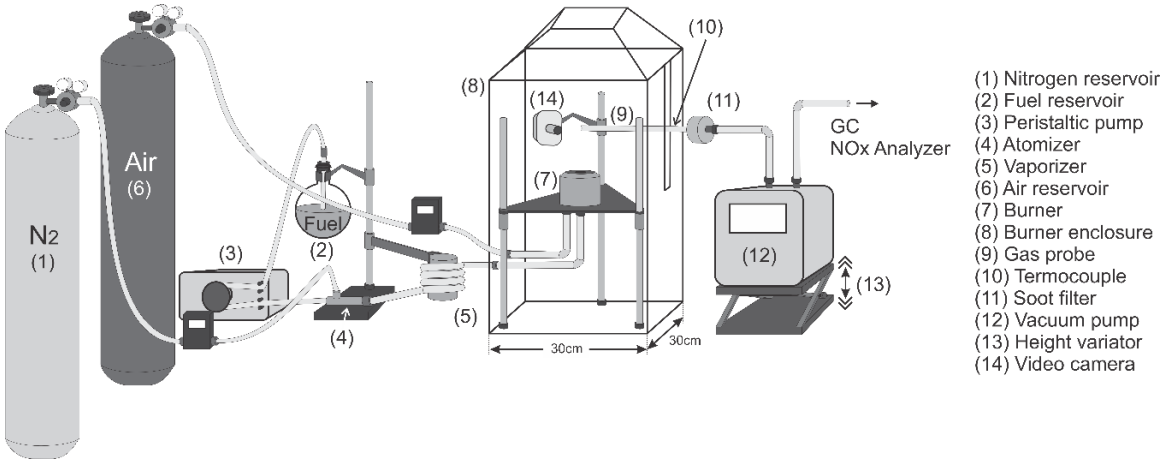

Figure 3.22. Experimental setup for combustion tests

This type of burner and flame have been used typically to test the soot tendencies of fuels. Gases such as methane and ethylene have been the most reported fuels, but liquid fuels such as *n*-heptane, dimethyl ether, liquefied-petroleum gas (LPG) and fuel surrogates have been burned to test soot emissions [138]–[144]. Moreover, mixtures of gas and liquid fuels have also been burned in this configuration to evaluate the influence of liquid in emissions and sooting tendency [145]–[148].

The line between the probe and the GC system is heated with a JCT Austria heating line to avoid condensation. Considering that the system is used to evaluate rosin- and turpentine- derivates, some simulations were performed to determine the required temperature. Specifically, ASPEN was used to estimate the dew point of the different mixtures (test molecule[1] + *n*-heptane); Peng-Robinson was selected as equation of state, although other EOS lead to similar values. For components not included in the software database (nopol, myrtenol, borneol, and AAME) the properties were computed by ASPEN from molecular weight, chemical structure, boiling point, specific gravity and enthalpy and Gibbs energy of formation, according to Table 3.7.

[1] Please note that the calculation was performed for all the molecules studied in this Thesis. Indeed, the same setup was used to assess AAME and the other probe molecules.

Table 3.7. Properties of components not included on ASPEN database

Compound	Nopol	Myrtenol	Borneol	AAME
Formula	$C_{11}H_{18}O$	$C_{10}H_{16}O$	$C_{10}H_{18}O$	$C_{21}H_{32}O_2$
Molecular weight (g/mol)	166.263	152.24	154.252	316.484
Boiling temperature (°C)	235	221.5	212.65	360
Specific gravity[c] @ 60°F	0.973	0.982	1.01	1.049
Std. Enthalpy of formation[d] (kJ/mol)	-241.95	-22.31	-272.72	-436.49
Std. Gibbs energy of formation[d] (kJ/mol)	21.45	13.03	-20.5	33.3

[a] From [137]; [b] from [149]

The dew points of the mixtures of model oleoresin-derivative compounds and *n*-heptane are shown in Table 3.8. Therefore, the lines between the atomizer and the burner, as well as the sampling probe and the GC system should be kept at > 200°C to avoid condensation.

Table 3.8. Dew points of different mixtures of oleoresin additives and *n*-heptane

Compound	Volume fraction (%)						
n-Heptane	100	95	95	95	95	95	98
Turpentine	0	5	0	0	0	0	0
Nopol	0	0	5	0	0	0	0
α-Terpineol	0	0	0	5	0	0	0
Myrtenol	0	0	0	0	5	0	0
Borneol	0	0	0	0	0	5	0
AAME	0	0	0	0	0	0	2
Dew point (°C)	**93.4**	**101.3**	**135.5**	**129.2**	**127.6**	**128.1**	**198.3**

3.3.2.3 Emissions

Carbon monoxide, carbon dioxide, oxygen, nitrogen, unburned hydrocarbon, nitric oxide, and nitrogen dioxide emissions were measured. An uncooled stainless-steel (4.3 mm internal diameter) and a quartz (0.6 mm internal diameter) probe were tested by placing them in the centerline of the flame to sample the combustion products; a PTFE (polytetrafluoroethylene) filter was used after the probe to remove the particulate material. An oil free vacuum pump, which has a PTFE diaphragm was used to transport the sample. The probe was located at different heights above burner (HAB).

A dried sample (i.e., a water trap was used) was driven to a NOx analyzer (Eco Physics CLD 700 EL ht, 0-10000 ppm, 0.1 ppm of lowest detection limit). Calibration

of NO and NO_2 are shown in Appendix E; NOx concentrations up to 50 ppm, where NO is the main nitrogen oxide, were expected. Uncertainty in NO-concentration is lower than 10% for concentration up to 30 ppm, and in NO_2-concentration is lower than 15% for concentrations below 1 ppm.

A wet sample (i.e., no water trap was used) was driven to a gas chromatograph (GC) to measure CO, CO_2, O_2, N_2, and UHC. A GC Agilent 7920A equipped with FID and TCD detectors was used. The GC system is shown in Figure 3.23. Initially, the ten-way valve is turned-off and the sample is collected in two loops. Once the ten-way valve is turned-on, the sample collected in one of the loops is driven to the FID (blue line) and the other is driven to the TCD line (red line). FID line has a DB-1 (100% Dimethylpolysiloxane, 50m x 0.32mm x 0.25 um), non-polar capillary column, which can separate hydrocarbons (C_1-C_{12}). TCD line has a Porapak QS (styrene/ethyl vinylbenzene, 8" x 0.125, 80/100) packed column, and then a three-way valve which allows (or not) the pass to a third column (Molecular Sieve 5A, 8" x 0.125, 80/100): the Porapak column retains the carbon dioxide (CO_2), and the Molecular Sieve column separates the other permanent gases (CO, H_2, N_2, O_2, etc.).

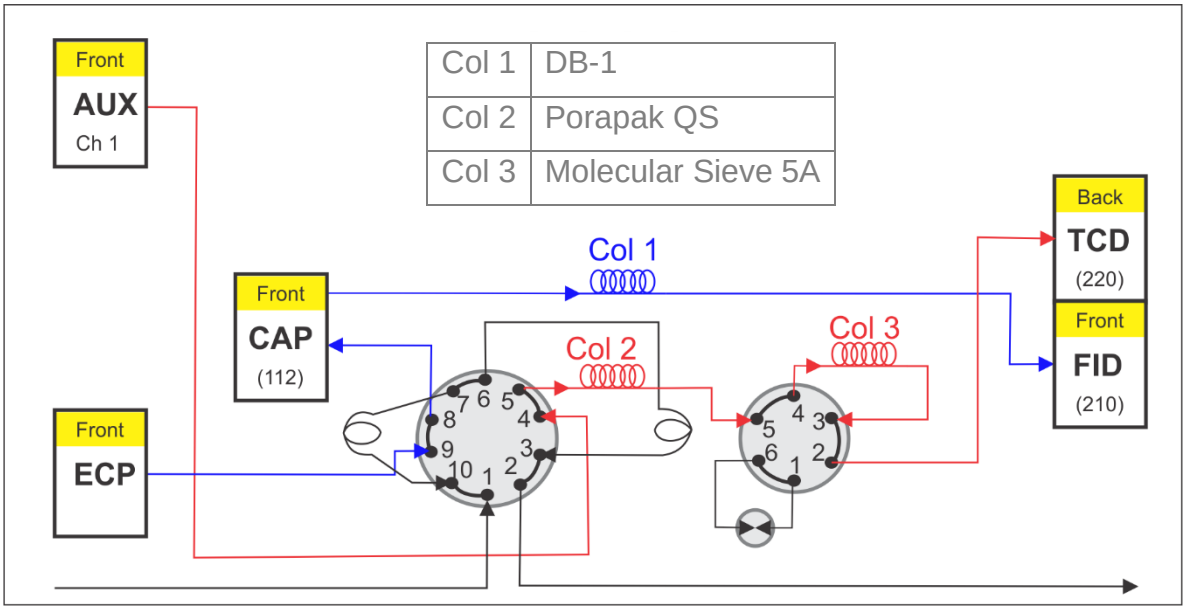

Figure 3.23. Internal setup of GC system

Thus, initially the three-way valve is turned-on, as shown in Figure 3.23, and the permanent gases different from CO_2 reach the Molecular Sieve column after

travelling through the Porapack column. Then, the three-way valve is turned-off and CO_2 is desorbed from the Porapack column (at about four minutes) while the other gases are trapped in the Molecular Sieve column. When the three-way valve is turned-on again, permanent gases except CO, which is strongly adsorbed on the Molecular Sieve, are separated, and reach the TCD detector.

Helium carrier gas was used with an average linear velocity of 22 cm/s through DB-1; the initial temperature (30°C) was held for 6 min and, then, a 10°C/min heating ramp up to 150°C (held for 10 min) was used, with a split ratio of 100 : 1 (applies only to the FID line). The inlet injection temperature was 250°C, whereas the temperature of FID and TCD detectors was 325°C and 250°C, respectively. The flame of FID detector was obtained by using 30 mL/min of hydrogen and 400 mL/min of air, and using nitrogen as make-up gas at 25 mL/min. Reference flow for TCD detector was adjusted at 44 mL/min, with a make-up flow of 2 mL/min of nitrogen. Retention time obtained by individual injection of pure species, and calibration of O_2 and N_2 are shown in Appendix F.

3.3.2.4 Measurement of flame dimensions

Videos of flames at Full HD 1920x1080 and 60 fps were recorded with a Nikon D3300 camera equipped with an AF-S DX Micro-NIKKOR 40mm f/2.8G lens. Each run was recorded three times for at least one minute. Videos were processed with the Image Processing Toolbox of Matlab®. The distance between the flame base and flame tip along the center line of the flame was calculated as the average flame height obtained from these video frames. Similar procedure can be performed for the lift-off height, by taking the average height from the burner rim to the flame base. Figure 3.24 depicts the algorithm used; the developed in Matlab® code to process the video frames and obtain the flame dimensions is shown in Appendix G.

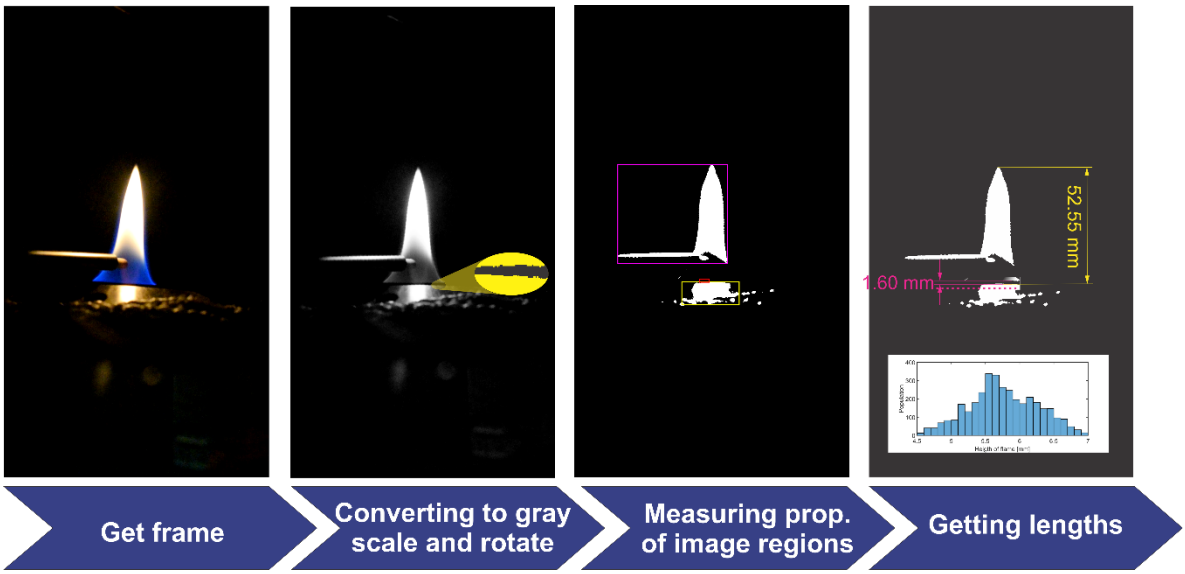

Figure 3.24. Algorithm to obtain flame dimensions

3.3.2.5 Temperature measurement

A type R thermocouple (Platinum-13% Rhodium vs Platinum thermocouple, -50 to 1768°C temperature range) was fixed in one point on the flame at 20% of the height of the flame, and the temperature was recorded for 15 minutes after getting a stable value. An image processing algorithm was used to digitalize the temperature values from the thermocouple device; Figure 3.25 presents the algorithm, and the Matlab® code is presented in Appendix H.

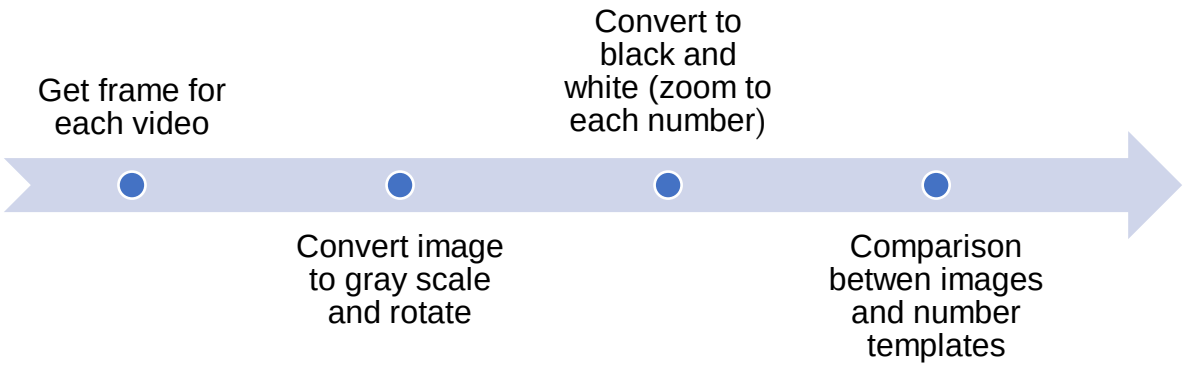

Figure 3.25. Algorithm to obtain temperature values from thermocouple

Radiation and heat transfer losses were included in the measurement according to Equations 2.32-34. Parameters of thermocouple, burner and surroundings used for temperature correction are shown in Table 3.9.

Table 3.9. Parameters for temperature correction

D_T (m)	0.0015	Thermocouple diameter
D_b (m)	0.025	Burner diameter
S_b (m^2)	4.91×10^{-4}	Cross-section area of burner
T_∞ (K)	298.15	Surrounding temperature

Previous experiments were performed to set the conditions of combustion tests. Flow of air and nitrogen (as carrier gas of *n*-heptane as fuel), and height and diameter of the probe were varied, and the stability of the flame was evaluated by measuring temperature and dimensions of the flame, and species concentrations. A stable flame was obtained at fuel (i.e., nitrogen carrier stream) and air flows between 353-499 and <1380 mL/min, respectively; however, at very low air flows the flame turns instable, and at air flows larger than 300 mL/min high dilution of species is observed. On the other hand, 1.5 times the height of flame (around 110 mm) appears to be an appropriate HAB of probe to obtain representative concentration of combustion products with minor variation of measured values. More details of the experiments to obtain optimum conditions for flames are shown in Appendix I.

3.3.3 Results and discussion

3.3.3.1 Flame temperature

The temperature correction for radiation and heat transfer losses of flames obtained with *n*-heptane and its blends with AAME was around 200 K. The temperature of the flame ranges between 900 and 1100 K, which can be considered low in comparison to the adiabatic flame temperature (see Figure 3.4). Some factors need to be considered in the comparison of experimental and maximum adiabatic flame temperatures: a) the actual location of the probe (i.e., HAB of thermocouple); b) the dilution of fuel with carrier gas and the consequent reduction in local fuel/air ratio; and, c) the possibility of incomplete combustion. The conduction losses, on the other hand, can be neglected because of the small diameter of the wire (<1µm). In particular, the effect of dilution of fuel with the nitrogen of the carrier stream absorbs sensible energy from the flame and reduces the flame temperature [68]. In addition, the experimental equivalence ratio for all flames is higher than 1.0 ($\phi \approx 1.3$), corresponding to fuel-rich mixtures and lower adiabatic flame temperatures.

Moreover, the experimental equivalence ratio was determined under the assumption that all the air from the annular region of the burner is mixed with the fuel, but if some air is not diffused into the fuel, the equivalence ratio is increased, resulting in lower “real” adiabatic flame temperatures.

As the position of thermocouple strongly affects the results, all measurements were conducted at 20% of flame HAB. Table 3.10 shows the flame HAB and the actual location of the thermocouple for different flames from pure *n*-heptane and blends with AAME. In some flames it was not possible to achieve the target HAB (i.e., 20%), as shown in Table 3.10. Particularly, the actual HAB of the thermocouple were significantly lower than the target for blends with higher contents of AAME. In fact, the flames obtained with these fuels were highly unstable (high variation in size), and, consequently, locating the thermocouple at 20% of the flame height was difficult. Probably the proximity between the dew point of these blends with the temperature of the evaporation system (around 195-198 and 200°C, respectively), was not enough to completely vaporize the AAME molecules. In addition, with the experimental setup available it was not possible to achieve temperatures higher than 200°C.

Table 3.10. HAB of thermocouple for flames with different contents of AAME

AAME content (vol.%)	Flame HAB (mm)	Thermocouple	
		HAB (mm)	Relative position (%)
0	46.70	9.22	19.74 +/- 0.97
0.1	48.91	11.12	22.73 +/- 1.10
1	49.66	7.66	15.42 +/- 1.94
2	53.75	9.00	16.75 +/- 1.97

The plot of the ratio of the flame temperature of AAME blends to that for pure *n*-heptane (T_o), Figure 3.26, indicates that the flame temperature is inversely proportional to the content of AAME. However, an increase in flame temperature with AAME would be expected from its higher estimated adiabatic flame temperatures; in fact, AAME possesses an adiabatic flame temperature higher than that for *n*-heptane (around 15 K), indicating that AAME combustion products are at a higher temperature than those from *n*-heptane, in agreement with the comparison

of alkanes and methyl esters of fatty acids presented by Glaude and coworkers [150] (with similar H/C molar ratio and number of carbons than AAME and estimated at similar conditions, i.e. 300K and atmospheric pressure). The discrepancy can be attributed to the high instability of the flames, especially for those obtained with AAME blended at 1 and 2% vol. with *n*-heptane: firstly, as an increase in the flame temperature is expected with higher values of HAB, probably the tendency of adiabatic flame temperature may be achieved with thermocouple fixed in the target position; secondly, the low temperature used for the vaporization system, which was very close to the estimated dew point of the blends, may have not been high enough to vaporize the methyl ester molecules, which can lead to liquid droplets of AAME affecting the diffusion and combustion process and reducing the flame temperature.

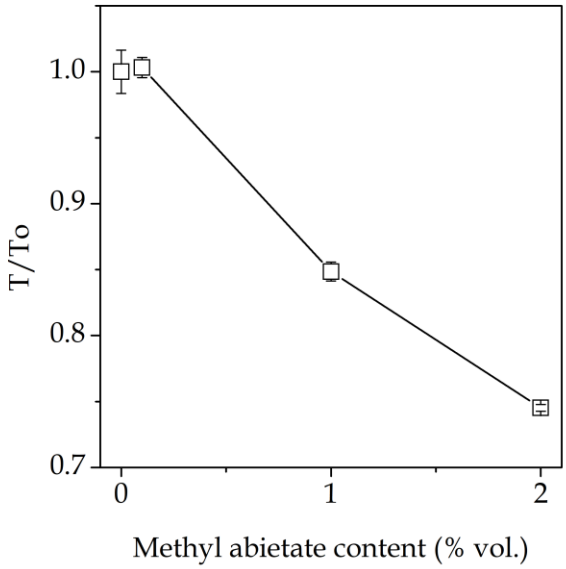

Figure 3.26. Influence of AAME content on flame temperature

3.3.3.2 NOx emissions

Emission index for nitrogen oxides (EI_{NOx}) in flames of AAME + *n*-heptane blends is shown in Figure 3.27. Emissions of NO_2 were low for all flames (up to 1.5 ppm), thus, NOx are mainly NO, which would be formed via the thermal mechanism. Therefore, the formation of nitrogen oxides is related to the flame temperature, which is associated to the energy released in combustion. Presence of AAME in the fuel

reduces EI_{NOx} in agreement with the decrease in flame temperature shown in Figure 3.26.

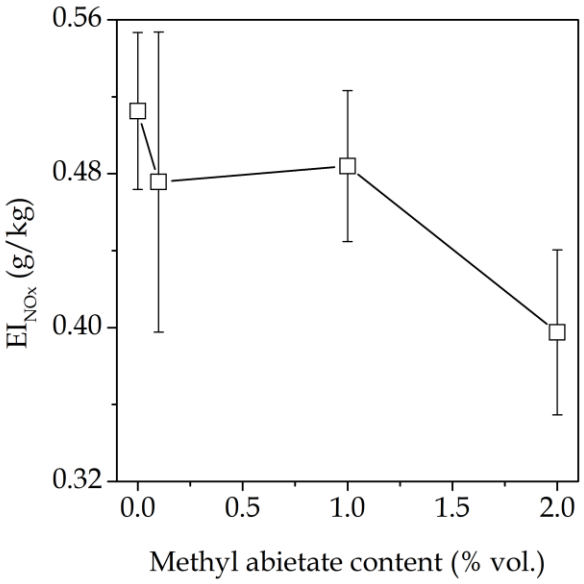

Figure 3.27. Influence of AAME content on NOx emissions

3.3.3.3 CO and UHC emissions

As the combustion is fuel-rich, a relatively high concentration of CO and UHC is expected although low amounts of CO and UHC indicate that more energy is extracted from the combustion (lower losses) [67]. Emission indices of CO and UHC for flames with different contents of AAME are shown in Figure 3.28. Emission index of CO is increased from 38 to 44 g_{co}/kg_{fuel} when *n*-heptane is blended with 2% vol. of AAME, supporting the hypothesis of an incomplete combustion, which would influence its performance as fuel. The decrease in CO emissions can be related to the decrease in O_2 consumption and the increase in the flame temperature.

Contrarily to the emission of CO and the flame temperature, the emission indices of UHC decrease with the content of AAME (Figure 3.29). If the vaporization of AAME was not complete, a deterioration in the combustion is expected. Besides, since less amount of *n*-heptane reaches the combustion zone as a consequence of the AAME presence, less unburned hydrocarbons are obtained, in agreement with the measured values. In addition, unburned AAME cannot be detected in the GC system because of the higher temperature required, which is above the recommended

values for the packed columns used to separate permanent gases. Consequently, the observed decrease in UHC emissions can be attributed to the decrease in *n*-heptane content in the liquid fuel, replaced by AAME.

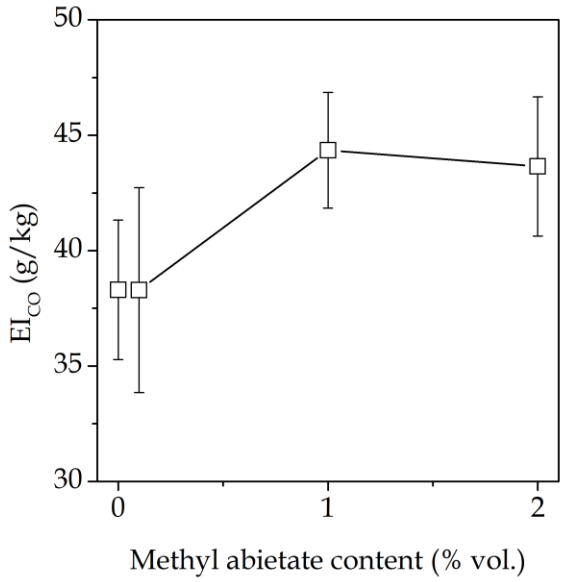

Figure 3.28. Influence of AAME content on CO emissions

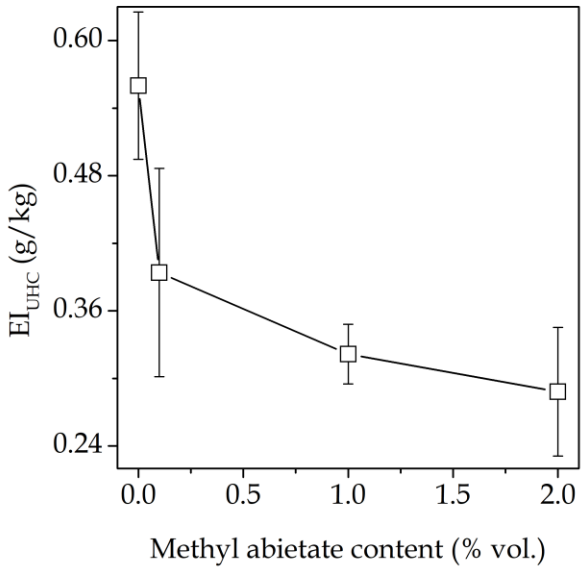

Figure 3.29. Influence of AAME content on UHC emissions

3.3.3.4 Flame size

Experimental flame heights obtained from videos of flames with AAME + *n*-heptane blends, and the corresponding values from the correlation by Roper [83] are compared to that of a pure *n*-heptane (H_o) flame in Figure 3.30. According to Roper's expression, the height of the flame is directly proportional to the volumetric flow of fuel and the stoichiometric air-to-fuel ratio. In this work, the higher the content of AAME in the fuel the higher the stoichiometric air-to-fuel ratio, but the volumetric fuel decreases because the higher average molecular weight of the blend translates into smaller number of moles of fuel. Moreover, the increasing of the stoichiometric ratio appears to be more important than the reduction of volumetric flow of fuel, and then, the predicted height of flame is directly proportional to the dosage of AAME.

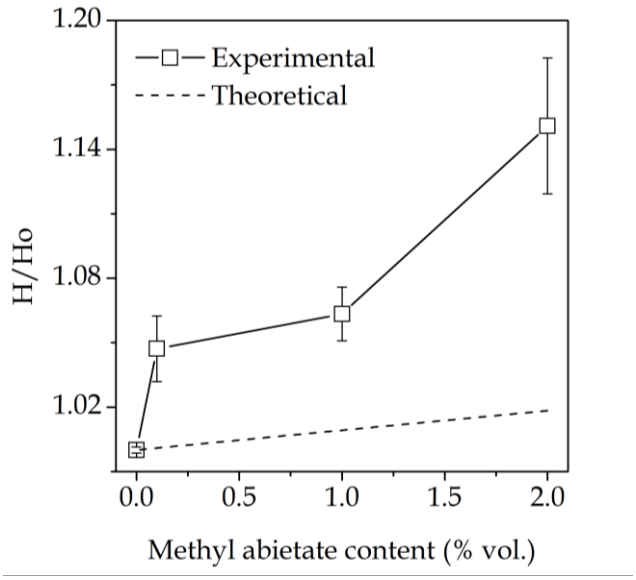

Figure 3.30. Influence of AAME content on flame height. The air viscosity and temperature of the fuel and surrounding used for the estimations were 1.78×10^{-5} m^2s, and 298 and 473 K, respectively.

The experimental results follow the same trend than the theoretical ones. Considering that the H/C ratio of fuel is decreased as AAME is increased, an increase in height of flame is to be expected because the larger availability of carbon atoms in the fuel molecules increase the combustion time allowing the flame to reach more larger heights [67].

3.3.4 Remarks of the section

Results of CO and flame temperature suggest a decrease in the performance of the combustion reaction when AAME is added to *n*-heptane. The temperature of the evaporation system was very close to the dew points estimated for the AAME + *n*-heptane blends. In fact, the lack of information on the experimental values of properties of rosin and some derivate molecules, mentioned in Section 3.1, made it necessary to estimate the thermal and thermochemical properties. Therefore, a temperature of 200°C in evaporation system may have not been high enough, leading to incomplete evaporation of the AAME. The presence of AAME in the combustion zone as liquid droplets (instead of vapor) is disadvantageous, decreasing the performance of combustion. On the other hand, other emissions are influenced positively by the incomplete combustion resulting from the presence of AAME, for instance the decrease in NOx emissions, which is a consequence of the decrease in flame temperature.

3.4 Conclusions

- ★ Estimation of thermal properties of rosin and rosin-derived compounds was necessary due to the lack of experimental information, specially boiling temperatures and heating values. In particular, a large discrepancy between estimated and measured boiling temperatures for rosin and rosin-derived compounds was observed, which can be attributed to the high complexity of rosin compounds and their derivates, the low accuracy of the group-contribution methods for the estimation of this kind of properties, and the molecular interactions of molecules neglected in the implemented methods. Estimated values of melting temperatures are similar than experimental ones and/or of the same magnitude order. Adiabatic flame temperatures of rosin-derived compounds are slightly lower than that for diesel but higher than that for biodiesel.
- ★ A sample of a calcium-based material from the local market in Colombia catalyzes the esterification reaction of rosin with methyl alcohol, yielding 55% conversion without solvent, at 3.5 h reaction time, 1 : 187 rosin : methyl alcohol molar ratio, catalyst load at 40 % with respect to the rosin, 64°C, and 500 rpm.

- ★ From the estimated properties of rosin-derived compounds, it is possible to conclude that reduction reaction increases significantly the lower heating value of rosin compounds, and methyl esterification reaction decreases appreciably the boiling and melting temperatures. Additionally, isomerization can be considered attractive because a significative difference in properties such as melting and boiling temperatures was found for components of rosin.
- ★ The benefits of rosin transformation could be insufficient for fuel applications. Indeed, the expected products will still have high tendency to remain as solid (and liquid) and, considering that biodiesel has often experienced filter clogging problems derived partially from its low melting point, it is likely that these transformations are unsuitable for fuel applications. Besides, Colombian legislation (Res. 9 0963/2014) requires a conversion > 96% for a methyl ester of biodiesel to be sold in the market, and although the chemical nature of esters produced from rosin differs from the typical esters of biodiesel, the low conversion of rosin also can be considered as a drawback for its fuel application.
- ★ Deterioration in the combustion performance of *n*-heptane blended with AAME was evidenced. The possible incomplete evaporation of the AAME would lead to the presence of AAME in the combustion zone as liquid droplets, resulting in low diffusivity of the fuel and air, and low combustion efficiency. Simultaneously, the low temperature of the flame conduces to a decrease in NOx emissions.

Chapter 4. Fuel characteristics of molecules from turpentine

Some applications of turpentine as fuel have been reported, as well as the use of some oxygenated-derived molecules in fuels and additive formulations, as discussed in Chapter 1. However, other oxygenated molecules which can be obtained from oleoresin compounds have not yet been tested as fuel, for instance nopol and myrtenol. The purpose of this chapter is to evaluate oxygenated molecules from turpentine to get insight into the actual influence of this kind of molecules in combustion reactions, and, at the same time, select the probe molecule with best performance for advanced tests. The main components of turpentine (α- and β-pinene), and some of their oxygenated-derived molecules (nopol, terpineol, myrtenol and borneol, selected based on the possibility to be synthesized under heterogeneous catalysis) were tested. Estimation of some properties of high interest in fuel applications, and experiments to measure the influence on combustion reactions were performed to the selected probe molecules.

4.1 Estimation of properties

4.1.1 Background

A general scheme for the analysis of the compounds proposed as test molecules from turpentine is depicted in Figure 4.1. The main components of turpentine are α- and β-pinene, accounting for up to 90 % of its composition; consequently, the properties of interest for turpentine depend on those of α- and β-pinene. Thus, the first part of the section is devoted to the individual evaluation of α- and β-pinene. In addition, the results of the combustion of these molecules lead to evaluating the influence of their oxyfunctionalization in the combustion performance.

Little information has been reported on the evaluation of α- and β-pinene in combustion reactions. Furthermore, the molecular structure of α- and β-pinene allows studying the influence of the position of an unsaturation (the only difference

between these isomer molecules) in combustion reactions; specifically, the carbon-carbon double bond is located inside the main cycle in α-pinene, whereas it is located outside the main ring in β-pinene.

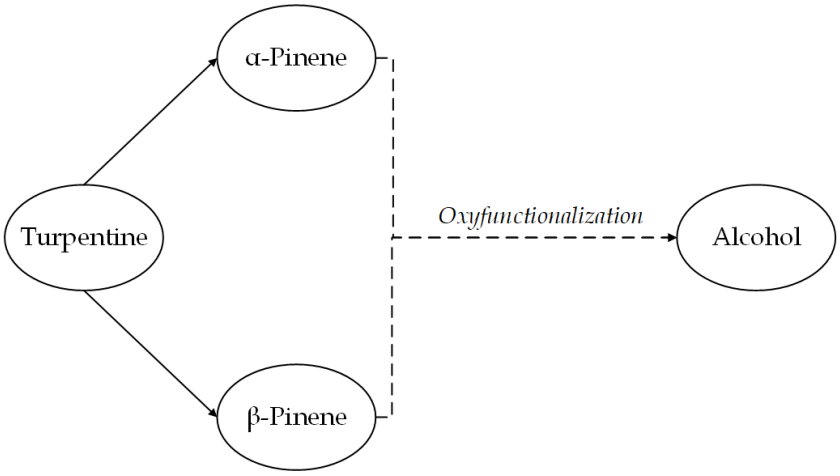

Figure 4.1. Relation of the tested molecules from turpentine

Transformation of turpentine is proposed because one of the most important drawbacks of using diesel as fuel is the PM emissions, and it is well-known that the presence of oxygen atoms in the molecules of the fuel can help to reduce these emissions [1], [2]. On the other hand, the properties of alcohols from terpenes are substantially different from alcohols such as methanol or ethanol, for instance, the volatility, viscosity, density, heat of combustion and lubricity, among others. Consequently, the terpene alcohols may be suitable additives or components for diesel fuel not only by reducing PM emissions, but by (probably) enhancing other important properties.

The probe molecules proposed to be evaluated are α- and β-pinene, nopol, α-terpineol, myrtenol and borneol. The molecular structures of these molecules are shown in Figure 4.2.

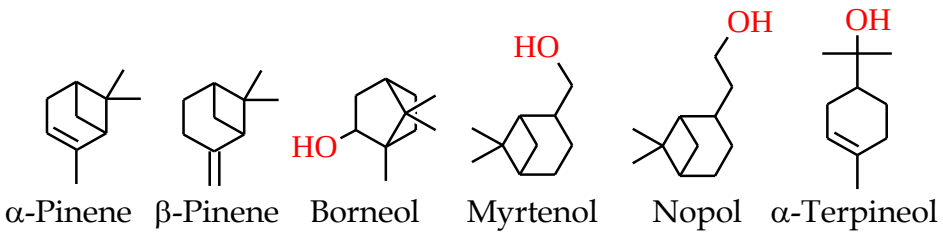

Figure 4.2. Molecules from turpentine

A thorough literature review of thermal and thermochemical properties for these molecules indicated that although those for α- and β-pinene have been reported, those for oxygenated probe molecules are lacking. Table 4.1 shows some important thermal and thermochemical properties of the probe molecules from turpentine. Heat of formation for α- and β-pinene differs around 10 kJ/mol, being the highest that for β-pinene. Melting and boiling temperatures for α- and β-pinene differ around 6 and 10°C, respectively, suggesting that the differences in thermal and thermochemical properties of α- and β-pinene are minor. Besides, the difference in melting temperature among borneol and α-terpineol is around 170°C, indicating that the oxyfunctionalization reaction of turpentine can produce oxygenated molecules with properties significantly different.

Table 4.1. Thermal and thermochemical properties of probe molecules

Probe molecule	MW (g/mol)	T_b[a] (°C)	T_m[b] (°C)	ΔH_f^{0}[c] (kJ/mol)
α-Pinene	136.23	156.14	-55	28.3
β-Pinene	136.23	166.04	-61	38.7
Nopol	166.26	235.00	ND	ND
Myrtenol	152.23	221.50	ND	ND
α-Terpineol	154.25	220.00	31-35	ND
Borneol	154.25	212.65	197.9-208	ND

[a]Boiling temperature from [137]; [b]melting temperature from [151]; [c]heat of formation at 25°C from [152].

4.1.2 Methodology

Estimations of changes in melting and boiling temperatures, and lower heating values were performed based on methods of Joback and Benson, using the same methodology presented in Chapter 3. In addition, the adiabatic flame temperatures were estimated with the methodology shown in Section 3.1.2.

4.1.3 Oxyfunctionalization of main turpentine components

Changes in melting and boiling temperatures (due to the oxyfunctionalization) for oxygenated molecules which can be obtained from main components of turpentine are shown in Figure 4.3. The values of changes in boiling temperatures for oxygenated molecules form turpentine are largely overestimated by Joback method. On the other hand, changes in melting temperature for borneol and α-terpineol estimated by Joback are significantly lower than the calculated from the experimental

values, suggesting that this method is not suitable for this kind of molecules. In all cases, the oxyfunctionalization of main components of turpentine translates into increased melting and boiling temperatures. However, given the low melting and boiling temperatures of α- and β-pinene, its derived-oxygenated molecules may still have thermal properties suitable for fuel applications.

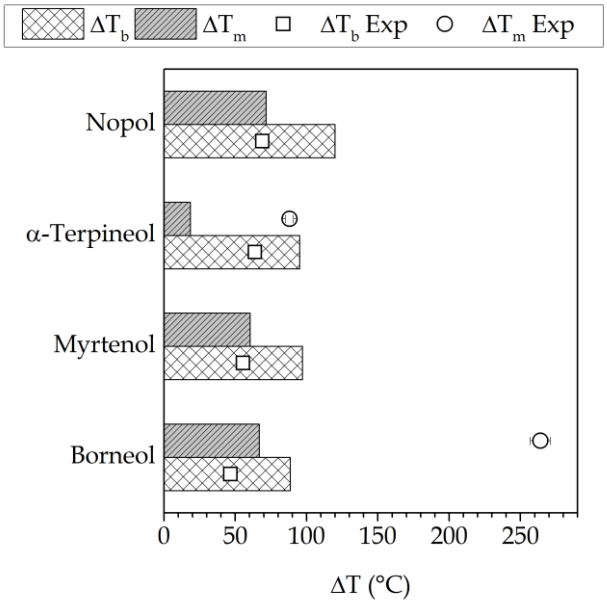

Figure 4.3. Changes in melting and boiling temperature due to oxyfunctionalization of main components of turpentine

The estimation of change of lower heating values for oxygenates molecules from turpentine can be seen in Figure 4.4a. LHV for oxygenated molecules are lower than that for α- and β-pinene (around 5 MJ/kg with Benson and Joback methods), indicating a reduction in the heat of combustion due to the oxyfunctionalization. Nopol displayed the highest estimated LHV, followed by α-terpineol, myrtenol and borneol, Figure 4.4b.

The estimation methods suggest that the hydroxyl group significantly reduce the heat of formation of the oxygenated molecules, decreasing their heat of combustion. From a chemical point of view, the presence of oxygen atoms in the molecules of fuel decreases the amount of energy which can be released in a combustion reaction because the high carbon-oxygen bonding energy means that more energy is consumed in breaking it.

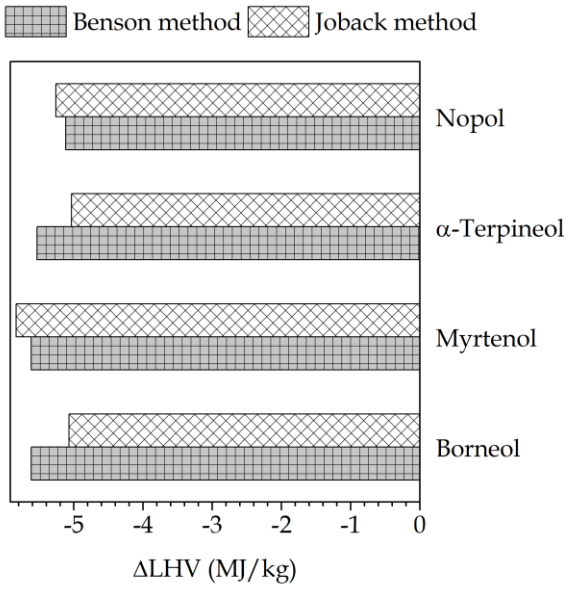

a)

LHV (MJ/kg)	Estimation method	
	Joback	Benson
α-pinene	42.3090	42.8878
β-pinene	42.5920	42.9539
Nopol	37.3322	37.8363
α-terpineol	37.2761	37.3534
Myrtenol	36.7550	37.3349
Borneol	37.5228	36.9896

b)

Figure 4.4. a) Delta of LHV due to oxyfunctionalization of main components of turpentine and b) LHV for probe molecules from turpentine and the

The adiabatic flame temperatures estimated for α- and β-pinene are shown in Figure 4.5a. Both compounds present similar temperatures, which are higher than those of diesel and biodiesel. At “engine conditions”, the maximum value of adiabatic flame temperature for diesel is 30 K lower than that for α- and β-pinene, while the difference with respect to biodiesel is almost 60 K, which can be explained by the much lower molecular weight of the pinenes. Thence, a higher release of energy is expected in the combustion of turpentine with respect to diesel and biodiesel.

Adiabatic flame temperatures for oxygenated molecules from turpentine are presented in Figure 4.5b. Nopol, myrtenol and α-terpineol display similar adiabatic flame temperatures which are slightly lower than α- and β-pinene, but higher than those for diesel (at maximum adiabatic flame temperature the difference between diesel and the alcohols is around 20 K). On the other hand, adiabatic flame temperature of borneol is lower than that for diesel but very close to biodiesel. Although adiabatic flame temperatures of molecules after oxyfunctionalization are decreased, the reduction is slight and the final values are similar to those for typical fuels, and even higher

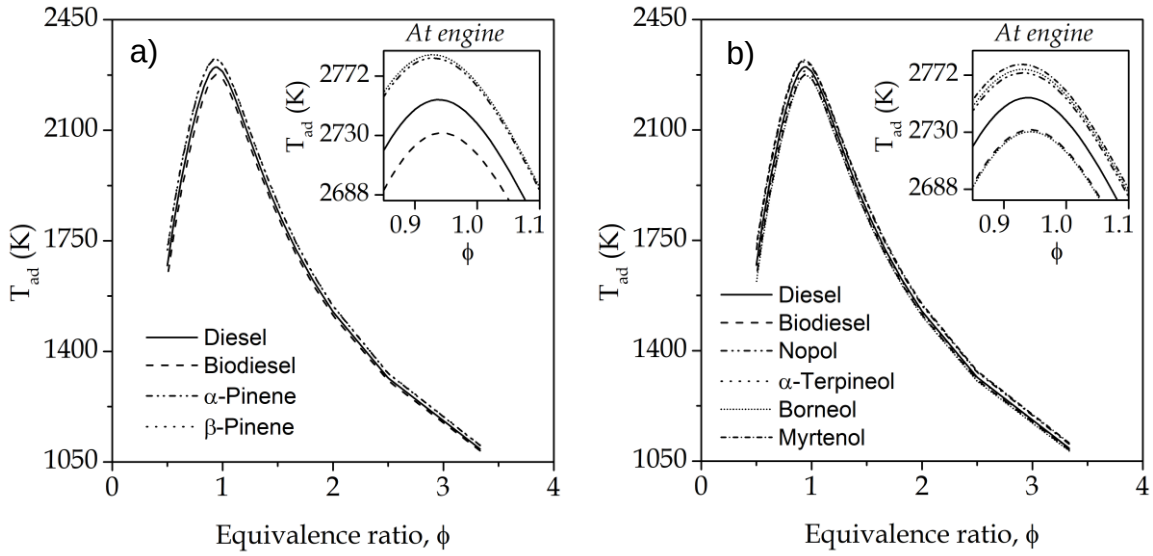

Figure 4.5. Adiabatic flame temperature for a) α- and β-pinene and b) nopol, α-terpineol, myrtenol and borneol compared to diesel and biodiesel at "ambient conditions" (i.e., constant pressure) and "engine conditions" (i.e., constant volume, shown in insert)

4.1.4 Remarks of the section

★ Heating values and melting and boiling temperatures for α- and β-pinene are suitable for fuel applications. These properties are even better than those for diesel and biodiesel.

★ Theoretical analysis of thermal and thermochemical properties shows that oxygenated molecules from turpentine have lower LHV and higher melting and boiling temperatures than those for the main components of turpentine. Although these changes are undesirable, thermal and thermochemical properties of molecules after oxyfunctionalization are still suitable for fuel applications. Indeed, they are liquid at ambient conditions, and present heating values similar to diesel and biodiesel, and higher adiabatic flame temperatures than diesel (with the exception of borneol, which is a solid fuel partially soluble in *n*-heptane, with thermochemical properties similar than biodiesel ones).

4.2 Laminar flames of blends of probe molecules from turpentine + *n*-heptane

4.2.1 Background

Despite the inherent limitations of laminar flames to gain actual insight into the oxidation kinetics of a fuel, this technique was used to evaluate the performance of

oleoresin-derived molecules as fuel because of different factors. Firstly, similarly to the actual operation of a diesel engine, diffusion plays a key role in laminar flames. Secondly, much lower amounts of sample are required (in comparison with techniques such as engine bench). Lastly, oppositely to shock tubes or rapid compression machines, it is a simple technique which allows qualitative comparison of the influence of different molecules (such as those derived from oleoresin) on the combustion performance.

Some relevant properties of the probe molecules (i.e., alcohols than can be obtained from oxifunctionalization of turpentine) and *n*-heptane are shown in Table 4.2. Except for borneol, all molecules are liquid at ambient conditions and fully soluble in *n*-heptane; although borneol is solid and partially soluble, complete dissolution in *n*-heptane was obtained at concentrations up to 5 % vol. The oxygen content of the as probe molecules is around 10 wt.%, which is significantly lower than that for typical alcohols used in fuel applications (e.g., 34.7 wt.% for ethanol) but similar than that for typical biodiesel (around 11 wt.%). The molecular weight of probe molecules is lower than that for diesel and biodiesel (not shown).

Table 4.2. Properties of components of fuels

Molecule	Formula	MW (g/mol)	Specific gravity[a]	Oxygen cont. (wt.%)	H/C molar ratio
α-Pinene	$C_{10}H_{16}$	136.23	0.86	0	1.60
β-Pinene	$C_{10}H_{16}$	136.23	0.87	0	1.60
Nopol	$C_{11}H_{18}O$	166.26	0.97	9.62	1.64
α-Terpineol	$C_{10}H_{18}O$	154.25	0.94	10.37	1.80
Myrtenol	$C_{10}H_{16}O$	152.23	0.98	10.51	1.60
Borneol	$C_{10}H_{18}O$	154.25	0.91	10.37	1.80
n-Heptane	C_7H_{16}	100.21	0.69	0	2.29

[a] From [153].

Although several molecules derived from oleoresin, including turpentine and α-terpineol, have shown potential to be used as biofuels (with promising results in engine tests), it is necessary to get insight into the actual effect of this type of molecules in the combustion. In particular, a few studies have focused on the influence of the position of unsaturation on emissions and combustion performance in alkenes [154], [155], but no information was found on the influence of the position and location (i.e., inside or outside) of unsaturation in cycloalkenes. This work is

perhaps the first to deal with combustion of terpene molecules in laminar flames to assess the influence of their molecular structure on the emissions and flame characteristics.

4.2.2 Methodology

Emissions, temperature, and dimensions of the flame were obtained from laminar flames of blends of *n*-heptane (as diesel surrogate) + probe molecules from turpentine (0.1, 1 and 5 vol. %), using the experimental setup detailed in Section 3.3.2.

4.2.3 Results and discussion

4.2.3.1 Temperature of the flame

Adiabatic flame temperature for the tested molecules is compared with that for *n*-heptane in Figure 4.6. The compounds that can be obtained directly from pine turpentine by separation, i.e., α- and β-pinene (the main components of turpentine) present similar adiabatic flame temperatures, which are higher (~50 K) than that of *n*-heptane, Figure 4.6a.

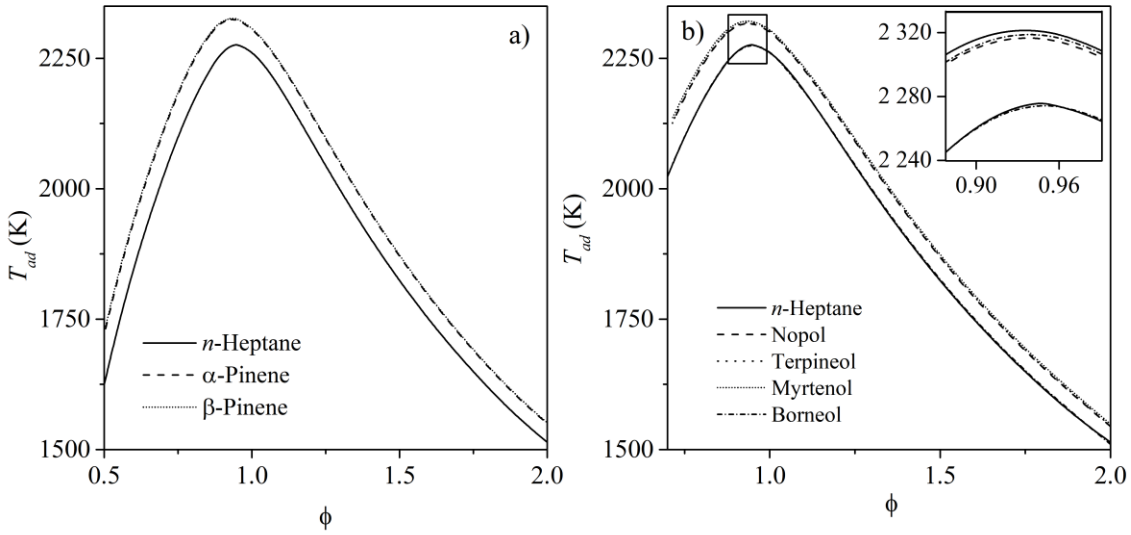

Figure 4.6. Adiabatic flame temperature of tested molecules compared to that for *n*-heptane at different equivalence ratios. a) α- and β-pinene; b) nopol, terpineol, myrtenol and borneol

On the other hand, among the terpenic alcohols that can be obtained from the transformation of oleoresin myrtenol and nopol, as well as terpineol display adiabatic flame temperatures higher (~40 K and 15 K, respectively) than *n*-heptane, whereas

that of borneol is slightly lower (~2 K), Figure 4.6b. Similar results were reported for the adiabatic flame temperature of normal alcohols (i.e., methanol, ethanol and *n*-butanol) with respect to their corresponding alkanes [150]. Thus, at a given H/C ratio and number of carbon atoms, it appears that the presence of oxygen in the molecule involves a slight reduction in adiabatic flame temperature, but this reduction is less than the loss in heating value (the decrease in the maximum adiabatic flame temperature due to oxyfunctionalization ranges between 2-4 %, whereas that for the heating value ranges between 11-13 %, see Figure 4.4b).

The presence of carbon-carbon double bonds in the molecule would be related with the higher adiabatic flame temperature, as observed when the peak of this temperature (which corresponds to an equivalence ratio of around 0.94) is represented as a function of the H/C ratio of the different molecules, Figure 4.7a. Indeed, myrtenol and nopol, as well as terpineol, display a double bond whereas borneol does not. In fact, alkenes commonly display higher adiabatic flame temperatures than alkanes due to the lower H/C molar ratios [150]. On the other hand, the lower H/C molar ratio for myrtenol and the higher number of carbon atoms in nopol explain the higher adiabatic flame temperature of myrtenol.

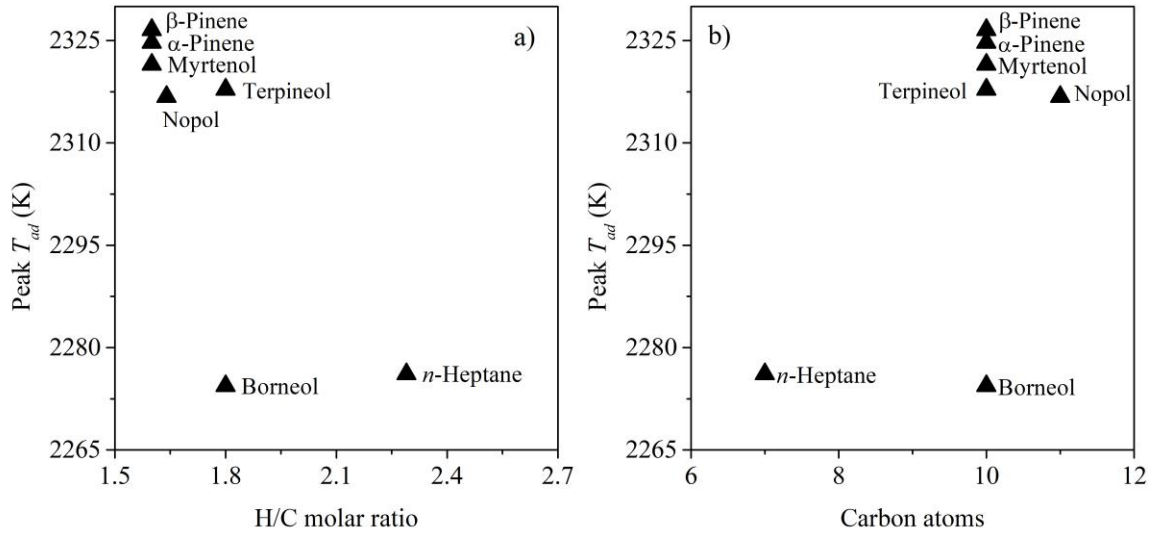

Figure 4.7. Adiabatic flame temperature for tested molecules. a) As a function of H/C molar ratio, and b) as a function of carbon atoms

Deviations in temperature measurements were below 25K for all flames, corresponding to an average experimental error of ~3%. *n*-Heptane blends with the probe molecules display flame temperatures between 1100 and 1200K, with corrections by radiation around 250K, which are low in comparison to the adiabatic flame temperature (see Figure 4.6). Similarly to flames with AAME in Section 3.3, location of the thermocouple and equivalence ratio may explain the rather low values of flame temperature obtained.

Table 4.3 shows the flame HAB and the actual location of the thermocouple for different flames of pure *n*-heptane and blends with the probe molecules. The relative position of the thermocouple was in all cases close to the 20% target (i.e., within 1%). However, it can be noticed that the position in the tests of *n*-heptane + β-pinene was significantly lower than the target (i.e., 20% respect to the HAB of flame).

Table 4.3. HAB of thermocouple for different flames from mixtures with *n*-heptane

Tested molecule added	Content (vol.%)	Flame HAB (mm)	Thermocouple	
			HAB (mm)	Relative position (%)
n-Heptane (reference)	0	46.70	9.22	19.74 +/- 0.97
α-Pinene	0.1	47.11	9.04	19.19 +/- 0.97
	1.0	50.85	9.29	18.26 +/- 0.76
	5.0	51.51	9.28	18.02 +/- 0.62
β-Pinene	0.1	46.81	8.36	17.85 +/- 0.82
	1	48.17	7.84	16.28 +/- 0.58
	5.0	47.87	7.27	15.18 +/- 0.57
Nopol	0.1	49.65	8.75	18.63 +/- 0.69
	1	54.19	10.29	19.00 +/- 0.78
	5	61.10	11.40	18.66 +/- 0.87
Terpineol	0.1	47.28	9.50	20.09 +/- 0.99
	1	50.23	9.89	19.68 +/- 1.03
	5	55.84	10.55	18.89 +/- 0.67
Myrtenol	0.1	47.65	8.10	18.99 +/- 0.99
	1	52.57	9.88	18.79 +/- 0.86
	5	55.12	11.14	20.20 +/- 1.02
Borneol	0.1	53.05	11.66	21.99 +/- 1.43
	1	59.21	11.16	18.84 +/- 0.94
	5	62.60	11.39	18.20 +/- 0.81

The influence of the content of tested molecules from turpentine on flame temperature is shown in Figure 4.8, where T^0 is the flame temperature for pure *n*-heptane. As observed, the flame temperature increases with the content of α-pinene, nopol, myrtenol and terpineol, whereas a small reduction is observed in the β-pinene and borneol blends. The values of flame temperature for β-pinene blends were significantly lower than those for α-pinene blends, see Figure 4.8a, which is not consistent with their similar adiabatic flame temperature. This could be explained by inaccuracy on the location of thermocouple (see Table 4.3).

The significant increase in the flame temperature in the blends with α-pinene, nopol, myrtenol and terpineol, and the slight reduction of flame temperature evidenced with borneol, agree with the adiabatic flame temperature. On the other hand, despite the higher estimated adiabatic flame temperature for myrtenol with respect to nopol, the measured flame temperatures of *n*-heptane + nopol blends were slightly higher than that with myrtenol (see Figure 4.8b). Considering that the main difference in the chemical structures of these two alcohols is the longest side-chain of nopol (see Figure 4.2), this feature would play an important role in combustion performance, as will be discussed below.

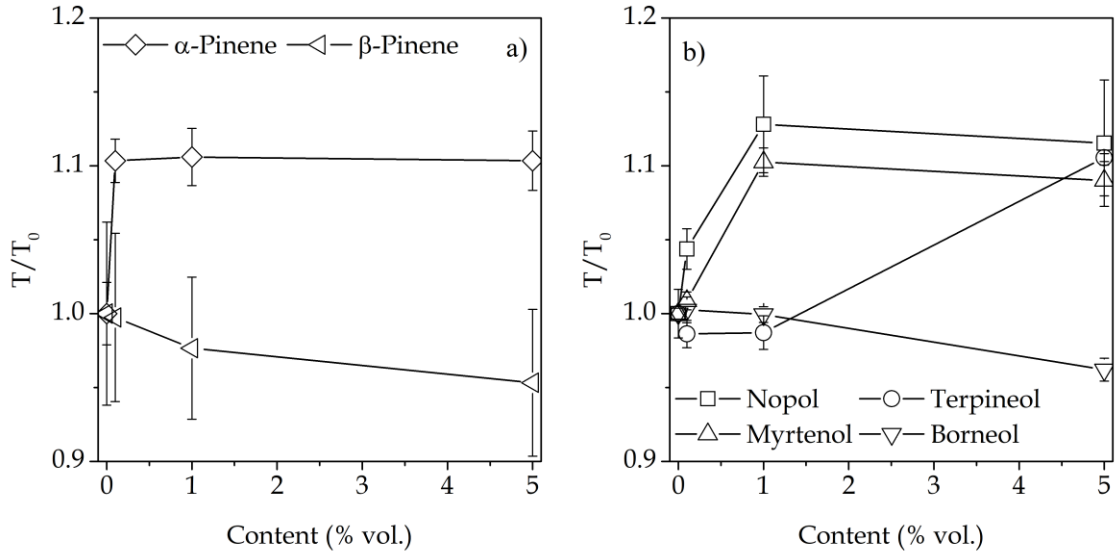

Figure 4.8. Influence of the content of probe molecules on flame temperature. a) α- and β-pinene; b) nopol, terpineol, myrtenol and borneol

4.2.3.2 NOx emissions

Figure 4.9a depicts a slight increase in NOx emissions with α-and β-pinene content in the blend, probably as a result of the higher flame temperature. Nevertheless, despite its apparent lower flame temperatures (no definitive values because of the lower relative HAB of the thermocouple), β-pinene blends display a slight increase in NOx emissions, supporting the hypothesis that the double bond outside the ring favors reactions with oxygenated species.

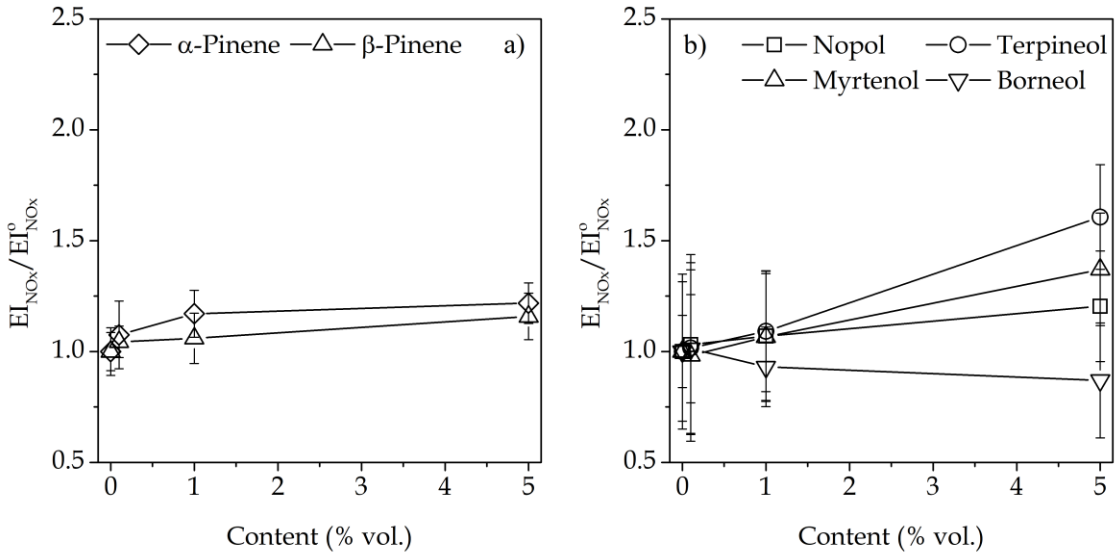

Figure 4.9. Influence of content of probe molecules on NOx emissions. a) For α- and β-pinene; b) for nopol, terpineol, myrtenol and borneol

NOx emissions from blends of *n*-heptane with alcohols are a consequence of the flame temperature and the consequent formation of thermal NO. Consistently, flames with borneol show a decrease in NOx emissions, whereas increases in NOx emissions are observed with the other alcohols (see Figure 4.9b).

4.2.3.3 CO and UHC emissions

The ratio between emission indices of CO for flames fueled with blends of *n*-heptane and turpentine-derived molecules, and those from pure *n*-heptane ($EI_{CO}{}^{o}$) are shown in Figure 4.10. Interestingly, CO is slightly reduced with β-pinene but increased with α-pinene (see Figure 4.10a). With regard to alcohols, a decrease in CO emissions is observed with myrtenol, terpineol and nopol (see Figure 4.10b), while an increase is observed with borneol.

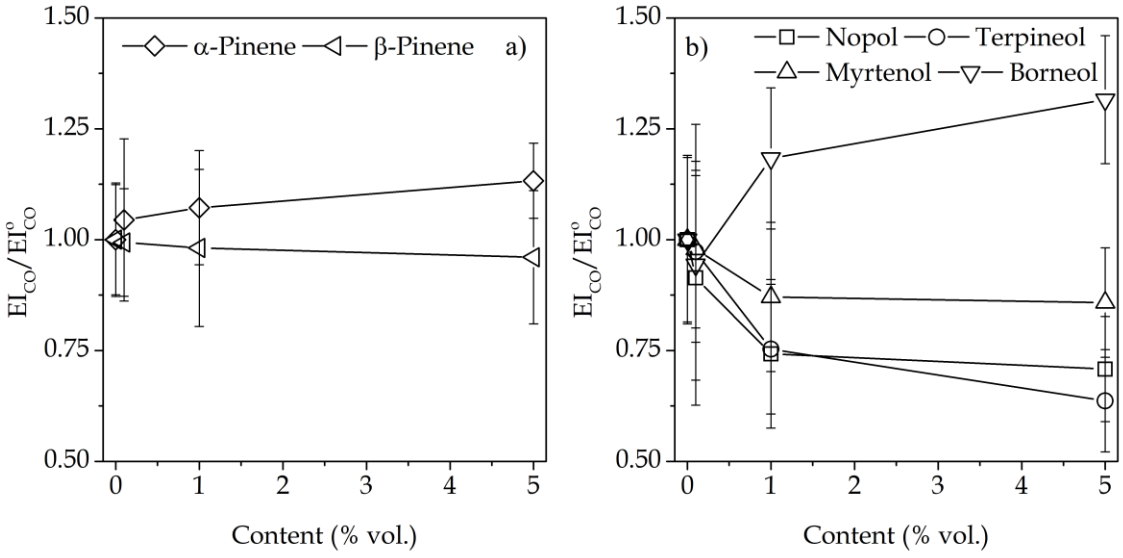

Figure 4.10. Influence of content of probe molecules on CO emissions. a) α- and β-pinene; b) nopol, terpineol, myrtenol and borneol

Regardless being isomers, α- and β-pinene display different influence on combustion. The increase in CO emission when α-pinene was added to *n*-heptane indicates a difficulty to achieve complete combustion, although the flame temperature for *n*-heptane + α-pinene was higher because of its relatively high enthalpy of formation. Conversely, combustion appears to be slightly benefited by the presence of β-pinene in the blends with *n*-heptane. Therefore, not just the presence of a double bond but also its position may be relevant for combustion. Particularly, the location of the instauration outside the ring would make of β-pinene a more reactive molecule.

Despite their more complex chemical structures, myrtenol, terpineol and nopol display better performance in combustion than *n*-heptane (even higher than those of α- and β-pinene, see Figure 4.10b), as a result of the oxygen content of oxyfunctionalized molecules. Emission index of CO with borneol as additive increases around 40% at 5 vol. % of the additive, indicating a deterioration in the combustion, in agreement with the results of flame temperature.

The ratio between emission indices of UHC for the blends and pure *n*-heptane ($EI_{UHC}{}^{o}$) are shown in Figure 4.11. α-Pinene decreases the emission of UHC and β-pinene does not affect this index (Figure 4.11a). Interestingly, all alcohol additives

display a reduction of UHC emissions at all contents, see Figure 4.11b. In view of α- and β-pinene differing only on the location of the double bond, it can be argued that its presence outside the ring favors the reactions of oxygenated intermediates (e.g., lower CO emissions in β-pinene) whereas the unsaturation inside the ring favors reactions with hydrocarbon species (e.g., lower UHC emissions in α-pinene). On the other hand, considering that all the studied flames are fuel-rich, these results suggest that the alcohols would supply the extra oxygen required to facilitate hydrocarbon oxidation.

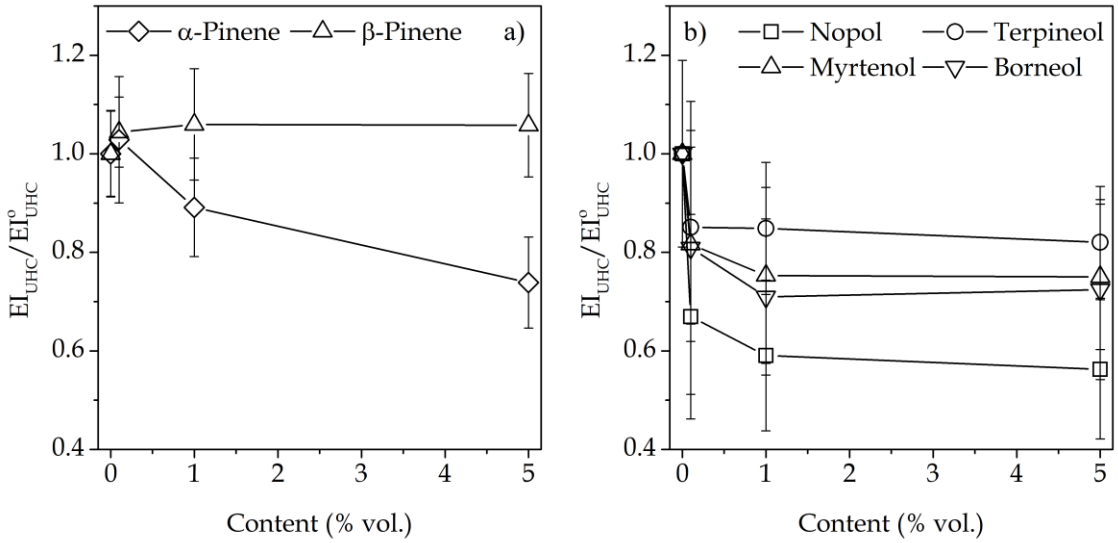

Figure 4.11. Influence of content of probe molecules on UHC emissions. a) For α- and β-pinene; b) for nopol, terpineol, myrtenol and borneol

The hydroxyl group of borneol is attached directly to the bi-cycle of the molecule (Figure 4.2), whereas in the other alcohols it is located at the end point of a side-chain. Since the performance of nopol was the best, followed by myrtenol and terpineol, while presence of borneol in the fuel may be detrimental to the combustion performance, the length of the chain would play an important role in the behavior of the fuel component. The interatomic distance between the main ring of the molecules and the OH group for each molecule was estimated with the density functional theory (DFT) by the Material Studio 2017 suite (see Figure 4.12). The geometry of each molecule was optimized and its energy minimized using the local density approximation (LDA) with the parameterizations developed by Perdew-Wang without any solvatation model [20].

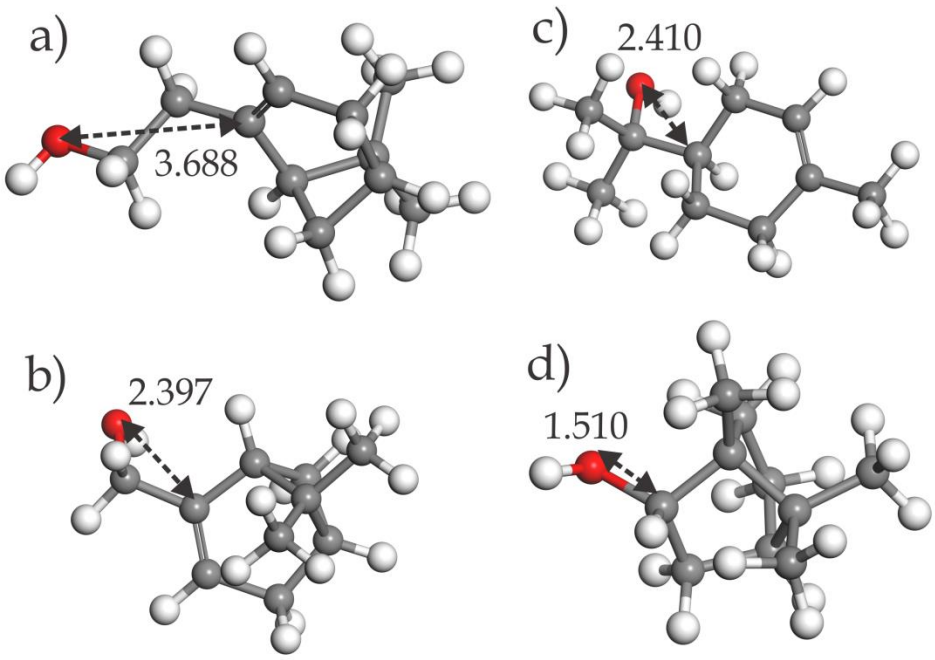

Figure 4.12. Interatomic distance (Å) between the OH group and the main ring of the molecules: a) nopol, b) myrtenol, c) terpineol and d) borneol

In can be observed that the performance of alcohols in combustion tests is correlated to the interatomic distance between the OH group and the main ring, that is, nopol > terpienol > myrtenol > borneol. In fact, by increasing the interatomic distance, the strain of the molecule resulting from the interaction between the hydroxyl group and the main ring of the molecule is reduced, increasing the reactivity of the molecules. Besides, the number of carbon(s) in the chain of the hydroxyl group can influence the properties of the intermediate species in a combustion reaction. For instance, Godwin and coworkers showed that *n*-pentanol has better emissions and engine efficiency than *n*-butanol [156], and that benzyl alcohol (with a structural resemblance to terpenic alcohols due to the hydroxyl group attached to a ring via a carbon chain) displayed better performance than linear and branched alcohols (i.e., *n*-butanol, isobutanol, and *n*-pentanol). On the other hand, analysis of the combustion mechanism of isopropanol and *n*-propanol led to propose that the intermediate species from *n*-propanol (i.e., propanal) are more active than those for isopropanol (i.e., acetone) [157], [158], suggesting that the longer the side-chain to which the hydroxyl group is attached the more active the intermediate species. This

would explain the performance of nopol, followed by myrtenol, terpineol and borneol. In addition, the good performance of nopol is favored by the presence of an extra carbon atom respect to other alcohols.

Lower CO and UHC emissions for flames obtained with blends of *n*-heptane and myrtenol, terpineol and nopol were observed with respect to those from *n*-heptane blended with α- and β-pinene. This indicates that the presence of oxygen in the molecules of fuel may improve the oxidation reaction of the fuels. For instance, myrtenol and α-pinene present a double bond inside the main ring in addition to having the same H/C molar ratio, and myrtenol displays better combustion performance with similar flame temperature and lower CO and UCH emissions than α-pinene. Probably, the oxygen atoms in the fuel increase the oxygen content in oxygen-deficient regions of the flame, overcoming possible diffusion problems of the fuel and air [159]. In addition, the carbon atoms with a hydroxyl group in close proximity display more propensity to be transformed into carbon dioxide than hydrocarbons or particulate matter [160].

4.2.3.4 Flame size

In agreement with the theoretical heights (i.e., obtained with Roper's expression), experimental results show an increase in flame tip height with the content of the turpentine-derived molecules in the blend, Figure 4.13, with a higher effect for alcohols. Furthermore, from a theoretical point of view, no difference in flame height between α- and β-pinene, and some minor changes for blends with alcohols can be expected, with borneol displaying the highest flame height. Although borneol indeed displays the largest experimental flame height, some differences are observed between α- and β-pinene flames.

According to Roper's expression, the height of the flame is directly proportional to the volumetric flow of fuel and stoichiometric air-to-fuel ratio. In this work, the higher the content of tested molecules the higher the molar stoichiometric air-to-fuel ratio, increasing the theoretical flame height. Experimental values of height of flame tip were larger than the theoretical ones, probably due to the actual molar stoichiometric air-to-fuel ratio being higher than the computed one (i.e., not all oxygen in the

oxidizer stream would diffuse into the reaction zone). Considering that the H/C ratio of fuel decreases as the content of oleoresin-based molecules increases (see Table 4.2), an increase in height of flame tip is to be expected because the larger availability of carbon atoms in the fuel molecules increase the combustion time allowing the flame to reach larger heights [67].

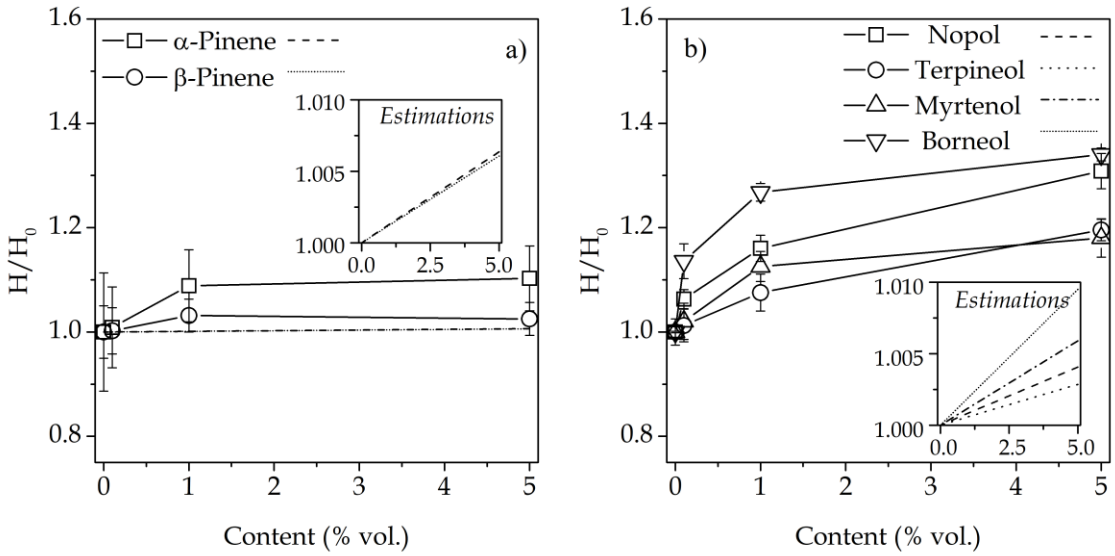

Figure 4.13. Influence of content of probe molecules on flame height. a) For α- and β-pinene; b) for nopol, terpineol, myrtenol and borneol

4.2.4 Remarks of the section

The high reactivity of β-pinene makes its combustion easier than α-pinene, where the carbon-carbon double bond is located inside the six-membered ring. Besides, and contrarily to β-pinene, the intermediates formed from the oxidation of α-pinene can promote the formation of CO. The thermal mechanism dominates the formation of nitrogen oxides from flames fueled with α- and β-pinene because their emissions are directly related to the temperature of the flame.

Significant reduction in CO and UHC emissions, and an appreciable increase in flame temperature was observed in the blends of nopol, terpineol and myrtenol with *n*-heptane, suggesting an improvement in combustion performance. Molecular structure appears to be a key factor in the combustion of monoterpenic alcohols, especially the position of the hydroxyl group. In particular, the longer the distance

between the OH group and the bi-cycle (or main ring) the better the performance of the molecule in combustion.

The fact that the interatomic distance is related to the strain of the molecule and that the number of carbons in the side-chain where hydroxyl group is attached to is associated to the reactivity of the intermediates formed in the oxidation of alcohols, can be related with the performance of the combustion reaction. Nopol (with two carbons between the OH group and the bi-cycle of the molecule), shows a better performance in combustion than myrtenol (which has similar structure but with just one carbon in between the OH group and the bi-cycle). α-terpineol, with just one 6-carbon ring, also displays good performance in combustion.

4.3 Conclusions

- ★ Based on estimations (and few available experimental values) of thermal and thermochemical properties, probe molecules from turpentine present high potential to be tested in fuel applications. Although both boiling and melting temperatures are increased with respect to the pinenes present in turpentine, and the LHV and adiabatic temperature of the flame are decreased after the oxyfunctionalization, oxygenates from main components of turpentine have similar thermochemical properties than diesel (in some cases better), stressing their potential as additive or component of diesel fuels.
- ★ The high reactivity of β-pinene makes its combustion easier than α-pinene, where the carbon-carbon double bond is located inside the six-membered ring. Besides, and contrarily to β-pinene, the intermediates formed from the oxidation of α-pinene can promote the formation of CO. The thermal mechanism dominates the formation of NOx species from flames fueled with α- and β-pinene.
- ★ Significant reduction in CO and UHC emissions, and an appreciable increasing in flame temperature were observed when nopol, α-terpineol and myrtenol were added to *n*-heptane, suggesting an improvement in combustion performance. Molecular structure appears to be a key factor in the combustion of monoterpenic alcohols, especially the position of the hydroxyl group. In particular, the longer the distance between the OH group and the bi-cycle (or

main ring) the better the performance of the molecule in combustion. As the interatomic distance is related to the molecule stress, and the number of carbons in the side-chain where hydroxyl group is attached, the reactivity of the intermediates formed in the oxidation of alcohols can be related with the performance of the combustion reaction. Nopol (with two carbons between the OH group and the bi-cycle of the molecule), shows a better performance in combustion than myrtenol (which has similar structure but with just one carbon in between the OH group and the bi-cycle). α-Terpineol, with just one 6-carbon ring, also displays good performance in combustion.

★ The turpentine-derived molecules display high potential as fuel component for combustion applications. Except borneol, all other tested molecules showed improvements in combustion performance derived from the increase in flame temperature and the decrease in UHC and CO emissions when these molecules were added to *n*-heptane, whereas the increase in NOx emissions can be attributed to the increase in flame temperature. In addition, the oxyfunctionalization of constituent molecules of turpentine leads to alcohols which display better performance in combustion reaction. This is particularly interesting because oxygenated molecules have additional advantages in fuel applications, such as reduction in particulate matter emissions.

This page intentionally left blank

Chapter 5. Oxyfunctionalized turpentine as biofuel

The chemical oxyfunctionalization of turpentine towards nopol, the estimation of some important properties in fuel applications, and the influence on emissions and flame characteristics of laminar flames fueled with oxyfunctionalized turpentine (oxyturpentine) are presented in this chapter in order to assess the potential of oxyturpentine as biofuel, specifically from the point of view of emissions and combustion.

5.1 Introduction

Interest in the utilization of renewable resources from biomass has been increasing in recent years, particularly to obtain high-added value products for industries such as polymers, food and even biofuels [161], [162]. Terpenes are found in many plants and some animal species, and are used as solvents, pharmaceuticals, and fragrances, among others [163].

Worldwide production of turpentine in the last decades is estimated at 330000 t/year, presenting a steady increase since the 1980s. Currently, major methods of turpentine production are from the Kraft process (70%) and from distillation of oleoresin (30%) [164]. The market value of turpentine in Colombia is 7-8 USD/gal. The fact that turpentine is a byproduct of paper industry and the increase in its production from oleoresin in countries such as China, among other reasons, have reduced significantly the price of turpentine, thus becoming an attractive source for biofuels. Likewise, some efforts have been focused on the improvement of the yield of oleoresin from pine trees. The oleoresin yield from *Pinus merkusii* is estimated around 40 g/tree/day with a yield of turpentine from oleoresin of around 20 % wt. [19]. The U.S. Department of Energy recently has assigned $6.3 million to increase at least five times the current yield of oleoresin from Pinus in order to make economically attractive the production of turpentine as a feedstock for biofuels.

Although turpentine has already been used in fuel applications, it is expected that oxygenated compounds derived from turpentine would display better performance because the oxygen content contributes to reduce soot formation and, therefore, particulate matter emissions and polycyclic aromatic hydrocarbons [1], [2]. In addition, other fuel properties such as lubricity (related to the engine durability) and flash point (related to the risk associated to storage and transport of fuels) are usually improved as a consequence of the oxygen content. Currently, some oxygenated molecules such as methyl esters and alcohols (mainly ethanol and *n*-butanol) are widely used as fuel components, but others are also interesting as components of future advanced biofuels [58]. In particular, combustion tests of different oxygenated molecules which can be obtained from turpentine (i.e., nopol, terpineol, and myrtenol) in blends with *n*-heptane showed a significant reduction in CO and UHC emissions, and an appreciable increasing in flame temperature, suggesting an improvement in combustion performance.

Nopol, with two carbons between the OH group and the bi-cycle of the molecule, showed better performance than myrtenol, terpienol and borneol. Therefore, nopol was selected as target molecule to be synthesized from turpentine, in order to obtain an oxygenate fuel; turpentine available in the local market in Colombia was used as raw material.

A search of turpentine producers in Colombia led to conclude that only one company produces turpentine at large-scale from conifers (Centro de Las Gaviotas, Vichada). Moreover, as the local market is dominated by imported turpentine, probably because of its lower price or the small amounts produced in Colombia, different samples of turpentine were purchased in the local market from Colombia and were characterized to select the most suitable for the oxyfunctionalization reaction.

5.2 Estimation of properties of oxyturpentine

5.2.1 Thermochemical properties

Estimations of thermochemical properties for turpentine and oxyturpentine with the methods proposed by Joback and Benson were carried out by using the typical concentration of turpentine from Colombia (see Table 1.2), and assuming that all the

β-pinene from turpentine is converted into nopol. Standard heat of formation (Δh_f^0) and LHV for turpentine and oxyturpentine are sown in Table 5.1.

Significant differences in the estimated values of the standard heat of formation are observed for Joback and Benson methods, both for turpentine and oxyturpentine. However, the changes in heat of formation due to the oxyfunctionalization (i.e., the difference between standard heat of formation of oxyturpentine and turpentine) are -95.0286 and -82.5888 MJ/mol for Joback and Benson, respectively, which are comparable. In addition, both methods give consistent results of LHV and a minor variation is observed.

Table 5.1. Thermochemical properties estimated for turpentine and oxyturpentine

Compound	Δh_f^0(MJ/mol)		LHV (MJ/kg)	
	Joback	**Benson**	**Joback**	**Benson**
Turpentine	-49.3799	13.1239	42.4556	42.9144
Oxyturpentine	-144.4085	-69.4649	40.1425	40.6478

The reduction in both the standard heat of formation and lower heating value for oxyturpentine with respect to turpentine is related to the insertion of the oxygen atom in the molecule of fuel. The oxyturpentine displays an estimated LHV lower than diesel but higher than biodiesel (44.7249 and 38.5599 MJ/kg, respectively, measured in this work). In addition, estimated *LHV* of oxyturpentine is higher than that for pure nopol (37.8363 MJ/mol, obtained by Benson method) due to the presence of α-pinene (LHV = 42.8878 MJ/kg, obtained by Benson method) in the mixture.

5.2.2 Adiabatic flame temperature

Adiabatic flame temperatures for turpentine and oxyturpentine were estimated from the chemical equilibrium of combustion reactions using the same methodology than in Chapter 3 and Chapter 4, and are presented in Figure 5.1; the results of nopol obtained in Chapter 4, as well as those for diesel and biodiesel are presented for comparison. Turpentine presents the highest maximum adiabatic flame temperature followed by oxyturpentine, pure nopol, diesel and biodiesel, suggesting the high potential of turpentine and oxyturpentine as diesel fuels.

The lower adiabatic flame temperature for oxyturpentine with respect to turpentine is ascribed to the presence of nopol (with one oxygen atom in its molecule). On the other hand, the difference of the maximum adiabatic flame temperature between turpentine and diesel is around 30 K, similar to that between α- and β-pinene and diesel. The reduction of the maximum adiabatic flame temperature due to the oxyfunctionalization of turpentine is just 7 K, oxyturpentine thus displaying an adiabatic flame temperature ~23 K higher than diesel.

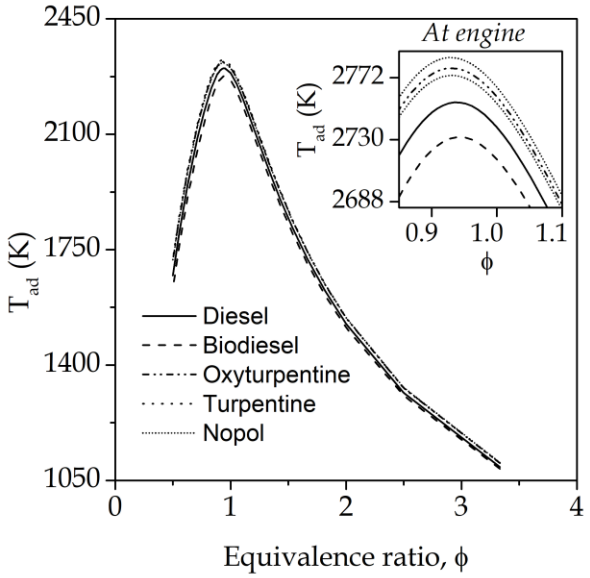

Figure 5.1. Adiabatic flame temperature for turpentine and oxyturpentine, compared to diesel, biodiesel and nopol at “ambient conditions” (i.e., constant pressure) and “engine conditions” (i.e., constant volume, shown in insert)

5.2.3 Remarks of the section

The presence of α-pinene in the oxyturpentine mixture can be favorable because its high heating value respect to nopol increases the amount of heat released in the combustion. On the other hand, although the LHV of oxyturpentine is slightly lower than that of diesel, its adiabatic flame temperature is higher.

5.3 Synthesis of oxyturpentine

5.3.1 Background

Different products can be obtained from the oxyfunctionalization of turpentine, mainly alcohols (see Table 5.2). Terpineol is usually obtained from α-pinene or limonene by hydration in the presence of acid catalysts. This transformation involves

the formation of an intermediate with a carbenium ion, which is subjected to nucleophilic attack by water molecule to form the alcohol [165]. The production of α-terpineol from α-pinene-rich turpentine under heterogeneous catalyst has been reported. Around 85 % conversion of α-pinene and 50% selectivity towards α-terpineol were obtained using Amberlyst 15 as catalyst and isopropyl alcohol as solvent [166]. The product of this kind of transformation (i.e., α-terpineol, unreacted α-pinene and other by-products and impurities) has been used directly in diesel engines and as an octane booster for gasoline fuels, showing improvements in engine performance and reducing some pollutants such as carbon monoxide [3], [38].

Table 5.2. Some products from oxyfunctionalization of turpentine

Compound	CAS	Formula	MW (g/mol)
α-Terpineol	98-55-5	$C_{10}H_{18}O$	154.25
Nopol	128-50-7	$C_{11}H_{18}O$	166.26
Borneol	507-70-0	$C_{10}H_{18}O$	154.25
Myrtenol	515-00-4	$C_{10}H_{16}O$	152.23
Verbenol	473-67-6	$C_{10}H_{16}O$	152.23
Pinocarveol	3917-59-7	$C_{10}H_{16}O$	152.23

MW Molecular Weight

If β-pinene is used as reactant and an appropriate solvent-catalyst system is selected, nopol can be produced instead. Nopol is a terpenic alcohol used in cosmetics and perfumes as fragrance compound, detergents, and soaps, among other applications [167]. Bain and coworkers [168] proposed a method for preparation of nopol using β-pinene and paraformaldehyde in the presence of homogeneous catalyst such as zinc chloride and with continuous heating, the so-called *Prins* condensation reaction, schematized in Figure 5.2.

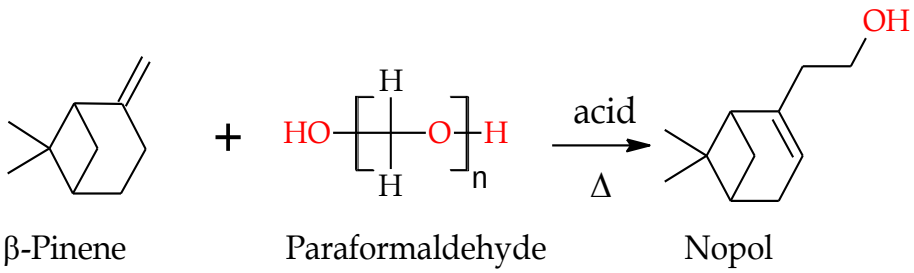

Figure 5.2. Nopol synthesis from β-pinene

Several solid catalysts have been reported for the *Prins* condensation of nopol from β-pinene and paraformaldehyde, such as Tin, Zirconia, Iron and Zinc supported on silicate materials such as SBA-15, MCM-41 and kenyaite [169]–[174], $ZnCl_2$ impregnated over montmorillonite [175], and sulfated zirconia [176]. All these materials present acid properties, which are desired for the reaction, and display high activity, with complete conversion of β-pinene and high selectivity towards nopol (>90 %) at optimal operation conditions.

Sn/MCM-41 catalyst, in addition to its high activity in the synthesis of nopol, has other properties such as easy synthesis and high stability (and thus high potential to be reused) [177]. Optimal loading of Sn has been found at low monolayer content, with coverage below 0.06 Sn nm^{-2} [178]. Additionally, kinetic studies of this material with toluene and ethyl acetate as solvent with pure β-pinene and paraformaldehyde have been conducted [177], [179].

In all the cases reported, nopol was produced from pure β-pinene, thus reducing the interest of these reactions to produce biofuels, due to practical, industrial and economic factors. In addition, some previous work showed the difficulty to scale-up the reaction, mainly as a consequence of the difficult scaling-up of the catalyst. Therefore, in this work *Prins* condensation reaction was performed to obtain nopol-rich oxyfunctionalized turpentine using turpentine as β-pinene source.

5.3.2 Methodology

5.3.2.1 Materials

Different samples of turpentine were purchased in the local Colombian market (Protokimica S.A., Indu Guim, Antioqueña de Químicos S.A, GMP Productos Químicos S.A, Prodeysa S.A., Proquimar S.A., Químicos JM and Franco LTDA). Paraformaldehyde powder, tetra-ethyl-orthosilicate (TEOS) and myristyl-trimethyl-ammonium bromide (MTABr), all analytical-grade, were purchased from Sigma-Aldrich. Toluene and ethyl acetate analytically-pure, and solution of ammonium hydroxide at 28-30% were supplied by JT Baker. Di-hydrated Tin chloride was from Alpha-Aesar.

5.3.2.2 Chromatographic characterization

The identification and quantification of components in the turpentine samples and reaction products (oxyfunctionalized turpentine) were performed by GC and GC-MS in an Agilent 7890 GC system coupled to Agilent 5975C VL MSD triple quadrupole mass detector and flame ionization detector (FID).

Both the inlet injection and detector temperatures were 250°C. A 1 µL sample was eluted using an DB-1 (30 m x 320 µm x 0.25 µm) capillary column (Agilent J&W). Helium was used as carrier gas. The initial temperature (70°C) was held for 1 min, and then, a 15°C/min heating ramp up to 180°C (held for 1 min) was used, with a split ratio of 25 : 1. Mass spectra were compared with the NIST database to identify the components of the mixture. Calibration of nopol, α- and β-pinene and toluene were performed and results are presented in Appendix J.

5.3.2.3 Catalyst preparation and characterization

Sn-MCM-41 catalyst with 0.5 wt.% Sn was prepared by the gel procedure at room temperature, as previously reported [180]. Briefly, 7.4 g of MTABr were dissolved in 326 mL of water with subsequent addition of 0.2 g of hydrated tin chloride, controlling the pH at 11.6 by adding ammonia solution. 28 g of TEOS was added dropwise to the solution at a rate of 0.6 mL/min keeping the solution stirred at 400 rpm. Once TEOS was added, stirring of the solution was continued for 1 h, followed by 1 h of decanting. Then, the precipitated solid was washed with water until negative test of chlorides (qualitative tests performed with silver nitrate). The solid was dried at 100°C overnight and calcined at 550°C for 5 h, with a heating ramp of 1°C/min.

Sn-MCM-41 was characterized by Atomic Absorption (AA) in a Thermo Elemental SOLAAR S4 whit a Tin lamp. X-ray diffraction (XRD) was conducted in a Bruker D8 Advance coupled with Cukα1 radiation generated at 40 kV and 40 mA, over a 2θ range from 0.5º to 10º with a step size of 0.02035º. Nitrogen adsorption/desorption isotherms at 77K were measured in a Micromeritics Gemini 2380; sample was previously outgassed at 150°C during 4 h. Fourier-transform infrared (FTIR) spectra for fresh and post reaction samples of catalysts were collected in a Perkin Elmer Spectrum 65 on diffuse reflection mode (Pike) with KBr powder.

5.3.2.4 Turpentine oxyfunctionalization

The performance of the reaction was evaluated in 2 mL vials under magnetic stirring and autogenous pressure. Stirring speed, reaction temperature, Sn-MCM-41 load, and paraformaldehyde : β-pinene molar ratio, were kept at 1000 rpm, 90°C, 20 wt.% with respect to β-pinene, and 1 : 1, respectively, for all reactions. Reaction time was varied from 0.5 to 24 h. The effect of the solvent was evaluated by comparing the reaction without solvent and with different amounts of solvent (toluene:β-pinene weight ratio up to 12).

To evaluate the stability and reusability of Sn-MCM-41, the same catalyst and reaction conditions were used in three reaction cycles, performing different aftertreatments in each cycle (washing with toluene or ethyl acetate), with subsequent filtering and drying. In addition, the same reaction conditions were evaluated at different scales: 2 mL, 250 mL and 10 L flask reactors, to assess the potential scaling-up of the reaction.

Conversion of β-pinene and selectivity to nopol were calculated from the species concentrations with the expressions in Equation 5.1 and Equation 5.2,

$$\text{Conversion}(\%) = \frac{(C_\text{i} - C_\text{f})_{\beta-\text{pinene}}}{(C_\text{i})_{\beta-\text{pinene}}} 100 \qquad \textbf{Equation 5.1}$$

$$\text{Selectivity}(\%) = \frac{(C_\text{f})_{\text{nopol}}}{(C_\text{i} - C_\text{f})_{\beta-\text{pinene}}} 100 \qquad \textbf{Equation 5.2}$$

where C_i and C_f are the initial and final concentrations, respectively.

The water content of oxyturpentine was measured with the Karl-Fischer technique based on ASTM D 4377 standard in a Metrohm 831 KF Coulometer.

5.3.3 Results and discussion

5.3.3.1 Catalyst synthesis and characterization

Actual content of Sn on Sn-MCM-41, evaluated by atomic absorption, was 0.42 wt.%, slightly lower than the target value. The XRD pattern of the synthesized material, Figure 5.3, shows the main peak at 2.6° 2θ and two smaller peaks at 4.5 and 5.2° 2θ, which are typical of hexagonal channels presented in MCM-41 materials (d_{100} = 33.19 Å, d_{110} = 19.06 Å and d_{200} = 16.43 Å, respectively) [172].

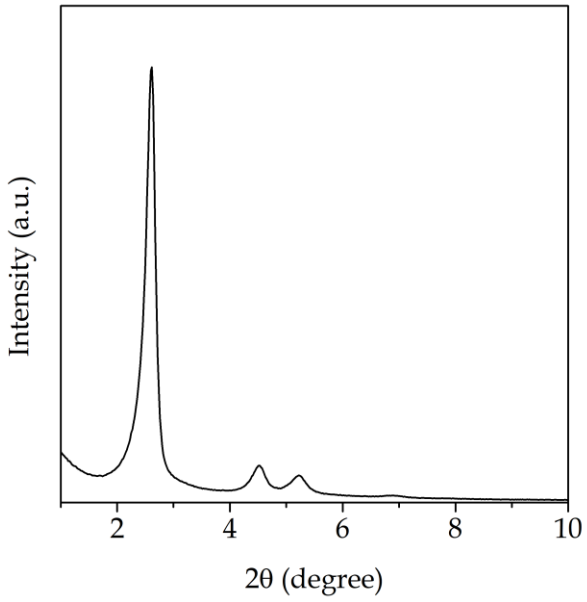

Figure 5.3. XRD pattern of Sn-MCM-41

Figure 5.4 shows the FTIR analysis of Sn-MCM-41.

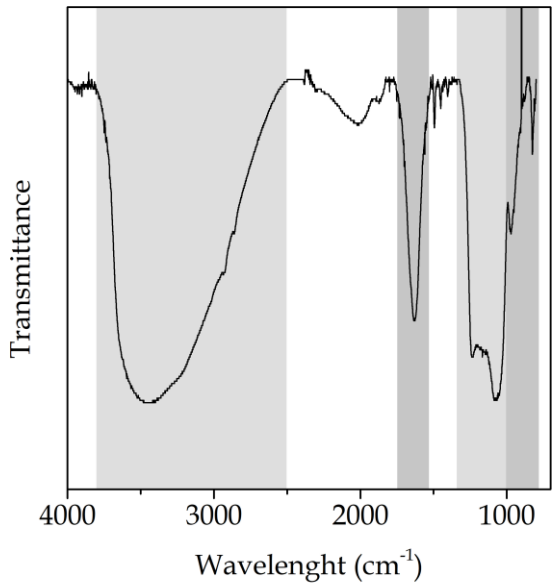

Figure 5.4. FTIR spectrum of Sn-MCM-41

The peaks observed between 800 and 1000 cm^{-1} can be attributed to bending and symmetric stretching vibrations of the Si—O—Si bond, while the peaks between 1000 and 1300 cm^{-1} are assigned to asymmetric vibrations of Si—O—Si bond. Entrapped water into the molecular structure of MCM-41 commonly shows a band

around 1600 cm^{-1} due to the bending vibrations of OH bond. The wide band in the region 2500-3800 cm^{-1} is related to OH stretching of adsorbed moisture on the support and/or of silanol groups [181].

BET area, and pore volume and diameter obtained by nitrogen adsorption on the synthesized Sn-MCM-41 were 1241 m^2/g, 0.8665 cm^3/g and 28 Å, respectively, which are typical values for MCM-41 materials [172]. The isotherm of nitrogen adsorption/desorption over the Sn-MCM-41, Figure 5.5, depicts a type IV isotherm, as expected for mesoporous materials, with a hysteresis loop type H4 (according to IUPAC classification [182]), which are typical properties of MCM-41 materials.

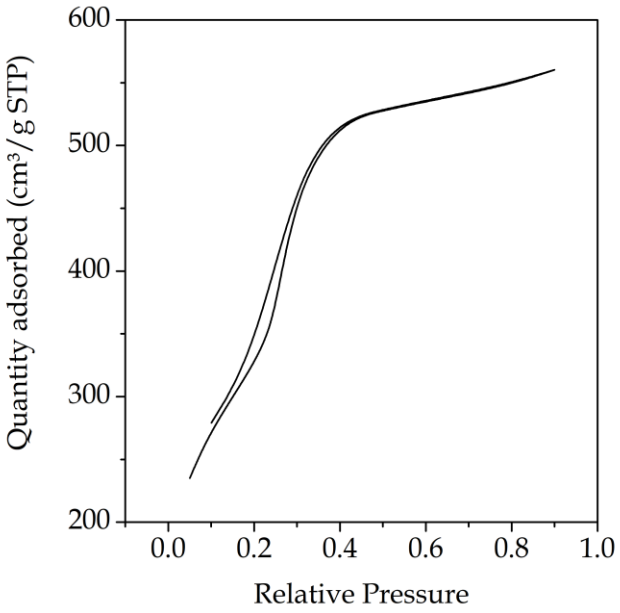

Figure 5.5. Nitrogen absorption/desorption isotherm of Sn/MCM-41

5.3.3.2 Characterization of turpentine and oxyturpentine

Contents of typical components of turpentine for the samples acquired in local market from Colombia, Table 5.3, shows that α-pinene is the main component in almost all the samples. α-pinene content on Sample 8, however (this sample is composed mainly by linear hydrocarbons, i.e., *n*-heptane and *n*-decane), is much lower, and no β-pinene was found; thus, this sample is not representative of turpentine and was discarded from the study. α-Pinene content is in the range 70-77 wt.% in most samples. β-pinene is the second major component in samples 2, 3

and 6 (8-10 wt.%), while Δ3-carene is present in higher concentration than β-pinene in samples 4, 5 and 7.

Table 5.3. Composition of turpentine from Colombian local market

Compound	Sample (wt.%)							
	1	**2**	**3**	**4**	**5**	**6**	**7**	**8**
α-Pinene	48.1	76.9	76.9	73.0	71.3	70.3	70.6	11.8
Camphene	0.7	2.3	2.3	2.9	2.6	1.1	2.5	0.0
β-Pinene	38.4	8.3	8.3	6.4	6.8	10.1	5.7	0.0
3-carene	1.7	3.8	3.8	13.3	14.0	3.9	14.7	19.4
Others	11.1	8.7	8.7	4.3	5.2	14.6	6.6	68.8

The sample labeled as 1, supplied by GMP Productos Químicos, was selected due to its highest β-pinene content, which would facilitate its oxyfunctionalization to nopol, representing the best scenario to evaluate the potential of nopol-rich turpentine as biofuel. A more detailed composition of the turpentine this sample is presented in Table 5.4 (left column). It can be observed that the third main component is limonene, with much smaller composition (ca 5 wt.%); the other compounds are present in much lower concentration (< 2 wt.%).

The composition of the oxyfunctionalized turpentine obtained without solvent at 1000 rpm, 90°C, 24 h, catalyst loaded at 20 wt.% with respect to β-pinene, and paraformaldehyde :β-pinene 1 : 1 molar ratio at vial scale is presented in Table 5.4 (right column).. In addition to the expected decrease in β-pinene content (because of its transformation into nopol), a significant decrease in limonene content, an increase in α-terpineol content, and the presence of new compounds such as α-longipinene and borneol at low contents is observed. In particular, the increase in α-terpineol, which can be derived from α-pinene and limonene, indicates that the reaction conditions (i.e., temperature, time, and presence of water), and the catalyst properties promote the oxyfunctionalization by hydration of these terpenes. Other components present in turpentine appear not to be affected by oxyfunctionalization.

The water content in the reaction product was 3430 ppm, in contrast with 153 ppm in turpentine, indicating that water is likely released in the depolymerization of paraformaldehyde during the reaction.

Table 5.4. Composition of turpentine and oxyturpentine (obtained without solvent at 24 h and at vial scale)

Compound	Turpentine (% wt.)	Oxyturpentine (% wt.)
α-Pinene	48.1	44.7
β-Pinene	38.36	0.1
Limonene	5.18	0.8
β-Myrcene	1.81	1.4
Longifolene	1.76	0.5
3-Carene	1.67	2.3
Camphene	0.73	2.1
α-Terpineol	0.68	4.7
(+)-Fenchone	0.48	1.4
Terpinolene	0.23	1.5
Isoborneol	0.09	0.7
m-Cymene	0.05	0.3
Nopol	0.00	31.0
α-Phellandrene	0.00	2.7
α-Longipinene	0.00	4.3
Borneol	0.00	0.6
Unidentified	0.93	1.0

5.3.3.3 Effect of solvent

Concentration of the different species in the reaction product (reaction time = 15 h) as a function of the amount of solvent (toluene) is shown in Figure 5.6. Total species concentration in Figure 5.6a shows that toluene is increased and other species are decreased, mainly due to the dilution effect. Although α-pinene outlet concentration does not appear to be influenced by the presence and amount of solvent, results indicate that α-pinene can react when no solvent is used (see Figure 5.6b). The non-linear trend of nopol content in free-solvent basis can be attributed to a trade-off between toluene (which favors nopol conversion) and α-pinene (which favors nopol conversion, especially in the absence of toluene) content.

Other reaction products (e.g., α-terpineol, α-longipinene, α-phellandrene, and borneol) are also favored in the absence of solvent. In particular, comparison of the contents for α-pinene and limonene compounds indicates that α-terpineol is likely formed from them, as previously reported [165].

The conversion of limonene and α- and β-pinene, as well as nopol selectivity, as a function of solvent content is shown in Figure 5.7. The selectivity to α-terpineol was not determined because it can be obtained either from limonene, α-pinene or β-pinene [165]. Conversion decreases in the order β-pinene > limonene >> α-pinene, and high selectivity to nopol is observed. The high conversion of limonene and α-pinene (in the reaction without solvent) and the presence of α-terpineol in the reaction product (confirmed by GS-MS) indicate that a side-reaction of oxyfunctionalization (i.e., hydration) of limonene and/or α-pinene is occurring, which has been reported previously [165],[166]. Moreover, considering that the aim of this study is to obtain oxygenated molecules from terpenes, the presence of α-terpineol in the reaction mixture is desirable.

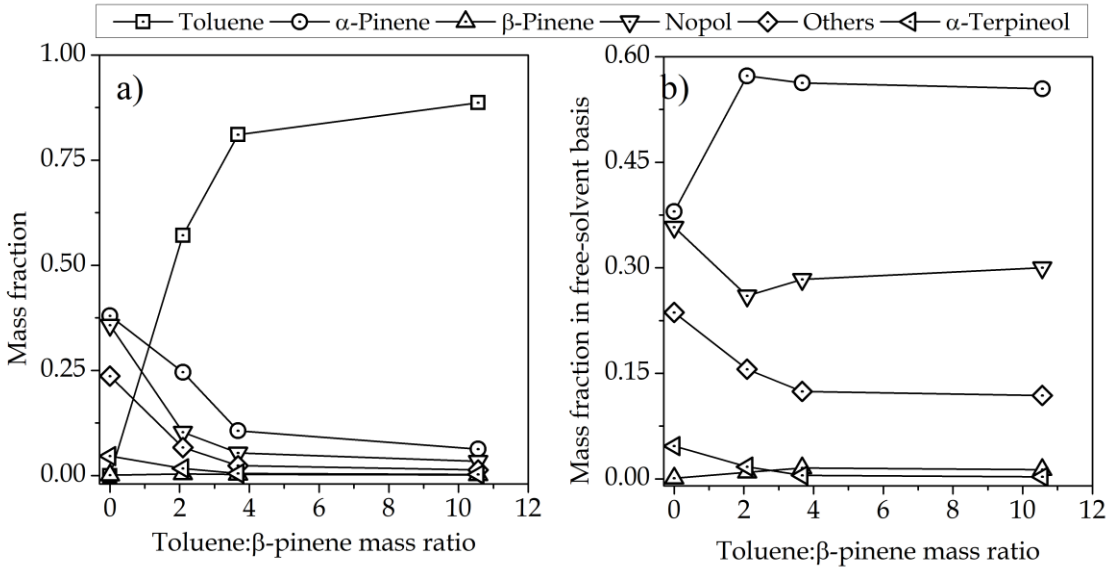

Figure 5.6. Effect of solvent on species concentration after reaction. a) Total species concentration, and b) species concentration in free-solvent basis. Reaction time = 15 h

A decrease in selectivity towards nopol is observed as the toluene : β-pinene mass ratio is decreased. Particularly, the lowest selectivity is observed at a ratio of 2, probably due to a change in the roles of toluene and α-pinene as solvents. Studies of the solvent effect on the reaction of pure β-pinene and paraformaldehyde over Sn-MCM-41 showed that both solvent polarity and solubility with paraformaldehyde are important in nopol synthesis [180]. In particular, the nature of the solvent and the Hansen solubility parameter (HSP) would indicate the adequacy of a solvent for the *Prins* condensation of nopol. For instance, toluene and ethyl acetate showed high

activity, and both are aprotic with an HSP parameter around 18 $MPa^{0.5}$. However, in the case of the reaction of turpentine in the absence of solvent, it is expected that α-pinene, as the main component of the mixture, performs the role of solvent. In fact, α-pinene is non-polar and aprotic, with an HSP parameter around 17 $MPa^{0.5}$, similar to toluene and ethyl acetate. Furthermore, nopol formation in the oxyfunctionalization of turpentine is favored in the absence of solvent, suggesting that the presence of toluene simultaneously with α-pinene decreases the probability of activation of β-pinene, perhaps due to the adsorption of toluene onto the active sites of the catalyst. Thus, the high performance of the reaction can be attributed to the presence of α-pinene to promote the activation of β-pinene and to maintain the catalyst activity.

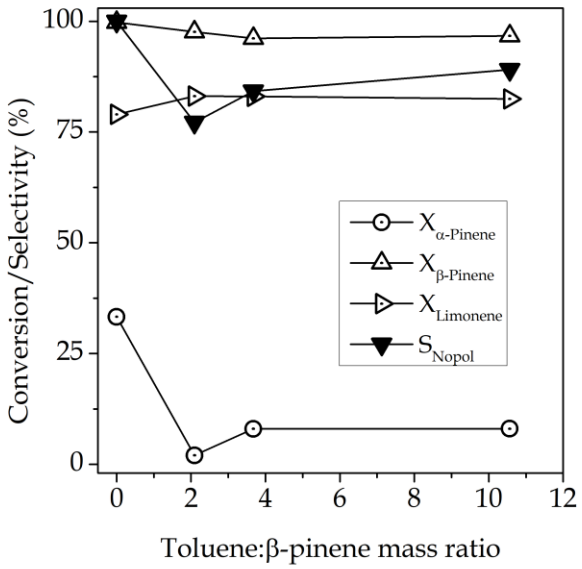

Figure 5.7. Performance of the reaction as a function of solvent content at 15 h reaction time (calculated in free-solvent basis)

5.3.3.4 Effect of reaction time

Figure 5.8 shows the effect of the reaction time on the performance of the reaction of turpentine with paraformaldehyde over Sn-MCM-41 without external solvent. β-Pinene from turpentine is consumed as the time is increased, with a conversion around 60% at 0.5 h reaction time, until almost complete consumption at 24 h. The α-pinene conversion trend reaches a maximum (around 30 %) at 15 h, indicating that, with enough time, α-pinene can react at the reaction conditions to produce

molecules such as α-terpineol, α-longipinene and/or α-phellandrene. The conversion of limonene is almost constant with time, suggesting that the reaction conditions and medium are suitable for its transformation, probably to α-terpineol, due to the presence of water.

β-Pinene can be considered more reactive than α-pinene because of its carbon-carbon double bond located outside the main ring (instead of inside the main ring, as α-pinene). Consequently, at low reaction time the conversion of β-pinene is considerably higher than that for α-pinene, because β-pinene reaches more easily the active sites of the catalyst. At high reaction times, when β-pinene is transformed almost completely, more active sites are available, allowing for α-pinene activation and reaction.

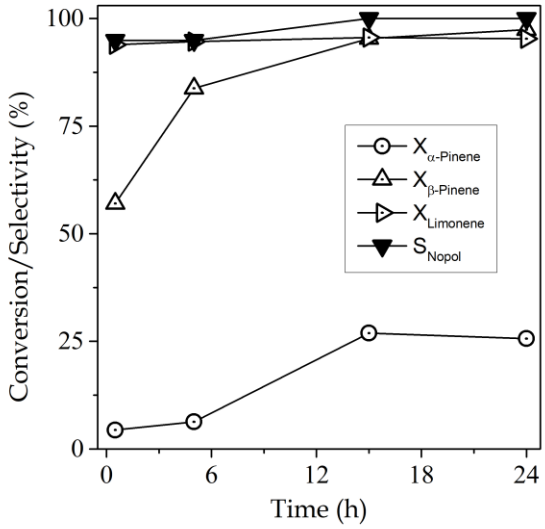

Figure 5.8. Performance of the reaction without solvent as a function of time.

Regarding the selectivity towards nopol, the reaction reaches the highest value at 15 h (>99%), indicating that somewhat the interaction between β-pinene and paraformaldehyde needs time “to build-up”. Probably, β-pinene is easily activated into the catalyst, favored by the high accessibility to the active sites due to the good textural properties of MCM-41 (i.e., high surface area and porosity, with enough pore diameter to β-pinene access), whereas the depolymerization of paraformaldehyde is not as fast. Therefore, at low reaction time the relatively low availability of formaldehyde would translate into β-pinene producing molecules other than nopol.

In any case, this effect can be considered low because the change in selectivity is just 5%.

5.3.3.5 Effect of reusability of the catalyst

The catalyst was subjected to two different post-reaction treatments before evaluating its activity in a new cycle, namely: washing with toluene and washing with ethyl acetate. Washing was performed after two consecutive reactions. The washing consists in stirring the catalyst sample at 1000 rpm at room temperature during 30 min, with a mass ratio of catalyst : washing agent (toluene or ethyl acetate) of 1 : 10. Then, the catalyst is filtered and dried and the washing procedure is repeated three times with each solvent. Finally, the catalyst is dried overnight at 100°C.

Figure 5.9 compares the β-pinene conversion and nopol selectivity of the fresh catalyst, and those of the used catalyst washed with: the used catalyst washed with toluene or ethyl acetate after the first reaction cycle (Tol or Eac, respectively), and the used catalyst washed after two consecutive reaction cycles with toluene or ethyl acetate (Tol+Tol or Eac+Eac, respectively). The same reaction conditions were maintained (vial scale, 1000 rpm, 90°C, 24 h, catalyst loaded at 20 wt.% with respect to β-pinene, and molar ratio of paraformaldehyde : β-pinene = 1 : 1) in all tests.

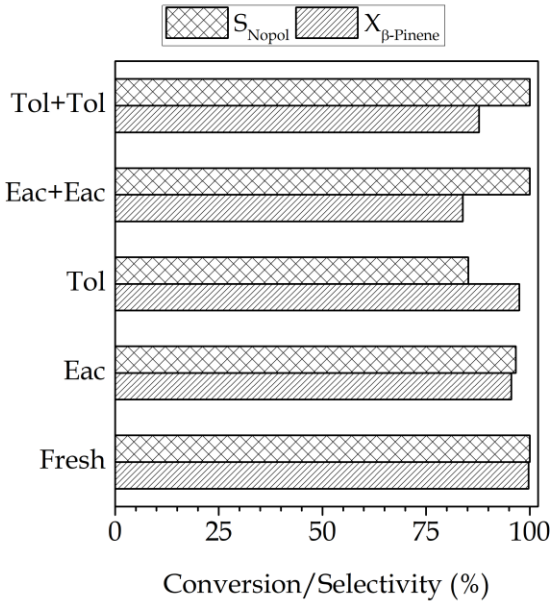

Figure 5.9. Catalysts stability by different aftertreatments. Reaction conditions: vial scale, 1000 rpm, 90°C, 24 h, catalyst loaded at 20% wt. with respect to β-pinene, and equimolar ratio of paraformaldehyde : β-pinene

A small decrease in conversion (1%) and a significant reduction in selectivity (16 %) was observed after washing the catalyst with toluene. Washing with ethyl acetate has a lower effect on selectivity (reduced by 5%) and a moderate effect on conversion (reduced by 2%). Thus, ethyl acetate appears to be a better medium for the washing procedure, perhaps because toluene can affect the catalytic properties of the solid by dissolving some species on the catalyst which can be important in the reaction (for instance, ions and impurities), as a consequence of its low polarity and the conditions of the washing procedure.

On the other hand, an increase in selectivity is observed after the second reaction cycle when the catalyst is washed with either toluene or ethyl acetate, but the conversion decreased. Since turpentine is a complex mixture, the probability of adsorption of some molecules in the catalyst is high, suggesting that the loss of activity can be associated with poisoning of the catalyst, leading to changes in conversion and selectivity after the second consecutive reaction cycle as a consequence. Precisely, FTIR spectra for Sn-MCM-41 sample after five cycles of reaction without solvent was compared with that for the fresh sample, Figure 5.10.

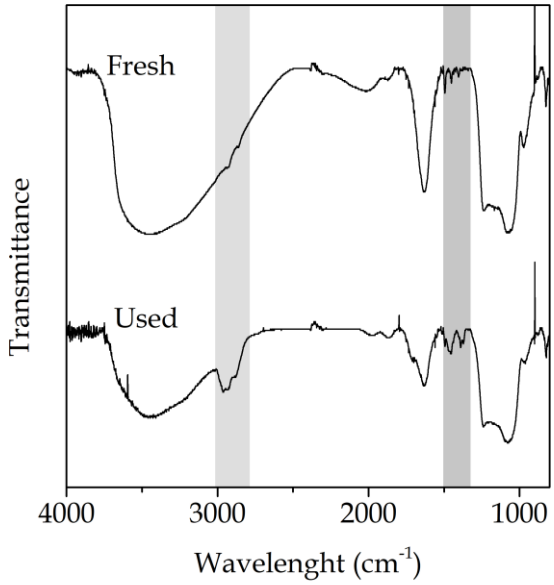

Figure 5.10. FTIR spectra for fresh and after reaction Sn-MCM-41 catalyst

For the used catalyst, the peaks between 1350 and 1500 cm^{-1} can be assigned to sp^3 C—H bending, while those present between 2600-3100 cm^{-1} are asigned to sp^3

C—H stretching vibrations [129], indicating that the adsorbed molecules onto the catalyst surface are aliphatic hydrocarbons from turpentine.

5.3.4 Remarks of the section

- ★ Sn-MCM-41 was synthesized and evaluated in the *Prins* condensation reaction of β-pinene-rich turpentine and paraformaldehyde, leading the formation of oxyturpentine (a nopol-rich mixture). The reaction was performed without any added solvent, the α-pinene present in the turpentine probably performing this role, because of its aprotic nature and solubility. These properties are very similar to toluene and ethyl acetate, which have displayed good performance as solvents in the production of nopol from pure β-pinene.
- ★ Complete conversion and selectivity towards nopol >99 % were observed in the transformation of β-pinene from turpentine. In addition, a significant amount of α-terpineol was obtained in the reaction product, probably due to the hydration of limonene and/or α-pinene. Nopol and α-terpineol are desirable products because the main objective of the transformation of turpentine is to oxyfunctionalize the terpene molecules, and it is expected that these molecules positively influence the combustion of diesel fuel, particularly reducing particulate matter emissions.
- ★ A reduction in conversion, simultaneously with an increase in selectivity towards nopol, was observed in three consecutive reaction cycles. The decrease in conversion can be attributed to a poisoning of catalyst.
- ★ The presence of nopol and α-terpineol in oxyturpentine makes this mixture a promising biofuel because of the well-known positive influence of oxygenated molecules on the diesel engine emissions, particularly on particulate matter. In addition, some fuel properties are expected to be improved such as lubricity and flash point, which are related to engine durability and fuel safety, respectively. However, further analysis of the main fuel properties of oxyturpentine is necessary to confirm its actual potential for fuel applications.

5.4 Laminar flames of blends of oxyturpentine + *n*-heptane

5.4.1 Methodology

Measurement of CO, CO_2, NOx and UHC emissions, and temperature and flame size were carried out according to the methodology detailed in Section 3.3.2. The laminar flames were obtained by burning blends of *n*-heptane with turpentine / oxyturpentine at 0.1, 1 and 5 vol.%; the oxyturpentine obtained in Section 5.3 was used without any purification, and the turpentine was the same than the feed of the oxyfunctionalization reaction. Results for blends of *n*-heptane with nopol are included as comparison.

5.4.2 Results and discussion

5.4.2.1 Temperature of flame

Measured temperature of the flames ranges between 1000 and 1100 K, and the temperature correction of losses is around 150-200 K. An equivalence ratio higher than the stoichiometric one, as well as the position of the thermocouple (ca. 20% with respect to the height of flame, see Table 5.5) would explain these rather low temperatures, as discussed in the previous chapters. The actual HAB of thermocouple of the flames are presented in Table 5.5; in all cases, the thermocouple was located close to the 20% target, i.e., within 1%.

Table 5.5. HAB of thermocouple for flames with different contents of turpentine and oxyturpentine

Turpentine/ oxyturpentine content (% vol.)		Flame HAB (mm)	Thermocouple	
			HAB (mm)	Relative position (%)
Turpentine	5	55.17	10.59	19.20 +/- 0.64
	1	49.92	9.75	19.53 +/- 0.86
	0.1	49.32	9.88	20.03 +/- 0.70
Oxyturpentine	5	58.39	10.89	18.65 +/- 0.91
	1	57.34	11.17	19.48 +/- 0.97
	0.1	54.36	10.44	19.21 +/- 0.97

The temperature of the flames of *n*-heptane + oxyturpentine / turpentine, and *n*-heptane + nopol blends are shown in Figure 5.11. The higher the content of turpentine and oxyturpentine the higher the temperature of flame. The profile of flame temperature for oxyturpentine is lower than that for nopol but higher than that

for turpentine. The presence of nopol in the oxyturpentine mixture apparently translates into a slight increase in the flame temperature (with respect to the turpentine blends), as observed with nopol and, α- and β-pinene in Section 4.2.3.1.

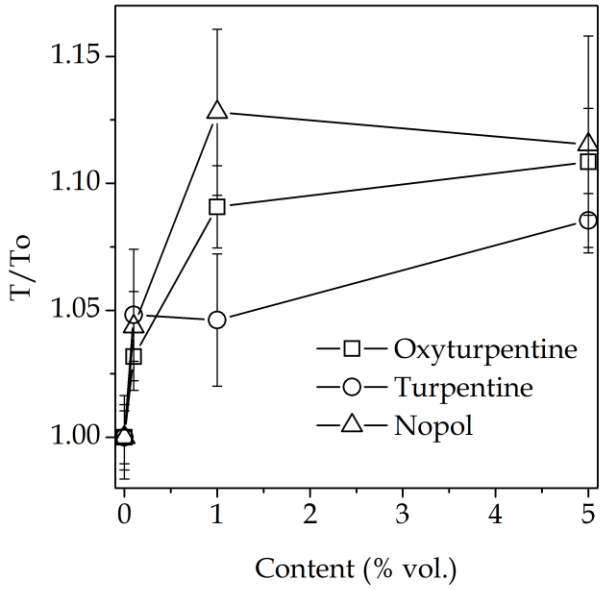

Figure 5.11. Influence of oxyturpentine, turpentine and nopol content on the temperature of flame

5.4.2.2 NOx emissions

Negligible effect on the emission index of NOx can be observed for turpentine, whereas nopol and oxyturpentine increase these emissions, see Figure 5.12. Such nil effect of turpentine was observed in the NOx emissions from the *n*-heptane + α- and β-pinene blends (see Figure 4.9). On the other hand, the increase in NOx emissions in the oxyturpentine and nopol blends can be mainly ascribed to the increase in flame temperature resulting from the presence of oxygen in the fuel. Although other factors such as the degree of unsaturation may impact NOx emission, in this case the main difference among turpentine, and nopol and oxyturpentine is the presence of oxygen in the latter molecules.

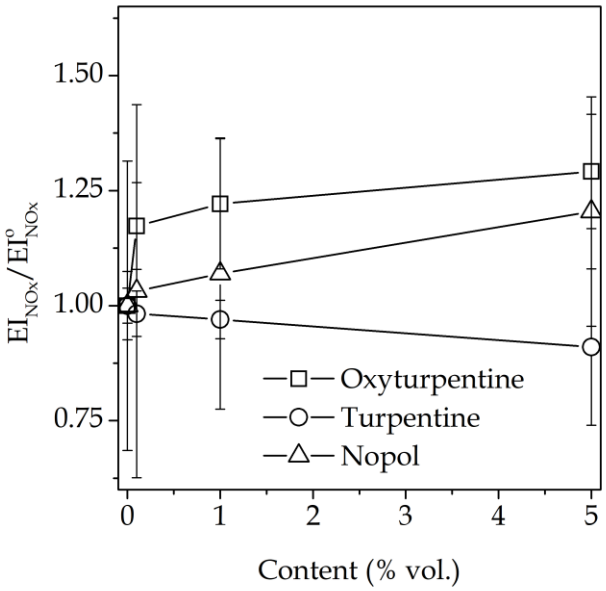

Figure 5.12. Influence of oxyturpentine, turpentine and nopol content on NOx emissions

5.4.2.3 CO and UHC emissions

The influence of oxyturpentine and turpentine in the fuel on CO emissions is shown in Figure 5.13.

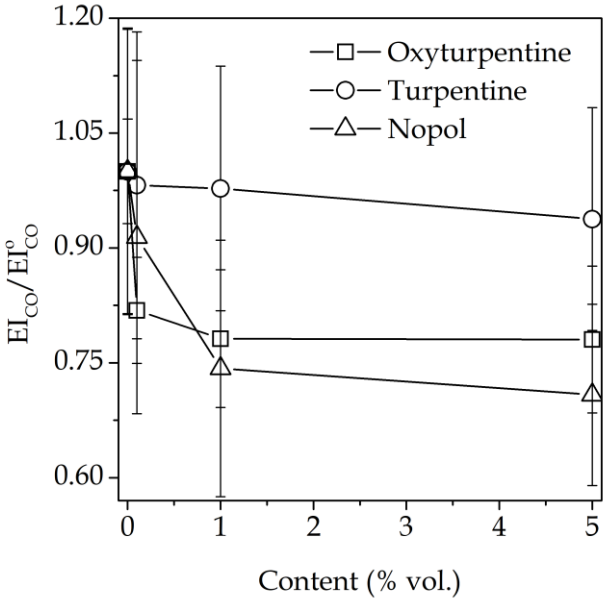

Figure 5.13. Influence of oxyturpentine, turpentine and nopol content on CO emissions

Similarly to nopol, oxyturpentine decreases the emission index of CO, indicating an improvement in the combustion by the presence of oxyturpentine as a consequence

of the oxygen content, particularly in the oxidation reactions. On the other hand, a slight decrease in CO emissions with turpentine content is observed, indicates that the trade-off between α- and β-pinene (β-pinene decreases and α -pinene increases CO emissions, see Figure 4.10) favors the latter, confirming the predominant role of β-pinene in the combustion. The content of nopol significantly improves the performance of oxyturpentine in the combustion, particularly in the reduction of CO emissions, because the oxygen atoms in the fuel allow more useful energy to be extracted from the fuel.

A strong effect of oxygen content and UHC emissions in coflow-diffusion flames is observed in Figure 5.14. Indeed, negligible effect is observed for flames with turpentine, which can be attributed to the high reactivity of β-pinene in turpentine (i.e., the same behavior was obtained with pure β-pinene, see Figure 4.11). On the other hand, the minor UHC emissions in the nopol blends with respect to oxyturpentine would be a consequence of its higher oxygen content. Thus, it can be argued that the carbon atoms surrounding oxygen atoms have a higher tendency to form directly CO_2 [160].

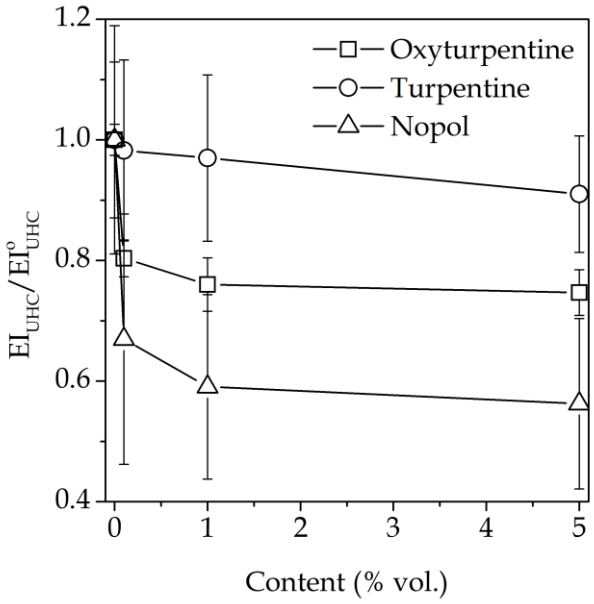

Figure 5.14. Influence of oxyturpentine, turpentine and nopol content on UHC emissions

5.4.2.4 Flame size

The relationship between the ratio of the height of flame of *n*-heptane + turpentine / oxyturpentine blends to that for pure *n*-heptane (H_o) is presented in Figure 5.15; both experimental results and estimation with Roper expression are presented.

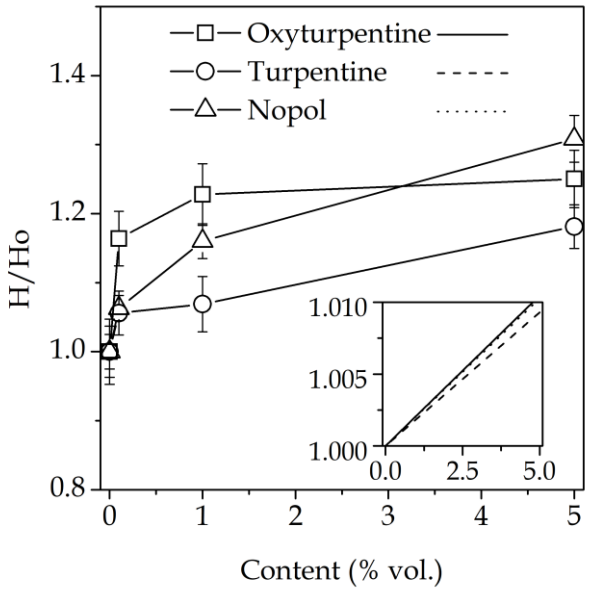

Figure 5.15. Influence of oxyturpentine, turpentine and nopol content on flame height

The height of flame increases with the content of oxyturpentine and turpentine for both experimental and estimated values, even for nopol. The increment of terpene content in the fuel increases the stoichiometric ratio and reduces the volumetric flow and the H/C molar ratio of the fuel, contributing to increase the height of the flame. The largest influence is observed for nopol, followed by oxyturpentine and turpentine (the same trend as the volumetric flow and the H/C molar ratio of the fuels).

5.4.2.5 Overall emissions

The performance of oxyturpentine as component of the fuel is similar to that of nopol and better than that of turpentine, as expected from the results of α- and β-pinene and nopol observed in Section 4.2.3. Figure 5.16 shows the effect on characteristics and emission of flames of oxyturpentine, turpentine and nopol blended separately at 5 %vol. with *n*-heptane.

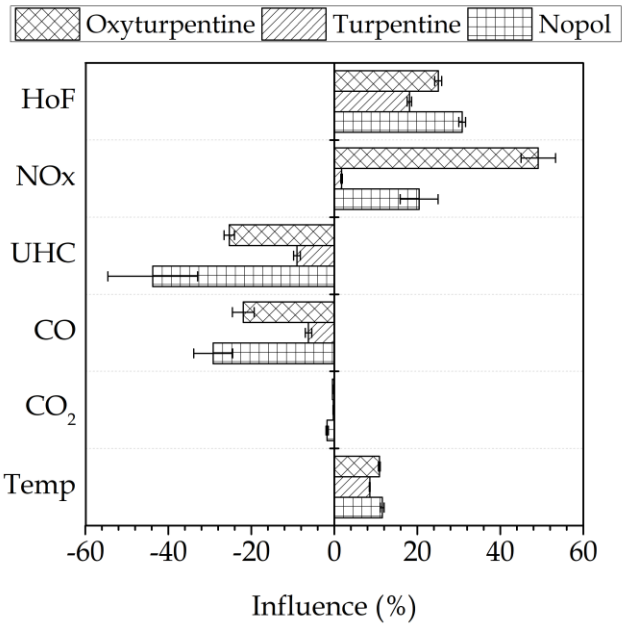

Figure 5.16. Influence of oxyturpentine and turpentine compared to nopol (5 vol.% blends) on flame size and temperature, and emissions (HoF height of flame)

Nil effect on carbon dioxide emissions is display for all fuels. The flame temperature is increased around 10 % with respect to pure *n*-heptane when the fuel was blended with nopol and oxyturpentine, and 8 % with turpentine. The increase in the temperature of the flame and the decrease in CO and UHC emissions are lower for oxyturpentine than nopol due to the presence of other compounds such as α-pinene (i.e., the decrease in CO emissions with nopol at 5 vol.% in *n*-heptane was ~30 %, whereas for oxyturpentine was ~20 % at the same conditions). In addition, NOx emission in flames with nopol in the fuel is increased by 50 % with respect to pure *n*-heptane, whereas that increase for flames with oxyturpentine is 25 %. However, as NOx concentrations measured from laminar flames were low (up to 20 ppm) a small change in concentration may result in a rather large percentage of change. Additionally, the performance of the combustion in the actual chamber may differ from that in the laminar flames, especially regarding the behavior of local temperature, as discussed below. At the same time, α- and β-pinene display a positive effect, such as higher adiabatic flame temperatures and LHV than nopol.

5.4.3 Remarks of the section

The effects observed on temperature, and CO, NOx and UHC emission lead to conclude that the molecular structure and oxygen content of fuel can enhance the

performance of combustion reaction. Nevertheless, the experimental setup used for the evaluation does not account the assessment of other fuel properties. For instance, the previous evaporation of the sample overcome typical drawbacks of the fuel atomization such as that due to high surface tension and viscosity of the fuel. According to the results, oxyturpentine has high performance in combustion, which suggests a high potential to be used as additive/component of diesel fuel.

5.5 Conclusions

- ★ The thermochemical properties of oxyturpentine can be considered suitable for diesel fuel applications. For instance, LHV of oxyturpentine is slightly lower and its adiabatic flame temperature is significantly higher than those for diesel fuel. The presence of α-pinene in the oxyturpentine mixture is positive because of its high heating value respect to nopol, increasing the amount of heat released in the combustion of the oxyturpentine mixture.
- ★ Oxyfunctionalization of turpentine to produce oxyturpentine showed good performance (complete conversion and selectivity towards nopol >99 %), becoming it in a promising procedure to obtain an oxygenated biofuel from turpentine. In addition, significant amount of α-terpineol was obtained in the reaction product, probably formed by the hydration of limonene and/or α-pinene. Nopol and α-terpineol are desirable products because the main objective of the transformation of turpentine is to oxyfunctionalize the terpene molecules.
- ★ The effects observed on temperature and CO, NOx and UHC emission lead to conclude that oxyturpentine improves the performance of combustion reaction at the evaluated conditions. This can be associated to the content of oxygen in the molecular structure of nopol, together with the relatively high LHV of α-pinene. Although the experimental setup used does not allow determining the effect on other physical and thermal properties, such as viscosity, density and melting and boiling points, oxyturpentine presents high potential to be used as additive/component of diesel fuel in terms of combustion reaction.

This page intentionally left blank

Chapter 6. Engine-bench tests of oxyturpentine as biofuel

This chapter presents an approximation to the properties and performance of oxyturpentine in actual fuel applications. The oxyfunctionalization reaction was scaled-up to study the effect of the change in reaction size and geometry as well as to obtain enough quantity of oxyturpentine to perform engine-bench tests. Then, the oxyturpentine was blended separately with diesel and biodiesel fuels at different volume ratios to measure several fuel properties, which are compared with fuel standards. Finally, an oxyturpentine-diesel volume ratio was selected according to its properties and the blend was prepared to carry out the engine tests. In these tests, the behavior of the fuel was evaluated through the diagnostics of the performance and emissions of an internal combustion engine.

6.1 Scaling-up of turpentine oxyfunctionalization

6.1.1 Background

The main objectives of scaling the reaction to produce oxyturpentine are to determine criteria to transfer from small to large scales, and obtain large amounts of the reaction product. Although the target for the large-scale reactor in the present work would be limited to laboratory or pilot-plant scale where the typical size of batch reactor is below 20 L [15], further scaling is reviewed to encourage future works on the evaluation of technical and economical feasibility of an industrial plant to produce the proposed fuel and to evaluate the theoretical criteria to scaling a batch reactor with actual data. The use of advanced techniques or further experiments starting from the results presented in this Thesis would conduce to obtain optimal parameters for the reaction at large scale.

Detailed information on the oxyfunctionalization of turpentine is presented in Chapter 5. The reaction conditions are summarized in Table 6.1. In addition, rounded bottom flask reactors (Pyrex-glass) in the range 50 - 10000 mL were used to perform the

scaling-up (please note that the synthesis in Chapter 5 was conducted in 2 mL size vials). Furthermore, the scaling was based on the characteristic dimensions of the spherical geometry (see Appendix A).

Table 6.1. Conditions for turpentine oxyfunctionalization

Reaction temperature (K)	363
Reaction time (h)	24
Stirring speed (rpm)	1000
Weight ratio of catalyst*	0.078
Reagents molar ratio	1 : 1

*With respect to turpentine

The dimensions of the spherical reactors selected for the scaling procedure are shown in Table 6.2. The geometrical factor (i.e., the ratio of diameters) for the scaling-up procedure from small to large scale is 5.25 [183].

Table 6.2. Properties of batch reactors for both small and large scales

	Small scale	**Medium scale***	**Large scale**
Capacity (mL)	50	250	10000
Inner diameter (mm)	51	81	269.8
Wall thickness (mm)	2	2	5

* Presented for comparison purposes

The volume of the reaction mixture in the small scale tests was 23.5 mL. Thence, the height of reaction mixture (from the bottom of the reactor to the vapor-liquid interface) is 1.98 cm, corresponding to an aspect ratio of 0.39; the surface area available to heat transfer at this scale is 31.94 cm^2. The volume of reaction mixture in the large scale is 3400 mL, corresponding to a height of fluid of 10.39 cm and maintaining the aspect ratio; the surface area available for heat transfer at this scale is 880.58 cm^2. The surface and volume scale factors for the small and large scale geometries shown in Table 6.2 are 27.57 and 144.73, respectively.

The reaction time necessary to obtain complete conversion of β-pinene in small scale was 24 h. As the residence time must be equal for both scales of batch reactors, the reaction time at large scale should be also 24 h. At the optimum reaction conditions of *Prins* reaction (pure β-pinene and toluene as solvent) at the small scale reaction, the estimation of the minimum stirring speed to ensure dispersion of the catalyst was 950 rpm, while 1000 rpm was obtained to be adequate in the reaction

with turpentine as β-pinene source and without solvent. Thence, agitation at 1000 rpm is a suitable value at this scale. Besides, this agitation regime avoids external mass transfer limitations [177], [179].

Depending on the goal of the mixing (e.g., equal liquid motion, equal suspension of solids, equal and uniform concentration, or equal rates of mass transfer for both scales, see Appendix A), several criteria can be found in the literature to determine the required agitation speed at a larger scale. Table 6.3 summarizes the results for the different criteria, evaluated for the large scale used in this work with the expressions presented in Appendix A.

Table 6.3. Scale-up values of speed of agitation

Parameters		**Agitator speed (rpm)**	
ρ_p Sn/MCM-41 (kg/m^3)	970[a]	Equal liquid motion	190
$\bar{d}_P$ Sn/MCM-41 (μm)	38-42[b]	Equal and uniform concentration	288
W_P Sn/MCM-41 (%)	7.8	Equal mass transfer	661
ρ_L Turpentine (kg/m^3)	862.1[c]	Equal heat transfer	331
ρ_L Oxyturpentine (kg/m3)	912.6[c]	Equal suspension of solids	466
υ_L Turpentine (mm^2/s)	1.7.E-06[c]	Minimum to suspension of solids[d]	366
υ_L Oxyturpentine (mm^2/s)	3.5.E-06[c]	Minimum to suspension of solids[e]	393
		Equal shaft speed	1000

[a]From [184]; [b]upper value from [177] was used for calculations in this work; [c]measured in this work; [d]computed with properties of turpentine; [e]computed with properties of oxyturpentine.

According to Table 6.3, the recommended speed of agitation at the large scale is lower than that for small scale (except for the equal shaft speed criterion), as a consequence of the increase in the agitator diameter. The speed of agitation to keep uniform concentration of liquid and equal heat transfer in the reaction mixture is less relevant because these values are lower than the minimum speed necessary to keep the catalyst suspended.

The higher the speed of agitation the lower the propensity to observe mass transfer limitation in batch reactors. If the lab scale is maintained in the reactor at 10 L and other criterium than the equal speed of shaft (the highest speed of agitation in Table 6.3) is used, the probability to get mass transfer limitations is high. In addition, the reaction at 10 L consumes high amounts of materials, where the production of the

catalyst plays an important role. Thus, the selection of the highest speed of agitation involves higher probability to successfully carry out the reaction just once.

With the criterion of equal shaft speed, the heat transfer may differ for both scales. An electrical heating mantle was used in this work. Thus, the heat is transferred by conduction to the outer wall of the reactor. Furthermore, the high thermal conductivity of the pyrex with respect to the reaction medium indicates that the controlling step in the overall heat transfer is the convection inside the reactor. Thence, the convective heat transfer coefficient was calculated for both scales at initial (i.e., turpentine mixture) and final (i.e., oxyturpentine) conditions. The overall and inside heat transfer coefficients are presented in Table 6.4 for both large and small scales.

Table 6.4. Heat transfer coefficient for small and large scales to produce oxyturpentine

Parameters		**Heat transfer parameters**		**Small**	**Large**
C_p (J/kgK)	1654.7[a]	Turpentine	h_i (W/m^{2}K)	209.2	364.8
k_{Pyrex} (W/mK)	1.3[b]		U (W/m^{2}K)	158.3	151.8
$k_{Turp.}$ (W/mK)	0.128[c]	Oxyturpentine	h_i (W/m^{2}K)	172.5	299.9
$k_{OxyT..}$ (W/mK)	0.1706[d]		U (W/m^{2}K)	136.3	139.3

[a]Estimated for turpentine with Joback method (see Section 2.1.3); [b]from [185]; [c]from [186]; [d]estimated with the correlation of Gharagheizi *et al* (see Appendix A).

Convective heat transfer coefficients are different in turpentine and oxyturpentine. In particular, the lower value for the oxyturpentine translates into a higher resistance to heat transfer as the reaction progresses. However, the effect would be similar at both scales because of the similar ratio of the “initial” and “final” heat transfer coefficients at both scales, that is, 209.2/172.5 ≈ 364.5/299.9.

Finally, assuming the same driving force for both scales and considering turpentine’s properties, the ratio of heat flow for both scales is,

$$\frac{Q_2}{Q_1} = \left(\frac{U_2}{U_1}\right)\left(\frac{A_2}{A_1}\right) = (0.9589)(27.57) = 23.44$$

Thence, the heat flow at large scale must be around 23 times that of the small scale to ensure similar temperatures in the reaction medium at both scales.

6.1.2 Experimental

Four different scales were tested to evaluate the effect of scaling-up, namely, mili scale (or vial-scale, 2 mL reactor), small scale (50 mL reactor), medium scale (250 mL reactor), and large scale (10 L reactor), after one, two and three consecutive cycles of reaction; washing with ethyl acetate was performed in between the cycles (see Chapter 5). The same catalyst and reaction conditions were maintained for each scale and each reaction cycle. The major difference between the scales was that the reaction at vial scale was conducted at autogenous pressure whereas the reaction occurred at ambient pressure (under reflux) at the other scales.

Catalyst synthesis was also scaled. The synthesis gel procedure at room temperature and 1500 mL was followed (as detailed in Section 5.3.2.3); several batches were necessary to obtain around 400 g of catalyst prior to the calcination. The reproducibility of the synthesis was evaluated by testing a sample from each batch in the oxyfunctionalization of turpentine; similar compositions for the reaction products were obtained in all cases, indicating that the catalysts synthesized in each batch display similar characteristics.

The composition of oxyturpentine obtained by GC analysis (see Section 5.3.2.2) of the mixture of the reaction product at large-scale (the addition of reaction products from each of the three consecutive cycles) is shown in Table 6.5 (the oxyturpentine for properties measurement and engine tests); this oxyturpentine was used for measuring fuel properties and in engine tests.

Table 6.5. Oxyturpentine composition

Compound	(% wt.)	Compound	(% wt.)
α-Pinene	47.1	Isoborneol	0.7
Nopol	31.7	Limonene	0.6
α-Terpineol	4.7	m-Cymene	0.5
β-Pinene	4.2	Longifolene	0.1
Δ3-Carene	3.7	(+)-Fenchone	0.1
α-Phellandrene	1.9	Terpinolene	0.1
β-Myrcene	1.8	Borneol	0.1
Camphene	1.6	Unidentified	0.9
α-Longipinene	1.2		

The main differences in the oxyturpentine synthesized at large scale (see Table 6.5) and vial scale (see Table 5.4) oxyfunctionalized turpentine are the content of unreacted β-pinene (lower conversion was obtained at large-scale), and the content of α-pinene (apparently, α-pinene reacts under vial-scale conditions, as suggested by its lower content simultaneously with higher α-longipinene content at that scale); these rather small differences can be attributed to the reaction pressure.

The performance of the reaction at different scales is shown in Figure 6.1. The higher the number of reaction cycles the lower the conversion of β-pinene at all scales (see Figure 6.1a), probably due to the poisoning of the catalyst which would not be completely addressed in the aftertreatment. However, the selectivity increases with the number of reaction cycles (see Figure 6.1b). In fact, some important properties in the catalyst, such as the availability of active sites and the presence of impurities, may change for the repetitive reactions, affecting the reaction performance. Furthermore, it is not uncommon that a decrease in selectivity may be observed at high conversion, and vice versa, which can explain the increase in selectivity.

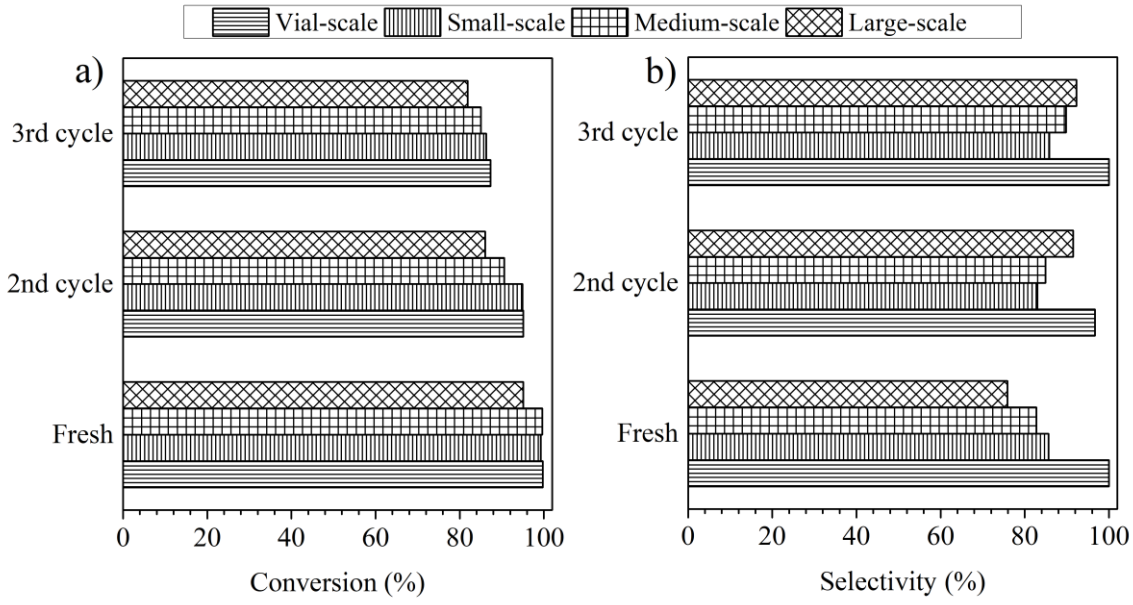

Figure 6.1. Effect of scaling-up on oxyfunctionalization of turpentine

The deterioration of the reaction performance was most severe at large scale, followed by medium and small scales. Obviously, parameters of the reaction at vial-scale (even for small-scale) are easier to control, and other effects, such as mixing

zones and mass transfer (due to the difference in the mixing regime), become more important as the scale is increased. This is likely the reason for the different trends observed for conversion and selectivity at different scales: an inversely proportional effect is evidenced for conversion, while no relation between selectivity and scale was observed.

6.1.3 Remarks of the section

The oxyfunctionalization reaction of turpentine was performed at the same conditions for different scales. The higher the scale the (slightly) lower the formation of nopol, that is, selectivity and conversion were decreased in comparison to the vial scale. Probably, differences in mixing and mass transfer aroused among scales. For instance, the criterium selected for the agitation speed at higher scales was the shaft speed, which was significantly higher than those for equal mass or heat transfer.

6.2 Fuel properties of the oxyturpentine

6.2.1 Methodology

Diesel without any oxygenated molecule, known as “first fill diesel”, was supplied by Repsol (Spain) and biodiesel was supplied by BioOils Energy (Spain). Nopol, α- and β-pinene and terpineol (analytical grade) were purchased from Sigma-Aldrich (USA). Composition of turpentine is presented in Chapter 5, and oxyturpentine composition is shown in Table 6.5. The main fuel properties of these substances and the method used in the measurements are shown in Table 6.6.

Melting temperatures of pure terpenes and derived alcohols (and consequently, those of turpentine and oxyturpentine) were measured but not detected. In the case of differential scanning calorimetry analysis, no abrupt heat change was recorded (see below), whereas no crystals were recorded by the optical detectors of cloud and pour points. Therefore, crystal formation in these samples is very slow and/or their size is smaller than the threshold used to calibrate the equipment (i.e., higher hydrocarbons). The melting temperature of terpineol is out of the range of the equipment, whereas that of nopol has not been reported.

Turpentine and oxyturpentine were blended separately with diesel and biodiesel; in all cases the concentration was kept below 20 vol.% because it was expected that

some properties, such as the heating value and the cetane number, would notably deteriorate at higher contents of oxyturpentine. The main properties for diesel fuels (e.g., density, viscosity, lubricity, flash point, and derived-cetane number) were measured to get a better assessment of the potential of oxyturpentine as a fuel component.

Table 6.6. Specifications of fuels

Property	Units	EN Method	Diesel	Biodiesel	α-Pinene	β-Pinene	Terpineol	Nopol	Turpentine	Oxyturpentine
C*	-	-	15.2	18	10	10	10	11	10	10.4
H*	-	-	29.1	34.9	16	16	18	18	16	16.9
O*	-	-	0	2	0	0	1	1	0	0.5
MW[a]	g/mol	-	212	284	136	136	154	166	136	149
ρ[b]	kg/m^3	3675	829	880	858	868	940	971	862	913
ν[c]	cSt	3104	2.5	4.3	1.3	1.4	28.6	13.4	1.3	3.5
WSD[d]	µm	12156	443	170	242	758	394	248	484	302
LHV[e]	MJ/kg	51123	42.9	37.0	42.2	41.5	37.3	37.9	42.3	39.7
DCN[f]	-	16715	64.4	58.1	22.2	18.5	15.4	19.6	20.2	19.8
CP[g]	°C	3015	-22.7	7.0	ND	ND	ND	ND	ND	ND
PP[h]	°C	3016	-19.6	7.0	ND	ND	ND	ND	ND	-94.8
CFPP[i]	°C	6371[†]	-22.6	9.0	ND	ND	ND	ND	ND	-36.0
CrP[j]	°C	2386	-28.2	-49.6	ND	ND	ND	ND	ND	ND
FP[k]	°C	2719	79.5	130	31	36	88	98	34	37
VP[l]	kPa	3007	~0	1.4	0.5	2.1	~0	~0	1.7	2.7
SP[m]	mm	3014	22.3	>50	15.7	NM	ND	ND	8.9	33.4
WC[n]	ppm	10337	117	411	682	126	190	470	153	3429

*Atoms; [†]ASTM method; [a]molecular weight (rounded values for visualization); [b]density at 15°C and 45% RH; [c]kinematic viscosity at 40°C; [d]wear scar diameter for lubricity; [e]Lower Heating Value; [f]derived-cetane number; [g]cloud point; [h]pour point; [i]cold filter pluggin point; [j]crystallization point; [k]flash point; [l]vapor pressure; [m]smoke point; [n]water content; ND not detected; NM not measured

All measurements were performed by triplicate, and the values were used to obtain the average and standard deviation. The limits for density, viscosity, lubricity, flash point and derived-cetane number for European diesel fuels established in the standards EN 590:2013+A1 and EN 14214:2013 V2+A1:2018 (diesel and biodiesel fuels, respectively) were used to compare the properties of the blends.

6.2.1.1 Physical properties

Vapor pressure was measured according to standard EN 3007 in the Vapor Pressure Tester ERAVAP model EV01 of Eralytics.

Density was measured based on standard EN 3675, using a 10 mL glass pycnometer and a climate chamber Ineltec (used to set the temperature and relative humidity of the sample to 15°C and 45 %, respectively).

Viscosity of the blends was measured based on standard EN 3104 using a Froton Viscosimeter 150 series and a thermal bath Tamson Zoetermeer-Holland TV 2000 to keep the samples at 40°C during the test.

Wear scar diameter was measured to quantify the lubricity of the blends, based on standard EN 12156-1, using a High Frequency Reciprocating Rig (HFRR) from PCS Instruments, and a microscope Optika SRZ-1 coupled to Motical 2500 digital camera.

6.2.1.2 Thermal properties

Distillation curves were measured based on standard EN 3405 in the Automated Distillation Tester AD-7 from Tanaka. The initial and final heat, and, bath and receiver temperatures were optimized for each sample. Barometric pressure for all runs was 948.0 $\pm$ 1.0 hPa.

Differential Scanning Calorimetry (DSC) was used to determine the crystallization point in a TA Q20 equipment, according to standard EN 2386. Around 10 mg of sample was placed in a crucible of aluminum hermetically closed. Once temperature is stabilized at 40°C, the sample was cooled to -80°C at 5°C/min. Then, the sample was kept at this temperature during 5 min and returned to 40°C, recording the heat flux.

6.2.1.3 Combustion and thermochemical properties

Flash point was measured in a Pensky-Martens Closed Cup Tester SETA PM-93 model 35000-0, which is based on standard EN 2719.

The smoke point was measured in a standard Smoke Point Lamp according to standard ASTM D1322, with previous calibration in accordance to this standard. The

sooting tendency index relates the molecular weight and the smoke point with the propensity of the fuel to form soot. This concept was extended to oxygenated molecules (OESI) with the following expression [187],

$$OESI = a' \left(\frac{n + {}^{m}/_{4} - {}^{p}/_{2}}{SP} \right) + b' \qquad \textbf{Equation 6.1}$$

where *n*, *m* and *p* are the coefficients of the chemical formula of the fuel ($C_nH_mO_p$), *SP* is the smoke point, and ***a'*** and ***b'*** are parameters depending on the experimental setup (43.588 mm-1 and -5.7177, respectively, for diffusion flames [187]).

The combustion- and ignition-delay times (CD and ID, respectively) were measured in a Cetane Ignition Delay 510 from PAC Instruments, and the derived-cetane number (DCN) was determined according to standard EN 16715.

Higher heating value was measured according to standard method EN 51123 in a Parr 1351 calorimetric pump, while the lower heating was obtained by subtracting the heat of vaporization ($\Delta h_{\mathrm{v}}^{0}$) from the HHV. The heat of vaporization was determined from the principle of corresponding states and by using the Pitzer correlation, according to Equation 2.17 and Equation 2.18.

6.2.1.4 Cold flow properties

Cloud and pour point, based on standard tests methods EN 3015 and 3016, respectively, were measured in an Automated Cloud and Pour Point Analyzer CPP 5Gs from PAC Instruments. Cold Filter Plugging Point (CFPP) was measured in the FPP 5Gs analyzer from PAC Instruments, according to the standard ASTM D6371.

6.2.2 Results and discussion

6.2.2.1 Physical properties

Density profiles of blends of the oxyfunctionalized turpentine (oxyturpentine), with diesel and biodiesel, are shown separately in Figure 6.2. The density of oxyturpentine is higher than that for diesel and biodiesel, and is above the upper limits for both standards. Density of oxyturpentine + diesel blends at contents lower than 20 vol.% is between the limits of standard EN 590:2013+A1; however, it should be kept in mind that the diesel used in this work presents a relatively low density.

Blends of oxyturpentine and biodiesel up to 20 vol.% are between the limits of standard EN 14214:2013 V2+A1:2018.

The density of nopol, α-pinene, and terpineol (the main components of the reaction product), presented in Table 6.6, was measured with the same methodology. A blend of nopol, α-pinene and terpineol (its composition was obtained by normalizing the oxyturpentine composition in Table 6.5) presents a density of 920.9 kg/m^3, in agreement with the value of oxyturpentine (912.6 kg/m^3).

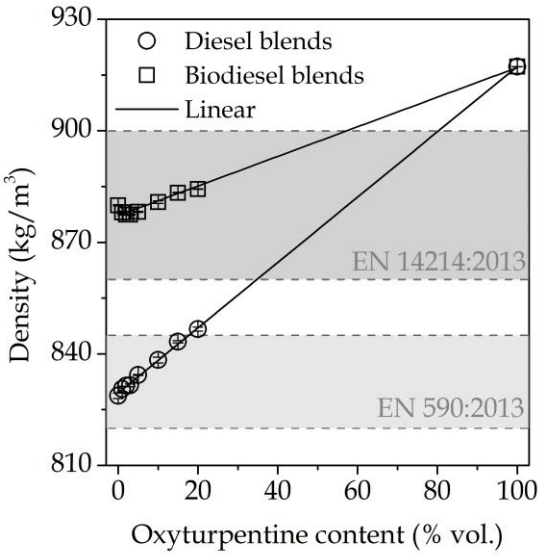

Figure 6.2. Density for blends of diesel and biodiesel with oxyturpentine

Density of blends was used to determine the specific volume (v), which is used to compute the partial volume for oxyfunctionalized turpentine ($\bar{v}_{\mathrm{ot}}$) and diesel or biodiesel ($\bar{v}_{\mathrm{d/b}}$) by considering each blend as binary solution (i.e., diesel-oxyfunctionalized turpentine, and biodiesel-oxyfunctionalized turpentine solutions), according to Equation 6.2,

$$\bar{v}_{\mathrm{ot}} = v + \left(1 - y_{\mathrm{ot}}\right)\frac{\mathrm{d}v}{\mathrm{d}y_{\mathrm{ot}}}$$

$$v_{\mathrm{d/b}} = v - y_{\mathrm{ot}}\frac{\mathrm{d}v}{\mathrm{d}y_{\mathrm{ot}}}$$

Equation 6.2

where y_{ot} represents the mass fraction of oxyfunctionalized turpentine. Although the concept of partial specific volume applies to single components, due to the intrinsic complexity of each blend we consider diesel and biodiesel as pseudo-components;

this is a common approach in evaluating properties of liquid fuels. Also, oxyturpentine is considered as a pseudo-component because of the similarity of its constituent molecules.

The relationship between density of blends of oxyturpentine + diesel and oxyturpentine appears to be linear, while that of blends with biodiesel clearly deviates from a linear behavior. Partial specific volumes for diesel-oxyturpentine, and biodiesel-oxyturpentine, determined according to Equation 6.2, are shown in Figure 6.3. Error bars represent the error obtained by propagation from the measurements.

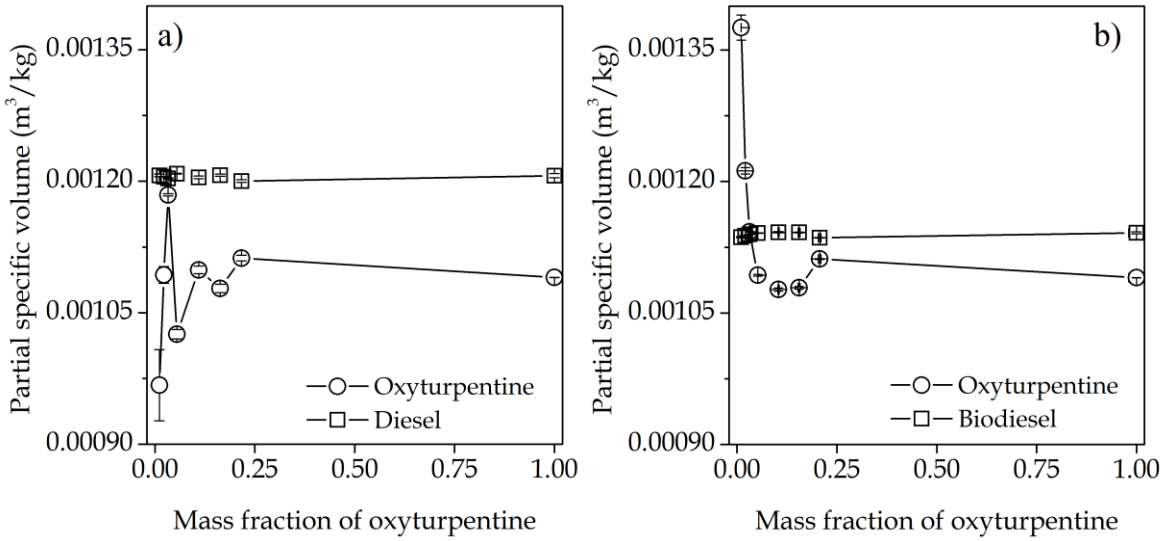

Figure 6.3. Specific volume of oxyfunctionalized turpentine blended with a) diesel and b) biodiesel

Oxyturpentine displays high interaction with both diesel and biodiesel. With diesel, the partial specific volume of oxyturpentine is lower than diesel one (see Figure 6.3a). The higher the oxyturpentine mass fraction, the higher the partial specific volume of oxyturpentine, while that for diesel is almost constant, indicating that the molecules of oxyturpentine interact with each other proportionally to its volume in the blend.

For blends with biodiesel, at low contents of oxyturpentine (up to 2 vol.%) the partial specific volume of oxyturpentine is higher than that of biodiesel, but at the other contents tested in present work the partial specific volume of oxyturpentine is lower than that for biodiesel (see Figure 6.3b), whereas the partial specific volume of

biodiesel is almost constant, similarly to diesel in blends of diesel-oxyturpentine. Thus, oxyturpentine molecules would be confined by biodiesel ones at oxyturpentine contents higher than 2% vol., occupying more volume under this limit.

Viscosity of blends of oxyturpentine with diesel and biodiesel is shown in Figure 6.4. The experimental values were used to obtain the interaction coefficient (G) of the Grunberg-Nissan correlation for kinematic viscosity of blends (υ), by means of Equation 6.3 [188],

$$\ln(\rho\upsilon) = x_1 \ln(\rho_1\upsilon_1) + x_2 \ln(\rho_2\upsilon_2) + x_1 x_2 G \qquad \textbf{Equation 6.3}$$

where x represents the molar fraction, ρ is the density of the blend, and subscripts 1 and 2 refer to the components of the binary blend.

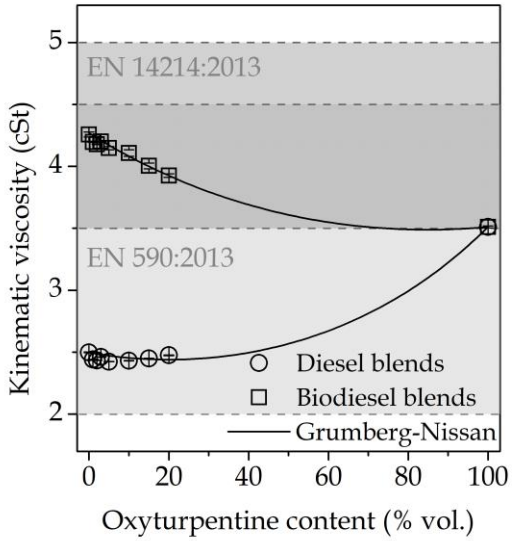

Figure 6.4. Viscosity for blends of diesel and biodiesel with oxyturpentine

Viscosity of oxyturpentine is higher than that of diesel but lower than that of biodiesel (see Figure 6.4). The viscosity of oxyturpentine is inside both standard limits for diesel and biodiesel (EN 590:2012+A1 and EN 14214:2013 V2+A1:2018, respectively), although in the comparison with the biodiesel standard its value is close to the lower limit. Experimental values of viscosity for blends of oxyturpentine with diesel are between the limits of the standard EN 590:2012+A1, whereas the corresponding values for blends of oxyturpentine and biodiesel are between the limits of the standard EN 14214:2013 V2+A1:2018.

Viscosities for nopol, α-pinene, and terpineol (see Table 6.6) do not follow a linear trend with the composition. Due to the presence of α-pinene, the viscosity of the oxyturpentine is low, even though nopol is in a high concentration and its viscosity is high. The high viscosity and density of nopol and terpineol limits their application as pure fuels.

The interaction coefficients of Grunberg-Nissan obtained for the blends of diesel and biodiesel with oxyturpentine were -0.604505 and -0.10006, respectively. The estimations of viscosity with this correlation are in good agreement with experimental data (see Figure 6.4).

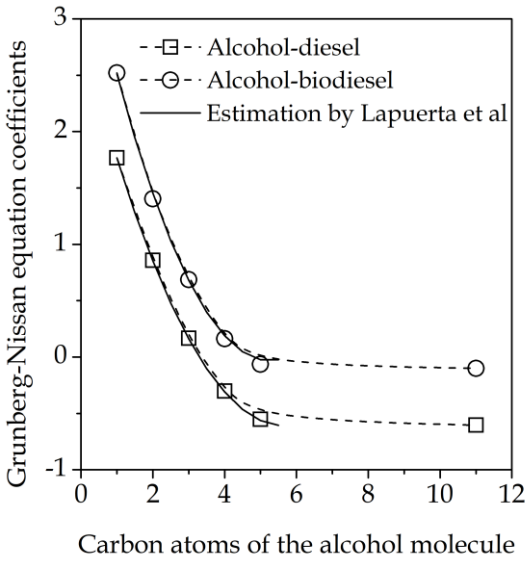

Figure 6.5. Interaction coefficients for Grunberg-Nissan correlation

Lapuerta and coworkers analyzed the interaction coefficients of the correlation of Grunberg-Nissan as a function of the number of carbon atoms in alcohols [189]. Although the oxyturpentine is not strictly an alcohol (it is a complex mixture where nopol is one of the main components), the values of interaction coefficients of the correlation of Grunberg-Nissan obtained from experimental viscosity for blends of diesel and biodiesel with oxyturpentine are projected into the results of blends of diesel and biodiesel with normal alcohols, as shown in Figure 6.5. Although the alcohols in oxyturpentine are not linear, and the other components in oxyturpentine can also interact with diesel and biodiesel, the result presented in Figure 6.5 seems

to indicate that the interaction between diesel and biodiesel with alcohol(s) from oxyturpentine follows a similar trend than with linear alcohols.

The results of the measurements of the wear scar diameter to evaluate the lubricity of the blends of diesel and biodiesel with oxyturpentine are presented in Figure 6.6; lubricity is a very important property for the performance and durability of the engine. All wear scar diameters measured in the present work for both diesel and biodiesel blended with oxyturpentine are lower than 460 µm, the limit established in the standard EN 590:2013+A1 for lubricity of diesel fuels. Oxyturpentine displays a wear scar diameter lower than that for diesel and higher than that for biodiesel. At low contents of oxyturpentine, the wear scar diameter of the blend is even lower than that for oxyturpentine for blends with diesel, indicating an interaction between oxyturpentine and diesel molecules for this property. Conversely, the wear scar diameter for biodiesel and oxyturpentine blends is proportional to the content of oxyturpentine.

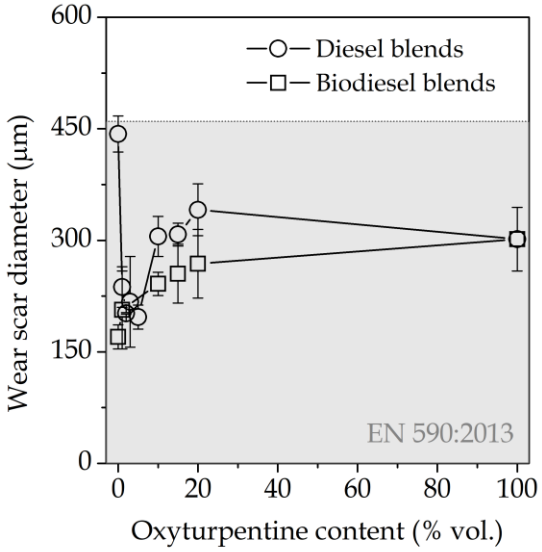

Figure 6.6. Lubricity for blends of diesel and biodiesel with oxyturpentine

Interestingly, the experimental value of lubricity of oxyturpentine is similar to that obtained for a mixture of nopol, α-pinene and terpineol (see Table 6.6). Thus, nopol and terpineol, which display good lubricity behavior, dominate the lubricant properties of the oxyturpentine.

The vapor pressure of blends of oxyturpentine with diesel was measured to evaluate the influence of volatile compounds of oxyfunctionalized turpentine in the fuel blend. Figure 6.7 displays the Reid pressure and the dry vapor pressure equivalent (DVPE), both obtained following the standard ASTM D 4953. Although the vapor pressure of fuel blend is increased with the content of oxyturpentine, experimental values obtained are still very low, and, therefore, no volatilization problems are expected. Thence, these blends can be used in diesel engines.

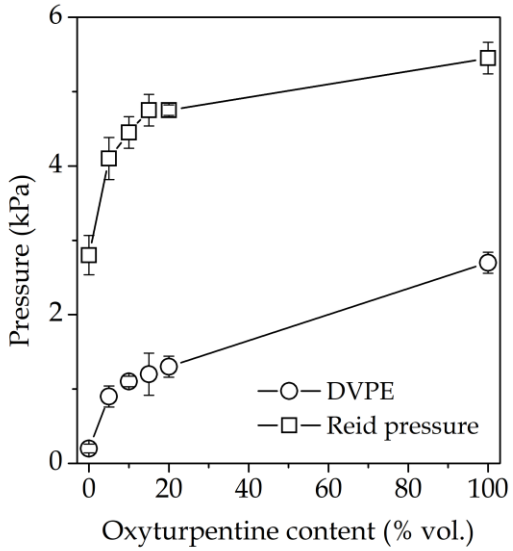

Figure 6.7. Reid Pressure and Dry Vapor Pressure Equivalent (DVPE) for blends of diesel with oxyturpentine

The measured values of Reid pressure for nopol, α-pinene, and terpineol (see Table 6.6) indicate that the Reid pressure for oxyturpentine is dominated by the most volatile compound, such as α-pinene or even more volatile ones.

6.2.2.2 Thermal properties

Distillation curves for diesel, biodiesel, turpentine, and oxyturpentine are shown in Figure 6.8. A similar trend between distillation curves of turpentine and biodiesel is observed, indicating a similar volatility of the components of these mixtures. Conversely, the boiling temperatures for biodiesel and turpentine differ around 175°C, indicating a considerable difference in the volatility of these fuels, with turpentine and biodiesel being highly and lowly volatile with respect to diesel.

Oxyfunctionalization of turpentine increases the range of boiling points of the mixture, its distillation curve becoming similar to diesel one. The boiling temperatures to recover 90 % vol. of distillated (T90) for diesel and oxyturpentine are 292, and 267°C, respectively. The s-shape of the distillation curve of oxyturpentine is the result of the presence of nopol and α-pinene. In addition, a broad range of boiling (130°C) is observed.

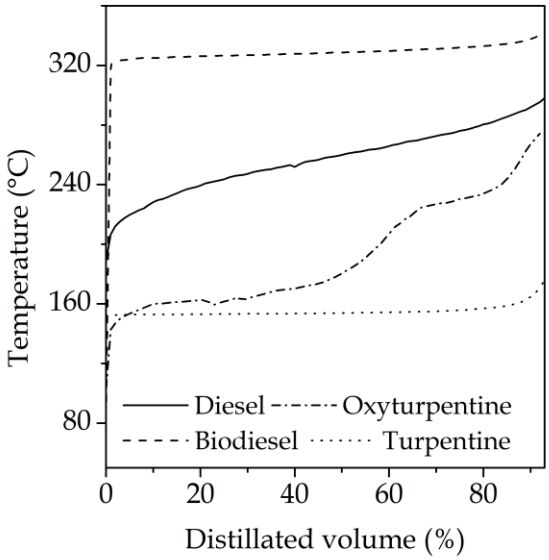

Figure 6.8. Distillation curves for diesel, biodiesel, turpentine and oxyturpentine

Measurement of heat flow of a sample as a consequence of changes in temperature allows the determination of crystallization point. Nopol, α- and β-pinene, terpineol, turpentine, and oxyturpentine display similar signal without any peak in the analyzed region of temperature. On the other hand, diesel and biodiesel show peak(s), see Figure 6.9a, which can be associated with the crystallization of the sample.

Biodiesel displays two peaks associated with saturated and unsaturated methyl esters in the mixture, whereas diesel displays only one peak. On the other hand, the crystallization points of the blends of diesel and biodiesel with oxyturpentine are shifted towards lower temperatures, Figure 6.9b. The crystallization point of diesel is decreased almost 2°C, whereas that for saturated and unsaturated esters in biodiesel were decreased by 5 and 9°C, respectively, with 20 vol.% of oxyturpentine in the blends. Low crystallization point is a highly desirable property of a fuel

particularly for cold weather, because of the lower propensity to experience problems associated with the presence of crystal in liquids, such as filter plugging.

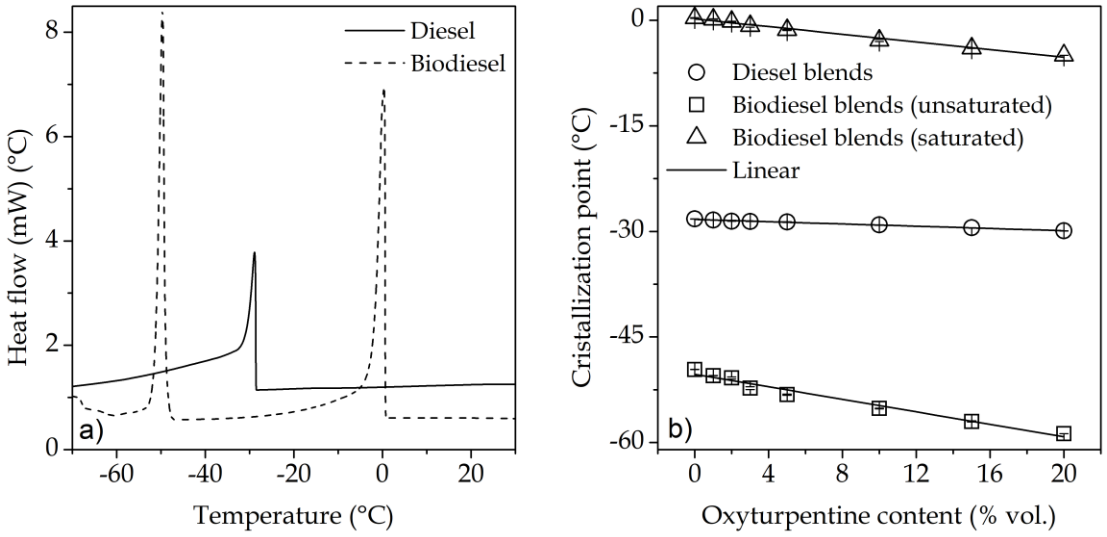

Figure 6.9. Crystallization temperatures for blends of diesel and biodiesel with oxyturpentine. a) Heat flow diagram and b) Crystallization points of blends

6.2.2.3 Combustion and thermochemical properties

The heating values of both oxyturpentine and its blends with diesel and biodiesel are lower than pure diesel and higher than biodiesel (see Figure 6.10).

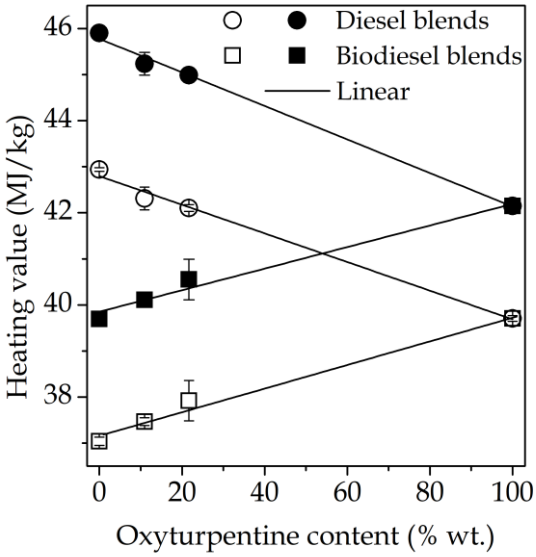

Figure 6.10. Heating values for blends of diesel / biodiesel with oxyturpentine. HHV: solid symbols; LHV: open symbols

However, such differences have been reported to affect only slightly engine combustion and performance, and emissions [1], [9], [10]. The presence of oxygen atoms in the molecule of nopol and terpineol decreases the heating value of oxyturpentine, as shown in Table 6.6. In addition, LHV measured for oxyturpentine was 39.71 MJ/kg, which is very close to that obtained from a mixture of its main components (40.34 MJ/kg).

The flash point (one of the most important properties of fuel because of its relationship with safety) for blends of diesel and oxyturpentine is shown in Figure 6.11. Although nopol displays a flash point higher than that for diesel (see Table 6.6), the presence of more volatile compounds in oxyturpentine, e.g., α-pinene, translates into flash points of the oxyturpentine + diesel blends being lower than that for diesel: indeed, oxyturpentine presents a very low flash point (37°C). However, the flash points of the blends of diesel and oxyturpentine at contents lower than 20 vol.% are higher than 55°C, which is the minimum value established by the standard EN 590:2013+A1. On the other hand, the flash points of nopol and terpineol are higher this minimum value and could be considered as safe fuels.

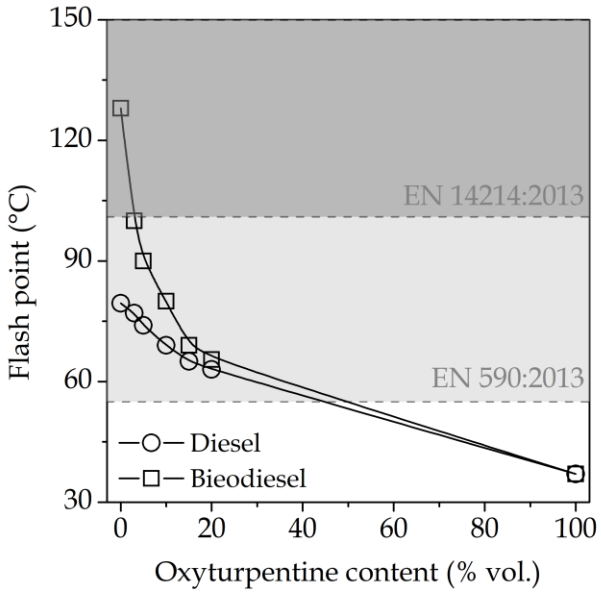

Figure 6.11. Flash point for blends of diesel and biodiesel with oxyturpentine

Figure 6.12 shows the smoke point for blends of diesel with oxyturpentine. The higher the smoke point, the lower the tendency to soot formation and particulate

matter (PM) emissions. The smoke point of oxyturpentine is ca. 11 mm higher than that for diesel, and at least 17 mm lower than that for biodiesel (the test with biodiesel surpassed the upper measure limit of the equipment). Thus, the sooting tendency of these fuel is diesel > oxyturpentine > biodiesel.

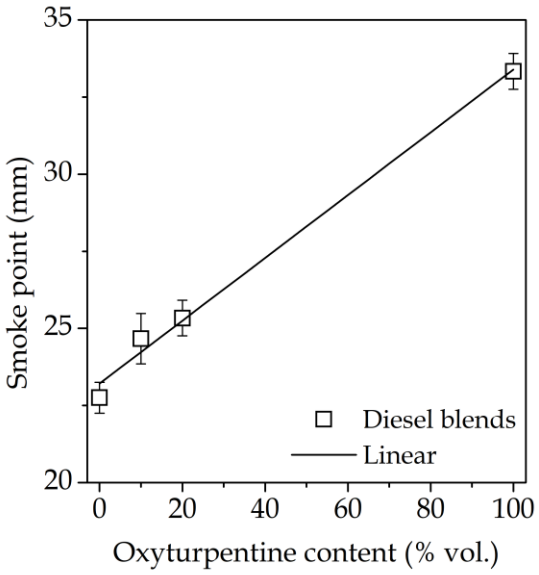

Figure 6.12. Smoke point for blends of diesel with oxyturpentine

The OESI values obtained for diesel, biodiesel, oxyturpentine, and some blends are shown in Table 6.7. The relationship of oxygen-extended sooting index with the oxyturpentine content is shown in Figure 6.13. It is evident that the OESI values for the blends are inversely proportional to the oxyturpentine content, which could be related with the lower molecular weight and higher oxygen content of the fuel obtained as oxyturpentine content is increased [187].

Table 6.7. Oxygenated-extended soot index for diesel, biodiesel, oxyturpentine and some blends

Parameter	Diesel	Biodiesel	Oxyturpentine	Oxyturpentine content* (%)	
				10	20
SP (mm)	22.75	>50	33.43	24.67	25.67
OESI	43.04	<22	18.78	38.27	37.87

* For blends with diesel, in volume basis

The low sooting tendency of oxyturpentine would be one of its major strengths as potential biofuel, because of the expected reduction in particulate material emission. The carbon atoms in close proximity of oxygen atoms have considerably less

propensity to produce soot, the effect of methyl ester group being higher than the hydroxyl group: carbons attached to the former are converted directly into CO_2, whereas some carbons attached to the latter are transformed into soot [160].

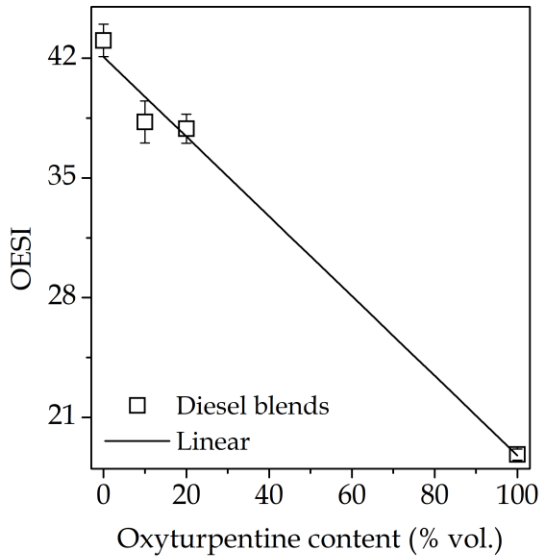

Figure 6.13. OESI values for diesel and oxyturpentine blends

The smoke point and OESI values are directly and inversely proportional, respectively, to oxyturpentine content in the diesel blend. Although the smoke point for nopol and terpineol was not obtained (the high viscosity led to flame attenuation making it not possible to register a length flame), the low value obtained for α-pinene (see Table 6.6) would suggest a high value for the other components of oxyturpentine, which implies lower OESI values. Consequently, a significant reduction in particulate material emissions would be expected with terpenic alcohols as fuel.

The derived-cetane number was obtained as a function of the ignition- and combustion-delay times (standard EN 16715). The ignition-delay is defined as the interval of time between the start of the injection and the start of the combustion in a diesel engine; the main processes involved in the ignition delay are atomization, vaporization, mixing of fuel with oxidant (diffusion), and pre-combustion reactions. The combustion-delay is defined as the interval of time between the start of the injection and the middle point of the dynamic pressure curve measured during the

combustion; this delay represents the time to reach the controlled phase of the combustion reaction.

The ignition- and combustion-delay times for oxyturpentine were notably higher than those for diesel and biodiesel (see Table 6.8). Consequently, ignition- and combustion-delay times for blends of diesel and oxyturpentine are slightly higher than that for diesel, but still similar to those for biodiesel. The increase in ignition- and combustion-delay times is related with a decrease in the ignitability of the fuel, impacting the efficiency and emissions from the engine (efficiency reduction and increase in emissions, such as carbon monoxide and unburnt hydrocarbons). This increase has been reported for oxygenated fuels as a consequence of the low cetane number resulting from the presence of oxygen in the molecule [190].

Table 6.8. Ignition- and combustion-delay times

Parameter	Diesel	Biodiesel	Oxyturpentine	Oxyturpentine content* (%)			
				5	10	15	20
ID (ms)	2.52	3.02	15.13	2.56	2.70	2.87	3.02
CD (ms)	3.79	4.13	37.66	3.92	4.12	4.37	4.60

*For blends with diesel, in volume basis; ID ignition-delay; CD combustion-delay

The results of the dynamic pressure curve and derived-cetane number are presented in Figure 6.14. Dynamic pressure curves obtained from combustion of biodiesel and oxyturpentine are shifted to the right with respect to diesel (see Figure 6.14a), as a consequence of the longer time to start the ignition and combustion for biodiesel and oxyturpentine with respect to the diesel.

The derived-cetane number for the blends of diesel and oxyturpentine are decreased with the increase in oxyturpentine content (see Figure 6.14b), whereas the ignition- and combustion-delay times increase. However, blends of diesel and oxyturpentine up to 20 vol.% present a derived-cetane number higher than 51 (the limit established in standard EN590:2013).

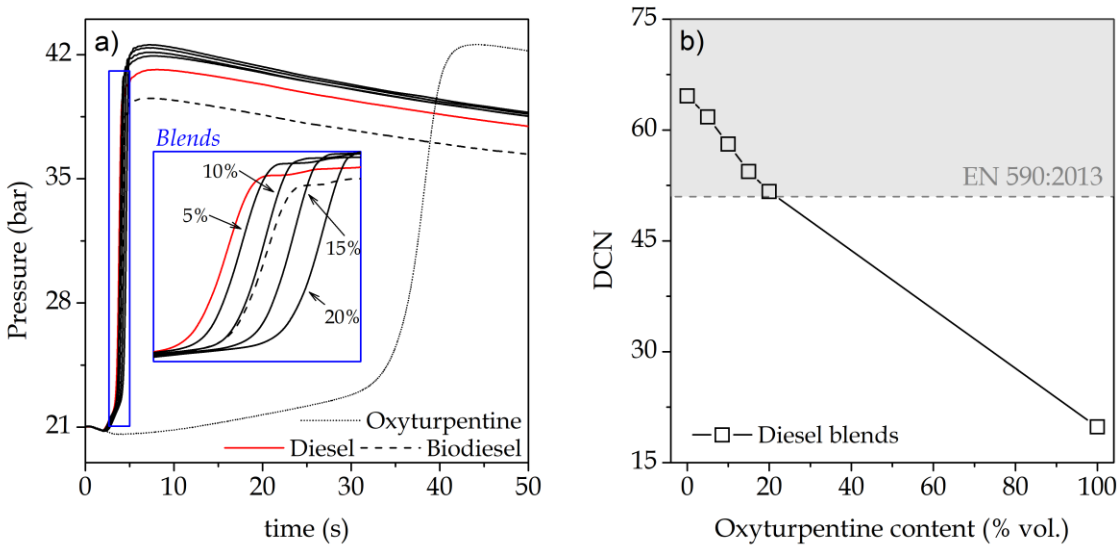

Figure 6.14. Results of derived-cetane number tests. a) Pressure dynamic curve for diesel, biodiesel, oxyturpentine, and diesel+oxyturpentine blends. b) Derived-cetane number as a function of oxyturpentine content

6.2.2.4 Cold-flow properties

Cold-flow properties have become important for biofuels, particularly biodiesel, because their fuel properties at low temperature negatively affect fuel delivery (i.e., filter plugging) and combustion behavior. Different tests can used to evaluate the possibility of a fuel to form solid particles, such as crystals, at low temperatures. Although the crystallization point may display this propensity, this temperature is associated with the bulk phase change of the fuel. In fact, the presence of substances such as paraffins can result in the formation of crystals at low temperature; if the amount of these crystals is large enough, their accumulation can generate the aforementioned problems. Pour, cloud, and cold filter plugging points help to identify the temperature at which the behavior of fuel begins to be problematic; these temperatures are shown in Figure 6.15.

The measured cloud, pour and CFPP temperature are decreased as oxyturpentine content is increased (with both diesel and biodiesel blends), indicating that the presence oxyturpentine decreases the trend to form crystals. For instance, with the blend of diesel and oxyturpentine at 20 vol.%, the required temperature to observe filter plugging of crystals was 0.6°C lower than that for diesel, while those differences for cloud and pour points were 2.5°C and 2.6°C, respectively. The effect of

oxyturpentine on biodiesel is stronger than that observed with diesel, obtaining a reduction of 3.5°C on CFPP and cloud point due to the oxyturpentine content.

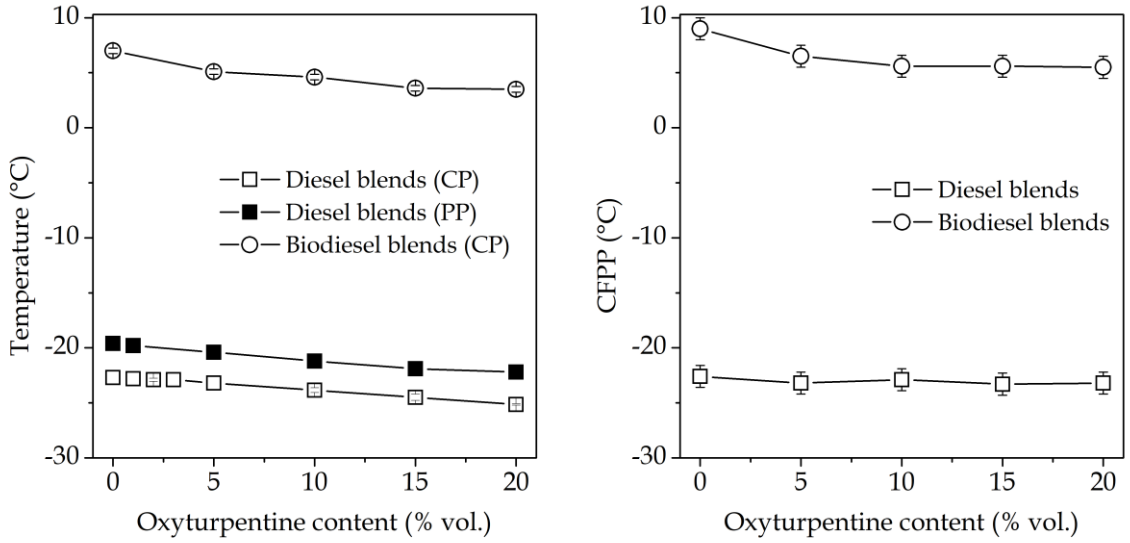

Figure 6.15. Cold-flow properties for diesel and biodiesel blended with oxyturpentine at different contents**.** a) Pour point (PP, solid symbols) and cloud point (CP, open symbols). b) CFPP

6.2.3 Remarks of the section

★ Fuel density is significantly affected by the presence of oxyturpentine up to 20 vol.% in blends with diesel, because of the high density of oxyturpentine. Oppositely, despite the higher viscosity of oxyturpentine, diesel + oxyturpentine blends present lower viscosity than diesel. Lubricity, on the other hand, is improved by the presence of oxyturpentine, especially at low content (1-5 vol.%).

★ The heating value, derived-cetane number, boiling temperatures (particularly the T90 temperature in the distillation curve), and flash point of oxyturpentine are considerably lower than those for diesel. Thus, the corresponding properties for the blends decrease with oxyturpentine content, due to the presence of oxygen atoms in the fuel molecules and the characteristic properties of nopol. Moreover, these properties for blends of diesel and oxyturpentine up to 20 vol.% are within the limits established by European standard EN 590:2013, which regulates the quality of diesel fuels.

★ Crystallization, cloud, pour, and cloud filter plugging points of diesel are decreased with oxyturpentine content, reducing the occurrence probability of

filter plugging by decreasing the temperature at which crystals may be formed in the fuel. In addition, the sooting tendency of diesel + oxyturpentine blends was also reduced with oxyturpentine content. Therefore, a reduction in emissions of particulate material from engine is expected with the use of oxyturpentine as fuel component.

6.3 Bench engine tests

6.3.1 Background

The use of oxygenated molecules as components of diesel fuel has increased in recent decades, mainly because biofuels are often oxygenated. Typical oxygenate molecules with fuel application are esters, alcohols aldehydes and ethers. In the case of alcohols, the influence of methanol, ethanol and *n*-butanol on engine performance and emissions have been studied [191]–[194]. For instance, reduction of some pollutants, such as particulate material, without affecting engine efficiency has been reported, but an increase in nitrogen oxides and hydrocarbon emissions has been also observed. Furthermore, “fuel properties” of the oxygenated molecule, e.g., density, viscosity or heating value, play a key role in its combustion performance in actual engines.

Oxyturpentine is composed by molecules with very different properties, in particular terpenes (mainly α-pinene) and alcohols (mainly nopol). For instance, the viscosity of nopol is considerably higher than that for α-pinene, the heating value of α-pinene is higher than that for nopol, and nopol is an alcohol whereas α-pinene is an unsaturated hydrocarbon. However, as previously discussed in this Thesis, this combination of properties leads to promising fuel properties. Specifically, a blend of diesel and oxyturpentine (20 vol.%) satisfies the fuel properties established by European standard EN 590:2014+A1. Thus, an assessing of the influence of oxyturpentine in the performance and emissions of a compression ignition Euro 6 engine is presented in this section.

6.3.2 Methodology

6.3.2.1 Experimental setup

The engine test bench used is composed of an engine coupled to a dynamometer, a fuel gravimetric system and a flowmeter to measure fuel and air consumption, respectively, and an exhaust gas and particle analyzers as shown in Figure 6.16.

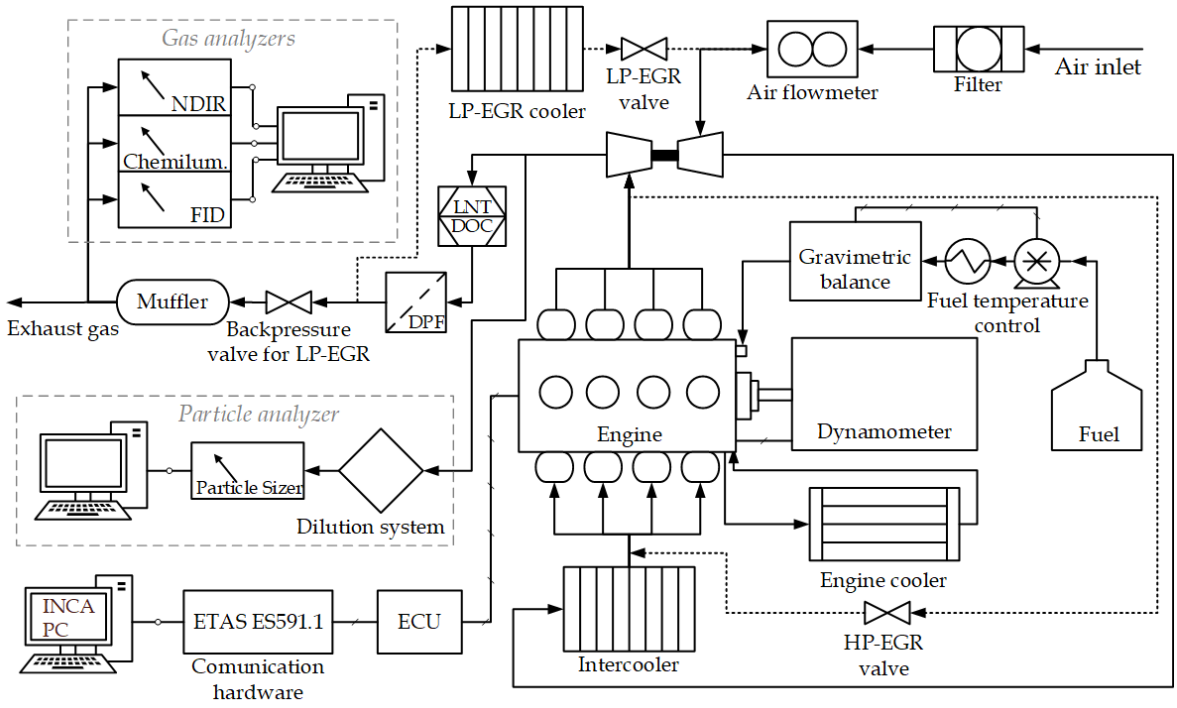

Figure 6.16. Experimental setup for engine tests

The engine used for the experiments is a common-rail direct injection diesel engine, with Euro 6 technology manufactured by Nissan, model K9K (1.5 dCi). The engine is equipped with double-loop exhaust gas recirculation system (low- and high-pressure, LP- and HP-EGR, respectively) which are managed according to the temperature of coolant: LP-EGR for high coolant temperature, and HP-EGR for low coolant temperature. The main specifications of the engine are summarized in Table 6.9, including the resistance force ($F_{(V)}$) as a function of the vehicle velocity (V), obtained from the coast-down procedure.

Aftertreatment is composed of a diesel oxidation catalyst (DOC), a diesel particle filter (DPF, wall-flow-type), and a lean NOx trap (LNT). The high-pressure EGR system is activated when the NOx trap purge is also activated.

Table 6.9. Engine specifications

Cylinders	4 (in line)
Valves/Cylinder	2
Displacement (cm^3)	1461
Stroke number	4
Stroke (mm)	80.5
Bore (mm)	76
Compression ratio	15.5 : 1
Injection	Common rail direct injection
Torque (max.)	260 Nm/1750-2500 rpm
Power (max.)	81 kW /4000 rpm
Aftertreatment system	DOC+DPF+LNT

An asynchronous electric dynamometer (Schenk Dynas III LI 250) is coupled to the engine through the rotating shaft to control the engine speed and torque. A Road Load Simulation system (RLS, Horiba) was used to simulate transmission, tires, gearbox, and other characteristics of the dynamics of a Nissan Qashqai 1.5 dCi, which represents one of the most popular sport utility vehicles (SUVs) in Europe. The main properties of the vehicle are shown in Table 6.10.

Table 6.10. Vehicle properties

Transmission	Manual, 6 gears
Differential ratio	4.13 : 1
1^{st}:2^{nd}:3^{rd}:4^{th}:5^{th}:6^{th} gear ratio	3.73 : 1.95 : 1.23 : 0.84 : 0.65 : 0.56 : 1
Coast-down constants*	89.6; 0.0659; 0.0391
Vehicle test mass (kg)	1470

*$F_{(V)}(\mathrm{N}) = f_0 + f_1 V(\mathrm{km/h}) + f_2 V(\mathrm{km/h})^2$

The hardware ETAS ES 591.1 was used to communicate the INCA PC software and the electronic control unit (ECU), keeping the original setting of the vehicle mapping. Signals from raw sensors such as the air and fuel consumption (the latter previously calibrated with an AVL 733s fuel gravimetric system [195]) were registered with the INCA PC software.

Analysis of exhaust gases consists in measurement of total hydrocarbon (THC), carbon monoxide, carbon dioxide, and nitrogen oxides (NOx=NO+NO_2) emissions. CO and CO_2 emissions were measured with non-dispersive infrared spectroscopy (NDIR) in a MIR 2M analyzer. THC emissions were measured with a flame ionization detector (FID) Graphite 52M-D, by pumping and filtering the sample at 190°C. NOx

emissions were measured using the chemiluminescence technique in a Topaze 3000 analyzer. These analyzers are integrated in a modular system acquired from Environnement and the signals are carried out to a suitable software. The modular system and software allow performing calibrations and span tests.

The particle analyzer consists of a sampling system, which dilutes the gas sample from upstream of the DPF with a rotating disk diluter model MD19-2E (set at 150°C to avoid hydrocarbon condensation) through a first dilution with a thermal conditioner model ASET15-4 (set at 300°C), a second dilution system (a blending chamber which cools down the sample) and an Engine Exhaust Particle Sizer (EEPS) spectrometer model 3090 from TSI, which is able to measure the number and size of particles. The dilution factors for the rotating disk and thermal conditioner were 64.73 : 1 and 6.18 : 1, respectively, leading a total dilution factor of 400 : 1. The particle mass was determined from the mobility diameter and particle number measured with EEPS, according to the following expression [196],

$$\rho = \rho_0 - (\rho_0 - \rho_p)\left[1 - \exp\left(C\left(\frac{\log D - \log D_0}{\log D_p - \log D_0}\right)^m\right)\right] \qquad \textbf{Equation 6.4}$$

where ρ and D are the particle apparent density and equivalent diameter, ρ_0 and ρ_p are the maximum and minimum particle apparent densities: 1.55 and 0.155 g/cm^3, respectively, D_0 and D_p are the minimum and maximum equivalent particle diameter: 0.03 and 1.0 µm, respectively, and m and C are coefficients determined by fitting experimental data [197], with values resulting in 4.28 and -6.908, respectively.

6.3.2.2 Fuel

The fuel used in the engine test is composed of diesel (80 vol.%) and oxyturpentine (20 vol.%). Although the main fuel properties of diesel and oxyturpentine were presented in Table 6.6, those for diesel are shown in Table 6.11 together with those for the diesel + oxyturpentine blend, to facilitate the analysis.

Table 6.11. Properties of the fuels tested in the engine

Property	Units	Method	Diesel	Blend
Mean molecular formula	-	-	$C_{15.05}H_{27.61}$	$C_{14.2}H_{25.5}O_{0.1}$
C content	wt.%	-	86.1	85.8
H content	wt.%	-	13.9	13.5
O atoms	wt.%	-	0.0	0.7
Molecular weight	kg/kmol	-	208.6	199.2
Stoichiometric fuel-air ratio	-	-	1/14.51	1/14.33
Density[a]	kg/m^3	EN 3675	829	847
Viscosity[b]	cSt	EN 3104	2.5	2.5
Lubricity (WSD[d])	µm	EN 12156-1	443	341
Lower Heating Value	MJ/kg	EN 51123	42.94	42.11
Derived-cetane number	-	EN 16715	64.4	51.7
Cloud point	°C	EN 3015	-22.6	-25.2
Pour point	°C	EN 3016	-19.6	-22.2
Cold filter plugging point	°C	ASTM D6371	-22.6	-23.2
Crystallization point	°C	EN 2386	-28.2	-29.9
Flash point	°C	EN 2719	79.5	63
Vapor pressure	kPa	EN 3007	~0	1.1
Smoke point	Mm	EN 3014	22.3	25.7

[a]At 15°C and 45% relative humidity; [b]at 40°C; [c]wear scar diameter.

6.3.2.3 Test protocol

The New European Diesel Cycle (NEDC) was selected as driving cycle for the tests. This cycle has been used in Europe during the last two decades years to certificate light-duty vehicles according to their fuel consumption and emissions, and is currently accepted by south American countries such as Colombia and Uruguay (Resolutions 1111 of 2013 and UNIT 1130:2013, respectively) and center American countries such as Costa Rica (decree 39724 MOPT-MINAE-S). The cycle includes four urban driving sub-cycles, where the maximum velocity is 50 km/h, and an extra-urban driving cycle, where the vehicle reaches 120 km/h. The cycle is started from cold-engine conditions and performed without any interruption. The total time for the driving cycle is 1180 seconds. Figure 6.17 depicts the NEDC cycle.

All tests were repeated three times to evaluate the repeatability, and the results were averaged. Each test was performed at different days to replicate the initial conditions of the engine, and the temperature in the test room was 25.23 $\pm$ 0.15 and 22.5 $\pm$ 0.95°C for the tests with diesel and diesel+oxyturpentine blend, respectively. These values respond to the respective local weather at the time of each test.

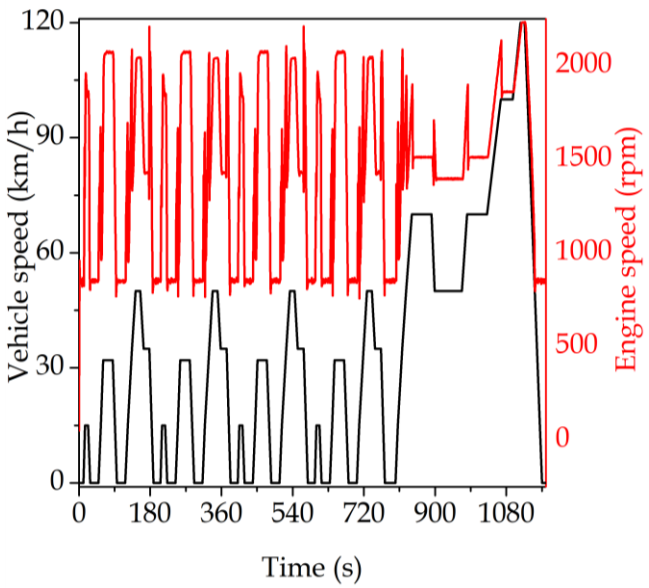

Figure 6.17. Scheme of the NEDC cycle

6.3.3 Results and discussion

6.3.3.1 Specific fuel and energy consumption

The instantaneous and cumulative fuel consumption for engine tests averaged from replicate measurements (the error band represents the standard deviations) using diesel and blend of diesel and oxyturpentine are shown in Figure 6.18. The instantaneous fuel consumption with the blend was slightly higher than that with diesel in the whole cycle. The maximum consumption in both cases was reached in the extra-urban sub-cycle, when the engine was accelerated for the vehicle to reach 120 km/h. The total fuel consumption for tests with diesel and blend were 871 $\pm$ 3 and 914 $\pm$ 20 g, respectively (see Figure 6.18b), thus, the increase in fuel consumption was around 5% for tests with the diesel+oxyturpentine blend with respect to that with diesel fuel for the NEDC. The lower heating value of the blend is around 1 MJ/kg (2%) lower than that for diesel (see Table 6.11) as a consequence of the oxygen content in the blend. On the other hand, the energy consumption, defined as the product of the fuel consumption and its lower heating value, was 37.40 + 0.13 MJ and 38.47 + 0.88 MJ for the whole cycle, for diesel and the blend diesel+oxyturpentine, respectively.

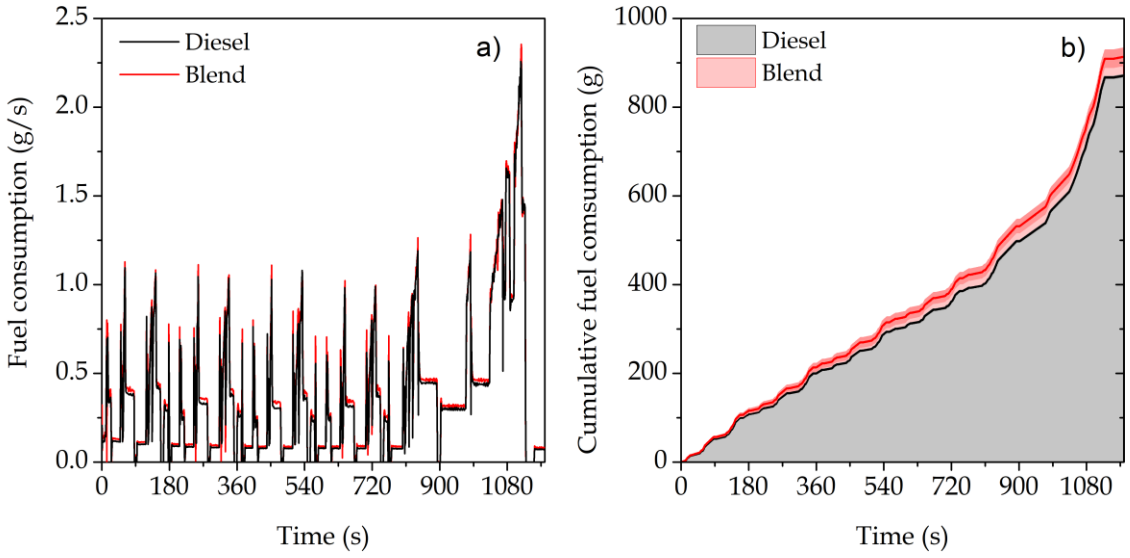

Figure 6.18. Fuel consumption: a) instantaneous and b) cumulative in the total NEDC

The difference on energy consumed amounts 2.9 %, which corresponds to a difference in engine efficiency of 0.37%. Since Euro 6 engines have more delayed combustion with respect to previous ones such as Euro 4 engines (with the purpose of reducing NO formation), higher ignition delays for the oxyturpentine blend (with lower cetane number, see Table 6.11) can explain the decrease in engine efficiency. Considering that the engine power is set to the same value, the decrease in fuel heating value, together with the decrease in engine efficiency, can explain the aforementioned increase in fuel consumption.

6.3.3.2 Equivalence ratio and EGR

The effect of the fuel formulation on the engine emissions is often an indirect effect, based on the equivalence ratio and on the exhaust gas recirculation (EGR). Although these are integrated or averaged quantities, they both affect local conditions at the combustion chamber, and consequently, have strong effect on the formation and destruction of pollutants. If no changes are observed on the equivalence ratio and on the EGR, the effect on emissions can then be attributed to the fuel molecular structure.

The equivalence ratio, defined as the fuel-air ratio at actual and stoichiometric conditions is shown in Figure 6.19. The equivalence ratio for both fuels is lower than 1.0 in almost all the cycle. Few exceptions appear for minor periods of time

corresponding to accelerations in the urban sub-cycle for both fuels, and in the case of regeneration of the lean NOx trap (at around 1070 s). In addition, as the cycle progressed along the urban sub-cycle, the equivalence ratio decreased for both fuels as a result of the increase in engine temperature.

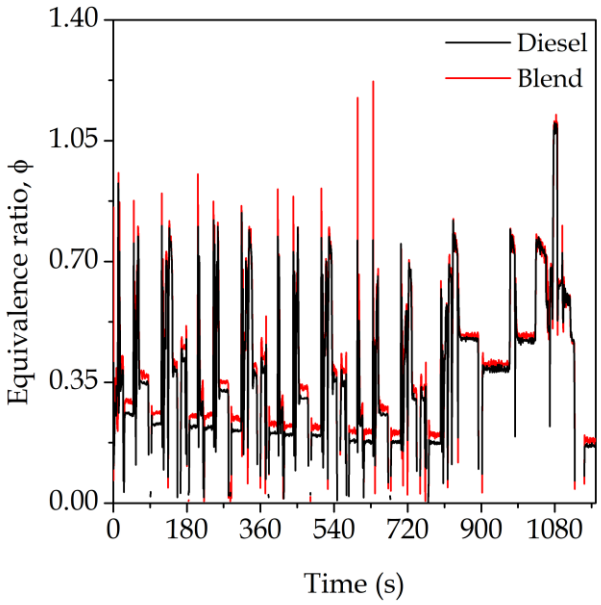

Figure 6.19. Instantaneous equivalence ratio

The measured total consumption of air mass for tests with diesel and the diesel + oxyturpentine blend was very similar (32.98 ± 0.02 kg and 33.15 ± 0.01 kg, respectively), indicating that the same amount of air was consumed in both tests. This result, together with the slight increase in fuel consumption for tests with the diesel + oxyturpentine blend with respect to the tests with diesel, means that the actual fuel-air ratio for the diesel + oxyturpentine blend is slightly higher than that for diesel. In addition, the stoichiometric fuel-air ratio for the blend is slightly higher than that for diesel fuel (see Table 6.11), correspondingly with its oxygen content. However, such reduction in stoichiometric fuel-air ratio is not enough to compensate the reduction in heating value, leading to a certain increase in equivalence ratio, which may favour the local formation of carbon monoxide and may hinder the local oxidation of hydrocarbons.

The instantaneous exhaust gas recirculation (EGR) rate is shown in Figure 6.20. The coolant temperature for tests with both diesel and the diesel+oxyturpentine blend

showed similar increase as the tests progresses (as shown ahead). Experiments with both fuels reach 65°C for coolant temperature at similar times (around 580 s with a variation lower than 6 s), and then the LP-EGR system was activated almost at the same time for both fuels, simultaneously to the deactivation of the low-pressure system. The total mass of exhaust gas recirculation were 6.19 ± 0.02 kg and 6.39 ± 0.05 kg for tests with diesel and blend of oxyturpentine and diesel, respectively, indicating that the total EGR for tests with the diesel+oxyturpentine blend was 3.2 % higher than that for test with diesel (in both cases the error in the measurements was lower than 1%).

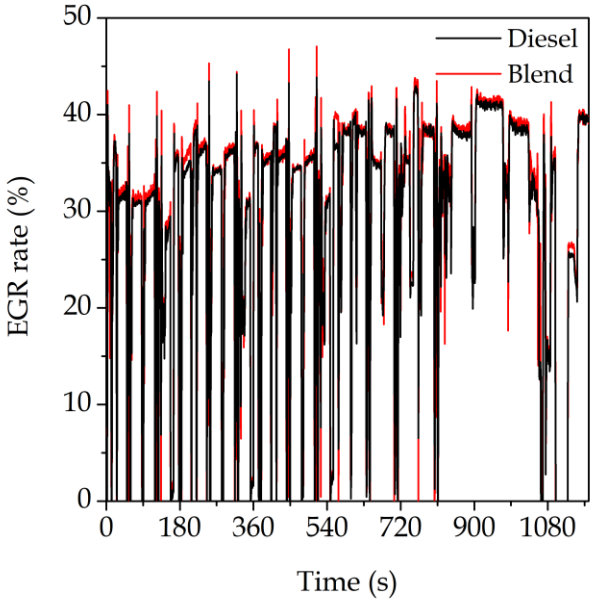

Figure 6.20. Instantaneous rate exhaust gas recirculation

6.3.3.3 Gaseous emissions

The emissions of CO registered for the tests with diesel and diesel + oxyturpentine blend during the NEDC are shown in Figure 6.21. The high peaks observed for both fuels at the start of the test in Figure 6.21a are attributed to the acceleration of the engine, stressed by the cold-start conditions. As the test progresses, CO emissions decrease due to the increase in engine temperature (for similar accelerations, the CO emissions are reduced in subsequent sub-cycles). In addition, another high peak is observed at the end of the NEDC due to the regeneration of the lean NOx trap.

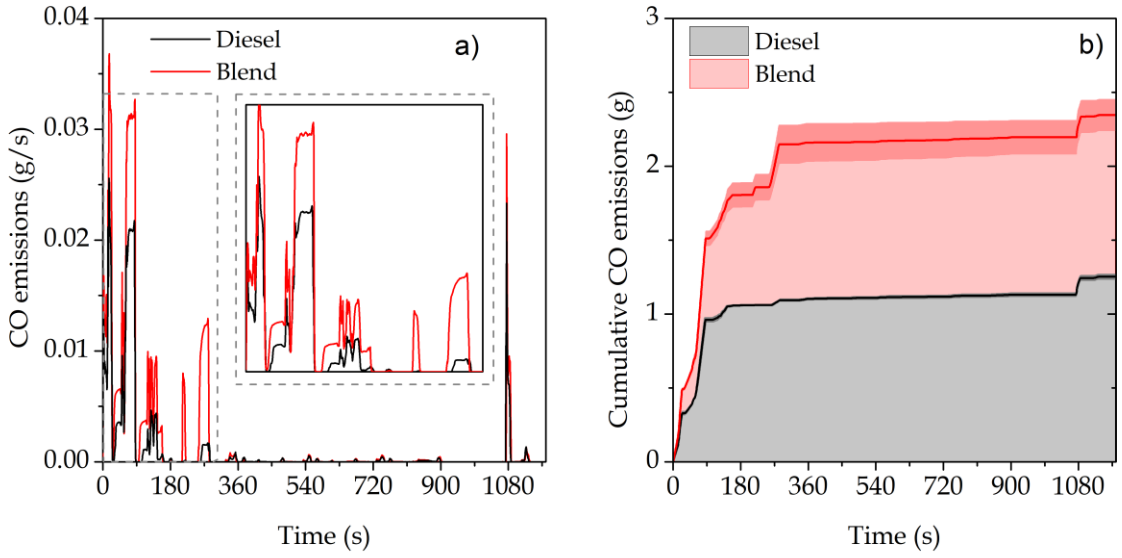

Figure 6.21. Emissions of carbon monoxide: a) instantaneous and b) cumulative in the total NEDC

The difference in CO emissions for tests with diesel and diesel + oxyturpentine blend after 300 s is almost constant, as shown in Figure 6.21b. This means that the main difference on the behavior of CO emissions among both fuels occurs at engine start, due to the low engine temperature.

Figure 6.22 shows the total hydrocarbons emissions of engine tests with and without oxyturpentine in diesel. As with CO emissions, the main differences among fuels are observed at the start of the NEDC. After 300 s, the difference in HC emissions between both fuels stabilizes, indicating that the deterioration of the combustion is due to the cold-engine start, which affects more the diesel + oxyturpentine blend than diesel fuel.

The lower excess of air in combustion with diesel+oxyturpentine blend with respect to that with diesel (see Figure 6.19), together with the increase in EGR in these tests, influence the CO and HC emissions. As aforementioned, the fuel properties of oxyturpentine lead to higher equivalence ratio and EGR when it is blended with diesel. The lower amount of air can hinder the mixing with fuel, and lead to higher emissions of CO and HC as a consequence of the increase in the local formation of CO and the decrease in local oxidation of hydrocarbons [198].

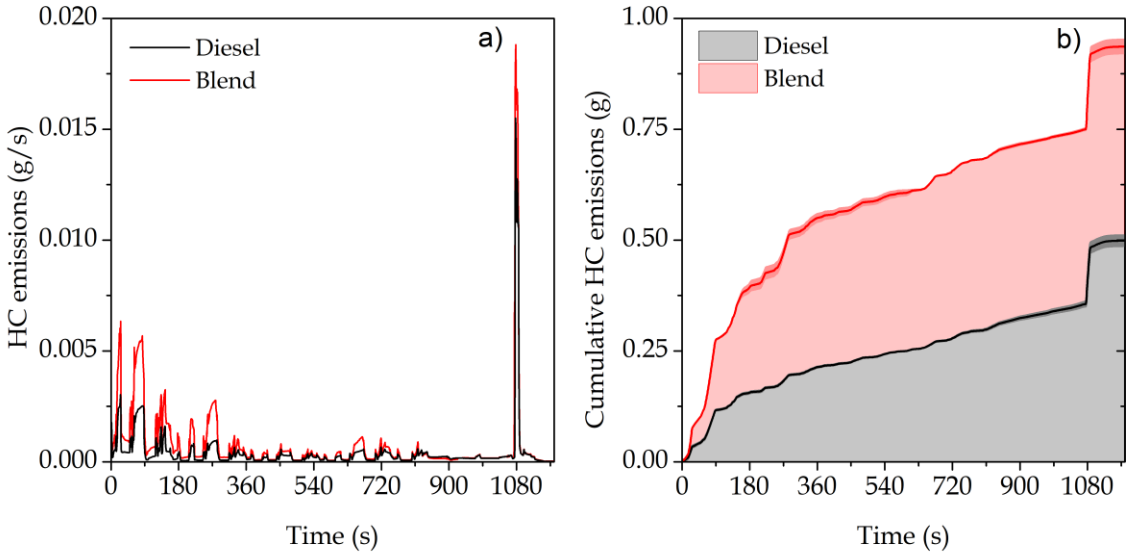

Figure 6.22. Emissions of total hydrocarbon: a) instantaneous and b) cumulative in the total NEDC

Apart from the effect of the equivalence ratio and the EGR, two additional effects may also contribute to the increase in CO and HC emissions at the beginning of the cycle, associated with surface tension and to volatility. The blend of diesel and oxyturpentine at 20 %vol. possesses similar viscosity than diesel fuel at the reference conditions (see Table 6.11). The increase in fuel density as a consequence of the addition of oxyturpentine can lead to an increase in surface tension of the fuel, as has been reported for blends of diesel and oxygenated molecules [199], [200]. Besides, the alcohol-hydrocarbon interactions can generate positive excess of surface tension, and consequently the surface tension of the blend can increase considerably [201].

Estimated values of a surface tension from the literature[2] are 33.2 mN/m, 32.1 mN/m and 27.1 mN/m for α-terpineol, nopol and β-pinene, respectively, whereas reported experimental surface tension for diesel and biodiesel is 26.4 mN/m and 30.1 mN/m, respectively [199]. Therefore, the surface tension of oxygenated molecules from turpentine would be higher than that of diesel and biodiesel, also than other oxygenated biofuels such as ethanol and butanol (20-22 mN/m). Thence, the presence of nopol and terpienol in the blend is expected to increase its surface

[2] ChemSpider, The Royal Chemical Society (Consulted in May of 2020).

tension. This increase may affect the atomization of the fuel, deteriorating the subsequent combustion; this phenomenon has been evidenced in combustion tests with blends of diesel with biodiesel [202], [203], especially at cold conditions [204].

Additionally, some difference in volatility between diesel and oxyturpentine is observed in distillation curves (see Figure 6.8) For instance, the temperature to recover 90 % of the diesel as distillate is 25°C higher than that for the diesel+oxyturpentine blend. In addition, at low distillated volume, the difference in boiling temperature is even larger, indicating that the evaporation of volatile components of oxyturpentine can decrease the local temperature and thus narrow the flammability limit range in which the flame can progress to burn the overleaned mixture which is formed far away from the burning sprays.

This effect has been observed with other volatile molecules such as ethanol, methanol, isopropanol and *n*-butanol [205], [206]. In any case, the volatility of oxyturpentine is higher than that for normal alcohols. In fact, the boiling temperature of α-pinene (the most volatile component of turpentine) is higher than that for normal alcohols (i.e. boiling temperature of pentanol is 138°C), while that for nopol and α-terpineol is even higher (230°C and 219°C boiling temperatures, respectively).

Figure 6.23 shows the accumulated emissions of CO and HC for each sub-cycle in comparison with the coolant temperature for both fuels. As the temperature is increased, the accumulated emission of CO and HC for urban sub-cycles are significantly reduced, leading to an improvement in the combustion process, as a consequence of the reduction in equivalence ratio (see Figure 6.19) and of the reduction in viscosity and surface tension with the increase in temperature.

Emission of nitrogen oxides are shown in Figure 6.24. The NOx emission by using diesel + oxyturpentine blend in the test is slightly lower than that for the diesel fuel during the entire NEDC (see Figure 6.24a). The differences in cumulative NOx emissions among fuels begin to be appreciable at around 360 s (Figure 6.24b) which means that these emissions become sensitive to the type of fuel only when the combustion chamber is hot enough.

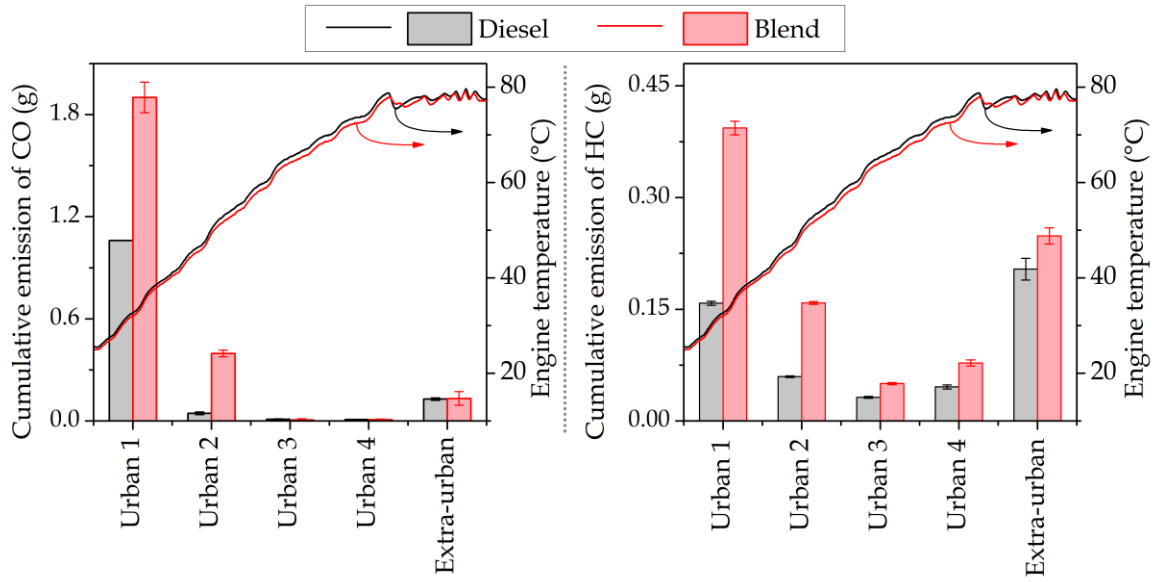

Figure 6.23. Cumulative emission for each sub-cycle of a) carbon monoxide and b) total hydrocarbons

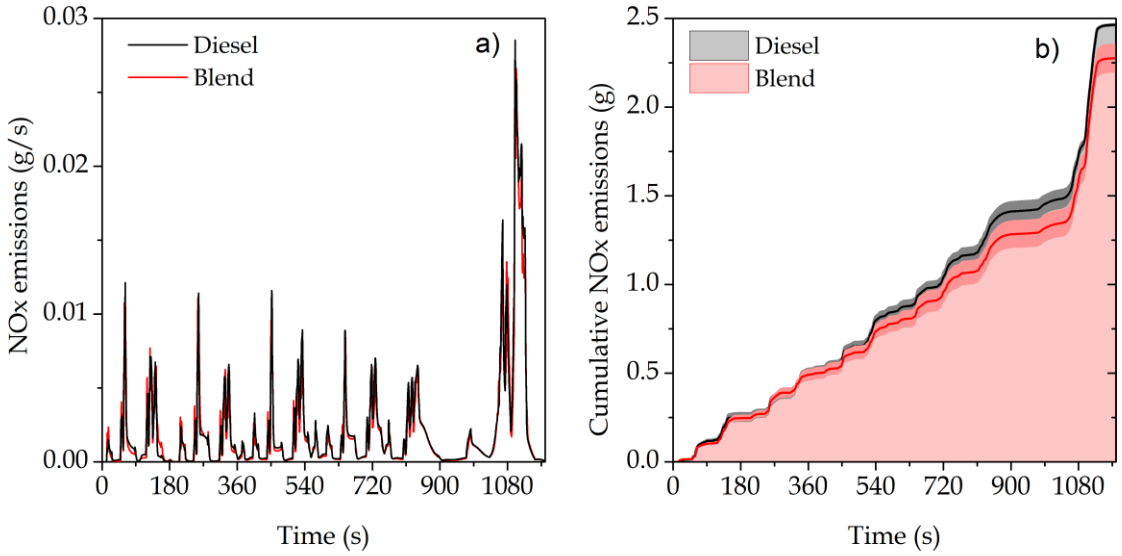

Figure 6.24. Emissions of oxides of nitrogen: a) instantaneous and b) cumulative in the total NEDC

The estimated adiabatic flame temperature for diesel fuel is very similar to that for oxyturpentine at stoichiometric conditions (see Figure 5.1). The decrease in NOx emission observed for the tests with the diesel+oxyturpentine blend can be mainly attributed to the increase in EGR, which leads to reduced local temperature in the combustion chamber.

Although a reduction in DCN was evidenced for the blend with respect to diesel and, often, this change is related to an increase in NOx emissions, two factors must be considered. Firstly, a high sensibility of EGR variations on engine performance, particularly on emissions, has been observed experimentally. Secondly, currently the effect of DCN on NOx emission is not clear (especially for Euro 6 engines, in which the efficiency can be decreased at the expense of avoiding excessive peaks of pressure and temperature in the combustion chamber). In fact, depending on the delay time caused by the decrease in DCN, NOx emissions can be either decreased or increased.

6.3.3.4 Particulate number

The number of particles - PN (including particle diameters ranged between 5.6 and 560 nm) emitted instantaneously during the tests with both diesel + oxyturpentine and diesel fuels is shown in Figure 6.25. The peaks of particles number observed in Figure 6.25a for both fuels are due to the acceleration of the engine. The particle number is notably reduced by the presence of oxyturpentine in the fuel (see Figure 6.25b).

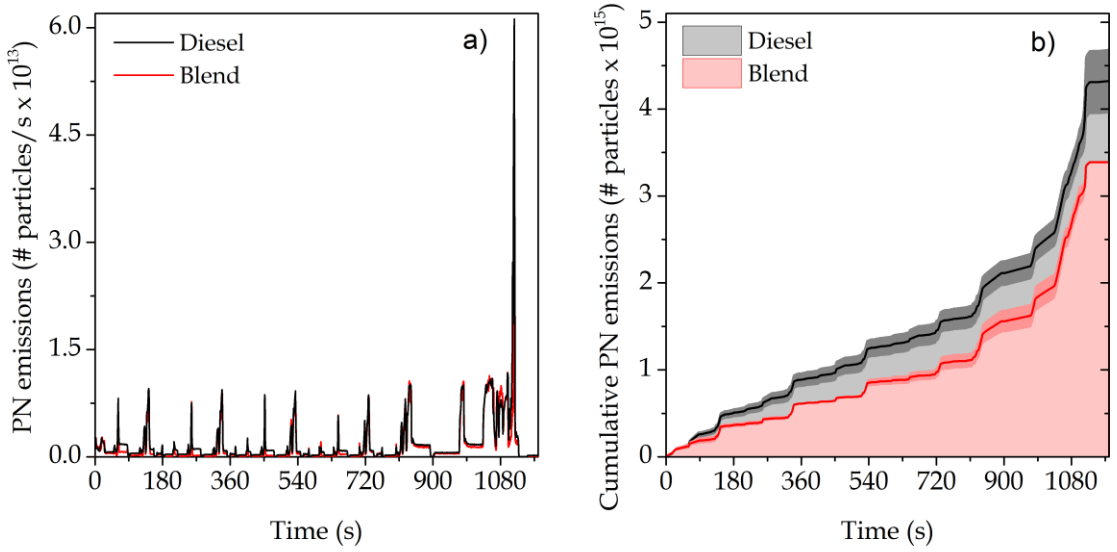

Figure 6.25. Number of particulate material (all sizes): a) instantaneous and b) cumulative in the total NEDC

This reduction is associated with the content of oxygen atoms in the fuel molecules, which promotes the oxidation of soot, and the reduction in aromatic compounds of

diesel (replaced by oxyturpentine in the blend). These factors, associated to the presence of oxyturpentine in the fuel, would be more important than the change in local temperature (as a consequence of the variation in EGR), suggesting that at the same EGR for diesel and diesel + oxyturpentine blend, the decrease in PM may be higher.

The instantaneous particle size analyzed from engine tests with and without oxyturpentine in the fuel is shown in Figure 6.26. The instantaneous particle size distribution was bimodal for both fuels in the whole NEDC. Thus, total number of particles are classified as nucleation mode (or small particles) and accumulation mode (or large particles) with the limit between these ranges being in 22.1 nm. This value was obtained as the average of the local minimum values from the bimodal behavior of all measurements. Small particles can be associated with liquid-nucleation whereas the large particles are mainly composed of soot.

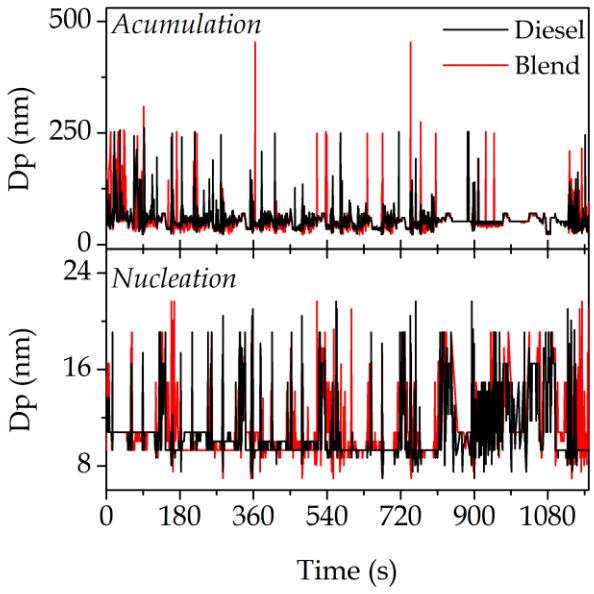

Figure 6.26. Instantaneous particle size

The total number of particles as a function of their size, accumulated for each sub-cycle and the total NEDC, is shown in Figure 6.27. A strong reduction in the total number of particles in nucleation mode can be observed in Figure 6.27a with the diesel + oxyturpentine blend with respect to that with diesel, whereas the number of accumulation mode particles is decreased in a lower extent. In each cycle, the

number of both small and large particles is lower for the diesel + oxyturpentine blend than for diesel fuel.

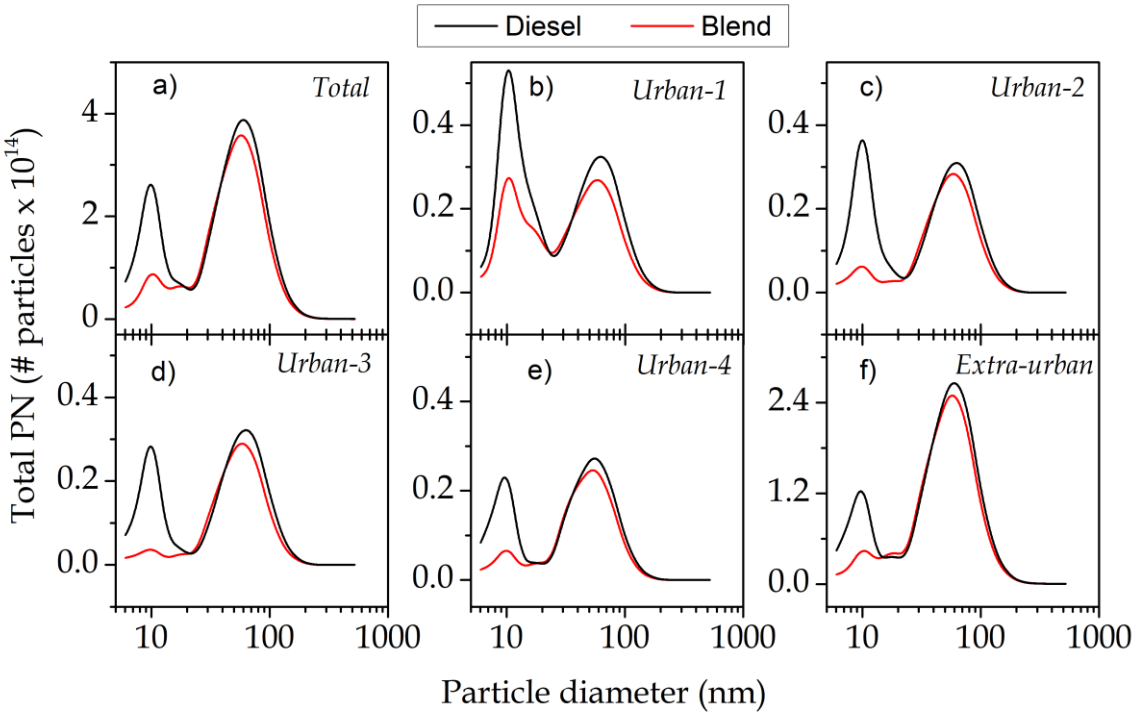

Figure 6.27. Total particle size distribution for a) the total NEDC and b-f) each sub-cycle of the NEDC

The cumulative particle size distribution for the first urban sub-cycle shown in Figure 6.27b depicts a high peak for the small particles in the tests with diesel, even higher than the corresponding large particles. The oxyturpentine in the fuel reduces considerably the small particles after the first urban cycle. The high content of small particles in the first urban cycle is mainly due to the cold-engine start. Probably, the hydrocarbon species remaining from the low-efficient combustion of diesel fuel at cold-start conditions tend to nucleate, favored by the low temperature of the engine, favored by the lower molecule volatility.

Due to the improvement in the combustion process as a consequence of the increase in engine temperature, the number of nucleation-mode particles for both fuels is decreased as the test progresses, avoiding the nucleation to form these particles (see Figure 6.27c-e). A high portion of the total number of particles is formed in the extra-urban cycle (see Figure 6.27f) because of the high consumption

of fuel (and thus equivalence ratio) to achieve the high vehicle speed. The average mobility diameter of nucleation-mode particles is 9.6 and 9.9 nm for diesel and diesel+oxyturpentine blend, respectively, whereas the average diameter of accumulation-mode particles is 58.8 nm for both fuels. The only difference in the particle size for nucleation-mode appears in the extra-urban cycle.

6.3.3.5 Particle mass

The mass of particles (PM) emitted from tests with both diesel + oxyturpentine and diesel fuels, obtained from the measurements of number and size particles, and using Equation 6.4 is shown in Figure 6.28. The acceleration of the engine promotes the formation of PM (peaks in Figure 6.28a). Both instantaneous and cumulative emissions of PM are higher for diesel than for the blend.

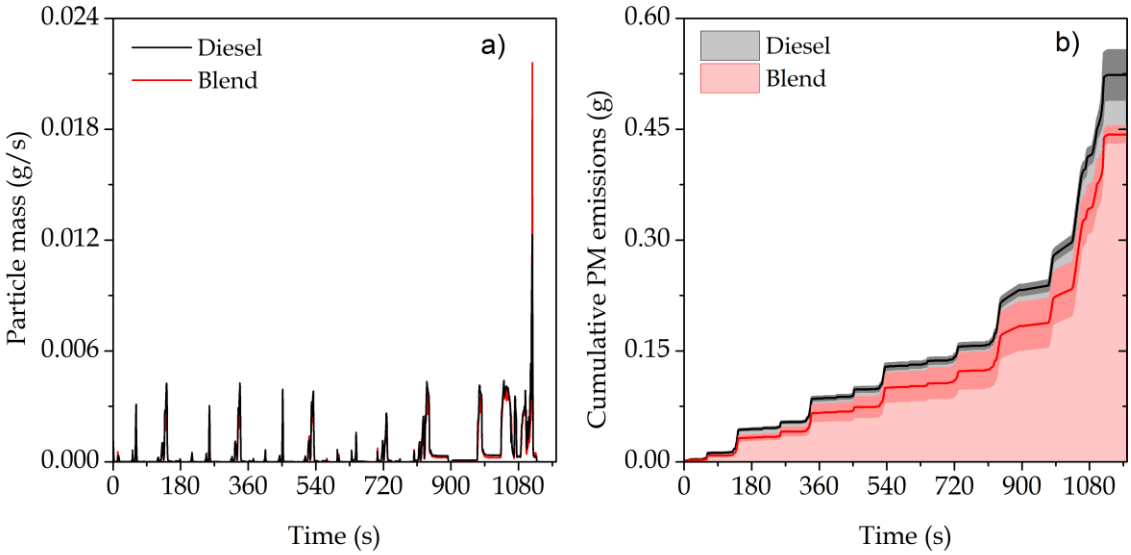

Figure 6.28. Mass of particulate material: a) instantaneous and b) cumulative in the total NEDC

The accumulation of mass of particles in each sub-cycle is shown in Figure 6.29. The main generation of particulate matter is in the extra-urban sub-cycle for both fuels, where the vehicle reaches the highest speed in the NEDC. In addition, in each sub-cycle, the mass of particle obtained from diesel + oxyturpentine blend is lower than that from diesel, being the most significative difference that for the extra-urban sub-cycle. The decrease in PM is lower than the reduction in particulate number (18 % and 28 % in PM and PN, respectively, for the total NEDC), because the reduction

in PN is based on a strong reduction in nucleation particles, which have minor contribution to the particle mass.

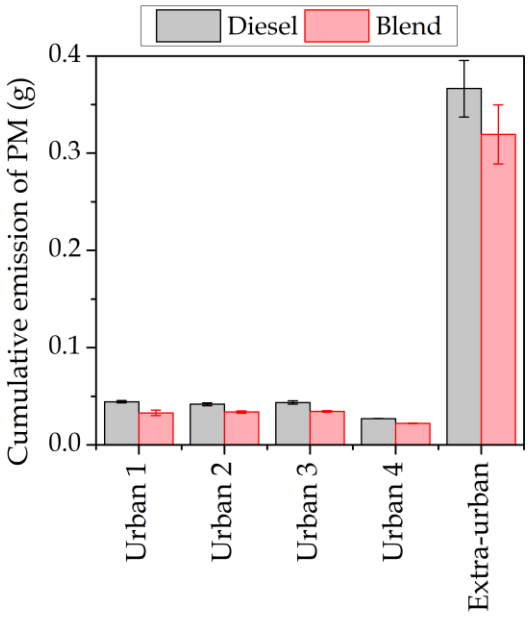

Figure 6.29 Cumulative emission of PM for each sub-cycle

6.3.3.6 Overall emissions in the NEDC

Total emissions of particles (number and mass), nitrogen oxides, carbon monoxide, and total hydrocarbons in the NEDC are shown in Figure 6.30 for diesel and diesel + oxyturpentine blend; the left panel represents the data per km, and the right panel represents the total value. No significant effect is observed in the emissions of carbon dioxide, whereas a ~18 %, ~28 % and ~13 % decrease is evidenced in particulate mass, particulate number and nitrogen oxides, respectively, due to the presence of oxyturpentine in the fuel. On the other hand, a large increase in carbon monoxide and hydrocarbons emissions (~47 % and ~44 % increase, respectively) is observed.

The increase on CO and HC emissions when oxyturpentine was added to diesel fuel is probably due to the higher equivalence ratio and EGR. Besides, the high density (and consequently high surface tension) and volatility of the oxyturpentine mixture respect to that for diesel, accentuated by the low temperature at cold-engine start conditions, can affect the atomization and diffusion processes in the fuel jet. On the other hand, some of the unburnt hydrocarbons remaining after the combustion

reaction of diesel+oxyturpentine blend appear to be more volatile and diffusive than those for diesel, thus leading to an increase in the emission of gaseous hydrocarbons.

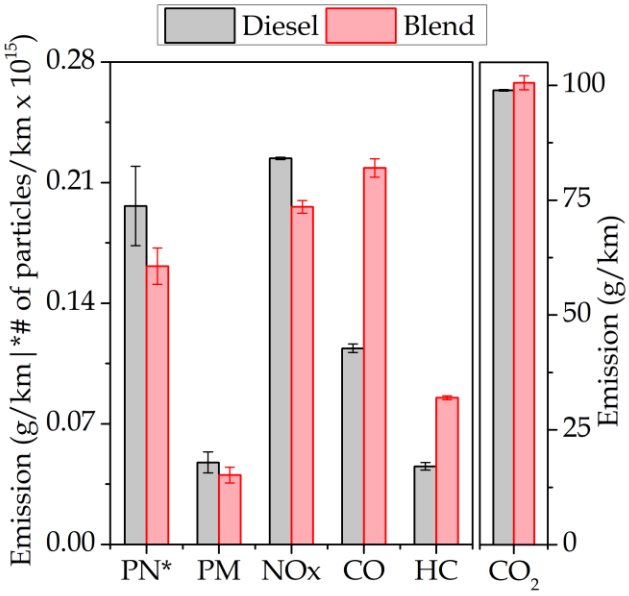

Figure 6.30. Total emissions from the NEDC

NOx emissions were reduced also as a consequence of the increase in EGR, which reduces the local temperature in the combustion chamber, and of the lower cetane number of the fuel, which, in the case of Euro 6 engine, with delayed injection, contributes to reduces temperature peaks and thus nitric oxide formation.

Reduction in particulate matter is a consequence of the presence of oxygen in the fuel molecules, which contributes to soot oxidation. Although typically alcohols reduce notably the particulate material, oxyturpentine has high content of α-pinene which has higher sooting tendency than nopol and diesel, but the trade-off is still dominated by nopol as evidenced by the reduction of PM emissions (despite the higher smoke point of oxyturpentine with respect to diesel).

The Euro 6 standard limits emissions have not been shown in Figure 6.30 because the measurement conditions are different to the ones used in this work. Particularly, the PM emissions were sampled upstream of the diesel particle filter DPF, see Figure 6.16, since the standard requires tailpipe measurements. However, it is well-

known that the efficiency of this type kind of filters is higher than 90% and the tailpipe PM and PN emissions are expected to be significantly lower than the measured values.

Additionally, the use of the Road Load Simulations (RLS) system implies slightly higher emissions than those measured from the actual vehicle (specially NOx emissions). For instance, the simulated cycle in RSL is more abrupt than a human driver and the gear position in RLS is kept in the third position (because it is the most used gear during the urban sub-cycles, the most representative sub-cycle in the NEDC), differing from an actual vehicle where the gear position is an input in the engine control unit (ECU).

These factors impact critical properties in the engine performance such as the combustion chamber temperature (due to the abrupt accelerations) and the injection strategy (which is delayed or advanced due to the gear position in comparison to actual vehicle). Likewise, the results of this work cannot be compared to the current Colombian regulation (Resolution 1111 of 2013) because it is based on Euro 4 regulation and the used engine is a Euro 6.

6.3.4 Remarks of the section

The results of engine tests performed with diesel and oxyturpentine blended at 20 % vol, with respect to diesel fuel are summarized:

- ★ Same carbon dioxide emissions for both fuels.
- ★ Increase in carbon monoxide and unburnt hydrocarbon emissions due to the increase in equivalence ratio and the higher surface tension and volatility of the oxyturpentine than those for diesel fuel.
- ★ Reduction in nitrogen oxides emissions as a consequence of the increase in equivalence ratio and EGR in the engine.
- ★ Significant reductions in particulate material and particle number, associated with the oxygen content of the fuel and the reduction in the aromatic content in the blend.

In diesel vehicles, particulate matter and nitrogen oxides emissions are the tightest ones, thus, their reduction is a highly positive finding with oxyturpentine as a component of diesel fuel.

6.4 Conclusions

- ★ Synthesis of large amounts of oxyturpentine was successfully performed. A slight decrease in activity was observed at large-scale reaction with respect to the vial-scale, which can be attributed to the mixing and mas transfer effects stressed by the scale factor.
- ★ The properties most affected by the presence of oxyturpentine (up to 20 vol.%) in blends with diesel were the lubricity, derived-cetane number, density, heating values, sooting tendency, and cold-flow properties. Although some of these changes in fuel properties impact negatively the blend (e.g., decrease in derived-cetane number and heating value, and increase in density), the final blend presents a good fuel profile. In fact, all the analyzed fuel properties of those blends are within the European standard EN 590:2013 and EN 14214:2013, indicating that they have high quality for diesel applications. In addition, the positive effect observed in other properties, such as lubricity and soot tendency, have positive implications on relevant aspects such as the engine durability and its emissions.
- ★ The results of engine tests performed with the diesel and oxyturpentine (20 vol.%) blend showed significant reductions in particulate material and number, attributed to the oxygen content of the fuel and the reduction in aromatic content, and nitrogen oxides emissions, attributed to the reduction in EGR in the engine. Considering that these emissions are tightly controlled in diesel engines, the blend may have high potential. However, carbon monoxide and hydrocarbons emissions were increased as a consequence of changes in EGR and the equivalence ratio (and probably due to the deterioration of fuel atomization and volatility) by the presence of oxyturpentine.

This page intentionally left blank

Chapter 7. General conclusions and main contributions

7.1. General conclusions

In order to better present the main findings of this Thesis, an overall overview of the results is first presented in Figure 7.1 which highlights the potential and shortcomings of oxygenated compounds from turpentine as biofuels, specifically as components of diesel blends. In particular, oxyfunctionalized turpentine was validated in engine bench tests with good results. However, despite rosin-derivatives' thermal and thermochemical properties, and good activity in the synthesis of methyl ester from rosin, the reduction and methyl esterification rosin proposed in present work would lead to compounds with properties not suitable for fuel applications.

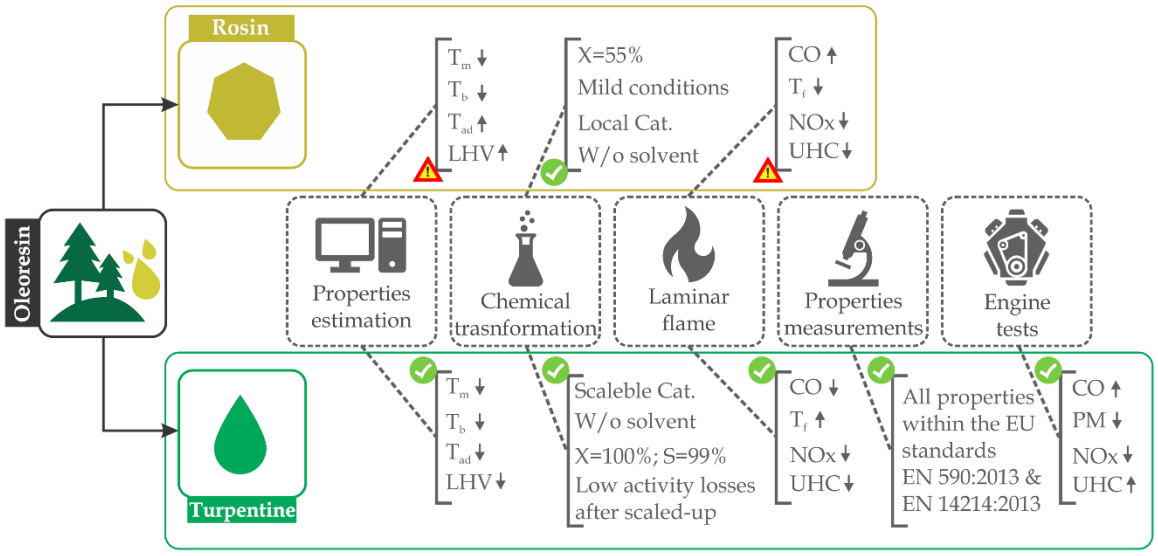

Figure 7.1. Overall overview of the results of the work

7.1.1. Rosin-derived compounds as fuel

Methyl esterification and reduction reactions significantly decrease the boiling and melting temperatures (stronger effect in methyl esterification) and increase the lower

heating value of rosin compounds (stronger effect in reduction). In addition, adiabatic flame temperature of rosin-derived compounds is slightly lower than that for diesel but higher than that for biodiesel. These results suggest the potential of rosin-derived compounds towards fuel applications.

The methyl esterification reaction of rosin with methyl alcohol was achieved successfully at mild conditions and using a low-cost catalyst. The steric effects and low molecular size of methyl alcohol with respect to rosin, together with the fact that the acid group in resin acids is attached to a tertiary carbon, makes the esterification of rosin with methyl alcohol a very difficult reaction. Moreover, little information is available on this transformation.

Some drawbacks were observed with the rosin-derived molecules. Firstly, the decrease in melting and boiling temperatures may not be sufficient for fuel applications, mainly because the expected products would still display high tendency to remain as solid, or to coalesce to form solid nuclei at low temperatures. Secondly, the highest conversion of rosin obtained in present work (and even the values reported in the literature) appears to be low for its application as fuel and, furthermore, does not achieve the value required by current regulations. Finally, the deterioration in the combustion performance observed for laminar flames of *n*-heptane (as diesel surrogate) + methyl ester of abietic acid (AAME, a probe molecule from the methyl esterification of rosin) blends at low contents of AAME suggests that some properties of the fuel were negatively affected by the presence of the rosin-derived compound. For instance, the strong increase in the dew point of the *n*-heptane + AAME blend leads to deterioration in the combustion process.

7.1.2. Turpentine-derived compounds as fuel

The boiling and melting temperatures of the oxygenated-derived compounds from turpentine are increased with respect to the corresponding components of turpentine. In addition, the lower heating value and adiabatic temperature of the flame are decreased after oxyfunctionalization. The final values for these properties of oxyturpentine are suitable for fuel application. In fact, oxygenates from main components of turpentine have similar thermochemical properties than diesel, in

some cases better, and these compounds are liquids at normal conditions (except to borneol), indicating their potential as additive or component of diesel fuels.

The combustion performance of selected oxygenated turpentine-derivates was evaluated in blends with *n*-heptane in a coflow diffusion burner; specifically, nopol, terpineol, myrtenol and borneol were chosen because they can be obtained from turpentine by heterogeneous catalysis and may display other properties relevant to fuel applications (e.g., viscosity). An improvement in combustion performance, particularly with nopol, α-terpineol and myrtenol, was observed, that is, a significant reduction in CO and UHC emissions, and an appreciable increasing in flame temperature were evidenced.

Molecular structure appears to be a key factor in the combustion of these molecules, especially the position of the hydroxyl group. In particular, the longer the distance between the OH group and the bi-cycle (or main ring) the better the performance of the molecule in combustion. The fact that the interatomic distance is related to the strain of the molecule, and that the number of carbons in the side-chain where the hydroxyl group is attached to is associated to the reactivity of the intermediates formed in the oxidation of alcohols, can be related with their performance on the combustion.

Nopol (with two carbons between the OH group and the bi-cycle of the molecule), shows a better performance in combustion than myrtenol (which has similar structure but with just one carbon in between the OH group and the bi-cycle). α-Terpineol, with just one 6-carbon ring, also displays good performance in combustion. Although the thermal and thermochemical properties of oxygenated molecules are slightly worse than those for turpentine components, the presence of oxygen in the fuel molecules improves the oxidation reactions, decreases the tendency carbon atoms in the proximity of the oxygen ones to form particulate material, and contributes to the formation of more carbon dioxide instead of hydrocarbons.

Nopol, which gives the best performance in combustion tests, was synthesized from turpentine (with high β-pinene content, slightly lower than that for α-pinene). The oxyfunctionalization reaction showed high performance (complete conversion and

selectivity towards nopol >99 %), becoming a promising procedure to obtain an oxygenated biofuel from turpentine. In addition, significant amount of α-terpineol was obtained in the reaction product, probably formed by the hydration of limonene and/or α-pinene. Moreover, synthesis of large amounts of oxyturpentine was successfully performed. A slight decrease in reaction activity was observed at large-scale reaction with respect to the vial-scale, which can be attributed to the mixing and mas transfer effects stressed by the scale factor.

The presence of nopol and α-terpineol in the oxyturpentine blend is highly desirable because the main objective of the transformation of turpentine is to oxyfunctionalize the terpene molecules. In addition, the presence of α-pinene in the oxyturpentine mixture is positive because of its high heating value respect to nopol, which increases the amount of heat released in the combustion, as well as its decrease of the viscosity of the mixture.

The effects observed on temperature and CO, NOx and UHC emission lead to conclude that oxyturpentine improves the performance of combustion reaction at the evaluated conditions, which can be associated to the oxygen present in the molecular structure of nopol together with the relatively high heating value of α-pinene.

To evaluate the fuel properties of the oxyturpentine, blends with diesel and oxyturpentine (up to 20 vol.%) were prepared, and several properties were measured. The properties mostly influenced by the presence of oxyturpentine were lubricity, derived-cetane number, density, heating values, sooting tendency, and cold-flow properties. Although some of these changes affect negatively the blend, such as the decrease in derived-cetane number and heating value, and the increase in density, the final blends displays good fuel characteristics. In fact, all the analyzed fuel properties of the blends are within the European standard EN 590:2013 and EN 14214:2013, indicating that they have high quality for diesel applications. Moreover, the positive effect observed in other properties, such as lubricity and soot tendency, have positive implications on relevant parameters, such as the engine durability and its emissions.

In the evaluated fuel properties only the lubricity of diesel was improved with low amounts of oxyturpentine, indicating that the most favorable application of oxyturpentine as additive is as lubricity improver. Other fuel properties which can be improved with low contents of additives such as oxidation state, corrosion, foam-formation and stabilization were not measured.

The results of engine tests performed with a diesel + oxyturpentine (20 vol.%) blend showed a significant reduction in particulate material and nitrogen oxides emissions as a result of the oxygen content of the fuel and the reduction in equivalence ratio in the engine. Considering that these emissions are tightly regulated in diesel engines, these results are highly encouraging. Furthermore, other oxygenated molecules, such as normal alcohols and biodiesel, have shown increase in NOx simultaneously with decrease in PM emissions.

The carbon monoxide and hydrocarbons emissions were increased as a consequence of changes in EGR and the equivalence ratio (and probably due to the deterioration of fuel atomization and fuel volatility) due to the presence of oxyturpentine. However, increase in CO and HC have been also reported with other oxygenated molecules such as methanol, ethanol, and n-butanol.

Laminar flames have shown a reduction in CO and HC emissions when oxyturpentine was added to *n*-heptane, simultaneously with an increased in NOx emissions, while the engine tests showed the opposite effect when oxyturpentine was added to diesel. This apparent contradiction can be associated to the differences in both experimental setups. For instance, in laminar flames the fuel injection is kept constant whereas in the engine is a function of the power output. In addition, the geometry of the combustion chamber in the engine (i.e., a closed space) affects key combustion parameters such as pressure, local temperature, and air availability, while the laminar flames are an open system. These factors may influence the emissions.

7.2. Future work

Future work which can be derived from the Thesis include:

- ★ The characterization of particulate material collected from emissions of oxyturpentine combustion, in particular, morphology, chemical composition, and structure, to complete the assessment of its potential as fuel additive.
- ★ Optimization of the engine injection parameters for the diesel + oxyturpentine blend.
- ★ Evaluation of fuel properties and engine performance of ternary diesel + oxyturpentine + biodiesel mixtures.
- ★ Determination of the surface tension of oleoresin derived molecules such as nopol, myrtenol, terpineol, α- and β-pinene, and oxyturpentine.
- ★ The simultaneous transformation of α- and β-pinene from turpentine to nopol and α-terpineol

7.3. Main contributions of the Thesis

7.3.1. Source code developed

Different source codes with their corresponding graphical user interface (GUI) were developed in Matlab® to facilitate data processing and analysis of the results. Figure 7.2a shows the GUIs used for the estimation of some flame properties, flow regimes and composition of the different streams in the coflow burner, starting from the prepared blends and system properties. Calculations were based on thermodynamic and flow properties of the involved compounds.

Figure 7.2b shows the GUI to facilitate the acquisition of flame properties from the videos recorded for each experiment. This code was particularly important because around 5400 videos (~180 GB of information) were processed. The source code uses image processing of Matlab according to Appendix G. The GUI for the acquisition and visualization of the data from the GC analysis is shown in Figure 7.2c-d. This source code reads the output files from GC software and extract the necessary information for the determination of the sample composition (including statistical analysis) and its visualization.

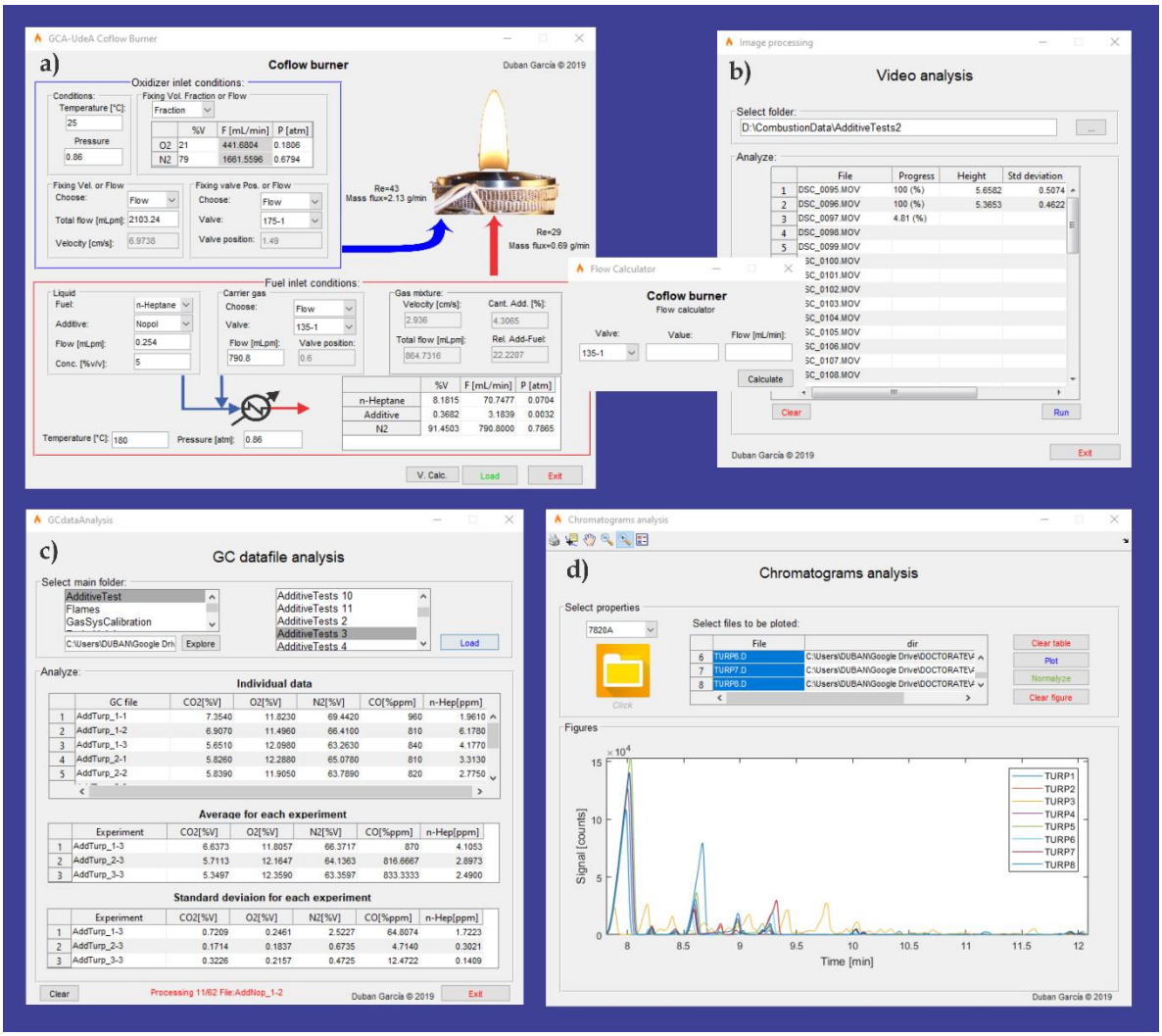

Figure 7.2. Graphical user interfaces for source codes developed in the thesis

7.3.2. Presentations and publications

Table 7.1 shows the events in which the results of the project were presented, either as oral presentations or posters.

Table 7.2 shows the publications derived from this work. All the papers are related to the main objectives of the Thesis, even the paper on the epoxidation of β-pinene because it was a product of the evaluation of oxyfunctionalization of oleoresin molecules.

Table 7.1. Participation in events

Work	Modality	Date
García, D. F., Alarcón, E. A., Bustamante, F., Villa, A. L. "Síntesis de metil-ester de colofonia mediante catálisis heterogénea." *XXVI Congresso Ibero-Americano De Catálise (CICAT 2018)*, Coimbra, Portugal. ISBN: 978-989-8124-23-4.	Poster	September 2018
García, D. F., Bustamante, F., Villa, A. L., Alarcón, E. A. *"*Compuestos de oleorresina de pino como aditivos del combustible diesel." *III Foro Regional Retos Y Oportunidades Del Cambio Climático Para Antioquia, Medellín, Colombia. Radicado #2019030074720 Gobernación de Antioquia.*	Oral presentation	December 2018
García, D. F., Bustamante, F., Villa, A. L., Alarcón, E. A. "Emissions from combustion of fuels with oleoresin-based compounds as additives." *9th European Combustion Meeting (ECM 2019)*, Lisbon, Portugal. Pereira S., and Costa, M., Book of papers of ECM 2019, Paper S5_AIII_36, Instituto Superior Técnico of Lisbon.	Poster	April 2019
García, D., Imbachi-Gamba, C., Jaramillo, M., Bustamante, F., Villa, A. L., and Alarcón, E. "A simple, selective and highly-active catalyst for the epoxidation of β-pinene." *26th North American Catalysis Society Meeting (NAM26 2019)*, Chicago, USA.	Poster	June 2019

Table 7.2. Publications

Work	Status
García, D., Bustamante, F., Alarcón, E., Donate, J.M., Canoira, L., Lapuerta, M. "Improvements of thermal and thermochemical properties of rosin by chemical transformation for its use as biofuel." *Waste Biomass Valorizatio*n, 2019 – DOI 10.1007/s12649-019-00863-y	*Published*
García, D., Bustamante, F., Villa, A. L., Lapuerta, M. and Alarcón, E. "Oxyfunctionalization of turpentine for fuel applications." *Energy & Fuels*, 2019 – DOI 10.1021/acs.energyfuels.9b03742	*Published*
García, D., Ramos, A., Rodríguez, J., Bustamante, F., Alarcón, E., Lapuerta, M. Impact of oxyfunctionalized turpentine on emissions from a diesel engine. *Energy*, 2020 – DOI 10.1016/j.energy.2020.117645	*Published*
García, D., Lapuerta, M., Villa, A.L., Alarcón, E., Bustamantea, F., "Influence of molecular structure of oleoresin-derived compounds on flame properties and emissions from laminar flames" *Environmental Science and Pollution Research,* 2020 – DOI 10.1007/s11356-020-09555-w	*Published*
García, D. F., Jaramillo, M., Bustamante, F., Villa, A. L., Alarcón, E. A. "Epoxidation of β-pinene with hydrogen peroxide under highly-active and low-cost catalyst." *Brazilian Journal of Chemical Engineering*, 2020.	*Accepted*
García, D. F., Bustamante, F., Villa, A. L., Alarcón, E. A. "Esterification of rosin with methyl alcohol using a low-cost material as heterogeneous catalyst." *Revista Facultad de Ingeniería UdeA*, 2020.	*Submitted*
García, D., Bustamante, F., Alarcón, E., Ballesteros, R., Lapuerta, M. Oxyfunctionalized turpentine: Evaluation of properties as automotive fuel.	*In preparation*

This page intentionally left blank

Appendix A. Scaling-up procedures

The first criterium to scale-up a reactor is by relating the residence time for both laboratory (subscript 1) and large (subscript 2) scales, which can be obtained from the relation between the generation per unit volume and the transport of mass by convection (Damkhöler I number), Equation A.1

$$Da_1 = Da_2$$

$$\left(\frac{R_i^{\pm} L}{VC}\right)_1 = \left(\frac{R_i^{\pm} L}{VC}\right)_2 \qquad \textbf{Equation A.1}$$

where $R_i^{\pm}$, L, V and C represent the characteristics variables of chemical generation, length, velocity and concentration, respectively. If initial and/or final concentration, and generation are the same for both scales, then $(L/V)_1 = (L/V)_2$, indicating that residence time for both scales must be equals.

Often, biomass conversion at laboratory scale is conducted in batch and liquid-phase reactors operating isothermally. For the analysis, spherical shape of reactor is chosen. Figure A.1 shows the geometrical parameters of a spherical batch reactor. The working volume inside the reactor fulfill the geometry of partial sphere. Main geometric parameters for partial spheres, according to Figure A.1 are represented by Equation A.2:

$$C = 2\sqrt{h(D-h)}$$

$$V = \frac{\pi}{6} h(3C^2 + h^2) \qquad \textbf{Equation A.2}$$

$$A = \pi h D$$

where C represents the radius of the surface of the reaction mixture at a level of liquid located at a height of h, V is volume occupy by the liquid and A is the surface area for heating transfer.

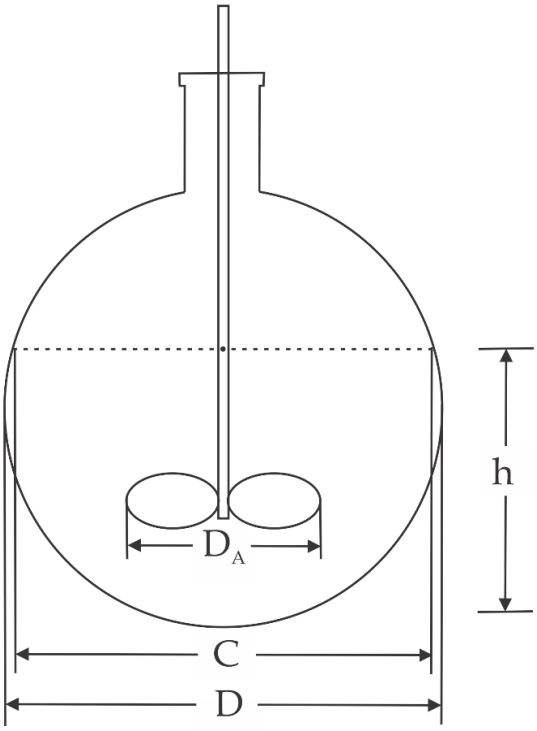

Figure A.1. Geometrical dimensions of reactor

By defining the aspect ratio of the system as $R = h/D$ and solving D from volume expression, Equation A.3 is obtained,

$$D = \frac{V}{\pi(R^2/2 - R^3/3)} \qquad \textbf{Equation A.3}$$

The scale-up factors are defined as the relation of surface (F_A) and volume (F_A) of large (state 2) and laboratory scale (state 1) and using Equation A.3, Equation A.4,

$$F_A = \frac{A_2}{A_1} = \left(\frac{D_2}{D_1}\right)^2$$

$$F_V = \frac{V_2}{V_1} = \left(\frac{D_2}{D_1}\right)^3 \qquad \textbf{Equation A.4}$$

Which mean that $F_A = {F_V}^{2/3}$. For lineal increasing of volume, the surface available for heat transfer increase but at the power of 2/3. Besides, the scale-up factor for diameters is defined as $F_D = D_2/D_1$, which represents the geometrical factor of scaling-up.

The scale-up rule to determine the agitator speed in large scale (N_2) is based on the scale-up ratio from reactor diameters (F_D) and agitator speed in laboratory scale (N_1), Equation A.5,

$$N_2 = N_1 \left(\frac{1}{F_D}\right)^n \qquad \textbf{Equation A.5}$$

where the value of n depends on the purpose of scale-up, thus: one for equal liquid motion, 3/4 for equal suspension of solids, 1/4 for equal and uniform concentration and 2/3 for equal rates of mass transfer for both scales.

The rate of heat transfer from an agitated batch reactor, for endothermic reactions, depends on the physical properties of the reaction mixture, heating medium, reactor geometry and agitation (type and size of agitator and degree of agitation). In this system, heat transfer is due to forced convection in the reaction mixture, conduction through the reactor wall and that for heating media, for instance, convection when the heating is by jackets. Heat transferred to the reaction mixture can be expressed as function of the overall hear transfer (U), the area of heat transfer (A) and the driving force of heat (ΔT), as $Q = UA\Delta T$. It is valid when the reaction mixture and heating medium have the same temperature, which means an idealized situation. In realistic situation the driving force of heat depends of temperatures in reactor and heating medium. A realistic driving force can be represented by Equation A.6,

$$\Delta T_{LMTD} = \frac{\left(T_2 - T_{h_2}\right) - \left(T_1 - T_{h_1}\right)}{\ln\left[\left(T_2 - T_{h_2}\right) \Big/ \left(T_1 - T_{h_1}\right)\right]} \qquad \textbf{Equation A.6}$$

Where T_h and T represent the temperature of heating medium and reaction mixture, respectively, and subscript 1 and 2 are for entering and leaving streams. The overall heat transfer coefficient (U) can be determined by resistances of the transfer heat, neglecting the fouling factor for both inside and outside films respect to the wall of the reactor, according to Equation A.7,

$$\frac{1}{U} = \frac{1}{h_i} + \frac{\mathrm{x}_w}{k} + \frac{1}{h_o} \qquad \textbf{Equation A.7}$$

where $h\ (W/m^2K)$, $k\ (W/mK)$ and $\mathrm{x}_w\ (m)$, represent the transfer coefficient, thermal conductivity and wall thickness of reactor, respectively, and subscripts i and

o represent inside and outside of the reactor. The resistance outside of reactor have been presented for heating type jacket but can be replaced by corresponding one with other kinds of heating. The heat transfer coefficient can be calculated from Nusselt number from Equation A.8. For the fluid inside the reactor and three blades propellers,

$$\frac{h_i D}{k} = 0.64\left(\frac{\rho N D_A^2}{\mu}\right)^{0.67}\left(\frac{C_p \mu}{k}\right)^{0.33}\left(\frac{\mu_b}{\mu_w}\right)^{0.14} \qquad \textbf{Equation A.8}$$

Values for thermal conductivity can be obtained in several databases or handbooks of fluids properties. Besides, several correlations have been proposed to estimate the thermal conductivity of liquids as a function of fluid properties such as critical pressure and temperature, acentric factor and boiling and melting temperature. The work of Latini and coworkers [207] collects the most popular correlations and they propose one more. Some of them are showed in Table A.1.

Table A.1. Correlations to estimate the thermal conductivity of liquids

Author	Correlation
Sato-Riedel	$k = \frac{1.1053}{\sqrt{MW}}\frac{3 + 20(1 - T_r)^{2/3}}{3 + 20(1 - T_{br})^{2/3}}$
Sheffy & Johnson	$k = 1.951\frac{1 - 0.00126(\mathrm{T} - T_m)}{MW^{0.3}T_m{}^{0.216}}$
Gharagheizi *et al*	$k = 1 \times 10^{-4}\left[10\omega + 2P_c - 2T + 4 + 1.908\left(T_b\frac{1.009B^2}{MW^2}\right) + \left(\frac{3.9287MW^4}{B^4}\right) + \frac{A}{B^8}\right]$ where, $A = 3.8588MW^8(1.0045B + 6.5152MW - 8.9756)$ $B = 16.0407MW + 2T_b - 27.9074$
Latini *et al*	$k = 0.434\left(\sqrt{5}\frac{(\Phi - T_r)^2}{\Phi + T_r}\right)^{0.158}$

k and MW are the thermal conductivity (W/mK) and molecular weight (g/mol), T_b and T_m are the boiling and melting temperature (K), P_c is the critical pressure (bar), T_r and T_{br} (K) are the reduced temperature and boiling temperature Φ is the sequence factor of Fibonacci (=1.618033);

To scale-up the reactor keeping similar bulk average temperatures (with equals heat transfer coefficients for both scales), Equation A.8 is used for both laboratory and large scales, obtaining Equation A.9,

$$N_2 = N_1 \left(\frac{D_{A_1}}{D_{A_2}}\right)^{0.46} \qquad \textbf{Equation A.9}$$

For exothermic reactors, the concept of power per unit volume can relates the consume of heat for both large and laboratory scales, $P/V \propto N^3 D_A^2$. The ratio of power per unit volume for large and laboratory scales can be expressed by Equation A.10,

$$(P/V)_2 = (P/V)_1 (F_D)^{0.62} \qquad \textbf{Equation A.10}$$

The consume of heat is proportional to the volume (same fluid in both scales) for exothermic reactions, but the area increases at the power of $2/3$, indicating less surface area available to transferring heat. In some cases, coils are added to increases the surface area. Consequently, the scale-up criterium of constant heat transfer is suitable when the reaction in a batch system is exothermal and the removal of heat is the predominant phenomena [15].

The agitation of liquid-solid systems such as heterogenous catalysis systems, requires special attention and some correlation have been proposed to calculate the minimum speed to keep solids in suspension. One of these correlations is proposed by Zwietering [208], Equation A.11,

$$N_{\min} = \Psi \left(\frac{D}{D_A}\right)^{\alpha} \left[\frac{\left(g(\rho_P - \rho_L)/\rho_L\right)^{0.45} \upsilon_L{}^{0.1} \bar{d}_P{}^{0.2} W_P{}^{0.13}}{D_A{}^{0.855}}\right] \qquad \textbf{Equation A.11}$$

where D_A and D are the diameter of agitator and reactor, respectively, ρ_P and ρ_L are de density of particles and liquid, respectively, υ_L is the kinematic viscosity of the liquid, W_P and $\bar{d}_P$ are the weight ratio of particles to liquid percentage and mean diameter of particles and, α and Ψ depend on the characteristics of the stirrer, for instance, 1.4 and 1.5, respectively, for agitator type propeller. $N_{\min}$ is in revolution per second.

Appendix B. Emission quantification

Starting from flame of oxygenate fuel, at lean combustion and considering water in stream of reaction product, the chemical reaction can be expressed by Equation B.1,

$$C_xH_yO_z + aO_2 + 3.76aN_2 \rightarrow xCO_2 + \frac{y}{2}H_2O + bO_2 + 3.76aN_2 + \text{Others} \quad \textbf{Equation B.1}$$

The mole fraction of species in combustion product in wet basis can be expressed as Equation B.2,

$$x_i^w = \frac{N_\text{i}}{N_T^w} = \frac{N_\text{i}}{x + y/2 + b + 3.76a} \quad \textbf{Equation B.2}$$

By removing water, the mole fraction of species in combustion product in dry basis can be expressed as Equation B.3,

$$x_i^D = \frac{N_i}{N_T^D} = \frac{N_i}{x + b + 3.76a} \quad \textbf{Equation B.3}$$

Combining Equation B.2 and Equation B.3, Equation B.4 is obtained,

$$\frac{\frac{N_i}{N_T^D}}{\frac{N_i}{N_T^W}} = \frac{N_T^W}{N_T^D} = \frac{\frac{N_i}{x + b + 3.76a}}{\frac{N_i}{x + y/2 + b + 3.76a}} = \frac{x + y/2 + b + 3.76a}{x + b + 3.76a} \quad \textbf{Equation B.4}$$

Now, performing an atomic balance of oxygen in Equation B.1 to obtain b, and introducing in Equation B.4, expression Equation B.5 is obtained,

$$\frac{N_T^W}{N_T^D} = \frac{4.76a + z/2 + y/4}{4.76a + z/2 - y/4} \quad \textbf{Equation B.5}$$

The mole fraction of oxygen in combustion product in wet basis can be expressed as Equation B.6,

$$x_{O2}^W = \frac{N_{O2}}{N_T^w} = \frac{b}{x + y/2 + b + 3.76a} \quad \textbf{Equation B.6}$$

And by replacing expression for b, obtained by atomic balance of oxygen, Equation B.7,

$$x_{O2}^{W} = \frac{a - x - z/2 - y/4}{z/2 + y/4 + 4.76a} \qquad \textbf{Equation B.7}$$

Variable a can be obtained from Equation B.7, as Equation B.8,

$$a = \frac{x + (1 + x_{O2}^{w})(z/2 + y/4)}{1 - 4.76x_{O2}^{W}} \qquad \textbf{Equation B.8}$$

Similar procedure but starting from mole fraction of oxygen in combustion product in dry basis leads to Equation B.9,

$$a = \frac{x + (1 - x_{O2}^{D})(y/4 - z/2)}{(1 - x_{O2}^{D}4.76)} \qquad \textbf{Equation B.9}$$

The relation between molar concentration of species in wet and dry basis can be expressed as Equation B.10,

$$\frac{x_i^D}{x_i^W} = \frac{N_T^W}{N_T^D} \qquad \textbf{Equation B.10}$$

Converting dry to wet basis or vice versa consists in computing the parameter a (stoichiometric coefficient of oxygen in reactant stream) by using Equation B.8 or Equation B.9, using it to computes the relation of total mol by using Equation B.5 and finally computing other concentration according to Equation B.10.

Large dilution in coflowing configuration is a big challenge to measure emissions. Coflowing air and carrier gas dilutes the emissions, and low concentration of CO, CO_2, NOx and O_2 are expected. A methodology used in literature and industry to overcome this drawback is to correct (or convert) the emissions to 15% oxygen concentration [77], which standardize the concentration of diluted samples. Procedure is similar to correction between wet and dry basis. By analogy with Equation B.10, concentration at desired conditions can be obtained from Equation B.11,

$$x_i^{\text{Desired}} = x_i^{\text{measured}} \left(\frac{N_T^{\text{Measured}}}{N_T^{\text{Desired}}} \right) \qquad \textbf{Equation B.11}$$

Equation B.12 and Equation B.13 can be used to obtain total mole in wet and dry basis, respectively,

$$N_T^W = 4.76\left[\frac{x + (1 + x_{O2}^W)(z/2 + y/4)}{1 - 4.76x_{O2}^W}\right] + y/4 + z/2$$ **Equation B.12**

$$N_T^D = 4.76\left[\frac{x + (1 - x_{O2}^D)(y/4 - z/2)}{(1 - 4.76x_{O2}^D)}\right] - y/4 + z/2$$ **Equation B.13**

Appendix C. Mathematical expressions for error propagation

The standard deviation of experimental concentrations, together with the experimental error associated to the other measurements involved in the computation of emission indices were considered to obtain the propagated error for each emission indices. The mathematical expressions for each contribution to the total error associated to the emission indices are presented in Table C.1.

Table C.1. Expressions for errors of emission indices

Equation	Error
Emission index $EI_i = \left(\frac{x \cdot x_i}{x_{CO2} + x_{CO}}\right)\left(\frac{MW_i}{MW_\mathrm{f}}\right)$	$\sigma_{EI_i} = EI_i\left[\frac{\sigma_x}{x} + \frac{\sigma_{x_i}}{x_i} + \frac{\sigma_{x_{CO_2}} + \sigma_{x_{CO}}}{x_{CO2} + x_{CO}}\right]$
Total number of moles in dry basis $N_T^d = 4.76\left[\frac{x + \left(1 - x_{O2}^d\right)(y/4 - z/2)}{\left(1 - 4.76x_{O2}^d\right)}\right] - y/4 + z/2$	$\sigma_{N_T^d} = 4.76N_T^d\left[\frac{\sigma_x + \sigma_{x_{O_2}^d}\left(\sigma_y/4 + \delta\sigma_z/2\right)}{x + \left(1 - x_{O2}^d\right)(y/4 - z/2)} + \frac{4.76\sigma_{x_{O_2}^d}}{\left(1 - 4.76x_{O2}^d\right)}\right] + \frac{\sigma_y}{4} + \frac{\sigma_z}{2}$
Molar fraction of species *i* at desired conditions $x_i^{\mathrm{desired}} = x_i^{\mathrm{measured}}\left(\frac{N_T^{\mathrm{measured}}}{N_T^{\mathrm{desired}}}\right)$	$\sigma_{x_i^{\mathrm{desired}}} = x_i^{\mathrm{desired}}\left[\frac{\sigma_{x_i^{\mathrm{measured}}}}{x_i^{\mathrm{measured}}} + \frac{\sigma_{N_T^{\mathrm{measured}}}}{N_T^{\mathrm{measured}}}\right]$
Molar fraction of species *i* in dry basis $x_i^d = x_i^w\frac{N_T^w}{N_T^d}$	$\sigma_{x_i^d} = x_i^d\left[\frac{\sigma_{x_i^w}}{x_i^w} + \frac{\sigma_{N_T^w/N_T^d}}{N_T^w/N_T^d}\right]$ $\sigma_{x_i^w} = x_i^w\left[\frac{\sigma_{x_i^d}}{x_i^d} + \frac{\sigma_{N_T^w/N_T^d}}{N_T^w/N_T^d}\right]$
Ratio of total moles in dry and wet basis $\frac{N_T^w}{N_T^d} = \frac{4.76a + z/2 + y/4}{4.76a + z/2 - y/4}$	$\sigma_{N_T^w/N_T^d} = \frac{N_T^w}{N_T^d}\left\{\left[\frac{4.67\sigma_a + \sigma_z/2 + \sigma_y/4}{4.76a + z/2 - y/4}\right] + \frac{4.67\sigma_a + \sigma_z/2 + \sigma_y/4}{4.76a + z/2 - y/4}\right\}$
Stoichiometric coefficient of oxygen $a = \frac{x + (1 + x_{O2}^w)(z/2 + y/4)}{1 - 4.76x_{O2}^w}$ $a = \frac{x + \left(1 - x_{O2}^d\right)(y/4 - z/2)}{\left(1 - x_{O2}^d 4.76\right)}$	$\sigma_a = a\left[\frac{\sigma_x}{x} + \frac{\sigma_{x_{O2}^w}}{1 + x_{O2}^w} + \frac{\sigma_z}{z} + \frac{\sigma_y}{y} + \frac{\sigma_{x_{O2}^w}}{x_{O2}^w}\right]$ $\sigma_a = a\left[\frac{\sigma_x}{x} + \frac{\sigma_{x_{O2}^d}}{1 + x_{O2}^d} + \frac{\sigma_z}{z} + \frac{\sigma_y}{y} + \frac{\sigma_{x_{O2}^d}}{x_{O2}^d}\right]$
Number of carbon atoms in the fuel	$\sigma_x = \left(NC_A + NC_{hep}\right)\cdot\sigma_{W_A}$

$x = NC_A \cdot W_A + NC_{hep} \cdot W_{hep}$	
Number of hydrogen atoms in the fuel $y = NH_A \cdot W_A + NH_{hep} \cdot W_{hep}$	$\sigma_y = \left(NH_A + NH_{hep}\right) \cdot \sigma_{W_A}$
Number of oxygen atoms in the fuel $z = NO_A \cdot W_A + NO_{hep} \cdot W_{hep}$	$\sigma_z = \left(NO_A + NO_{hep}\right) \cdot \sigma_{W_A}$
$MW_{\mathrm{f}} = MW_A W_A + MW_{hep} \cdot W_{hep}$	$\sigma_{MW_{\mathrm{Fuel}}} = \left(MW_A + MW_{hep}\right) \cdot \sigma_{W_A}$

Symbols

a	Stoichiometric coefficient of oxygen per one mole of fuel
b	Parameter to balancing the chemical reaction
x_i	Molar fraction of species *i*
x	Number of carbon atoms in the fuel
y	Number of hydrogen atoms in the fuel
z	Number of oxygen atoms in the fuel
N	Number of moles
NC	Number of carbon atoms in pure components
NH	Number of hydrogen atoms in pure components
NO	Number of oxygen atoms in pure components
MW	Molecular weight, g/mol
W	Mass fraction

Subscripts and superscripts

d	Dry basis
f	Fuel
i	Species *I* in combustion product
hep	*n*-Heptane
w	Wet basis
A	Added molecule (nopol, myrtenol, terpineol, borneol and α- and β-pinene)
T	Total species
W	Mass fraction

Appendix D. GC technique to combustion gases

Table D.1. Some configurations used for GC analysis of combustion gases

Reference	Column(s)	Detector	Gases
Bannett, D. [209]	I Porapak Q; II delay coil; III 5A molecular sieve	TCD	N_2, O_2, CH_4, N_2O and CO_2
Solomon, P. [209]	I Porapak Q; II Molecular Sieve 13X. Usage 6-port valve to bypass column II	TCD	N_2, O_2, CH_4, N_2O and CO_2
Nand S. & Sarkar M. [210]	I Porapak Q; II Molecular sieve 5A. Usage 6-port valve to bypass column II	TCD	N_2, O_2, CH_4, CO, CO_2, ethane, propane, isobutene, n-butane
Dhole, V. & Kadam, V. [211]	I Porapak Q; II Molecular sieve 5A. Usage 6-port valve to bypass column II	TCD	CO, CO_2, CH_4, O_2 and N_2
Li, X. & Guan, Z. [212]	I PLOT Al_2O_3; II Porapak Q & Molecular sieve 5A; three valves	FID & TCD	H_2, CO_2, O_2, N_2, CH_4 and CO by TCD; C_{11}-HCs by FID
Rogies, F. et. al. [213]	I Poraplot U; II Molsieve 5A; III DB-1. Into two GC systems.	FID & TCD	CO_2, CO and $<C_4$-HCs by TCD; C_8-HCs by FID
Zeewu, J., et. al. [214]	ShinCarbon ST column; usage of methanizer to converts CO and CO2 into CH4	FID/TCD	CO and CO_2 in very low levels, O_2 and N_2
Zou, J. & Wang, C. [213]	I PoraBOND Q PT; II CP-Molsieve 5Å PT; III HayeSep Q as precolumn. Two valves (6 and 10 ports)	TCD	Ar, O_2, H_2, N_2, CH_4, CO_2, CO and C_1-C_2-HCs.
Ji, Z. [215]	HP-PLOT Q	TCD	N_2, CH_4, CO_2, C_2C_6, H_2O, C_7-HCs

Appendix E. Calibration of NO and NO_2

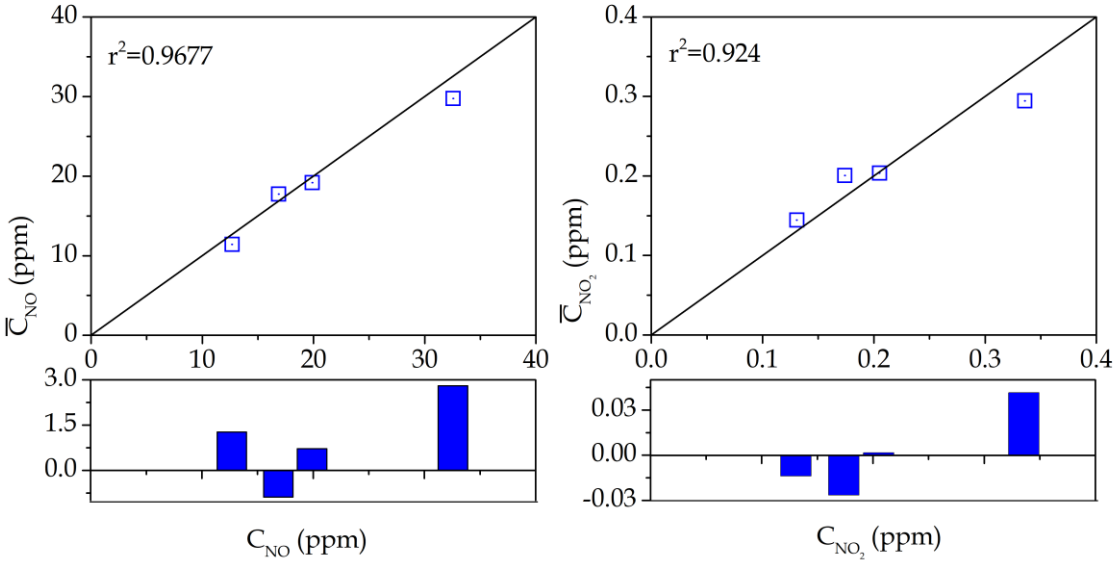

Figure E.1. Parity plots of NO and NO_2 calibration

Appendix F. Calibration of combustion species measured by GC

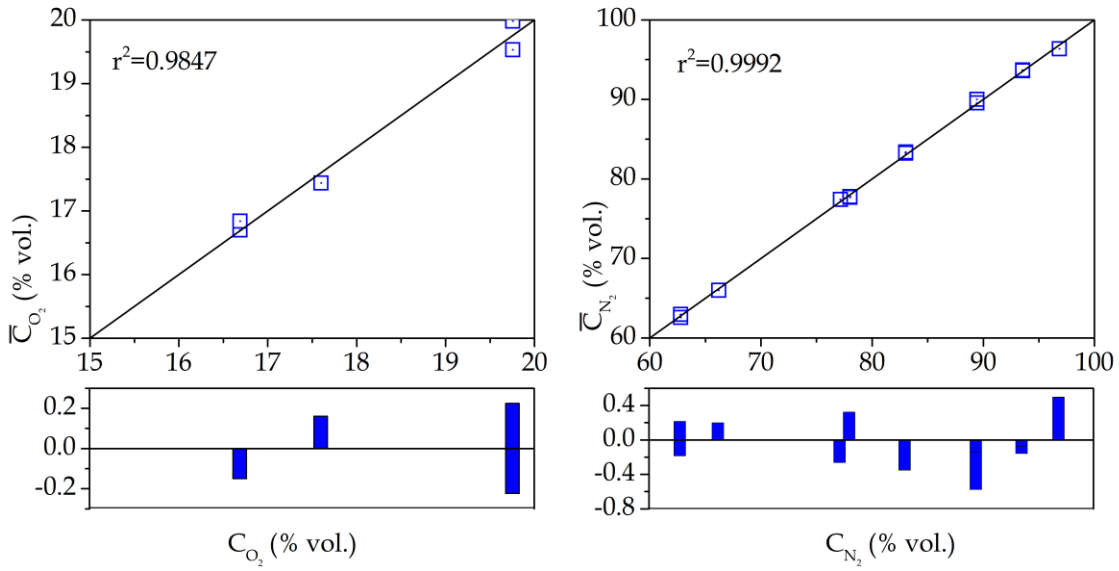

Figure F.1. Parity plots of O_2 and N_2 calibration

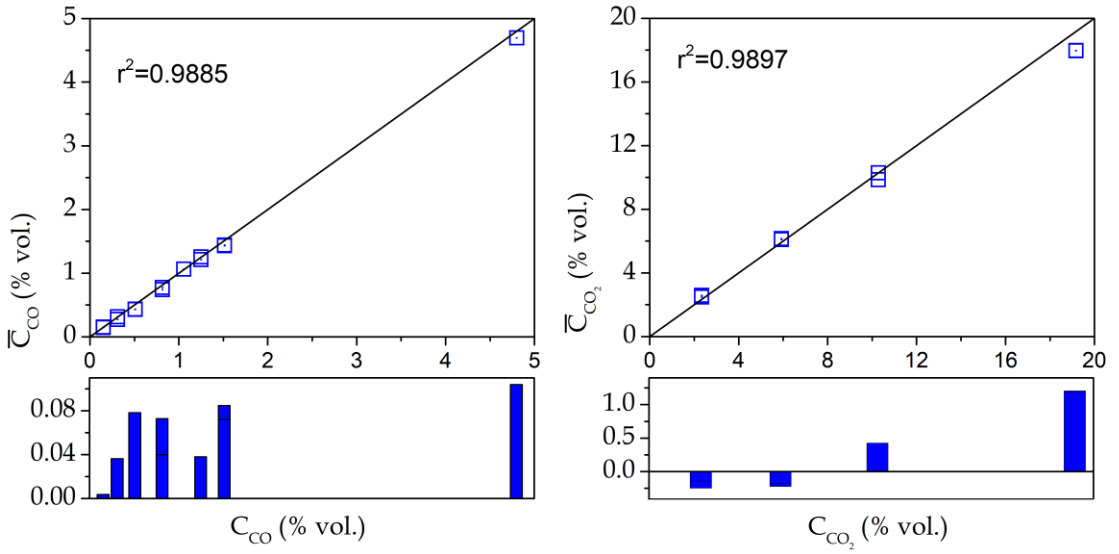

Figure F.2. Parity plots of CO and CO_2 calibration

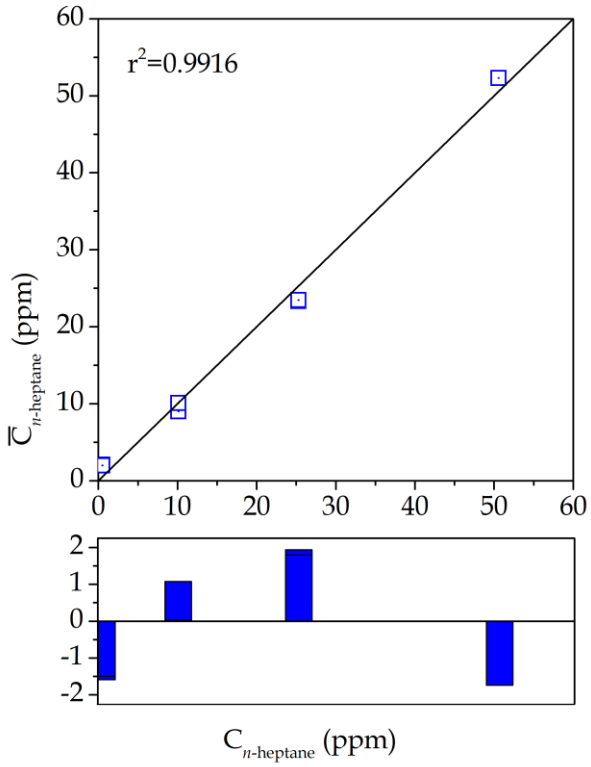

Figure F.3. Parity plots of *n*-heptane calibration

Appendix G. Source code for getting flame size

```
function [FlameHeight, LiftOff]=GetFrames(File,indice,handles)
Video = VideoReader(File);
Duration=Video.Duration;
FPS=Video.FrameRate;
if Duration<60 %Only one minute of video!
    NumberFrames=round(Duration*FPS);
else
    NumberFrames=round(60*FPS);
end
FlameHeight=zeros(1,NumberFrames);
LiftOff=zeros(1,NumberFrames);
Paso=1;
DataTable=get(handles.ProcessingTable,'data');
Angle=3.55;
ZoomLiftOff=[773.5 533.5 144 106];
alea=randi(NumberFrames,1,5);
for k = 1:Paso: NumberFrames
    Perc={[num2str(100*k/NumberFrames,'%.2f'),' (%)']};
    DataTable(indice,2)=Perc;
    set(handles.ProcessingTable,'data',DataTable)
    pause(0.01)
    Frame=read(Video,k);
    GrayFrame = rgb2gray(Frame);
    GrayFrame = imrotate(GrayFrame,Angle);
    Flame = GrayFrame > 95;
    stats = regionprops('table',Flame,'BoundingBox')
    try
        A=stats.BoundingBox;
        A=sortrows(A,3);
        if A(end-1,1)+A(end-1,3)>A(end,1)
            BurnerIndex=length(A(:,1))-2;
        else
            BurnerIndex=length(A(:,1))-1;
        end
        ZoomLiftOff1=[A(BurnerIndex,1)+A(BurnerIndex,3)- ...
10,A(BurnerIndex,2)+(A(BurnerIndex,4)/2)- ...
 (ZoomLiftOff(4)/2),A(BurnerIndex,3),ZoomLiftOff(4)];
    catch
        A=[];
        ZoomLiftOff1=ZoomLiftOff;
    end
    Flame2 = imcrop(GrayFrame,ZoomLiftOff1);
    Flame2 = Flame2 < 25;
    try
        stats2 = regionprops('table',Flame2,'BoundingBox');
        A2=stats2.BoundingBox;
```

```
47          A2=sortrows(A2,4);
48      catch
49          A2=[];
50      end
51      try
52          A3=[ZoomLiftOff1(1)+A2(end,1) ZoomLiftOff1(2)+ ...
53  A2(end,1) A2(end,3) A2(end,4)];
54          bandera=1;
55      catch
56          A3=A2;
57          bandera=2;
58      end
59      for ia=1:length(alea)
60          if isequal(alea(ia),k)
61              if bandera==1
62                  Figure1=figure('NumberTitle','off','Name', ...
63  'Flame Height') ;
64                  imshow(GrayFrame);
65                  hold on
66                  rectangle('Position', A(end,:),'EdgeColor' ...
67  ,'m', 'LineWidth', 1)
68                  rectangle('Position', A(BurnerIndex,:), ...
69  'EdgeColor','y', 'LineWidth', 1)
70                  rectangle('Position', A3,'EdgeColor','r', ...
71   'LineWidth', 1)
72                  print(Figure1,'-dpng','-r600',[File(1:end- ...
73  4),'_SALIDA',num2str(k)])
74                  set(Figure1,'Visible','off')
75                  clearvars Figure1
76              end
77          end
78      end
79      try
80          if bandera==1
81              if length(A(:,1))>2
82                  FlameHeight(k)=(A(end,1)+A(end,3))- ...
83  (A(BurnerIndex,1)+A(BurnerIndex,3));
84              else
85                  FlameHeight(k)=(A(2,1)+A(2,3))-(A(1,1)+A(1,3));
86              end
87              LiftOff(k)=A2(end,3);
88          end
89      catch
90          FlameHeight(k)=-1.01;
91          LiftOff(k)=-1.01;
92      end
93      bandera=2;
94  end
95  Perc=0;
96  Conversion=(8/823.11);
97  FlameHeight=Conversion.*FlameHeight(FlameHeight>0);
98  LiftOff=Conversion.*LiftOff(LiftOff>0);
99  FlameHeight(~any(~isnan(FlameHeight)))=[];
100 LiftOff(~any(~isnan(LiftOff)))=[];
```

An example of a plot generated in Line 74 is shown in Figure G.1,

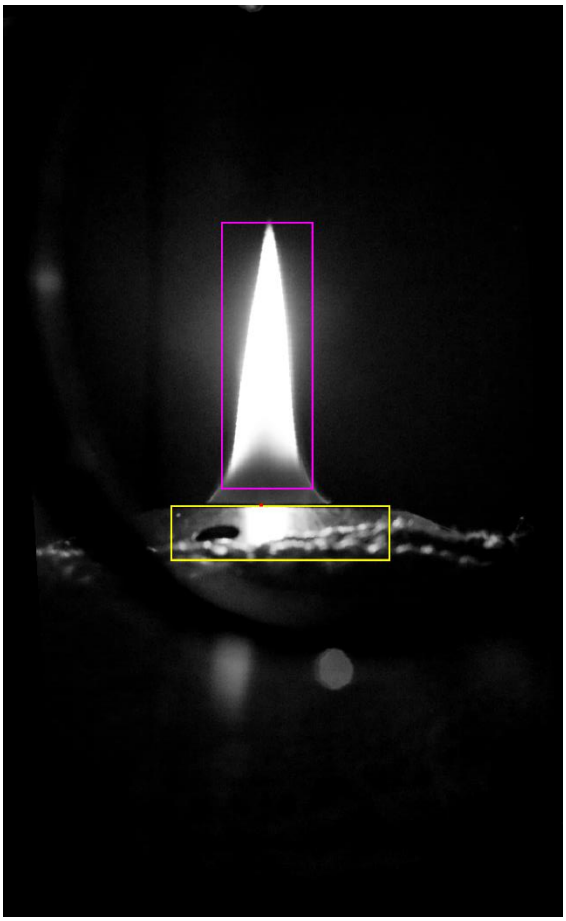

Figure G.1. Picture obtained as a support of the analysis

Appendix H. Source code for getting temperatures

```
clear all, clc, close all, clear all
% Read image
MainFolder='D:\CombustionData\AdditiveTests2';
Additives={'b-Pinene'};
load templatesDN2.mat
global templates
for i=1:length(Additives)
    Files1=dir([MainFolder,'\',Additives{i},'\Temperature']);
    for j=1:length(Files1)
        if Files1(j).isdir==0
            Video = VideoReader([MainFolder, ...
'\',Additives{i},'\Temperature\',Files1(j).name]);
            NumberFrames=round(Video.FrameRate*Video.Duration);
            Acum=0;
            disp(['File: ',Files1(j).name])
            for k=60:NumberFrames-60
                Acum=Acum+1;
                Time=Video.FrameRate*Acum;
                Frame=read(Video,k);
                %detect one point to fixing the zoom on numbers
                FrameFiltered = imsubtract(Frame(:,:,1), ...
rgb2gray(Frame));
                %Use a median filter to filter out noise
                FrameFiltered = medfilt2(FrameFiltered, [3 3]);
                % Convert the grayscale image into a binary image
                FrameFiltered = im2bw(FrameFiltered,0.18);
                % Remove all those pixels less than 300px
                FrameFiltered = bwareaopen(FrameFiltered,300);
                % Label all the connected components in the
image.
                FrameFiltered2 = bwlabel(FrameFiltered, 8);
                % A set of properties for each labeled region.
                stats = regionprops(FrameFiltered2,
'BoundingBox');
                for ii=1:length(stats)
                    A(ii,:)=stats(ii).BoundingBox;
                end
                A=sortrows(A,4,'descend');
                GrayFlame = rgb2gray(Frame);
                GrayFlame=imrotate(GrayFlame,0);
                GrayFlameCrop1 = imcrop(GrayFlame,A(1,:));
                GrayFlameCrop2 = imcrop(GrayFlame,A(2,:));
                GrayFlameCrop3 = imcrop(GrayFlame,A(3,:));
                threshold1 = graythresh(GrayFlameCrop1);
                threshold2 = graythresh(GrayFlameCrop2);
                threshold3 = graythresh(GrayFlameCrop3);
```

```
47                  imagen1 =~im2bw(GrayFlameCrop1,threshold1);
48                  imagen2 =~im2bw(GrayFlameCrop2,threshold2);
49                  imagen3 =~im2bw(GrayFlameCrop3,threshold3);
50                  % Remove objects containing fewer than 100 pixels
51                  imgn1 = bwareaopen(imagen1,1000);
52                  imgn2 = bwareaopen(imagen2,1000);
53                  imgn3 = bwareaopen(imagen3,1000);
54                  % Compute the number of letters in template file
55                  num_letras=size(templates,2);
56                  % Resize letter (same size of template)
57                  img_r1=imresize(imgn1,[54 22]);
58                  img_r2=imresize(imgn2,[54 22]);
59                  img_r3=imresize(imgn3,[54 22]);
60                  letter1=read_number(imcomplement(img_r1), ...
61  num_letras);
62                  letter2=read_number(imcomplement(img_r2), ...
63  num_letras);
64                  letter3=read_number(imcomplement(img_r3), ...
65  num_letras);
66                  % Letter concatenation
67                  word=[letter1 letter2 letter3];
68                  Temperature(Acum)=str2double(word);
69              end
70              save(['SalidasT\',Files1(j).name(1:end-...
71  4),'.mat'],'Temperature')
72              clearvars Temperature word letter1 letter2 letter3...
73  img_r1 img_r2 img_r3
74          end
75      end
76  end

77  function number=read_number(image,num_digits)
78  global templates
79  comp=[ ];
80  for n=1:num_digits
81      sem=corr2(templates{1,n},image);
81      comp=[comp sem];
82  end
83  try
84      vd1=find(comp==max(comp));
85      if length(vd1)<2
86          vd=vd1;
87      else
88          vd=vd1(1);
89      end
90  catch
91      vd=1;
92  end
93  if vd==1
94      number='0';
95  elseif vd==2
96      number='1';
97      elseif vd==3
98      number='2';
99      elseif vd==4
100     number='3';
101     elseif vd==5
```

```
102         number='4';
103         elseif vd==6
104         number='5';
105         elseif vd==7
106         number='6';
107         elseif vd==8
108         number='7';
109         elseif vd==9
110         number='8';
111         elseif vd==10
112         number='9';
113     else
114         number='-';
115     end
```

An example of the analysis is shown in Figure H.1,

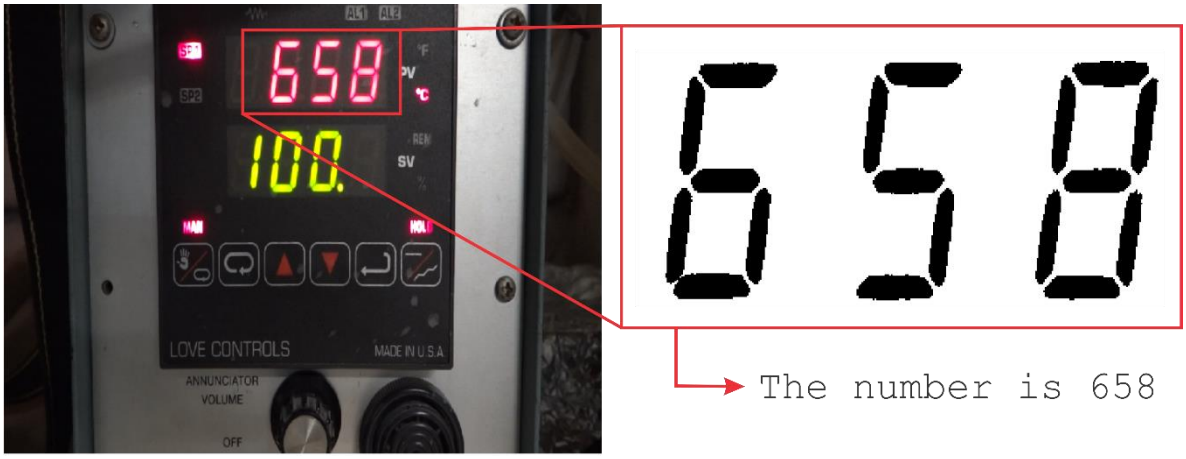

Figure H.1. Picture obtained as a support of the analysis

Appendix I. Previous experiments to set combustion conditions

To evaluate the influence of different fuels (diesel surrogate with different additives) on the flame and emissions, several variables must be fixed. Intrinsic variables of the flame such as carrier gas flow, air flow and fuel/air ratio, and sampling properties such as sample flow and probe properties (internal diameter, HAB and material) must be analyzed. Temperature, species concertation and flame size were measured as a function of flame and sampling variables. When the measured temperature and composition data kept constant, the flame reached the thermal/chemical equilibrium [216]. In all cases, the pump was set to provide 0.243 mL/min of volumetric flow of pure *n*-heptane as fuel, the thermocouple was fixed at 9.76 mm from the fuel port and a gas sampling probe was located at half-height of the flame.

I.1. Flame stability

I.1.1. Probe selection

Three different probes were tested to analyze the influence mainly of probe diameter, on the performance of sampling, specifically in species concentration of reaction product. A quartz (0.6 mm internal diameter) and uncooled stainless-steel probes (1.93- and 4.3-mm internal diameter) were selected to be tested. UHC did not detected by using quartz and stainless-steel (1.93 mm internal diameter) probes, still changing the height of the probe. 4.3 mm internal diameter (stainless-steel) probe, on the other hand, allows the detection of UHC and separation of gases species were well defined even by changing the height of probe.

I.1.2. Influence of flow of carrier gas

According to a literature revision, laminar flames are tested with fuel velocities between 1 to 50 cm/s, getting Reynolds numbers for fuel under 2000 [141]–[147], [217]–[223]. Our burner and facilities lead a variation in volumetric flow of carrier gas

(nitrogen) up to 1000 mL/min. This mean that the velocity of carrier gas-fuel mixture must be lower than ca. 3.5 cm/s, which conduce a Reynolds number for fuel of ca. 40 (laminar flow). 0.95, 1.45, 1,95, 2.45, 2.95 and 3.4 cm/s were tested as nitrogen-fuel mixture velocities by setting 200, 350, 500, 650, 800 and 950 mL/min of nitrogen. Air flow was fixed at 2100 mL/min (7cm/s velocity and a Reynolds number for air of 44). The influence of stream flow of carrier gas on height of flame is showed in Figure I.1,

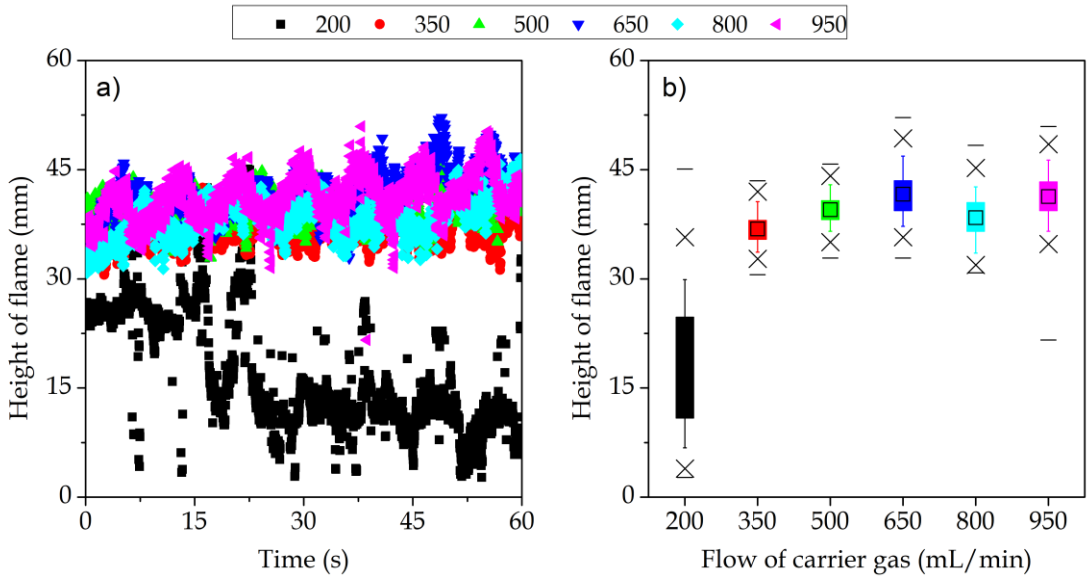

Figure I.1. Influence of stream flow of carrier gas on height of flame

In Figure I.1a, the tendencies suggest that the height of the flame exhibit a variation around an average value in time. At 200 mL/min of nitrogen, the height of flame displays high variation. The height of the flame apparently increases with the flow of carrier gas as showed in Figure I.1b. The variation in height of the flame is lowest at 350 and 400 mL/min of nitrogen, because the range of the data is about 13 mm in contrast with other nitrogen flows where this ranges is higher than 17 mm. Likewise, the range between second and third percentile is 2.5 mm for flames at 350 and 500 mL/min, while for other nitrogen flows this range is higher than 4 mm. Some outliers are presented at these flows, but they represent less than 2% of all measurements.

Temperature of the flame at different stream flow of carrier is showed in Figure I.2. As discussed previously, the flame at 200 mL/min display more instability than other stream flows of gas carrier because temperature shows high oscillation. Likewise,

all tendencies in Figure I.2a exhibit a variation around an average value in time. The higher the stream flow of carrier gas, the lower the temperature, probably due to a convection phenomenon. The variation in temperature for flames at 350 and 500 mL/min nitrogen flow is lowest than other nitrogen flows tested in present work. This suggests more stability for flames at 350 and 500 mL/min nitrogen flow, with measurement variations about 20°C, contrasting with more than 26°C for other stream flows of carrier gas, as showed in Figure I.2b.

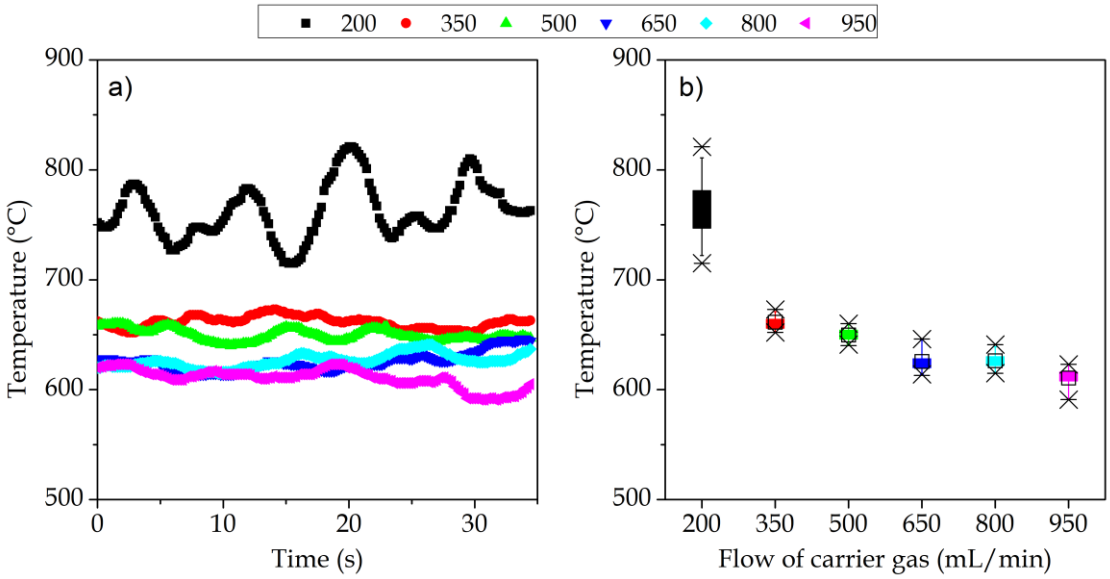

Figure I.2. Influence of stream flow of carrier gas on temperature of flame

The NO-concentration of flames at different stream flow of carrier gas are showed in Figure I.3. In Figure I.3a, it is possible to appreciate that all measurements exhibit a variation in NO-concentration around an average value in time. NO-concentration at extreme values of stream flow of carrier gas tested in present work display similar values (about 1 ppm). The flame size at different stream flows of carrier gas presents a variation, while the probe is fixed at same position for all flames, which means different relative position of probe on the flames. This variation in relative position of probe could explain the variation in NO-concentration for different stream flows of carrier gas. The variation in NO-concentration of flames at different stream flows of carrier is ca. 0.5 ppm (Figure I.3b). This variation is probably due to the change in flame size.

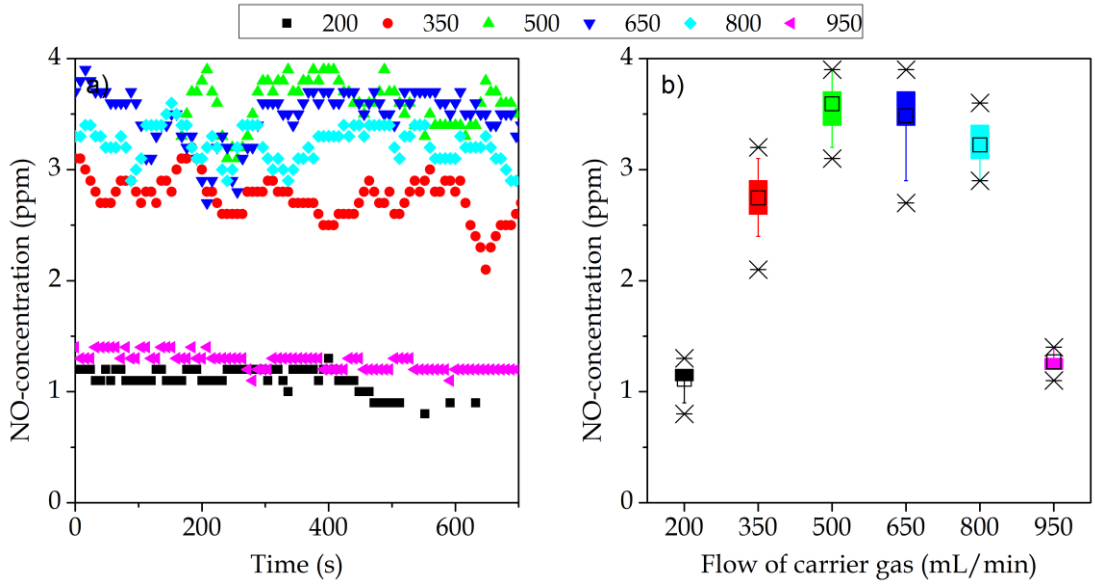

Figure I.3. Influence of stream flow of carrier gas on NO-concentration of flame

I.1.3. Influence of flow of air

Most experiments for laminar flames involve air velocities between 1 to 120 cm/s, getting Reynolds numbers for oxidant under 2000 [141]–[147], [217]–[223]. 0, 630, 1374 and 2118 mL/min stream flow of air were tested, which conduce to 0, 2, 4.6 and 7 cm/s. The height of the flame at these air flows is showed in Figure I.4.

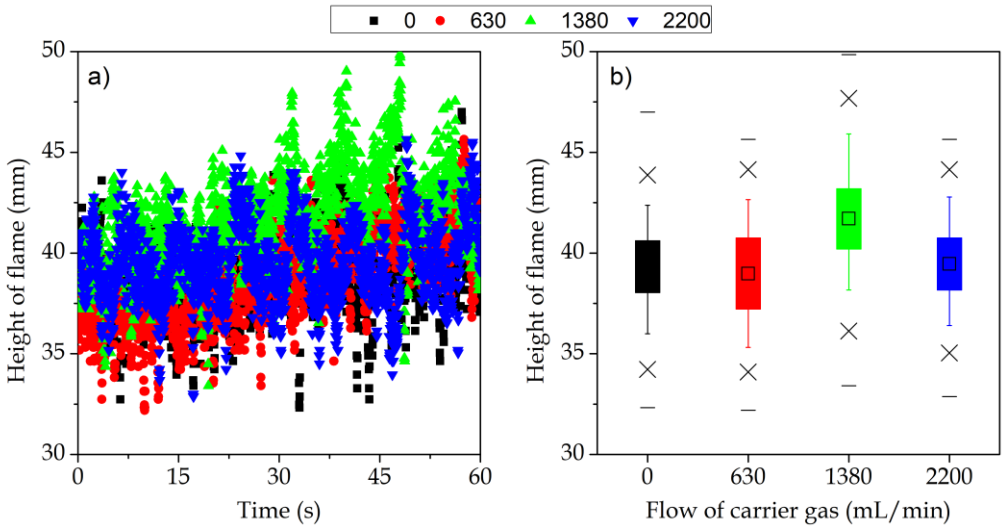

Figure I.4. Influence of stream flow of air on height of flame

Similar behavior of height of flame in time at different stream flows of air are displayed in Figure I.4a. In Figure I.4b, it is most evident the similar variation of the

Temperature performance of flames at different stream flow of air are showed in Figure I.5. The flame without coflowing air has more variation in temperature than other air flows (more than 50°C, view Figure I.5a and the flame a 1380 mL/min display the lowest variation (about 15°C). This result suggests that 1380 mL/min of stream flow of air is better than other tested air flows for flame stability in terms of temperature (view Figure I.5b).

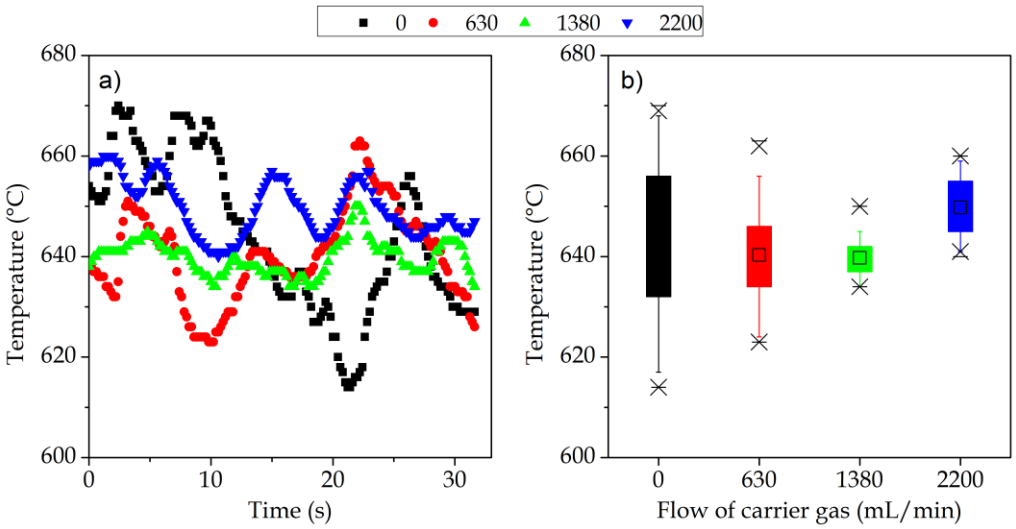

Figure I.5. Influence of stream flow of air on temperature of flame

Figure I.6 shows the performance of NO-concentration of flames at different stream flow of air. Appreciable variation in NO-concentration is showed in Figure I.6a for air flow of 2200 mL/min, and an increasing in nitric oxide production is observed at this stream flow of air. The higher the stream flow of air, the higher the NO-concentration. This suggests that the production of nitrogen oxides is proportional to the amount of nitrogen available, which can be explained by Zeldovich mechanism [77].

As no variation in size, species concentration and temperature of the flame is related with flame stability, recommended values for the nitrogen flow (as carrier gas) and air flow are ranged between 353-499, and >0-1380 mL/min, respectively.

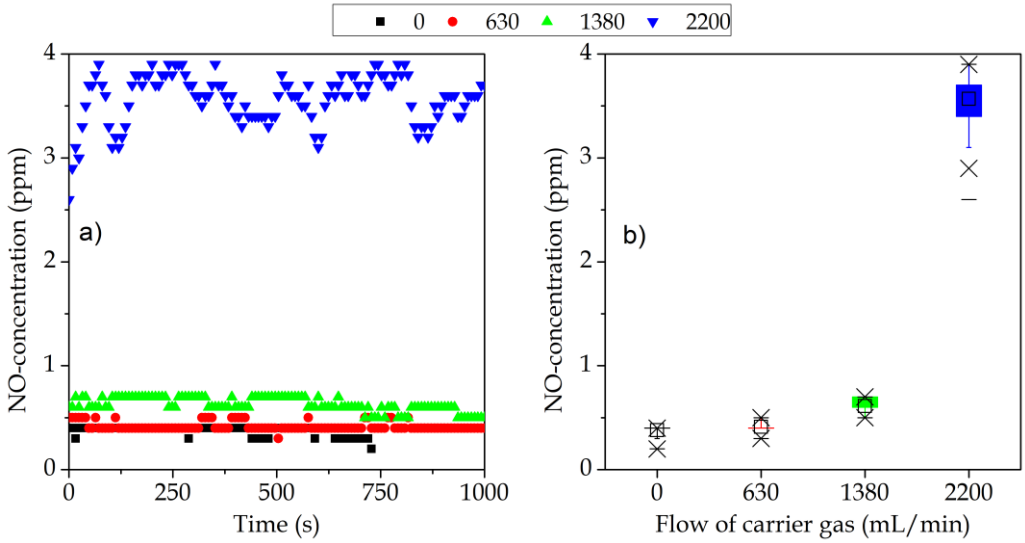

Figure I.6. Influence of stream flow of air on NO concentration of flame

I.2. Height of probe

The height of probe (stainless-steel and 4.3 mm internal diameter) must be fixed in a position over the flame and in a centerline to tests different additives. For it, it is important to guarantee that species concentration does not change in time [140], [216], [222], [224], [225]. Works such as those from Drake and coworkers [226], and, Fujimori and coworkers [216], establish a height of probe equivalent to twice the flame height as minimum distance to get stable NOx emission index for turbulent coflow diffusion flames, since Hemanson and coworkers [224] did not find changes in concentrations of CO and UHC between 1.1 and 1.2 times the flame height, by using coflow diffusion flames in turbulent regime.

A flame obtained by burning pure *n*-heptane as fuel, fueled at 0.3 mL/min, nitrogen as carrier gas at 500 mL/min (*n*-heptane loaded at 15 % vol.), air as oxygenating stream at 200 mL/min, which results in a height of flame of 74.4 mm, is used as target flame to evaluate height of the probe. 88, 110 and 132 mm (1.2, 1.5 and 1.8 times the height of the flame) of height of probe above burner (HAB) were selected as heights of probe to be tested. Concentration of CO, CO_2, O_2, N_2, NO_2 and UHC (*n*-heptane) of samples at different probe HAB are showed in Figure I.7.

According to Figure I.7, amount of air taken in sampling is proportional to the height of probe, since higher the HAB of probe, higher de O_2 and N_2-concentration. A high

amount of air is undesirable because other species are diluted, as is showed in Figure I.7 for concentration of CO, CO_2 and NO but at low HAB of probe, the variation in concertation is considerable, for instance for NO, as showed in Figure I.7 also, which mean am instability of this specie. 1.5 times the height of flame (in this case 110 mm) appear to be an appropriate HAB of probe to obtain appreciable concentration of combustion products with reasonable variation.

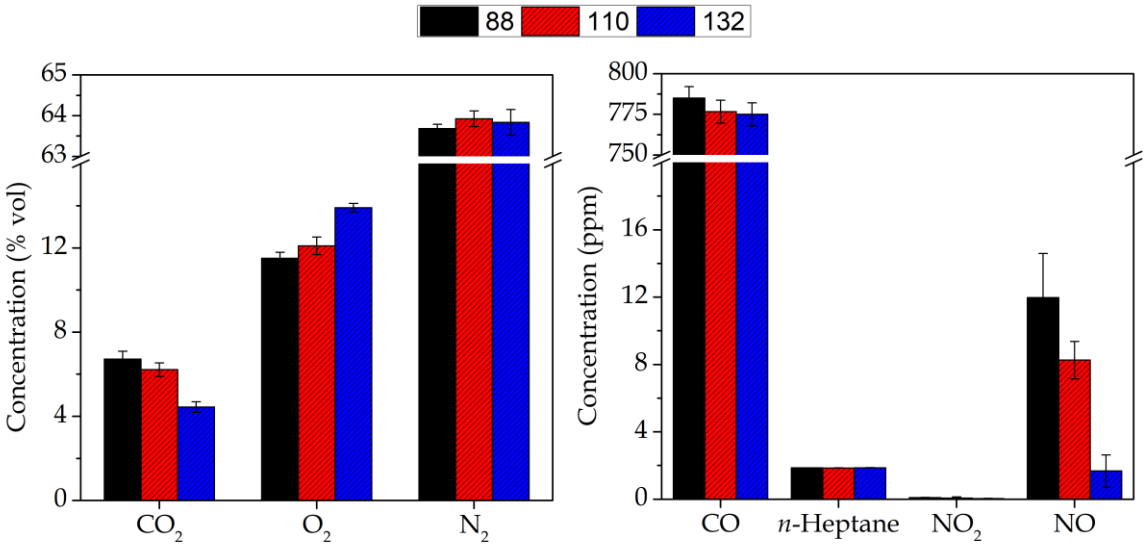

Figure I.7. Influence of height of probe on species concentration

Appendix J. Species calibration for oxyfunctionalization reaction

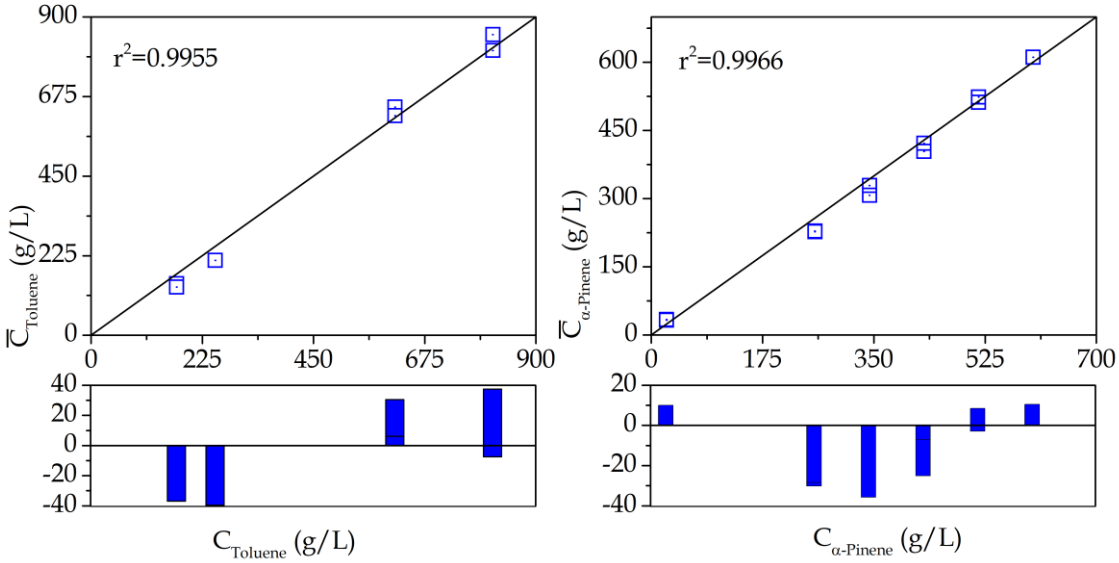

Figure J.1. Parity plots of calibration of toluene and α-pinene

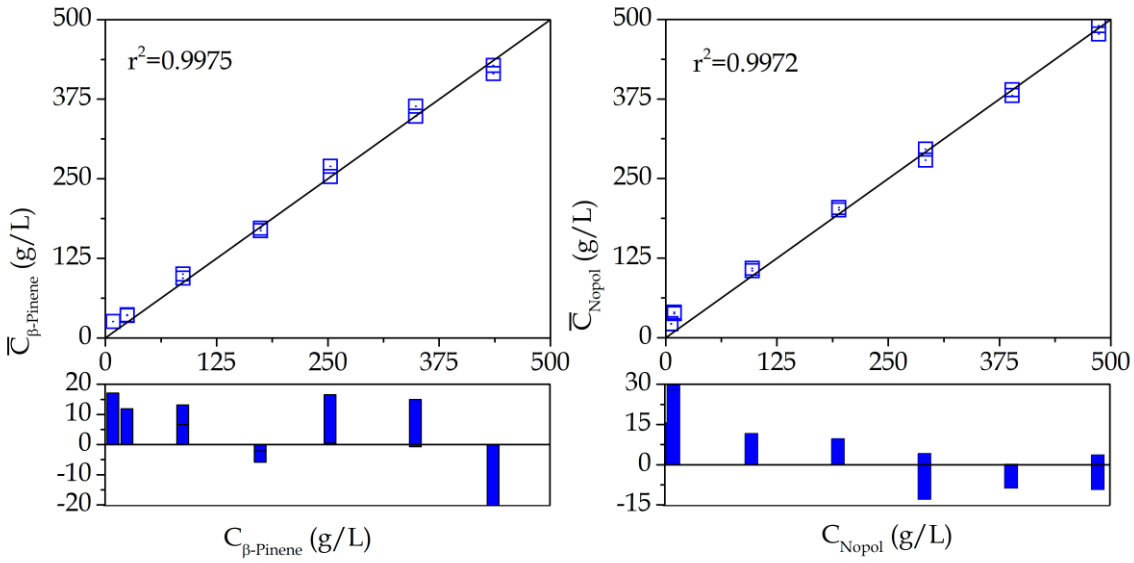

Figure J.2. Parity plots of calibration of β-pinene and nopol

Bibliography

[1] J.K. Mwangi, W.-J. Lee, Y.-C. Chang, C.-Y. Chen, L.-C. Wang, An overview: Energy saving and pollution reduction by using green fuel blends in diesel engines, Appl. Energy. 159 (2015) 214–236. doi:10.1016/j.apenergy.2015.08.084.

[2] A. Groysman, Fuel Additives, in: Corros. Syst. Storage Transp. Pet. Prod. Biofuels, Springer Netherlands, Dordrecht, Netherlands, 2014. doi:10.1007/978-94-007-7884-9_2.

[3] R. Vallinayagam, S. Vedharaj, W.M. Yang, C.G. Saravanan, P.S. Lee, K.J.E. Chua, S.K. Chou, Impact of ignition promoting additives on the characteristics of a diesel engine powered by pine oil–diesel blend, Fuel. 117 (2014) 278–285. doi:10.1016/j.fuel.2013.09.076.

[4] J. Campos-Fernández, J.M. Arnal, J. Gómez, M.P. Dorado, A comparison of performance of higher alcohols/diesel fuel blends in a diesel engine, Appl. Energy. 95 (2012) 267–275. doi:10.1016/j.apenergy.2012.02.051.

[5] S. Kumar, J.H. Cho, J. Park, I. Moon, Advances in diesel–alcohol blends and their effects on the performance and emissions of diesel engines, Renew. Sustain. Energy Rev. 22 (2013) 46–72. doi:10.1016/j.rser.2013.01.017.

[6] L. Wei, C.S. Cheung, Z. Huang, Effect of n-pentanol addition on the combustion, performance and emission characteristics of a direct-injection diesel engine, Energy. 70 (2014) 172–180. doi:10.1016/j.energy.2014.03.106.

[7] L. Li, J. Wang, Z. Wang, H. Liu, Combustion and emissions of compression ignition in a direct injection diesel engine fueled with pentanol, Energy. 80 (2015) 575–581. doi:10.1016/j.energy.2014.12.013.

[8] A. Khalid, M.D. Anuar, A. Sapit, A. Razali, B. Manshoor, M. Fawzi, I. Zaman, Experimental investigation of emissions characteristics of small diesel engine fuelled by blended crude palm oil., Appl. Mech. Mater. 660 (2014) 462–467. doi:10.4028/www.scientific.net/AMM.660.462.

[9] S. Chattopadhyay, R. Sen, Fuel properties, engine performance and environmental benefits of biodiesel produced by a green process, Appl. Energy. 105 (2013) 319–326. doi:10.1016/j.apenergy.2013.01.003.

[10] A. Khalid, S.A. Osman, M.N. Mohamad Jaat, N. Mustaffa, S.M. Basharie, B. Manshoor, Performance and emissions characteristics of diesel engine fueled by biodiesel derived from palm oil., Appl. Mech. Mater. 315 (2013) 517–522, 7 pp. doi:10.4028/www.scientific.net/AMM.315.517.

[11] M. Mofijur, M.G. Rasul, J. Hyde, A.K. Azad, R. Mamat, M.M.K. Bhuiya, Role of biofuel and their binary (diesel–biodiesel) and ternary (ethanol–biodiesel–diesel) blends on internal combustion engines emission reduction, Renew. Sustain. Energy Rev. 53 (2016) 265–278. doi:10.1016/j.rser.2015.08.046.

[12] C.D. Rakopoulos, A.M. Dimaratos, E.G. Giakoumis, D.C. Rakopoulos, Study of turbocharged diesel engine operation, pollutant emissions and combustion noise radiation during starting with bio-diesel or n-butanol diesel fuel blends, Appl. Energy. 88 (2011) 3905–3916. doi:10.1016/j.apenergy.2011.03.051.

[13] V. Raghavan, Combustion Technology: Essentials of Flames and Burners, John Wiley & Sons Ltd., Chichester, United Kingdom, 2016. doi:10.1002/9781119241775.

[14] G.M. Monsalve-Bravo, H.M. Moscoso-Vasquez, H. Alvarez, Scaleup of batch reactors using phenomenological-based models, Ind. Eng. Chem. Res. 53 (2014) 9439–9453. doi:10.1021/ie500587r.

[15] A.K. Coker, Modeling of Chemical Kinetics and Reactor Design, 1st ed., Gulf Professional Pub, Houston, USA, 2001. doi:10.1021/i260051a007.

[16] S. Rezzi, A. Bighelli, V. Castola, J. Casanova, Composition and chemical variability of the oleoresin of Pinus nigra ssp. laricio from Corsica, Ind. Crops Prod. 21 (2005) 71–79. doi:10.1016/j.indcrop.2003.12.008.

[17] A.J.D. Silvestre, Rosin: Major sources, properties and applications, in: M.N. Belgacem, A. Gandini (Eds.), Monomers, Polym. Compos. from Renew. Resour., 1st ed., Elsevier, Oxford, United Kingdom, 2008. doi:10.1016/B978-0-08-045316-3.00004-1.

[18] R. Höfer, Chapter 3B – The pine biorefinery platform chemicals value chain, in: A. Pandey, R. Höfer, M. Taherzadeh, M. Nampoothiri, C. Larroche (Eds.), Ind. Biorefineries White Biotechnol., 1st ed., Elsevier, Amsterdam, Netherlands, 2015: pp. 127–155. doi:10.1016/B978-0-444-63453-5.00004-5.

[19] A. Sukarno, E. Hardiyanto, S. Marsoem, M. Na'iem, Oleoresin production, turpentine yield and components of pinus merkusii from various indonesian provenances, J. Trop. For. Sci. 27 (2015) 136–141.

[20] J. Degenhardt, T.G. Köllner, J. Gershenzon, Monoterpene and sesquiterpene synthases and the origin of terpene skeletal diversity in plants, Phytochemistry. 70 (2009) 1621–1637.

doi:10.1016/J.PHYTOCHEM.2009.07.030.

[21] R. Alén, Pulp Mills and Wood-Based Biorefineries, in: Ind. Biorefineries White Biotechnol., Elsevier, Amsterdam, Netherlands, 2015. doi:10.1016/B978-0-444-63453-5.00003-3.

[22] B. Holmbom, Extraction and utilization of non-structural wood and bark components, in: R. Alén (Ed.), Biorefining For. Resour., Paper Engineers' Association/Paperi ja Puu Oy, Jyväskylä, Finland, 2011.

[23] D.F. Zinkel, J. Rusell, Naval stores : Production, chemistry, utilization, 1st ed., New York, NY : Pulp Chemicals Association, New York, USA, 1989.

[24] L. Jiazheng, High content enviromental protection alcohol ether fuel for vehicle, CN Patent N°. 101100618A, 2008.

[25] L. Jiazheng, High-performance additive for high-content alcohol fuel for vehicles spark ignition engine, CN Patent N°. 101100619, 2008.

[26] L.J.C. Youchun, Preparation of environmentally-friendly liquid fuel with high heat value, CN Patent N°. 101531927, 2009.

[27] B.E. Woomer, L.H. Yen, C.K. Sing, Fuel oil additives, US Patent N°. 5203878, 1993.

[28] Y. Zhang, Methanol fuel for vehicle, CN Patent N°. 103387855, 2013.

[29] E. Hatziemmanouil, Method for refining vegetable oils and additive therefore, and their use as substitute of diesel fuel, US Patent N°. 2008009999A2, 2012.

[30] C.R. Lescura, Additive for internal combustion engines, BR Patent N°. 2007002126, 2009.

[31] B.V. Shankar, Turpentine oil (0 to 30%) fuel system to enhance petrol vehicle average, IN Patent N°. 2001MU00351A, 2005.

[32] V.K. Gupta, G. Kumar, J. Kandpal, V.K. Agrawal, Diesel fuel-turpentine oil blends as substitute fuels for compression ignition engines, IN Patent N°. 2004DE01925, 2006.

[33] R. Karthikeyan, N. V. Mahalakshmi, Turpentine blend composition with diesel oil, IN Patent N°. 211874, 2008.

[34] S. Liang, Biological diesel fuel and its production, CN Patent N°. 1563279, 2005.

[35] R. Vallinayagam, S. Vedharaj, W.M. Yang, P.S. Lee, K.J.E. Chua, S.K. Chou, Combustion performance and emission characteristics study of pine oil in a diesel engine, Energy. 57 (2013) 344–351. doi:10.1016/j.energy.2013.05.061.

[36] R. Vallinayagam, S. Vedharaj, W.M. Yang, C.G. Saravanan, P.S. Lee, K.J.E.

Chua, S.K. Chou, Emission reduction from a diesel engine fueled by pine oil biofuel using SCR and catalytic converter, Atmos. Environ. 80 (2013) 190–197. doi:10.1016/j.atmosenv.2013.07.069.

[37] R. Vallinayagam, S. Vedharaj, W.M. Yang, P.S. Lee, K.J.E. Chua, S.K. Chou, Pine oil–biodiesel blends: A double biofuel strategy to completely eliminate the use of diesel in a diesel engine, Appl. Energy. 130 (2014) 466–473. doi:10.1016/j.apenergy.2013.11.025.

[38] R. Vallinayagam, S. Vedharaj, W.L. Roberts, R.W. Dibble, S.M. Sarathy, Performance and emissions of gasoline blended with terpineol as an octane booster, Renew. Energy. 101 (2017) 1087–1093. doi:10.1016/j.renene.2016.09.055.

[39] R. Vallinayagam, S. Vedharaj, N. Naser, W.L. Roberts, R.W. Dibble, S.M. Sarathy, Terpineol as a novel octane booster for extending the knock limit of gasoline, Fuel. 187 (2017) 9–15. doi:10.1016/j.fuel.2016.09.034.

[40] B.G. Harvey, M.E. Wright, R.L. Quintana, High-Density Renewable Fuels Based on the Selective Dimerization of Pinenes, Energy & Fuels. 24 (2010) 267–273. doi:10.1021/ef900799c.

[41] H.A. Meylemans, R.L. Quintana, B.G. Harvey, Efficient conversion of pure and mixed terpene feedstocks to high density fuels, Fuel. 97 (2012) 560–568. doi:10.1016/j.fuel.2012.01.062.

[42] N.I. Tracy, D. Chen, D.W. Crunkleton, G.L. Price, Hydrogenated monoterpenes as diesel fuel additives, Fuel. 88 (2009) 2238–2240. doi:10.1016/j.fuel.2009.02.002.

[43] C. Kaplan, M. Alma, A. Tutuş, M. Çetinkaya, F. Karaosmanoğlu, Engine Performance and Exhaust Emission Tests of Sulfate Turpentine and No:2 Diesel Fuel Blend, Pet. Sci. Technol. 23 (2005) 1333–1339. doi:10.1081/LFT-200038176.

[44] R. Karthikeyan, N. Mahalakshmi, Performance and emission characteristics of a turpentine–diesel dual fuel engine, Energy. 32 (2007) 1202–1209. doi:10.1016/j.energy.2006.07.021.

[45] R. Yumrutaş, M.H.H. Alma, H. Özcan, Ö. Kaşka, Investigation of purified sulfate turpentine on engine performance and exhaust emission, Fuel. 87 (2008) 252–259. doi:10.1016/j.fuel.2007.04.019.

[46] B.P. Anand, C.G. Saravanan, C.A. Srinivasan, Performance and exhaust emission of turpentine oil powered direct injection diesel engine, Renew. Energy. 35 (2010) 1179–1184. doi:10.1016/j.renene.2009.09.010.

[47] P. Knuuttila, Wood sulphate turpentine as a gasoline bio-component, Fuel. 104 (2013) 101–108. doi:10.1016/j.fuel.2012.06.036.

[48] I.T. Clark, E.E. Harris, Catalytic cracking of rosin 2, J. Am. Chem. Soc. 74 (1952) 1030–1032. doi:10.1021/ja01124a046.

[49] R. Coll, S. Udas, W.A. Jacoby, Production of diesel fuel additives from the rosin acid fraction of crude tall oil, Prog. Thermochem. Biomass Convers. (2001) 1540–1549. doi:10.1002/9780470694954.ch127.

[50] R. Coll, S. Udas, W.A. Jacoby, Conversion of the rosin acid fraction of crude tall oil into fuels and chemicals, Energy & Fuels. 15 (2001) 1166–1172. doi:10.1021/ef010018a.

[51] J. Mikulec, A. Kleinová, J. Cvengroš, L. Joríková, M. Banič, Catalytic transformation of tall oil into biocomponent of diesel fuel, Int. J. Chem. Eng. 2012 (2012) 1–9. doi:10.1155/2012/215258.

[52] J.M. Anthonykutty, K.M. Van Geem, R. De Bruycker, J. Linnekoski, A. Laitinen, J. Räsänen, A. Harlin, J. Lehtonen, Value Added Hydrocarbons from Distilled Tall Oil via Hydrotreating over a Commercial NiMo Catalyst, Ind. Eng. Chem. Res. 52 (2013) 10114–10125. doi:10.1021/ie400790v.

[53] J.M. Anthonykutty, J. Linnekoski, A. Harlin, J. Lehtonen, Hydrotreating reactions of tall oils over commercial NiMo catalyst, Energy Sci. Eng. 3 (2015). doi:10.1002/ese3.70.

[54] N. Xiao-an, J. Jian-chun, D. Wei-di, C. XIA, Study on Synthesis and Properties of Biodiesel Oil from Rosin, Chem. Ind. For. Prod. 27 (2007) 79–81.

[55] A. Bernas, T. Salmi, D.Y. Murzin, J.-P. Mikkola, M. Rintola, Catalytic transformation of abietic acid to hydrocarbons, Top. Catal. 55 (2012) 673–679. doi:10.1007/s11244-012-9846-7.

[56] M. Gürü, U. Karakaya, D. Altıparmak, A. Alıcılar, Improvement of Diesel fuel properties by using additives, Energy Convers. Manag. 43 (2002) 1021–1025. doi:10.1016/S0196-8904(01)00094-2.

[57] A. Keskin, M. Gürü, D. Altiparmak, Influence of tall oil biodiesel with Mg and Mo based fuel additives on diesel engine performance and emission., Bioresour. Technol. 99 (2008) 6434–8. doi:10.1016/j.biortech.2007.11.051.

[58] European-Parliament, Directive (EU) 2018/2001 of the European Parliament and of the council of 11 December 2018, (2018).

[59] G. Totten, S. Westbrook, R. Shah, Fuels and Lubricants Handbook: Technology, Properties, Performance, and Testing, 2nd ed., ASTM International, West Conshohocken, USA, 2003. doi:10.1520/MNL37-EB.

[60] R.A. Kishore Nadkarni, Guide to ASTM Test methods for the analysis of petroleum products and lubricants, West Conshohocken, USA, 2007. doi:ASTM Stock No. MNL44–2nd.

[61] T. Someya, Advanced combustion science, Springer-Verlag Japan, Tokyo, Japan, 2011. doi:10.1007/978-4-431-68228-8.

[62] E.L. Keating, Liquid fuels, in: L.L. Faulkner (Ed.), Appl. Combust., 2nd ed., CRC Press/Taylor & Francis, Boca Raton, USA, 2007: pp. 251–300.

[63] A. Bhattacharya, S. Shivalkar, Re-tooling Benson's group additivity method for estimation of the enthalpy of formation of free radicals: C/H and C/H/O Groups, J. Chem. Eng. Data. 51 (2006) 1169–1181. doi:10.1021/je0503960.

[64] K.G. Joback, R.C. Reid, Estimation of pure-component properties from group-contributions, Chem. Eng. Commun. 57 (1987) 233–243. doi:10.1080/00986448708960487.

[65] D. García, F. Bustamante, E. Alarcón, J.M. Donate, L. Canoira, M. Lapuerta, Improvements of Thermal and Thermochemical Properties of Rosin by Chemical Transformation for Its Use as Biofuel, Waste and Biomass Valorization. (2019) 1–12. doi:10.1007/s12649-019-00863-y.

[66] M. Lapuerta, J.J. Hernández, O. Armas, Kinetic Modelling of Gaseous Emissions in a Diesel Engine, in: SAE Tech. Pap. 2000-01-2939, SAE International, 2000. doi:10.4271/2000-01-2939.

[67] S.R. Turns, An introduction to combustion: concepts and applications, 2nd ed., McGraw-Hill, Singapore, 2000.

[68] C.E. Baukal, The John Zink Hamworthy combustion handbook Volume 1, Fundamentals, 2nd ed., CRC Press/Taylor & Francis, Boca Raton, USA, 2013. (accessed March 7, 2019).

[69] H. Janbazi, O. Hasemann, C. Schulz, A. Kempf, I. Wlokas, S. Peukert, Response surface and group additivity methodology for estimation of thermodynamic properties of organosilanes, Int. J. Chem. Kinet. 50 (2018) 681–690. doi:10.1002/kin.21192.

[70] E.S. Domalski, E.D. Hearing, Estimation of the thermodynamic properties of hydrocarbons at 298.15 K, J. Phys. Chem. Ref. Data. 17 (1988) 1637–1678. doi:10.1063/1.555814.

[71] G.N. Roganov, P.N. Pisarev, V.N. Emel'yanenko, S.P. Verevkin, Measurement and prediction of thermochemical properties. Improved Benson-type increments for the estimation of enthalpies of vaporization and standard enthalpies of formation of aliphatic alcohols, J. Chem. Eng. Data. 50 (2005)

1114–1124. doi:10.1021/je049561m.

[72] N. Cohen, Revised group additivity values for enthalpies of formation (at 298 K) of carbon-hydrogen and carbon-hydrogen-oxygen compounds, J. Phys. Chem. Ref. Data. 25 (1996) 1411–1481. doi:10.1063/1.555988.

[73] S.W. Benson, D.M. Golden, G.R. Haugen, R. Shaw, F.R. Cruickshank, A.S. Rodgers, H.E. O'neal, R. Walsh, Additivity rules for the estimation of thermochemical properties, Chem. Rev. 69 (1969) 279–324. doi:10.1021/cr60259a002.

[74] M. Lapuerta, J. Rodríguez-Fernández, F. Oliva, Determination of enthalpy of formation of methyl and ethyl esters of fatty acids, Chem. Phys. Lipids. 163 (2010) 172–181. doi:10.1016/j.chemphyslip.2009.11.002.

[75] J. Warnatz, U. (Ulrich) Maas, R.W. Dibble, Combustion : physical and chemical fundamentals, modeling and simulation, experiments, pollutant formation, 3rd ed., Springer Berlin Heidelberg, New York, USA, 2006.

[76] D.P. Mishra, Experimental combustion: An introduction, CRC Press/Taylor & Francis, Boca Raton, USA, 2014. doi:10.1201/b17027.

[77] S. Turns, Pollutant emissions, in: J.P. Holamn, J. Lloyd (Eds.), An Introd. to Combust. Concepts Appl., 2nd ed., McGraw-Hill, Singapore, 2000: pp. 550–597.

[78] I.G. Hughes, T.P.A. Hase, Measurements and their Uncertainties: A Practical Guide to Modern Error Analysis, Oxford University Press, New York, USA, 2010.

[79] C.K. Law, Combustion physics, Cambridge University Press, Cambridge, United Kindown, 2006. doi:10.1017/CBO9780511754517.

[80] I. Glassman, R.A. Yetter, N.G. Glumac, Combustion, 5th ed., Elsevier, Waltham, USA, 2015. (accessed March 31, 2017).

[81] P.J. Van Tiggelen, Flame and combustion, Combust. Flame. 111 (1997) 353. doi:10.1016/s0010-2180(97)00009-6.

[82] A.W. Date, Analytic combustion: With thermodynamics, chemical kinetics, and mass transfer, Cambridge University Press, New York, USA, 2011. doi:10.1017/CBO9780511976759.

[83] F.G. Roper, C. Smith, A.C. Cunningham, The prediction of laminar jet diffusion flame sizes: Part II. Experimental verification, Combust. Flame. 29 (1977) 227–234. doi:10.1016/0010-2180(77)90113-4.

[84] M. Lackner, F. Winter, A.K. Agarwal, Handbook of combustion, Vol. 1, Wiley-VCH, Weinheim, Germany, 2010. (accessed March 5, 2018).

[85] J. Ballester, T. García-Armingol, Diagnostic techniques for the monitoring and control of practical flames, Prog. Energy Combust. Sci. 36 (2010) 375–411. doi:10.1016/j.pecs.2009.11.005.

[86] E.L. Keating, Combustion engine testing, in: L.L. Faulkner (Ed.), Appl. Combust., 2nd ed., CRC Press/Taylor & Francis, Boca Raton, USA, 2007: pp. 337–382.

[87] J. Heywood, Internal Combustion Engine Fundamentals, 1st ed., McGraw-Hill, New York, USA, 1988.

[88] C.E. Baukal, Industrial combustion testing, CRC Press/Taylor & Francis, Boca Raton, USA, 2011.

[89] M. Ikegami, Soot Formation Fundamentals, in: T. Someya (Ed.), Adv. Combust. Sci., Springer-Verlag Japan, Tokyo, Japan, 1993: pp. 161–204. doi:10.1007/978-4-431-68228-8_5.

[90] L.F. Fieser, W.P. Campbell, Hydroxyl and amino derivatives of dehydroabietic acid and dehydroabietinol, J. Am. Chem. Soc. 61 (1939) 2528–2534. doi:10.1021/ja01878a080.

[91] A. Tschirch, M. Wolff, The occurrence of abietic acid in resin oil, Arch. Der Pharm. (Weinheim, Ger. 245 (1908) 1–4.

[92] S.R.C. of Syracuse, SciFinder data, New York, USA, n.d.

[93] M. Kono, R. Maruyama, Chemistry of coccids produced in Japan. XI. The resinous constituents of Ceroplastes rubens Mask. I, Nippon Nogei Kagaku Kaishi. 12 (1936) 512–520.

[94] I. Kutan, Separation of pimaric acid from resin of ordinary pine Pinus silvestris, Zhurnal Prikl. Khimii (Sankt-Peterburg, Russ. Fed. 36 (1963) 1149–1151.

[95] E.N. Shmidt, V.A. Pentegova, High-boiling neutral compounds from the oleoresin of Pinus silvestris, Izv. Sib. Otd. Akad. Nauk SSSR, Seriya Khimicheskikh Nauk. (1968) 144–146.

[96] A. Rollett, P. Tabakoff, S. Feimer, Acid constituents of sandarac resin, Monatshefte Fuer Chemie. 50 (1928) 1–5.

[97] J. De Pascual Teresa, A. San Feliciano, del C.M.J. Miguel, Components of Juniperus oxycedrus fruits, An. Quim. 70 (1974) 1015–1019.

[98] L.C. Chang, L.L. Song, E.J. Park, L. Luyengi, K.J. Lee, N.R. Farnsworth, J.M. Pezzuto, A.D. Kinghorn, Bioactive constituents of Thuja occidentalis, J. Nat. Prod. 63 (2000) 1235–1238. doi:10.1021/np0001575.

[99] P.K. Grant, C. Huntrakul, D.R.J. Sheppard, Diterpenes of Dacrydium bidwillii,

Aust. J. Chem. 20 (1967) 969–972. doi:10.1071/CH9670969.

[100] M.Y. Lazarev, M. V Zaretskii, X-ray structural analysis of levopimaric acid, Sin. Org. Soedin. (1970) 127–137.

[101] R. Lombard, J. Ebelin, The hydrogenation of the resin acids of pine gums. II., Bull. Soc. Chim. Fr. (1953) 930–936.

[102] I.I. Bardyshev, K.A. Cherches, Dehydroabietic and palustric acids as component parts of the rosin of Picea excelsa, Dokl. Akad. Nauk SSSR. 116 (1957) 959–960.

[103] W. Gu, S. Wang, Synthesis and antimicrobial activities of novel 1H-dibenzo[a,c]carbazoles from dehydroabietic acid, Eur. J. Med. Chem. 45 (2010) 4692–4696. doi:10.1016/J.EJMECH.2010.07.038.

[104] N.F. Komshilov, High-melting abietic acid, Zhurnal Prikl. Khimii (Sankt-Peterburg, Russ. Fed. 30 (1957) 1111–1115.

[105] W. Nong, X. Chen, L. Wang, J. Liang, H. Wang, L. Long, Y. Huang, Z. Tong, Measurement and correlation of solid-liquid equilibrium for abietic acid+alcohol systems at atmospheric pressure, Fluid Phase Equilib. 367 (2014) 74–78. doi:10.1016/j.fluid.2014.01.018.

[106] J.S. Yadav, G. Baishya, U. Dash, Synthesis of (+)-amberketal and its analog from l-abietic acid, Tetrahedron. 63 (2007) 9896–9902. doi:10.1016/j.tet.2007.06.063.

[107] M. Tsutsui, Japanese pine resins. XI. The isolation of resin acid by the brucine salt technique: the isolation of retene-type acids, Nippon Kagaku Kaishi. Pure Chem. (1953) 496–498.

[108] G.C. Harris, T.F. Sanderson, Resin acids. I. An improved method of isolation of resin acids; isolation of a new abietic-type acid, neoabietic acid., J. Am. Chem. Soc. 70 (1948) 334–339. doi:10.1021/ja01181a104.

[109] G. V Pigulevskii, V.G. Kostenko, Neoabietic and abietic acids-primary resin acids from oleoresin of the Siberian fir (<i>Abies sibirica<i>), Zhurnal Prikl. Khimii (Sankt-Peterburg, Russ. Fed. 33 (1960) 439–444.

[110] S.M. Murray, R.A. O'Brien, K.M. Mattson, C. Ceccarelli, R.E. Sykora, K.N. West, J.H. Davis, The fluid-mosaic model, homeoviscous adaptation, and ionic liquids: Dramatic lowering of the melting point by side-chain unsaturation, Angew. Chemie - Int. Ed. 49 (2010) 2755–2758. doi:10.1002/anie.200906169.

[111] M. Ash, I. Ash, Handbook of Paint and Coating Raw Materials, Volumes 1-2, 2nd ed., Synapse Information Resources, Inc.., Endicott, USA, 2013.

[112] I. Ash, Michael; Ash, Handbook of Plastics and Rubber Additives, Volumes 1-

2, 2nd ed., Synapse Information Resources, Inc.., Endicott, USA, 2013.

[113] A. Wypych, Databook of Plasticizers, 2nd ed., ChemTec Publishing, Toronto, Canada, 2017.

[114] R. Lewis, Sax's Dangerous Properties of Industrial Materials, 12th ed., John Wiley & Sons, New York, USA, 2012. doi:10.1002/0471701343.

[115] W.L. Boatright, A.D. Crum, Nonpolar-volatile lipids from soy protein isolates and hexane-defatted flakes, J. Am. Oil Chem. Soc. 74 (1997) 461–467. doi:10.1007/s11746-997-0107-z.

[116] S. Liu, S. Yu, F. Liu, C. Xie, P. Zhang, Synthesis of methyl abietate catalyzed by acidic functional ionic liquid sulfonic alkylimidazole p-toluenesulfonate., Linchan Huaxue Yu Gongye. 27 (2007) 11–14.

[117] A. Abad, M. Arno, L. R.Domingo, R. J.Zaragoza, Synthesis of (+)-podocarp-8(14)-en-13-one and methyl-(+)-13-oxo-podocarp-8(14)-en-18-oate from abietic acid, Tetrahedron. 41 (1985) 4937–4940. doi:10.1016/S0040-4020(01)96734-1.

[118] M.A. González, J. Correa-Royero, L. Agudelo, A. Mesa, L. Betancur-Galvis, Synthesis and biological evaluation of abietic acid derivatives, Eur. J. Med. Chem. 44 (2009) 2468–2472. doi:10.1016/j.ejmech.2009.01.014.

[119] M. Zhang, P. Xiang, J. Mo, Q. Lan, Y. Zhang, Methyl esterification method of rosin resin acid with low toxicity., CN patent N°. 105712875A, 2016.

[120] P. Mäki-Arvela, B. Holmbom, T. Salmi, D.Y. Murzin, Recent progress in synthesis of fine and specialty chemicals from wood and other biomass by heterogeneous catalytic processes, Catal. Rev. - Sci. Eng. 49 (2007) 197–340. doi:10.1080/01614940701313127.

[121] X. Wang, G. Liu, X. Qiu, Catalytic esterification of rosin by solid acid., Huaxue Shijie. 31 (1990) 207–210.

[122] X. Wang, L. Wang, X. Chen, D. Zhou, H. Xiao, X. Wei, J. Liang, Catalytic methyl esterification of colophony over ZnO/SFCCR with subcritical CO2: catalytic performance, reaction pathway and kinetics., R. Soc. Open Sci. 5 (2018) 172124. doi:10.1098/rsos.172124.

[123] Y. Liu, M. Lv, L. Li, H. Yu, Q. Wu, J. Pang, Y. Liu, C. Xie, S. Yu, S. Liu, Synthesis of Rosin Methyl Ester Using PTSA/ZrO 2 /Mo-MCM-41 Mesoporous Molecular Sieves, Catal. Letters. 149 (2019) 1911–1918. doi:10.1007/s10562-019-02782-y.

[124] J.A. Hudy, Resin Acids. Gas Chromatography of Their Methyl Esters, Anal. Chem. 31 (1959) 1754–1756. doi:10.1021/ac60155a017.

[125] J.K. Volkman, D.G. Holdsworth, D.E. Richardson, Determination of resin acids by gas chromatography and high-performance liquid chromatography in paper mill effluent, river waters and sediments from the upper Derwent Estuary, Tasmania, J. Chromatogr. A. 643 (1993) 209–219. doi:10.1016/0021-9673(93)80555-M.

[126] L. Wang, S. Ding, P. Gan, X. Chen, D. Zhang, X. Wei, X. Wang, A supported nano ZnO catalyst based on a spent fluid cracking catalyst (FC3R) for the heterogeneous esterification of rosin., React. Kinet. Mech. Catal. 119 (2016) 219–233. doi:10.1007/s11144-016-1022-9.

[127] E.K. Plyler, Infrared Spectra of Methanol, Ethanol, and n-Propanol, J. Res. Natl. Bur. Stand. (1934). 48 (1952) 281–286. (accessed October 25, 2018).

[128] M. Mandal, P. Borgohain, P. Begum, R.C. Deka, T.K. Maji, Property enhancement and DFT study of wood polymer composites using rosin derivatives as co-monomers, New J. Chem. 42 (2018) 2260–2269. doi:10.1039/C7NJ03825A.

[129] R.T. Morrison, R.N. Boyd, R. Zugazagoitia Herranz, P. Fiedler, Química orgánica, Addison Wesley Longman, Nucalpan de Juarez, Mexico, 1998.

[130] G. Wypych, Handbook of Fillers, 3rd ed., ChemTec Publishing, Toronto, Canada, 2010.

[131] P.G. Jessop, D.A. Jessop, D. Fu, L. Phan, Solvatochromic parameters for solvents of interest in green chemistry, Green Chem. 14 (2012) 1245–1259. doi:10.1039/c2gc16670d.

[132] M. Galván-Ruiz, J. Hernández, L. Baños, J. Noriega-Montes, M.E. Rodríguez-García, Characterization of Calcium Carbonate, Calcium Oxide, and Calcium Hydroxide as Starting Point to the Improvement of Lime for Their Use in Construction, J. Mater. Civ. Eng. 21 (2009) 694–698. doi:10.1061/(ASCE)0899-1561(2009)21:11(694).

[133] M.I. Zaki, H. Knözinger, B. Tesche, G.A.H. Mekhemer, Influence of phosphonation and phosphation on surface acid–base and morphological properties of CaO as investigated by in situ FTIR spectroscopy and electron microscopy, J. Colloid Interface Sci. 303 (2006) 9–17. doi:10.1016/J.JCIS.2006.07.011.

[134] R.S. Putra, A. Liyanita, N. Arifah, E. Puspitasari, Sawaludin, M.N. Hizam, Enhanced Electro-Catalytic Process on the Synthesis of FAME Using CaO from Eggshell, Energy Procedia. 105 (2017) 289–296. doi:10.1016/j.egypro.2017.03.316.

[135] S. Kaewdaeng, P. Sintuya, R. Nirunsin, Biodiesel production using calcium

oxide from river snail shell ash as catalyst, Energy Procedia. 138 (2017) 937–942. doi:10.1016/j.egypro.2017.10.057.

[136] S. McAllister, l J.-Y. Chen, A.C. Fernandez-Pello, Fundamentals of combustion processes, Springer US, New York, USA, 2011. doi:10.1007/978-1-4419-7943-8.

[137] C.L. Yaws, Yaw's thermophysical Properties of Chemicals and Hydrocarbons, Electronic, Knovel, New York, USA, 2009.

[138] J. Ye, P.R. Medwell, M.J. Evans, B.B. Dally, Characteristics of turbulent *n*-heptane jet flames in a hot and diluted coflow, Combust. Flame. 183 (2017) 330–342. doi:10.1016/j.combustflame.2017.05.027.

[139] Y. Kang, Q. Wang, X. Lu, H. Wan, X. Ji, H. Wang, Q. Guo, J. Yan, J. Zhou, Experimental and numerical study on NOx and CO emission characteristics of dimethyl ether/air jet diffusion flame, Appl. Energy. 149 (2015) 204–224. doi:10.1016/j.apenergy.2015.03.135.

[140] D.Y. Kiran, D.P. Mishra, Experimental studies of flame stability and emission characteristics of simple LPG jet diffusion flame, Fuel. 86 (2007) 1545–1551. doi:10.1016/j.fuel.2006.10.027.

[141] M. Kholghy, M. Saffaripour, C. Yip, M.J. Thomson, The evolution of soot morphology in a laminar coflow diffusion flame of a surrogate for Jet A-1, Combust. Flame. 160 (2013) 2119–2130. doi:10.1016/j.combustflame.2013.04.008.

[142] M. Lapuerta, J. Barba, A.D. Sediako, M.R. Kholghy, M.J. Thomson, Morphological analysis of soot agglomerates from biodiesel surrogates in a coflow burner, J. Aerosol Sci. 111 (2017) 65–74. doi:10.1016/j.jaerosci.2017.06.004.

[143] M.R. Kholghy, J. Weingarten, A.D. Sediako, J. Barba, M. Lapuerta, M.J. Thomson, Structural effects of biodiesel on soot formation in a laminar coflow diffusion flame, Proc. Combust. Inst. 36 (2017) 1321–1328. doi:10.1016/j.proci.2016.06.119.

[144] M.R. Kholghy, Y. Afarin, A.D. Sediako, J. Barba, M. Lapuerta, C. Chu, J. Weingarten, B. Borshanpour, V. Chernov, M.J. Thomson, Comparison of multiple diagnostic techniques to study soot formation and morphology in a diffusion flame, Combust. Flame. 176 (2017) 567–583. doi:10.1016/j.combustflame.2016.11.012.

[145] L.D. Pfefferle, J.B. Zimmerman, D.D. Das, W.J. Cannella, C.S. McEnally, C.J. Mueller, T.A. Kwan, Sooting tendencies of diesel fuels, jet fuels, and their surrogates in diffusion flames, Fuel. 197 (2017) 445–458.

doi:10.1016/j.fuel.2017.01.099.

[146] D.D. Das, W.J. Cannella, C.S. McEnally, C.J. Mueller, L.D. Pfefferle, Two-dimensional soot volume fraction measurements in flames doped with large hydrocarbons, Proc. Combust. Inst. 36 (2017) 871–879. doi:10.1016/j.proci.2016.06.047.

[147] T. Zhang, L. Zhao, M.J. Thomson, Effects of n-propylbenzene addition to n-dodecane on soot formation and aggregate structure in a laminar coflow diffusion flame, Proc. Combust. Inst. 36 (2017) 1339–1347. doi:10.1016/j.proci.2016.05.026.

[148] A.G. Mouis, T.A. Litzinger, Y. Wang, V. Iyer, S. Iyer, M. Linevsky, R.J. Santoro, V. Katta, Effects of a JP-8 surrogate and its components on soot in laminar, N2-diluted ethylene co-flow diffusion flames from 1 to 5atm, Combust. Flame. 162 (2015) 1987–1995. doi:10.1016/j.combustflame.2014.12.017.

[149] C. GmbH, Cheméo (High Quality Chemical Properties), Predict Chem. Phys. Prop. (2016). https://www.chemeo.com/ (accessed January 14, 2019).

[150] P.A. Glaude, R. Fournet, R. Bounaceur, M. Molière, Adiabatic flame temperature from biofuels and fossil fuels and derived effect on NOx emissions, Fuel Process. Technol. 91 (2010) 229–235. doi:10.1016/j.fuproc.2009.10.002.

[151] Knovel Corporation, Knovel Critical Tables, 2nd ed., Knovel, Norwich, New York, 2008.

[152] C.L. Yaws, Yaws' Handbook of Thermodynamic Properties for Hydrocarbons and Chemicals, Electronic, Knovel, New York, USA, 2009.

[153] C.L. Yaws, Thermophysical Properties of Chemicals and Hydrocarbons, 2nd ed., Elsevier, Amsterdam, Netherlands, 2014. doi:10.1016/C2013-0-12615-3.

[154] P. Hellier, M. Talibi, A. Eveleigh, N. Ladommatos, An overview of the effects of fuel molecular structure on the combustion and emissions characteristics of compression ignition engines, Proc. Inst. Mech. Eng. Part D J. Automob. Eng. 232 (2018) 90–105. doi:10.1177/0954407016687453.

[155] A. Fridlyand, S.S. Goldsborough, K. Brezinsky, Single pulse shock tube study on the effects of double bond position in unsaturated hydrocarbons and fatty acid methyl esters, in: Fall Tech. Meet. East. States Sect. Combust. Inst. 2013, Combustion Institute, 2013: pp. 304–309.

[156] D.J. Godwin, V.E. Geo, S. Thiyagarajan, M.L.J. Martin, T. Maiyalagan, C.G. Saravanan, F. Aloui, Effect of hydroxyl (OH) group position in alcohol on performance, emission and combustion characteristics of SI engine, Energy

Convers. Manag. 189 (2019) 195–201. doi:10.1016/j.enconman.2019.03.063.

[157] P.S. Veloo, F.N. Egolfopoulos, Studies of n-propanol, iso-propanol, and propane flames, Combust. Flame. 158 (2011) 501–510. doi:10.1016/j.combustflame.2010.10.001.

[158] T.S. Norton, F.L. Dryer, The flow reactor oxidation of C1-C4 alcohols and MTBE, Symp. Combust. 23 (1991) 179–185. doi:10.1016/S0082-0784(06)80257-2.

[159] J.D. Naber, D.L. Siebers, Effects of gas density and vaporization on penetration and dispersion of diesel sprays, in: SAE Tech. Pap. 960034, 1996. doi:10.4271/960034.

[160] A. Eveleigh, N. Ladommatos, R. Balachandran, A. Marca, Conversion of oxygenated and hydrocarbon molecules to particulate matter using stable isotopes as tracers, Combust. Flame. 161 (2014) 2966–2974. doi:10.1016/j.combustflame.2014.05.008.

[161] D.M. Carari, M.J. Da Silva, Fe(NO3)3-catalyzed monoterpene oxidation by hydrogen peroxide: An inexpensive and environmentally benign oxidative process, Catal. Letters. 144 (2014) 615–622. doi:10.1007/s10562-013-1189-x.

[162] C. Fang, J.J. Dai, H.J. Xu, Q.X. Guo, Y. Fu, Iron-catalyzed selective oxidation of 5-hydroxylmethylfurfural in air: A facile synthesis of 2,5-diformylfuran at room temperature, Chinese Chem. Lett. 26 (2015) 1265–1268. doi:10.1016/j.cclet.2015.07.001.

[163] A. Corma Canos, S. Iborra, A. Velty, Chemical routes for the transformation of biomass into chemicals, Chem. Rev. 107 (2007) 2411–2502. doi:doi.org/10.1021/cr050989d.

[164] J.J.W. Coppen, G.A. Hone, Gum naval stores: turpentine and rosin from pine resin, Food and Agriculture Organization of the United Nations, Rome, Italy, 1995. http://www.fao.org/docrep/018/v6460e/v6460e.pdf.

[165] P.A. Robles-Dutenhefner, K.A. Da Silva, M.R.H. Siddiqui, I. V Kozhevnikov, E. V Gusevskaya, Hydration and acetoxylation of monoterpenes catalyzed by heteropoly acid, J. Mol. Catal. A Chem. 175 (2001) 33–42. doi:10.1016/S1381-1169(01)00217-5.

[166] G. Yang, Y. Liu, Z. Zhou, Z. Zhang, Kinetic study of the direct hydration of turpentine, Chem. Eng. J. 168 (2011) 351–358. doi:10.1016/j.cej.2011.01.037.

[167] M. Ash, I. Ash, Nonoxynol-14 to Noramer 1000, in: Ind. Chem. Thes., 5th ed., Synapse Information Resources, Inc., Massachusetts, USA, 2009.

[168] J.P. Bain, Nopol. I. The Reaction of β-Pinene with Formaldehyde, J. Am. Chem. Soc. 68 (1946) 638–641. doi:10.1021/ja01208a032.

[169] M. Selvaraj, P.K. Sinha, Highly selective and clean synthesis of nopol over well-ordered mesoporous tin silicate catalysts, New J. Chem. 34 (2010) 1921–1929. doi:10.1039/c0nj00080a.

[170] A.L. Villa de P, E. Alarcón, C. Montes de C, Nopol synthesis over Sn-MCM-41 and Sn-kenyaite catalysts, Catal. Today. 107–108 (2005) 942–948. doi:10.1016/j.cattod.2005.07.049.

[171] M. V. Patil, M.K. Yadav, R. V. Jasra, Prins condensation for synthesis of nopol from β-pinene and paraformaldehyde on novel Fe-Zn double metal cyanide solid acid catalyst, J. Mol. Catal. A Chem. 273 (2007) 39–47. doi:10.1016/j.molcata.2007.03.054.

[172] E.A. Alarcón, A.L. Villa, C.M. de Correa, Characterization of Sn- and Zn-loaded MCM-41 catalysts for nopol synthesis, Microporous Mesoporous Mater. 122 (2009) 208–215. doi:10.1016/j.micromeso.2009.03.003.

[173] C. Chu, The Effect of Aromatic Structure on Soot Formation in a Laminar Co-flow Diffusion Flame, University of Toronto, 2016.

[174] D.M. Do, S. Jaenicke, G.K. Chuah, Mesoporous Zr-SBA-15 as a green solid acid catalyst for the Prins reaction, Catal. Sci. Technol. 2 (2012) 1417–1424. doi:10.1039/c2cy20084h.

[175] M.K. Yadav, R. V. Jasra, Synthesis of nopol from β-pinene using ZnCl2 impregnated Indian Montmorillonite, Catal. Commun. 7 (2006) 889–895. doi:10.1016/j.catcom.2006.04.002.

[176] S. V. Jadhav, K.M. Jinka, H.C. Bajaj, Synthesis of nopol via Prins condensation of β-pinene and paraformaldehyde catalyzed by sulfated zirconia, Appl. Catal. A Gen. 390 (2010) 158–165. doi:10.1016/j.apcata.2010.10.005.

[177] A.L. Villa, L.F. Correa, E.A. Alarcón, Kinetics of the nopol synthesis by the Prins reaction over tin impregnated MCM-41 catalyst, Chem. Eng. J. 215–216 (2013) 500–507. doi:10.1016/j.cej.2012.11.030.

[178] D. Casas-Orozco, E. Alarcón, C.A. Carrero, J.M. Venegas, W. McDermott, E. Klosterman, I. Hermans, A.L. Villa, Influence of Tin Loading and Pore Size of Sn/MCM-41 Catalysts on the Synthesis of Nopol, Ind. Eng. Chem. Res. 56 (2017) 6590–6598. doi:10.1021/acs.iecr.7b00789.

[179] D. Casas-Orozco, E. Alarcón, A.L. Villa, Kinetic study of the nopol synthesis by the Prins reaction over tin impregnated MCM-41 catalyst with ethyl acetate

as solvent, Fuel. 149 (2015) 130–137. doi:10.1016/J.FUEL.2014.08.067.

[180] E.A. Alarcón, L. Correa, C. Montes, A.L. Villa, Nopol production over Sn-MCM-41 synthesized by different procedures – Solvent effects, Microporous Mesoporous Mater. 136 (2010) 59–67. doi:10.1016/j.micromeso.2010.07.021.

[181] R.Y. Abrokwah, V.G. Deshmane, D. Kuila, Comparative performance of M-MCM-41 (M: Cu, Co, Ni, Pd, Zn and Sn) catalysts for steam reforming of methanol, J. Mol. Catal. A Chem. 425 (2016) 10–20. doi:10.1016/j.molcata.2016.09.019.

[182] K.S.W. Sing, Reporting physisorption data for gas/solid systems with special reference to the determination of surface area and porosity, Pure Appl. Chem. 57 (2007) 603–619. doi:10.1351/pac198557040603.

[183] A.K. Coker, Scale-Up in Reactor Design, in: Gulf Professional Publishing (Ed.), Model. Chem. Kinet. React. Des., 1st ed., Gulf Professional Publishing, Houston, USA, 2001: pp. 1034–1081. doi:10.1016/b978-088415481-5/50015-2.

[184] H. Nagata, M. Takimura, Y. Yamasaki, A. Nakahira, Syntheses and Characterization of Bulky Mesoporous Silica MCM-41 by Hydrothermal Hot-Pressing Method, Mater. Trans. 47 (2006) 2103–2105. doi:10.2320/matertrans.47.2103.

[185] B. Adrian, D.K. Allan, Heat Transfer Handbook, John Wiley & Sons, New Jersey, USA, 2003.

[186] R. Chhabra, V. Shankar, Coulson and Richardson's Chemical Engineering, Volume 1A - Fluid Flow - Fundamentals and Applications, 7th ed., Elsevier, 2018.

[187] A. Llamas, M. Lapuerta, A.M. Al-Lal, L. Canoira, Oxygen extended sooting index of FAME blends with aviation kerosene, Energy & Fuels. 27 (2013) 6815–6822. doi:10.1021/ef401623t.

[188] L. Grunberg, A.H. Nissan, Mixture law for viscosity, 164 (1949) 799–800. doi:10.1038/164799b0.

[189] M. Lapuerta, J. Rodríguez-Fernández, D. Fernández-Rodríguez, R. Patiño-Camino, Modeling viscosity of butanol and ethanol blends with diesel and biodiesel fuels, Fuel. 199 (2017) 332–338. doi:10.1016/j.fuel.2017.02.101.

[190] H. Song, K.S. Quinton, Z. Peng, H. Zhao, N. Ladommatos, Effects of oxygen content of fuels on combustion and emissions of diesel engines, Energies. 9 (2016) 28. doi:10.3390/en9010028.

[191] Q. Xia, K. Wang, Z. Han, W. Tian, A comparative study of combustion and

emission characteristics of butanol isomers on a diesel engine with dual fuel butanol isomers/diesel compound combustion, Fuel. 254 (2019) 115581. doi:10.1016/j.fuel.2019.05.164.

[192] H. Wei, C. Yao, W. Pan, G. Han, Z. Dou, T. Wu, M. Liu, B. Wang, J. Gao, C. Chen, J. Shi, Experimental investigations of the effects of pilot injection on combustion and gaseous emission characteristics of diesel/methanol dual fuel engine, Fuel. 188 (2017) 427–441. doi:10.1016/j.fuel.2016.10.056.

[193] A. Taghizadeh-Alisaraei, A. Rezaei-Asl, The effect of added ethanol to diesel fuel on performance, vibration, combustion and knocking of a CI engine, Fuel. 185 (2016) 718–733. doi:10.1016/j.fuel.2016.08.041.

[194] M. Lapuerta, J.J. Hernández, D. Fernández-Rodríguez, A. Cova-Bonillo, Autoignition of blends of n-butanol and ethanol with diesel or biodiesel fuels in a constant-volume combustion chamber, Energy. 118 (2017) 613–621. doi:10.1016/j.energy.2016.10.090.

[195] O. Armas, R. García-Contreras, A. Ramos, On-line thermodynamic diagnosis of diesel combustion process with paraffinic fuels in a vehicle tested under NEDC, J. Clean. Prod. 138 (2016) 94–102. doi:10.1016/j.jclepro.2016.01.023.

[196] M. Lapuerta, O. Armas, A. Gómez, Diesel particle size distribution estimation from digital image analysis, Aerosol Sci. Technol. 37 (2003) 369–381. doi:10.1080/02786820300970.

[197] P. Ahlvik, L. Ntziachristos, J. Keskinen, A. Virtanen, Real time measurements of diesel particle size distribution with an electrical low pressure impactor, in: SAE Tech. Pap. 980410, 1998. doi:10.4271/980410.

[198] J. Cha, S. Kwon, D. Kim, S. Park, Effects of equivalence ratio on the near-stoichiometric combustion and emission characteristics of a compression ignition (CI) engine, Fuel Process. Technol. 106 (2013) 215–221. doi:10.1016/j.fuproc.2012.07.028.

[199] B. Esteban, J.R. Riba, G. Baquero, R. Puig, A. Rius, Characterization of the surface tension of vegetable oils to be used as fuel in diesel engines, Fuel. 102 (2012) 231–238. doi:10.1016/j.fuel.2012.07.042.

[200] M. Das, M. Sarkar, A. Datta, A.K. Santra, Study on viscosity and surface tension properties of biodiesel-diesel blends and their effects on spray parameters for CI engines, Fuel. 220 (2018) 769–779. doi:10.1016/j.fuel.2018.02.021.

[201] R.S. Myers, H. Lawrence Clever, The surface tension and density of some hydrocarbon + alcohol mixtures at 303.15 K, J. Chem. Thermodyn. 6 (1974) 949–955. doi:10.1016/0021-9614(74)90216-X.

[202] F.J. Salvador, J. Gimeno, J. De La Morena, M. Carreres, Using one-dimensional modeling to analyze the influence of the use of biodiesels on the dynamic behavior of solenoid-operated injectors in common rail systems: Results of the simulations and discussion, Energy Convers. Manag. 54 (2012) 122–132. doi:10.1016/j.enconman.2011.10.007.

[203] A. Broatch, B. Tormos, P. Olmeda, R. Novella, Impact of biodiesel fuel on cold starting of automotive direct injection diesel engines, Energy. 73 (2014) 653–660. doi:10.1016/j.energy.2014.06.062.

[204] O. Armas, R. García-Contreras, Á. Ramos, A.F. López, Impact of animal fat biodiesel, GTL, and HVO fuels on combustion, performance, and pollutant emissions of a light-duty diesel vehicle tested under the NEDC, J. Energy Eng. 141 (2015). doi:10.1061/(ASCE)EY.1943-7897.0000237.

[205] E. Alptekin, Evaluation of ethanol and isopropanol as additives with diesel fuel in a CRDI diesel engine, Fuel. 205 (2017) 161–172. doi:10.1016/j.fuel.2017.05.076.

[206] M. Lapuerta, J.J. Hernández, J. Rodríguez-Fernández, J. Barba, A. Ramos, D. Fernández-Rodríguez, Emission benefits from the use of n-butanol blends in a euro 6 diesel engine, Int. J. Engine Res. 19 (2018) 1099–1112. doi:10.1177/1468087417742578.

[207] G. Latini, G. Di Nicola, M. Pierantozzi, A critical survey of thermal conductivity literature data for organic compounds at atmospheric pressure and an equation for aromatic compounds, in: Energy Procedia, Elsevier, 2014: pp. 616–625. doi:10.1016/j.egypro.2014.01.066.

[208] T.N. Zwietering, Suspending of solid particles in liquid by agitators, Chem. Eng. Sci. 8 (1958) 244–253. doi:10.1016/0009-2509(58)85031-9.

[209] D. Bennett, P. Solomon, Analysis of gas mixtures by gas chromatography, J. Chromatogr. A. 26 (1967) 593–595. doi:10.1016/S0021-9673(00)84195-3.

[210] S. Nand, M.K. Sarkar, One-step analysis of a mixture of permanent gases and light hydrocarbons by gas chromatography, J. Chromatogr. A. 89 (1974) 73–75. doi:10.1016/S0021-9673(01)84160-1.

[211] V. Dhole, V. Kadam, Analysis of Flue Gases with GC and TCD Detection, Nasik, India, 2011. doi:Thermo Fisher Scientific Application Note 10351.

[212] X. Li, Z. Guan, Analysis of Permanent Gases and Light Hydrocarbons Using Agilent 7820A GC With 3-Valve System, Beijing, China, 2009. doi:Agilent Technologies Application Note 5990-4667.

[213] F. Rogies, A. Hoffmann, J. Rijks, Design and Evaluation of A Capillary GC

Analyzer for Automated Simultaneous Analysis of Permanent Gases and Light Hydrocarbons in Natural Gases, Mülheim an der Ruhr, Germany, 1994. doi:Gerstel Application Note 7/1994.

[214] J. de Zeewu, K. Oden, B. Burger, K. Sellers, A Simple Solution for Permanent Gas Analysis by Gas Chromatography using a FID/Methanizer Detection, Bellefonte, USA, 2017. doi:Restek Corporation Application Note.

[215] Z. Ji, GC/TCD Analysis of A Natural Gas Sample on A Single HP-PLOT Q Column, USA, 2000. doi:Agilten Technologies Application Note 228-387.

[216] T. Fujimori, D. Riechelmann, J. Sato, Effect of liftoff on NOx emission of turbulent jet flame in high-temperature coflowing air, Symp. Combust. 27 (1998) 1149–1155. doi:10.1016/S0082-0784(98)80517-1.

[217] A. Abdelgadir, I.A. Rakha, S.A. Steinmetz, A. Attili, F. Bisetti, W.L. Roberts, Effects of hydrodynamics and mixing on soot formation and growth in laminar coflow diffusion flames at elevated pressures, Combust. Flame. 181 (2017) 39–53. doi:10.1016/j.combustflame.2017.01.003.

[218] H. Dong, Y. Zhang, Z. Gu, Effects of diluents on NOx formation in coflow CH4/air diffusion flames, Korean J. Chem. Eng. 31 (2014) 1002–1007. doi:10.1007/s11814-014-0035-1.

[219] N.J. Kempema, M.B. Long, Combined optical and TEM investigations for a detailed characterization of soot aggregate properties in a laminar coflow diffusion flame, Combust. Flame. 164 (2016) 373–385. doi:10.1016/j.combustflame.2015.12.001.

[220] S. Cao, B.A.V. Bennett, B. Ma, D. Giassi, D.P. Stocker, F. Takahashi, M.B. Long, M.D. Smooke, Effects of fuel dilution and gravity on laminar coflow methane-air diffusion flames: A computational and experimental investigation, in: 8th US Natl. Combust. Meet. 2013, 2013: pp. 3458–3466.

[221] J. Gore, N.J. Zhan, NOx emission and major species concentrations in partially premixed laminar methane/air co-flow jet flames, Combust. Flame. 105 (1996) 414–418. doi:10.1016/0010-2180(95)00177-8.

[222] C.E. Lee, C.B. Oh, J.H. Kim, Numerical and experimental investigations of the NOx emission characteristics of CH4-air coflow jet flames, Fuel. 83 (2004) 2323–2334. doi:10.1016/j.fuel.2004.07.001.

[223] B.C. Connelly, M.B. Long, M.D. Smooke, R.J. Hall, M.B. Colket, Computational and experimental investigation of the interaction of soot and NO in coflow diffusion flames, Proc. Combust. Inst. 32 I (2009) 777–784. doi:10.1016/j.proci.2008.06.182.

[224] J.C. Hermanson, E. Ghaem-Maghami, H. Johari, CO/unburned hydrocarbon emissions of strongly-pulsed turbulent diffusion flames, Combust. Sci. Technol. 176 (2004) 1855–1866. doi:10.1080/00102200490504481.

[225] Y.-H. Liao, J.C. Hermanson, The CO/NOx Emissions of Swirled, Strongly Pulsed Jet Diffusion Flames, Combust. Sci. Technol. 186 (2014) 849–868. doi:10.1080/00102202.2014.885511.

[226] M.C. Drake, S.M. Correa, R.W. Pitz, W. Shyy, C.P. Fenimore, Superequilibrium and thermal nitric oxide formation in turbulent diffusion flames, Combust. Flame. 69 (1987) 347–365. doi:10.1016/0010-2180(87)90126-X.